

Spin orbit interaction and Majorana fermions in carbon nanotubes and Rashba nanowires

Inauguraldissertation
zur
Erlangung der Würde eines Doktors der Philosophie

vorgelegt der
Philosophisch-Naturwissenschaftlichen Fakultät
der Universität Basel

von
Jelena Klinovaja
aus St. Petersburg, Russland

Basel, 2013

Originaldokument gespeichert auf dem Dokumentenserver der Universität Basel
edoc.unibas.ch



Dieses Werk ist unter dem Vertrag „Creative Commons Namensnennung-Keine
kommerzielle Nutzung-Keine Bearbeitung 2.5 Schweiz“ lizenziert. Die vollständige Lizenz
kann unter
creativecommons.org/licenses/by-nc-nd/2.5/ch
eingesehen werden.



Namensnennung-Keine kommerzielle Nutzung-Keine Bearbeitung 2.5 Schweiz

Sie dürfen:



das Werk vervielfältigen, verbreiten und öffentlich zugänglich machen

Zu den folgenden Bedingungen:



Namensnennung. Sie müssen den Namen des Autors/Rechteinhabers in der von ihm festgelegten Weise nennen (wodurch aber nicht der Eindruck entstehen darf, Sie oder die Nutzung des Werkes durch Sie würden entlohnt).



Keine kommerzielle Nutzung. Dieses Werk darf nicht für kommerzielle Zwecke verwendet werden.



Keine Bearbeitung. Dieses Werk darf nicht bearbeitet oder in anderer Weise verändert werden.

- Im Falle einer Verbreitung müssen Sie anderen die Lizenzbedingungen, unter welche dieses Werk fällt, mitteilen. Am Einfachsten ist es, einen Link auf diese Seite einzubinden.
- Jede der vorgenannten Bedingungen kann aufgehoben werden, sofern Sie die Einwilligung des Rechteinhabers dazu erhalten.
- Diese Lizenz lässt die Urheberpersönlichkeitsrechte unberührt.

Die gesetzlichen Schranken des Urheberrechts bleiben hiervon unberührt.

Die Commons Deed ist eine Zusammenfassung des Lizenzvertrags in allgemeinverständlicher Sprache:
<http://creativecommons.org/licenses/by-nc-nd/2.5/ch/legalcode.de>

Haftungsausschluss:

Die Commons Deed ist kein Lizenzvertrag. Sie ist lediglich ein Referenztext, der den zugrundeliegenden Lizenzvertrag übersichtlich und in allgemeinverständlicher Sprache wiedergibt. Die Deed selbst entfaltet keine juristische Wirkung und erscheint im eigentlichen Lizenzvertrag nicht. Creative Commons ist keine Rechtsanwaltsgesellschaft und leistet keine Rechtsberatung. Die Weitergabe und Verlinkung des Commons Deeds führt zu keinem Mandatsverhältnis.

Genehmigt von der Philosophisch-Naturwissenschaftlichen Fakultät auf Antrag von

Prof. Dr. Daniel Loss

Prof. Dr. Pascal Simon

Basel, den 11. December 2012

Prof. Dr. Jörg Schibler
Dekan

Summary

Spin physics plays a fundamental role in many fields of modern condensed matter, notably for spintronics and spin-based quantum computation. At the heart of this lies the spin orbit interaction (SOI), a relativistic effect that is responsible for many fascinating phenomena discovered recently, such as topological insulators, Majorana fermions, spin effects in strongly correlated materials and in optical lattices. The main focus of this PhD work is on spin phenomena and, in particular, on the microscopic origin of SOI in graphene nanostructures and on phenomena connected to it.

The last decades have seen remarkable experimental progress in fabrication of high-purity carbon nanotubes (CNTs). Similar developments have taken place in the field of graphene. This progress paved the way to use carbon-based materials for spin-based effects that are fundamental both for quantum information processing and spintronics. One goal in spintronics is the control of spin by electric fields or gates since this is fast and local, and thus much superior over magnetic field control of spins. The key to such electric control is spin orbit interaction, as it couples charge and spin degrees of freedom.

We have studied SOI effects in carbon nanotubes and other carbon-based materials. The theory we have developed allowed us to explain several experiments on SOI in CNT quantum dots. Moreover, we have proposed a more efficient spin-manipulation in quantum dots by means of e.g. electron dipole spin resonance (EDSR). The SOI also opens up new possibilities for striking effects such as helical modes, modes which transport opposite spins in opposite directions, and Majorana Fermions (MFs), particles that are their own antiparticles, in carbon nanotubes, single- and bilayer graphene.

Majorana fermions in semiconducting nanowires have attracted wide attention over the past years, partially due to their non-Abelian statistics, which is of great interest for topological quantum computation. In our work, we have studied the wavefunction structure and shown that the various MF wavefunctions have different localization lengths in real space and interference between them leads to pronounced oscillations of the MF probability density, which can serve as a signature of MFs in experiments. In the case of a transparent normal-superconducting junction, the MF leaks out from the superconducting into the normal section of the wire and is delocalized over the entire normal section. The interplay between a uniform and a spatially periodic magnetic fields in Rashba nanowires leads to a competition of phases with two topological gaps closing and reopening, resulting in unexpected reentrance behavior. Besides the topological phase with localized Majorana fermions (MFs) we find new phases characterized by fractionally charged fermion (FF) bound states of Jackiw-Rebbi type. The system can be fully gapped by the magnetic fields alone, giving rise to FFs that transmute into MFs upon turning on superconductivity.

Spin orbit interaction is also of a great use for the manipulation of spin states in quantum dots. For example, we have developed a scheme for implementing the CNOT gate over qubits encoded in a pair of electron spins in a double quantum dot. The scheme is based on exchange and spin orbit interactions and on local gradients in Zeeman fields. The switching times for the proposed CNOT gate can be as fast as a few nanoseconds for

realistic parameter values in GaAs semiconductors.

Spin-orbit interaction is not the only interesting hallmark of spin physics. Another quantity of interest is the spin susceptibility, which is connected to the Rudermann-Kittel-Kasuya-Yosida (RKKY) interaction - indirect exchange interaction between spins over relatively large distances mediated by itinerant carriers, determines the magnetic properties of the system. Moreover, it can provide a mechanism for manipulation of spin over larger distances. This is of great interest for the field of spin qubits in order to build scalable quantum computing architectures. We have studied RKKY interaction in CNTs and graphene nanoribbons in the presence of both spin orbit interactions and magnetic fields. In metallic CNTs the RKKY interaction depends strongly on the sublattice and, at the Dirac point, is purely ferromagnetic (antiferromagnetic) for the localized spins on the same (different) sublattice, whereas in semiconducting CNTs the spin susceptibility depends only weakly on the sublattice and is dominantly ferromagnetic. The spin orbit interactions break the SU(2) spin symmetry of the system, leading to an anisotropic RKKY interaction of Ising and Moryia-Dzyaloshinsky form, besides the usual isotropic Heisenberg interaction. Quite remarkably, parameter regimes could be identified that show strong anisotropies. This opens the door for magnetism in these low-dimensional carbon systems that can be controlled by electric fields.

Contents

Summary	i
1 Introduction	1
Bibliography	8
2 Helical modes in carbon nanotubes generated by strong electric fields	11
2.1 Introduction	12
2.2 Tight-binding model for CNTs	12
2.3 Effective low-energy theory	14
2.4 Spectrum and helical states	16
2.5 Valley suppression	17
2.6 Conclusions	18
Bibliography	19
3 Carbon nanotubes in electric and magnetic fields	21
3.1 Introduction	22
3.2 Model	24
3.2.1 Hopping Hamiltonian	25
3.2.2 Spin-orbit interaction	26
3.2.3 Electric fields	27
3.2.4 Magnetic fields	29
3.3 π and σ bands	29
3.3.1 π band hopping Hamiltonian	30
3.3.2 σ band hopping Hamiltonian	32
3.3.3 $\pi\sigma$ hybridization	33
3.4 Effective Hamiltonian for the π band	37
3.5 Field screening	39
3.5.1 Linear response of the π band	40
3.5.2 Analysis of the Kubo integral	43
3.5.3 Exact charge response	46
3.5.4 Field screening	48
3.6 Analysis of the low-energy theory	50
3.6.1 Spectrum without electric field	50

3.6.2	Helical modes	51
3.6.3	Valley suppression	56
3.6.4	External magnetic fields in armchair CNTs	58
3.7	Resonant spin transitions	61
3.7.1	Without dc electric field	62
3.7.2	With static electric field	65
3.8	Conclusions	66
	Bibliography	67
4	Electric-Field Induced Majorana Fermions in Carbon Nanotubes	71
4.1	Introduction	72
4.2	Armchair nanotube low-energy spectrum	73
4.3	Majorana bound states	75
4.4	Interaction effects	77
4.5	Conclusions	79
	Bibliography	80
5	Composite Majorana Fermion Wavefunctions in Nanowires	83
5.1	Introduction	84
5.2	Model	85
5.3	Majorana fermions in the superconducting section	87
5.3.1	Regime of strong SOI and rotating frame	88
5.3.2	Weak SOI regime: Near the topological phase transition	93
5.4	Majorana fermions in NS junctions	96
5.4.1	NS junction in the strong SOI regime	97
5.4.2	NS junction in the weak SOI regime	100
5.5	Conclusions	102
5.A	Finite nanowire	103
5.B	Exact solution in strong SOI regime	104
	Bibliography	105
6	Transition from fractional to Majorana fermions in Rashba nanowires	109
6.1	Introduction	110
6.2	Model	110
6.3	Case I - period $4k_{so}$	112
6.4	Case II - period $2k_{so}$	115
6.4.1	Case IIa - $\mathbf{B}_n \perp \boldsymbol{\alpha}$	115
6.4.2	Case IIb - $\mathbf{B}_n \parallel \boldsymbol{\alpha}$	116
6.5	Electron-electron interactions	116
6.6	Conclusions	117
6.A	MF and FF wavefunctions for different regimes	117
	Bibliography	120

CONTENTS

7 Helical States in Curved Bilayer Graphene	123
7.1 Introduction	124
7.2 Curved bilayer graphene with SOI	124
7.3 Numerical calculation	128
7.4 Conclusions	130
Bibliography	131
8 Giant SOI due to rotating magnetic fields in graphene nanoribbons	133
8.1 Introduction	134
8.2 Graphene nanoribbon	135
8.3 Rashba spin orbit interaction	137
8.4 Rotating magnetic field	137
8.5 Helical modes	138
8.6 Numerics	140
8.7 Stability against edge defects.	140
8.8 Majorana fermions.	140
8.9 Conclusions.	141
Bibliography	142
9 Exchange-based CNOT gates for ST-qubits with spin orbit interaction	145
9.1 Introduction	146
9.2 Model	147
9.3 Parallel geometry	151
9.3.1 Conditional phase gate C_{23}	151
9.3.2 Swap gates π_{12} and π_{34}	154
9.3.3 CNOT gate	156
9.4 Perpendicular geometry	158
9.5 Conclusions	159
Bibliography	161
10 RKKY interaction in carbon nanotubes and graphene nanoribbons	163
10.1 Introduction	164
10.2 Formalism for RKKY	166
10.3 Carbon nanotubes	167
10.3.1 Effective Hamiltonian	167
10.3.2 Spin orbit interaction	168
10.4 RKKY in the absence of SOI	169
10.4.1 Metallic nanotubes	169
10.4.2 Semiconducting nanotubes	170
10.5 RKKY in the presence of SOI	173
10.6 RKKY with magnetic field	176
10.7 Spin Fluctuations	178
10.7.1 Metallic nanotubes	179

10.7.2 Semiconducting nanotubes	180
10.8 Graphene nanoribbons	181
10.8.1 The effective Hamiltonian	181
10.8.2 Spin susceptibility	182
10.9 Conclusions	183
Bibliography	184
Acknowledgements	189
Curriculum Vitae	191
List of Publications	193

Chapter 1

Introduction

Spin physics plays a fundamental role in many fields of modern condensed matter physics, notably for spintronics and spin-based quantum computation. At the heart of this lies the spin orbit interaction (SOI), a relativistic effect derived from the Dirac equation. This interaction couples spin and orbital degrees of freedom.¹ In condensed matter physics the SOI gives rise to many striking phenomena such as topological insulators, Majorana fermions, spin effects in quantum dots, in strongly correlated materials, and in optical lattices. In this thesis we consider a subset of them; however, the work done demonstrates the richness of the field. We focus in particular on spin effects in semiconducting nanowires and carbon-based materials such as graphene, bilayer graphene (BLG), graphene nanoribbons (GNRs), and carbon nanotubes (CNTs). Graphene is a two-dimensional honeycomb lattice composed of carbon atoms [2, 3]. Graphene nanoribbons are finite size sheets of graphene, and carbon nanotubes are sheets of graphene rolled up to cylinders [4]. The experimental techniques for creating, isolating, and analyzing these materials have by now remarkably matured, such that characteristics that have previously been obscured by disorder effects can now be experimentally resolved.

Below we discuss in more detail some of the most striking effects occurring in these systems due to the presence of the spin orbit interaction.

Energy splittings. One of the most obvious consequences of the presence of SOI in a system is a modification of the energy spectrum. In general, the SOI breaks the rotation invariance of spin space and lifts the spin degeneracy of energy levels. The resulting energy splittings can be measured directly in experiments, allowing one to get a direct access to the SOI strength. Several experiments performed on carbon nanotube quantum

¹Its origin can be intuitively understood from the following reasoning [1]. An electric field in the lab frame is seen as an effective magnetic field in the rest system of the moving electron. The effective Hamiltonian can be derived directly from the Dirac equation. This Hamiltonian of a general form can be incorporated into the effective continuum theory of condensed matter via the framework of the tight-binding model, by projecting onto the subspace spanned by the orbitals of each individual atom (see Chapters 2 and 3). This allows us not only to estimate the strength of the SOI but also to gain insight about symmetries of the system.

dots [5, 6, 7] have confirmed our theory of the SOI arising from curvature effects [8, 9].

Helical modes: spin filters and Cooper pair splitters. The breaking of the spin degeneracy and the opening of gaps in the spectrum is not only interesting from a fundamental point of view but it is also of importance for many applications in terms of potential spin devices with radically new functionality. For example, the SOI in carbon nanotubes enables the generation of helical modes in an all-electric setup [8, 9]. Helical modes are rather special conduction modes, where opposite spins are transported in opposite directions, which makes them sought-after for practical implementations. In particular, helical modes pave the way towards the realization of spin filters. Such filters are of a great importance for the field of spintronics which is based on the generation and control of spin polarized currents by purely electric means. Helical modes have also been proposed for implementing Cooper pair splitters [10]. This is a quantum device where Cooper pairs are extracted from a superconductor in such a way that the partners of a pair are spatially separated but their spin-singlet state is left intact. This enables the creation of entanglement over long distances carried by electrons in solid state systems. Such devices, which are of great interest for quantum computing and quantum communication, would also allow one to test the Einstein-Podolsky-Rosen paradox and Bell inequalities. These tests would provide information about fundamental properties of our world such as non-locality of quantum matter.

Majorana fermions and fractional fermions. Majorana fermions [11] (MFs), being their own antiparticles, have attracted much attention in recent years in condensed matter physics [12, 13, 14, 15, 16, 17, 18, 19]. Besides being of fundamental interest, these exotic quantum particles have the potential for being used in topological quantum computing due to their non-Abelian statistics [12]. In particular, the possibility of realizing them as bound states at the ends of semiconducting nanowires in the proximity of an *s*-wave bulk superconductor has led to much research activity in condensed matter. In this scheme, helical modes are generated in the presence of Rashba SOI by applying an external magnetic field. The proximity induced superconductivity couples states with opposite momenta and spins, hence helical modes. If also a spatially varying magnetic field is present, one can generate fractional fermions [20], analogously to Jackiw-Rebbi fermion bound states [21]. Fractional fermions were postulated by Su, Schrieffer, and Hegger in polyacetylene long ago [22]. However, there the half-charge is masked as they appear in pairs due to spin degeneracy. Quite remarkably, however, with the rotational spin symmetry being broken, this degeneracy is absent in the setup proposed in our work [20], and thus the fractional charge is for the first time directly amenable to experimental observation.

Electric control of spin qubit states (EDSR). The manipulation of the electron spin by time-dependent external fields is extremely important for quantum computing and spintronics. Traditionally, a time-dependent magnetic field, coupling to the electron spin via the Zeeman energy, is utilized for Rabi flopping. However, the combination of time-dependent electric fields and spin-orbit coupling gives rise to an all-electric control of the electron spin [so called electric dipole spin resonance (EDSR)]. By applying an electric

field in such a way that the induced SOI favours a spin direction perpendicular to the spin quantization axis of the quantum dot, we demonstrate that resonant spin transitions are possible [9]. The manipulation by an electric field rather than by a magnetic field allows one to perform more operations at the same time because the former can be applied locally with high precision via gates, whereas this is rather difficult to achieve with magnetic fields.

Spin based quantum computing. Quantum computing [23] is based on encoding, manipulating, and measuring quantum information encoded in the state of a collection of quantum two-level systems - qubits. Spin-1/2 is an ideal implementation of a qubit, since it is a natural two-level system, and every pure state of a spin-1/2 corresponds to a state of a qubit. For this reason, spins have been considered as carriers of quantum information in a variety of proposals [24]. The initial proposal [25] called for spins in quantum dots electrically manipulated by the exchange interaction and local time-dependent Zeeman fields. A variety of other encoding schemes and manipulation techniques [26, 27] rely upon encoded qubits. In these schemes, the simplicity of qubit states and minimal number of physical carriers of quantum information are traded for less stringent requirements on experimental implementations. The optimization in the encoding and manipulation protocols is always guided by the state of the art in experiments. Recent results suggest that spin qubits can reside in a variety of material hosts with novel properties. For example, quantum dots in graphene [28] and in carbon nanotubes [29] are less susceptible to the decoherence due to nuclei and spin orbit interaction. However, GaAS remains the most promising route to spin qubits for the near future due to the highly advanced experimental techniques developed for this material.

Spin orbit interaction not only defines the spin levels (splittings) in quantum dots but can also be used for the manipulation of quantum states. For example, the SOI induces a Dzyaloshinskii-Moriya (DM) exchange interaction between two neighboring quantum dots that can be controlled by gates, enabling fully controlled precession of the singlet-triplet-qubit state on the Bloch sphere [30]. Moreover, the SOI affects or quite often even determines electron spin decoherence in quantum dots, so a complete understanding of the SOI becomes highly desirable.

Anisotropic RKKY interaction. The Rudermann-Kittel-Kasuya-Yosida (RKKY) interaction [31, 32, 33], an indirect exchange interaction between two localized spins via spinful charge carriers, is not only a fundamental characteristics of the host system but also finds interesting and useful applications, historically mostly in low-dimensional magnetism. A more recent one is the controlled long-range coupling of spins between distant quantum dots, [34, 35], which is needed in scalable quantum computing architectures such as the surface code [36] built from spin qubits [37]. In addition, the RKKY interaction, enhanced by electron-electron interactions, can initiate a nuclear spin ordering that leads to striking effects such as helical nuclear magnetism at low temperatures [38, 39]. Spin orbit effects break the SU(2) spin-symmetry of the itinerant carriers and thus lead to - besides the effective Heisenberg interaction - anisotropic RKKY terms of Moryia-Dzyaloshinsky and of Ising form. Quite remarkably, when the Fermi level is tuned close

to the gap opened by the SOI in semiconducting nanotubes, we find that the isotropic and anisotropic terms become of comparable size [40]. This has far reaching consequences for ordering in Kondo lattices with RKKY interaction, because this opens up the possibility to have magnetic phase transitions in low-dimensional systems at finite temperature that are tunable by electric gates.

This thesis is organized as follows. In Chapters 2 and 3 we study the interplay of strong electric fields, magnetic fields, and spin-orbit interactions in carbon nanotubes [8, 9]. Focusing on the second shell π and σ orbitals, we derive an effective low-energy theory describing the electrons near the two Dirac points. We also check our main results versus numerical simulations. This theory allows us to predict several striking effects. One of them is the appearance of (spin-filtered) helical modes in an all-electric setup. For perfect armchair nanotubes, there are two pairs of helical modes, one for each valley, transporting up-spins in one direction and down-spins in the opposite direction. This helicity is perfect in that the average spin is non-zero only for this one spin component and zero for all others. Furthermore, we show that the EDSR effect may be implemented by a time-dependent electric field perpendicular to the CNT. The typical Rabi frequencies which can be achieved in this system are in the MHz-GHz range.

The realization of the helical modes in carbon nanotubes opens a new perspective for generation of Majorana fermions in carbon-based systems [17]. In Chapter 4 we discuss such a scenario. By placing the CNT on top of an s -wave superconductor and tuning the Fermi level and the electric field, one can induce pairing of Kramers partners from opposite Dirac points. This pairing opens up inequivalent gaps for the exterior and the interior branches. The Majorana modes obtained are stabilized by either tuning the electric field such that the exterior gap acquires a predominantly s -wave character or by increasing the temperature to remove the pairing in the interior branches.

In Chapter 5 we focus on the spinor-wavefunction for MFs and derive analytical expressions for various limiting cases, loosely characterized as weak and strong SOI regimes [18]. We find that these solutions are superpositions of states that come, in general, from different extremal points of the energy dispersion, one centered around zero-momentum and the others around the Fermi points. Despite having nearly disjoint support in momentum-space, all such contributions must be taken into account, in general, in order to satisfy the boundary conditions imposed on the spinor-wavefunctions in real space. As a consequence of this composite structure of the MF wavefunctions, there will be more than one localization length that characterizes a single MF. The superposition also gives rise to interference effects that lead to pronounced oscillations of the MF probability density in real space. If only a section of the wire is covered with a superconductor, a normal-superconducting (NS) junction is formed. For this case, we find that the MF becomes delocalized over the entire normal section, while still being localized in the superconducting section, as noted in a numerical study by Chevallier *et al.* [41]. Here, we will find analytical solutions for this problem, valid in the weak and strong SOI regime. Depending on the length of the normal section, the support of the MF wavefunction is, again, centered at zero momentum

or the Fermi momenta.

In hybrid systems considered in Chapter 5 a topological phase with a MF at each end of the nanowire is predicted to emerge once an applied uniform magnetic field exceeds a critical value [19]. As pointed out recently [42], the Rashba SOI in such wires is equivalent to a helical Zeeman term, and thus the same topological phase with MFs is predicted to occur in hybrid systems in the presence of a helical field but without SOI [43, 44]. In Chapter 6 we go a decisive step further and address the question, what happens when *both* fields are present, an internal Rashba SOI field as well as a helical—or more generally—a spatially varying magnetic field [20]. Quite remarkably, we discover that due to the interference between the two mechanisms the phase diagram becomes surprisingly rich, with reentrance behavior of MFs and new phases characterized by fractionally charged fermions (FF), analogously to Jackiw-Rebbi fermion bound states [21]. Since the system is fully gapped by the magnetic fields at certain Rashba SOI strengths (in the absence of superconductivity), these FFs act as precursors of MFs into which they transmute by turning on superconductivity.

Carbon nanotubes (see Chapter 4) are not the only candidate among carbon-based systems to host helical modes or Majorana fermions. Topologically confined bound states in bilayer graphene, predicted to occur if a gap and band inversion is enforced by gates [45], provide a good basis for MFs. Quite remarkably, these states are localized in the region where the voltage changes sign, are independent of the edges of the sample, and propagate along the direction of the gates, thus effectively forming a quantum wire. In Chapter 7 we address the spin degrees of freedom in such BLG wires [46]. It is the goal of this work to include spin physics and to show that it gives rise to striking effects. In particular, we uncover a mechanism enabling *helical modes* propagating along the wires. In analogy to Rashba nanowires, topological insulators, and CNTs, such modes provide a platform for a number of interesting effects such as spin-filtering and Majorana fermions. Here, the SOI plays a critical role and in order to substantially enhance it, we consider a BLG sheet with local curvature. Two pairs of top and bottom gates define the direction of the quantum wire, which is chosen in such a way that it corresponds to a ‘semi-CNT’ of zigzag type. In this geometry, the energy levels of the mid-gap states cross in the center of the Brillouin zone. A magnetic field transverse to the wire in combination with intervalley scattering leads to an opening of a gap between two Kramers partners at zero momentum.

In Chapter 7 we show that helical modes can be generated also in graphene nanoribbons by a spatially varying magnetic field or by Rashba SOI with a uniform magnetic field. [47] We demonstrate that the opening of the SOI gap is universal for both semiconducting and metallic graphene armchair nanoribbons independent of the mechanism that induces the spin orbit interaction, leading to a helical regime with nearly perfect spin polarization. Moreover, we have checked numerically that the helical regime is robust against boundary defects. All this makes graphene nanoribbons promising candidates for spin effects and spintronics applications. Our proposal is also a next step in bringing topological features to graphene systems. Topological states proposed by Kane and Mele [48] turned out to be experimentally undetectable due to the small intrinsic SOI of graphene. In contrast,

we show that if a GNR in the helical regime is brought into proximity to an s-wave superconductor, the system can be tuned into a topological phase that supports Majorana fermions. This opens up the possibility to use GNR for topological quantum computing.

Spin orbit interaction effects find their place also in quantum dots, which are of an important use for quantum computation. We study the implementation of the CNOT gate for ST-qubits in Chapter 9. The setup consists of an array of quantum dots with controlled growth direction and the relative orientation of the dots. Pairs of neighboring dots build the ST-qubits, where the quantization axis is determined by an externally applied magnetic field \mathbf{B} . Moreover, we introduce an inhomogeneity in magnetic fields, \mathbf{B}_i , by local micromagnets or by the hyperfine field. The resources used for time-dependent control are the exchange interaction $J_{ij}(t)$ and the SOI vector $\beta_{ij}(t)$. If the SOI vector β is parallel to the external (\mathbf{B}) and local magnetic fields (\mathbf{B}_i), we are able to construct a perfect scheme for the CNOT gate based on the $\pi/4$ -phase gate, $U_{\pi/4}$, consisting of four basic steps. Two of the steps involve interaction of spins that belong to different qubits, and open the possibility of leakage errors. Under the condition of total control over the system parameters, we show that the leakage can be eliminated. In the other two steps, the tuning of the exchange interaction enables perfect swap gates even in the presence of field gradients and SOI. Motivated by recent results on the surface code, we shortly comment also on the 2D architecture. Here we encounter a situation in which the SOI vector β and the magnetic fields, \mathbf{B} and \mathbf{B}_i , are perpendicular. In this case, the leakage to the non-computational space with $S_z \neq 0$ is inevitable, however, it can be made very small.

In Chapter 10 we study the Rudermann-Kittel-Kasuya-Yosida interaction in carbon nanotubes and graphene nanoribbons at zero temperature in the presence of spin orbit interaction.[40] The spin susceptibility in metallic CNTs, characterized by a Dirac spectrum (gapless and linear), crucially depends on whether the localized spins that interact with each other are from the same or from different sublattices. In particular, if the Fermi level is tuned exactly to the Dirac point where the chemical potential is zero the interaction is of ferromagnetic type for spins on A - A or B - B lattice sites, whereas it is of antiferromagnetic type for spins on A - B lattice sites. In semiconducting CNTs, with a sizable bandgap, the spin susceptibility depends only slightly on the sublattices. In all cases, the spin susceptibility is an oscillating function that decays as $1/R$, where R is the distance between the localized spins. The spin orbit interaction breaks the spin degeneracy of the spectrum and the direction invariance of the spin space. As a result, the spin susceptibility is described by a tensor $\chi_{\alpha\beta}$ that has two non-zero off-diagonal components $\chi_{xy} = -\chi_{yx}$, the finite values of which signal the presence of SOI in the system. Moreover, the RKKY interaction is also anisotropic in the diagonal terms, $\chi_{zz} \neq \chi_{xx} = \chi_{yy}$. Quite surprisingly, we find that all non-zero components, diagonal and off-diagonal, can be tuned to be of equal strength by adjusting the Fermi level. These anisotropies, giving rise to Ising and Moriya-Dzyaloshinski RKKY interactions, thus open the possibility to have magnetic order in low-dimensional systems at finite temperature. Metallic armchair GNRs behave similarly to metallic CNTs. Indeed, in both cases the spin susceptibil-

ity shows a strong dependence on the sublattices with, however, different fast oscillating prefactors. A Rashba-like SOI interaction can be generated in armchair GNR by periodic magnetic fields. In contrast to CNTs with intrinsic SOI, this field-generated SOI can be gauged away giving rise to a simple structure of the spin susceptibility tensor.

Bibliography

- [1] J. J. Sakurai, *Modern Quantum Mechanics* (Addison-Wesley, Reading, MA, 1994).
- [2] K. S. Novoselov, A. K. Geim, S. V. Morozov, D. Jiang, M. I. Katsnelson, I. V. Grigorieva, S. V. Dubonos, and A. A. Firsov, *Nature* **438**, 197 (2005).
- [3] A. H. Castro Neto, F. Guinea, N. M. R. Peres, K. S. Novoselov, and A. K. Geim, *Rev. Mod. Phys.* **81**, 109 (2009).
- [4] R. Saito, G. Dresselhaus, and M. S. Dresselhaus, *Physical Properties of Carbon Nanotubes* (Imperial College Press, London, 1998).
- [5] F. Kuemmeth, S. Ilani, D. C. Ralph, and P. L. McEuen, *Nature* **452**, 448 (2008).
- [6] T. S. Jespersen, K. Grove-Rasmussen, J. Paaske, K. Muraki, T. Fujisawa, J. Nygård, and K. Flensberg, *Nat. Phys.* **7**, 348 (2011).
- [7] F. Pei, Edward A. Laird, G. A. Steele, and L. P. Kouwenhoven, arXiv:1210.2622.
- [8] J. Klinovaja, M. Schmidt, B. Braunecker, and D. Loss, *Phys. Rev. Lett.* **106**, 156809 (2011).
- [9] J. Klinovaja, M. Schmidt, B. Braunecker, and D. Loss, *Phys. Rev. B* **84**, 085452 (2011).
- [10] K. Sato, D. Loss, and Y. Tserkovnyak, arXiv:1003.4316.
- [11] E. Majorana, *Nuovo Cimento* **14**, 171 (1937).
- [12] A. Y. Kitaev, *Physics-Uspekhi* **44**, 131 (2001).
- [13] Y. Tanaka, T. Yokoyama, and N. Nagaosa, *Phys. Rev. Lett.* **103**, 107002 (2009).
- [14] M. Sato and S. Fujimoto, *Phys. Rev. B* **79**, 094504 (2009).
- [15] R. M. Lutchyn, J. D. Sau, and S. Das Sarma, *Phys. Rev. Lett.* **105**, 077001 (2010).
- [16] Y. Oreg, G. Refael, and F. von Oppen, *Phys. Rev. Lett.* **105**, 177002 (2010).
- [17] J. Klinovaja, S. Gangadharaiah, and D. Loss, *Phys. Rev. Lett.* **108**, 196804 (2012).
- [18] J. Klinovaja and D. Loss, *Phys. Rev. B* **86**, 085423 (2012).
- [19] J. Alicea, *Rep. Prog. Phys.* **75**, 076501 (2012).
- [20] J. Klinovaja, P. Stano, and D. Loss, *Phys. Rev. Lett.* **109**, 236801 (2012).
- [21] R. Jackiw and C. Rebbi, *Phys. Rev. D* **13**, 3398 (1976).

- [22] W. P. Su, J. R. Schrieffer, and A. J. Heeger, Phys. Rev. Lett. **42**, 1698 (1979).
- [23] M. A. Nielsen and I. L. Chuang, Quantum Computation and Quantum Information (Cambridge University Press, Cambridge, UK, 2000).
- [24] C. Kloeffel and D. Loss, arXiv:1204.5917.
- [25] D. Loss and D. P. DiVincenzo, Phys. Rev. A **57**, 120 (1998).
- [26] J. Levy, Phys. Rev. Lett. **89**, 147902 (2002).
- [27] S. C. Benjamin, Phys. Rev. A **64**, 054303 (2001).
- [28] B. Trauzettel, D. V. Bulaev, D. Loss, and G. Burkard, Nat. Phys. **3**, 192 (2007).
- [29] D. V. Bulaev, B. Trauzettel, and D. Loss, Phys. Rev. B **77**, 235301 (2008).
- [30] J. Klinovaja, D. Stepanenko, B. I. Halperin, and D. Loss, Phys. Rev. B **86**, 085423 (2012).
- [31] M. A. Ruderman and C. Kittel, Phys. Rev. B **96**, 99 (1954).
- [32] T. Kasuya, Prog. Theor. Phys. **16**, 45 (1956).
- [33] K. Yosida, Phys. Rev. **106**, 893 (1957).
- [34] N. J. Craig, J. M. Taylor, E. A. Lester, C. M. Marcus, M. P. Hanson, and A. C. Gossard, Science **304**, 565 (2004).
- [35] Y. Rikitake and H. Imamura, Phys. Rev. B **72**, 033308 (2005).
- [36] D. S. Wang, A. G. Fowler, and L. C. L. Hollenberg, Phys. Rev. A **83**, 020302 (2011).
- [37] L. Trifunovic, O. Dial, M. Trif, J. R. Wootton, R. Abebe, A. Yacoby, and D. Loss, Phys. Rev. X **2**, 011006 (2012).
- [38] P. Simon and D. Loss, Phys. Rev. Lett. **98**, 156401 (2007).
- [39] B. Braunecker, P. Simon, and D. Loss, Phys. Rev. B **80**, 165119 (2009).
- [40] J. Klinovaja and D. Loss, Phys. Rev. B **87**, 045422 (2013).
- [41] D. Chevallier, D. Sticlet, P. Simon, and C. Bena, Phys. Rev. B **85**, 235307 (2012).
- [42] B. Braunecker, G. I. Japaridze, J. Klinovaja, and D. Loss, Phys. Rev. B **82**, 045127 (2010).
- [43] S. Gangadharaiah, B. Braunecker, P. Simon, and D. Loss, Phys. Rev. Lett. **107**, 036801 (2011).

- [44] M. Kjaergaard, K. Wolms, and K. Flensberg, Phys. Rev. B **85**, 020503(R) (2012).
- [45] I. Martin, Y. M. Blanter, and A. F. Morpurgo, Phys. Rev. Lett. **100**, 036804 (2008).
- [46] J. Klinovaja, G. J. Ferreira, and D. Loss, Phys. Rev. B **86**, 235416 (2012).
- [47] J. Klinovaja and D. Loss, Phys. Rev. X **3**, 011008 (2013).
- [48] C. L. Kane and E. J. Mele, Phys. Rev. Lett. **95**, 226801 (2005).

Chapter 2

Helical modes in carbon nanotubes generated by strong electric fields

Helical modes, conducting opposite spins in opposite directions, are shown to exist in metallic armchair nanotubes in an all-electric setup. This is a consequence of the interplay between spin-orbit interaction and strong electric fields. The helical regime can also be obtained in chiral metallic nanotubes by applying an additional magnetic field. In particular, it is possible to obtain helical modes at one of the two Dirac points only, while the other one remains gapped. Starting from a tight-binding model we derive the effective low-energy Hamiltonian and the resulting spectrum.

This chapter has been published in Physical Review Letters 106, 156809 (2011).

2.1 Introduction

Carbon based solid state physics has attracted much attention over the past decades. One of the best studied structures in this field is the carbon nanotube (CNT), a hexagonal lattice of carbon atoms rolled up to a cylinder [1]. The experimental techniques for creating, isolating, and analyzing CNTs have by now remarkably matured, such that characteristics that have previously been obscured by disorder can now be experimentally resolved [2, 3, 4, 5]. An example is the spin-orbit interaction (SOI), which is generally small in CNTs [6, 7, 8, 9], yet can affect electron spin decoherence in CNT quantum dots [10, 11], or allow spin control [12, 13] and spin filtering [14]. A complete understanding of the SOI in CNTs becomes therefore desirable.

In this Letter, we investigate the effect of SOI in combination with a strong electric field in single-wall CNTs within an effective low-energy theory. In particular, we identify experimentally accessible parameter regimes in which SOI and electric fields create helical modes without the need for magnetic fields. This must be contrasted with the helical modes in one-dimensional metals with Rashba SOI, which can be created only with an additional magnetic field that opens a gap at the crossing point of the two Rashba-shifted parabolas [14, 15]. Helical modes, conduction channels transporting opposite spins in opposite directions, naturally lead to spin filtering, but they have also potential application as Cooper pair splitters [16] and, if in proximity with a superconductor, lead to Majorana bound states at the edges of the conductor [17]. Helical modes have also attracted much attention recently in the context of topological insulators [18]. Such physics may be achieved in CNTs in an all-electric setup.

Perfect helical modes appear in armchair CNTs, while in metallic chiral CNTs the spins of the left and right moving modes are not precisely opposite. In the latter, however, perfect helicity can be restored in one Dirac point by an additional magnetic field, whereas the other Dirac point becomes insulating at these energies. This corresponds to the effective suppression of one valley for the low-energy physics.

2.2 Tight-binding model for CNTs

The effective theory is based on a comprehensive model which incorporates the curvature effects for nearest-neighbor hopping and orthogonal orbitals [1]. Charge effects in CNTs due to electric fields have been considered before [19, 20, 21]. Here, we also include spin effects induced by external uniform electric fields (see Fig. 2.1). For this we start from a tight-binding description of the honeycomb lattice on a cylinder surface where we include all orbitals of the second shell and the hybridization of the π and the σ bands. The screening of the electric field by electron-electron interactions is treated on the mean-field level. The corresponding Hamiltonian is

$$H = H_{\text{bs}} + H_{\text{SO}} + H_E^{(1)} + H_E^{(2)}. \quad (2.1)$$

The band structure Hamiltonian H_{bs} includes the hopping of electrons between orbitals of neighboring carbon atoms and accounts for the orbital energies $H_{\text{bs}} = t_{ij}^{\mu\mu'} c_{i\mu\lambda}^\dagger c_{j\mu'\lambda} + \varepsilon_s c_{is\lambda}^\dagger c_{is\lambda}$. Here $c_{i\mu\lambda}$ are the electron operators, i and j are nearest neighbor sites on the honeycomb lattice, $\lambda = \pm 1$ is the spin in z -direction, and μ runs over the second shell orbitals with $\mu = s$ the s orbital and $\mu = p_r, p_t, p_z$ the p orbitals pointing in radial, tangential and z -direction (see Fig. 2.1). The π band is formed by the p_r orbitals, while the σ band is formed by p_t, p_z, s . Summation over repeated indices is assumed. The hopping amplitude $t_{ij}^{\mu\mu'}$ between (j, μ') and (i, μ) is a linear combination of the four fundamental hopping amplitudes $V_{ss}, V_{sp}, V_{pp}^\pi, V_{pp}^\sigma$ [1] with coefficients depending on the relative orientation of the orbitals μ and μ' [22]. The energy difference between s and p orbitals is ε_s .

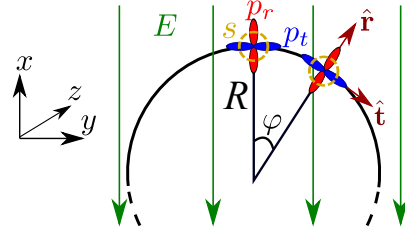


Figure 2.1: Cross section of a CNT in a uniform electric field E . The orientation of the orbitals p_r, p_t as well as the local coordinate system $\hat{\mathbf{r}}, \hat{\mathbf{t}}$ depends on the azimuthal angle φ . The s orbital is indicated by the dashed circles. The electric field E is oriented along the x -direction of the global coordinate system. The z -direction is along the nanotube.

The atomic SOI is modeled by the on-site Hamiltonian $H_{\text{SO}} = i\Delta_{\text{SO}}\varepsilon^{\mu\nu\eta}c_{i\mu\lambda}^\dagger S_{\lambda\lambda'}^\nu c_{i\eta\lambda'}$, where now $\mu, \eta = p_r, p_t, p_z$, $\varepsilon^{\mu\nu\eta}$ is the Levi-Civita symbol, and $\Delta_{\text{SO}} = 6\text{meV}$ [23]. The index $\nu = r, t, z$ labels the spin components in the local coordinate system, i.e., $S^r = S^x \cos \varphi_i + S^y \sin \varphi_i$, $S^t = S^y \cos \varphi_i - S^x \sin \varphi_i$, with φ_i the azimuthal angle of site i (see Fig. 2.1) and $S^{x,y,z}$ the spin Pauli matrices (with eigenvalues ± 1).

An electric field oriented perpendicular to the tube axis affects the electrons in two ways. First, the orbital energies are modulated by the electrostatic potential gradient. This is described by the on-site energy Hamiltonian $H_E^{(1)} = eE^*R \cos(\varphi_i)c_{i\mu\lambda}^\dagger c_{i\mu\lambda}$, where E^* is the screened electric field, e is the electron charge, and R is the CNT radius. This Hamiltonian induces a rearrangement of charges on the CNT surface and so, by Coulomb interaction, leads to screening of E . Hence, $H_E^{(1)}$ depends on the screened field inside the tube E^* , which we find in the linear regime to be given by $E^* = E/\gamma$ with $\gamma \simeq 5$, in agreement with Refs. [19, 20, 21]. However, the renormalization of the Fermi velocity v_F [20] is found to be negligible for the parameters used in this paper.

Second, an electrostatic potential $\phi(\mathbf{r})$ varying on the lattice scale induces intra-atomic transitions between orbitals μ and μ' because generally $\langle \mu | \phi(\mathbf{r}) | \mu' \rangle \neq 0$. Most important is the $s-p_r$ transition because of two reasons: 1) It is the only transition directly coupling π and σ bands, thus giving rise to a first order effect in the $s-p_r$ coupling strength. 2) Its strength is determined by the unscreened field E and not by $E^* < E$. Indeed, the

induced potential ϕ_{ind} cancels in $H_E^{(2)}$, i.e. $\langle p_r | \phi_{\text{ind}}(r) | s \rangle = 0$, as ϕ_{ind} is approximately an even function in r about $r = R$. Based on these arguments, we keep only the s - p_r transition. The validity of this approximation was also verified numerically. The resulting Hamiltonian is $H_E^{(2)} = -eE\xi_0 \cos(\varphi_i) c_{ip_r\lambda}^\dagger c_{is\lambda} + \text{H.c.}$, where $\xi_0 = -\langle p_r | r | s \rangle = \frac{3a_B}{Z} \simeq 0.5\text{\AA}$ with a_B the Bohr radius and $Z \simeq 3.2$, where we have assumed hydrogenic wave functions for the second shell carbon orbitals.

Table 2.1: The effective Hamiltonian for CNTs. $a \simeq 2.4\text{\AA}$ is the lattice constant. θ is the chiral angle ($\theta = \frac{\pi}{6}$ for armchair CNTs). $\sigma_{1,2}$ are the Pauli matrices in sublattice space. $S^{x,y,z}$ are the spin operators (eigenvalues ± 1). $(V_{ss}, V_{sp}, V_{pp}^\pi, V_{pp}^\sigma, \varepsilon_s) = -(6.8, 5.6, 3.0, 5.0, 8.9)$ eV [1], $\Delta_{\text{SO}} = 6$ meV [23]. The Fermi velocity is $v_F = \sqrt{3}|V_{pp}^\pi|a/2\hbar \simeq 0.95 \times 10^6$ m/s.

$H_{\text{orb}}^{\text{cv}} = \hbar v_F (\Delta k_{\text{cv}}^t \sigma_1 + \tau \Delta k_{\text{cv}}^z \sigma_2)$	$\hbar v_F \Delta \mathbf{k}_{\text{cv}} = \hbar v_F \begin{pmatrix} \Delta k_{\text{cv}}^t \\ \Delta k_{\text{cv}}^z \end{pmatrix} = \tau \frac{V_{pp}^\pi (V_{pp}^\pi - V_{pp}^\sigma)}{8(V_{pp}^\pi + V_{pp}^\sigma)} \begin{pmatrix} a \\ R \end{pmatrix}^2 \begin{pmatrix} -\cos 3\theta \\ \sin 3\theta \end{pmatrix} \simeq \tau \frac{5.4 \text{ meV}}{R[\text{nm}]^2} \begin{pmatrix} -\cos 3\theta \\ \sin 3\theta \end{pmatrix}$
$H_{\text{SO}}^{\text{cv}} = \alpha S^z \sigma_1 + \tau \beta S^z$	$\alpha = \frac{\sqrt{3}\varepsilon_s \Delta_{\text{SO}} (V_{pp}^\pi - V_{pp}^\sigma)}{18(V_{sp})^2(R/a)} \simeq \frac{-0.08 \text{ meV}}{R[\text{nm}]} \quad \beta = \frac{-\sqrt{3}\Delta_{\text{SO}} V_{pp}^\pi \cos 3\theta}{3(V_{pp}^\pi + V_{pp}^\sigma)(R/a)} \simeq \frac{-0.31 \text{ meV}}{R[\text{nm}]} \cos 3\theta$
$H_{\text{SO}}^{\text{el}} = \tau e E \xi S^y \sigma_2$	$\xi = -\frac{\Delta_{\text{SO}}}{3V_{sp}} \xi_0 \simeq 2 \times 10^{-5} \text{ nm} \quad eE\xi \simeq 0.2 \text{ meV for } E = 1 \text{ V/nm}$

*) see also Refs. [6, 7, 8, 9].

2.3 Effective low-energy theory

The microscopic model allows us to formulate an effective low-energy theory for the π band near the Dirac points \mathbf{K} and \mathbf{K}' . As explained, we include the curvature effects and the s - p_r transition $H_E^{(2)}$ important for the SOI, and neglect the other inessential interactions. We have tested this against numerical solutions of the full Hamiltonian [Eq. (2.1)]. We also checked that additional trigonometrically modulated perturbations, such as s - p_t transitions or sublattice staggered potentials, do not change the spectrum qualitatively.

Hamiltonian (2.1) can be written as $H = H_\pi + H_\sigma + H_{\pi\sigma}$, where H_π and H_σ describe the π and σ bands, and $H_{\pi\sigma}$ the $\sigma\pi$ coupling. For momenta k close to a Dirac point $\|H_{\pi\sigma}\| \ll \|H_\pi - H_\sigma\|$. In perturbation theory we obtain $H_\pi^{\text{eff}} = H_\pi + H_{\pi\sigma}[H_\pi - H_\sigma]^{-1}H_{\pi\sigma} + \mathcal{O}((a/R)^2)$. Here we keep only terms up to second order in the small parameter a/R and the small energies Δ_{SO} , $eE\xi_0$ which must be compared to typical hopping amplitudes \sim eV. $H_{\pi\sigma} \simeq H_{\text{bs}}^{\pi\sigma} + H_{\text{SO}}^{\pi\sigma} + H_E^{(2)}$, where the superscript $\pi\sigma$ refers to the terms coupling the π and the σ bands. We calculate the effective Hamiltonian for the π band

$$H_\pi^{\text{eff}} = H_\pi^0 + H_{\text{orb}}^{\text{cv}} + H_{\text{SO}}^{\text{cv}} + H_{\text{SO}}^{\text{el}}, \quad (2.2)$$

where the last three terms are explicitly listed in Table 2.1, including numerical values for typical CNTs. Furthermore, $H_\pi^0 = \lim_{R \rightarrow \infty} H_\pi = \hbar v_F(k_G^0 \sigma_1 + k \tau \sigma_2)$ is the π band

Hamiltonian for flat graphene with periodic boundary conditions, with $\tau = \pm 1$ labeling the two inequivalent \mathbf{K} and \mathbf{K}' points and k the momentum along the tube measured from the corresponding Dirac point. For semiconducting CNTs, $k_G^0 = (n - \tau\delta/3)/R \neq 0$ leads to a gap $2\hbar v_F |k_G^0|$, where $n \in \mathbb{Z}$ is the subband index and $\delta = (N_1 - N_2) \bmod 3$ for a (N_1, N_2) -CNT. In the following, we consider only the lowest subband in metallic CNTs defined by $k_G^0 = 0$ [1].

$H_{\text{orb}}^{\text{cv}}$ describes the curvature induced k -shift of the Dirac points [6, 9], e.g., $\mathbf{K} \rightarrow \mathbf{K} - \Delta\mathbf{k}_{\text{cv}}$, with $\Delta\mathbf{k}_{\text{cv}} = (\Delta k_{\text{cv}}^t, \Delta k_{\text{cv}}^z)$. The shift Δk_{cv}^z is parallel to the tube and can be removed by a gauge transformation shifting the origin of k . For non-armchair CNTs, $\Delta k_{\text{cv}}^t \neq 0$ and gaps are introduced by the curvature $H_{\text{orb}}^{\text{cv}}$. $H_{\text{SO}}^{\text{cv}}$ contains the curvature induced SOI [6, 7, 9, 8]. It contains only S^z because $S^{r,t}$ depend on $\cos \varphi$ and $\sin \varphi$, which average out in the φ integration.

On the other hand, $H_E^{(2)} \propto \cos \varphi$ which, in combination with the SOI terms involving $S^t = S^y \cos \varphi - S^x \sin \varphi$, leads to a nonvanishing $H_{\text{SO}}^{\text{el}} \propto S^y \sigma_2 \Delta_{\text{SO}} e E \xi_0 \int d\varphi \cos^2 \varphi$ [24]. Since the term proportional to S^r couples only within the σ band, it leads to negligible higher order corrections. Hence,

$$H_{\text{SO}}^{\text{el}} = \tau e E \xi S^y \sigma_2, \quad (2.3)$$

where $\xi = -\xi_0 \Delta_{\text{SO}} / 3V_{sp}$. This is one of our main results.

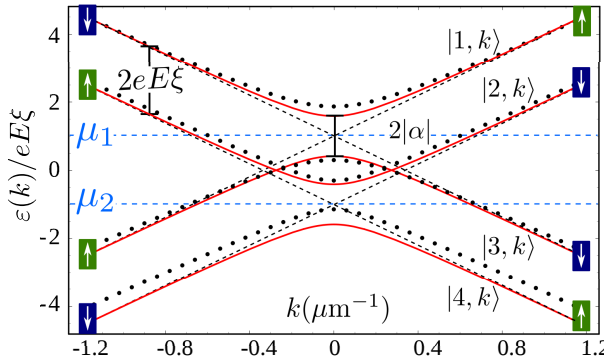


Figure 2.2: Energy dispersion $\varepsilon(k)$ of a $(10,10)$ armchair nanotube (implying $R = 0.67\text{nm}$). The solid (red) lines show the analytical results [see Eq. (2.4) and Tab. 2.1] and the dots show numerical results obtained from H in Eq. (2.1). The axial k -shift Δk_{cv}^z has been removed in both, the numerical and the analytical spectrum. The arrows correspond to the S^y projections and are reversed for $E \rightarrow -E$. The field strength is $E = 1 \frac{\text{V}}{\text{nm}}$ so that the splitting $2eE\xi \simeq 0.4\text{meV}$ and the gap $2|\alpha| \simeq 0.24\text{meV}$. The dashed lines indicate the spectrum for the case $\alpha = 0$ with the spin-degeneracies at $k = 0$. The dashed gray (light blue) lines indicate chemical potentials at which only helical modes exist [see Eq. (2.5)].

2.4 Spectrum and helical states

First we focus on armchair CNTs, assuming that Δk_{cv}^z has been gauged away. Furthermore, $\Delta k_{\text{cv}}^t = 0$ and $\beta = 0$ so that the physics is completely determined by the interplay of $H_{\text{SO}}^{\text{el}}$ and $\alpha S^z \sigma_1$. In Fig. 2.2, we show the spectrum for a (10,10)-CNT in an electric field of 1V/nm. For $|k| \gg |\alpha/\hbar v_F|$, $H_{\text{SO}}^{\text{el}}$ aligns the spin in y -direction. For the right-moving branch ($\tau\sigma_2 = 1$, positive slope) the energy of the $S^y = \uparrow$ state is higher than the energy of the $S^y = \downarrow$ state by $2eE\xi$. For the left-moving branch ($\tau\sigma_2 = -1$, negative slope) the $S^y = \downarrow$ state is higher in energy. Without the term $\alpha S^z \sigma_1$ the spectrum would be spin-degenerate at $k = 0$ (dashed lines in Fig. 2.2). Unlike in usual one-dimensional conductors [15, 14] these degeneracies cannot be lifted by a uniform magnetic field because hybridization between the crossing bands requires the combination of spin flip and sublattice hybridization. This is, however, caused precisely by $\alpha S^z \sigma_1$, which is generated by virtual transitions to the σ band that result in the simultaneous spin and sublattice hybridization. As a result, a gap of size $2|\alpha|$ is opened at each degeneracy point. The resulting spectrum, shown in Fig. 2.2, at the \mathbf{K} point has four branches, the subbands $|m, k\rangle$, given by

$$\varepsilon(k) = \pm eE\xi \pm \sqrt{\alpha^2 + (\hbar v_F k)^2}. \quad (2.4)$$

An equivalent spectrum exists at \mathbf{K}' . The spin orientations on the branches for $|k| \gg |\alpha/\hbar v_F|$ are identical at both Dirac points (arrows in Fig. 2.2). For general k , the S^y expectation value in state $|m, k\rangle$ is given by

$$\langle m, k | S^y | m, k \rangle = \pm k / \sqrt{(\alpha/\hbar v_F)^2 + k^2}, \quad (2.5)$$

where for $eE\xi > 0$ the $+$ corresponds to subbands $m = 1, 4$ in Fig. 2.2, and the $-$ to $m = 2, 3$ (and vice versa for $eE\xi < 0$). Note also that the expectation values of S^x and S^z in all states give zero, so that only $\langle S^y \rangle \neq 0$. In this sense, the states are always perfectly spin-polarized, even though the measured total spin is not unity. The bands crossing the chemical potentials μ_1 and μ_2 indicated in Fig. 2.2 have $\langle S^y \rangle \simeq \pm 0.95$. We also note that electron-electron interactions generally lead to an enhancement of the gap $2|\alpha|$ [14].

Fig. 2.2 shows the analytical spectrum Eq. (2.4) for an armchair CNT in comparison with a numerical diagonalization of Hamiltonian (2.1). The qualitative features of the spectrum are well preserved by the effective theory.

If, in an armchair CNT, the chemical potential is tuned to μ_1 or μ_2 (see Fig. 2.2), the remaining conducting modes are helical, i.e., the direction of motion is coupled to the spin direction. In the present case, the spin points along $\mathbf{E} \times \mathbf{v}$, where $\mathbf{v} = \pm v_F \hat{\mathbf{z}}$ for right and left movers, respectively. In particular, this implies that $\mathbf{E} \rightarrow -\mathbf{E}$ also reverses the helicity, thus inverting the spin filtering. We note that the helical modes are stable against small deviations from the (N, N) -CNT (armchair) case with chiral angle $\theta = \frac{\pi}{6}$. The additional terms βS^z and $\hbar v_F \Delta k_{\text{cv}}^t \sigma_1$, which appear for $\theta \neq \frac{\pi}{6}$, partially align the spin in z -direction and open gaps at the zero-energy crossing points. We find that for metallic chiral CNTs, e.g. with $(N+3, N)$ and $N \simeq 10 - 20$, that are close to the armchair limit,

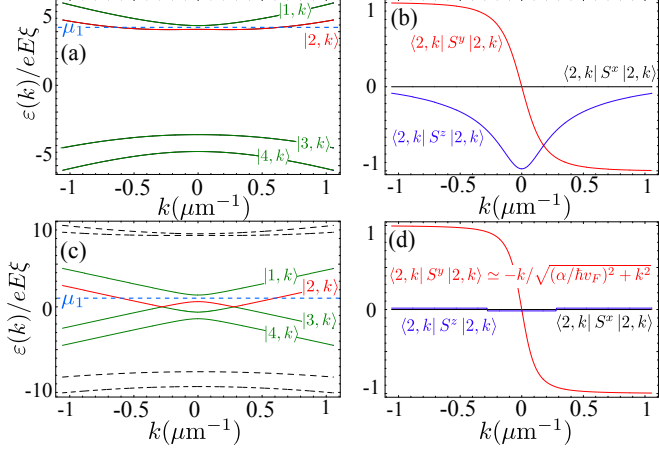


Figure 2.3: Chiral (17,14)-CNT with electric field $E = 1\text{V/nm}$ ($eE\xi \simeq 0.2\text{meV}$). (a) The spectrum and (b) the spin expectation values at the \mathbf{K}/\mathbf{K}' point for the $|2,k\rangle$ subband and magnetic field $B_z = 0$. For $B_z = 0.81\text{T}$, the bands (c) at \mathbf{K}' (dashed lines) are gapped, while the spectrum at \mathbf{K} (solid lines) has the same form as in the armchair case [Eq. (2.4)]. The size of the gap is $2|\alpha| = 0.16\text{meV}$. The spin expectation values (d) at \mathbf{K} for $|2,k\rangle$ follow closely the armchair case [see Eq. (2.5)].

good spin polarization ($\langle S^y \rangle \sim 90\%$ and $\langle S^z \rangle < 20\%$) can still be obtained (see also Fig. 2.3).

2.5 Valley suppression

In chiral $(N + 3l, N)$ -CNTs, with $l = 1, 2, \dots$, it is possible to mostly restore the armchair spectrum and spinor properties for one Dirac point by the further application of a magnetic field B_z along the tube. As mentioned above, $\theta < \frac{\pi}{6}$ results in $\cos(3\theta) \neq 0$, thus leading to two additional terms in the Hamiltonian: a transverse k -shift $\hbar v_F \Delta k_{cv}^t \sigma_1$ and an effective Zeeman field $\tau \beta S^z$. These terms have opposite signs at different Dirac points. The field B_z leads to terms of the same form, yet with equal signs at both Dirac points, so that the chirality-induced $\cos(3\theta)$ -terms can be canceled at one of the Dirac points, whereas they are doubled at the other. Indeed, the orbital effect of B_z adds $\Delta k_B^t = \pi B_z R / \Phi_0$ to Δk_{cv}^t , with Φ_0 the magnetic flux quantum. The Zeeman effect of B_z adds $\mu_B B_z S^z$ to $\tau \beta S^z$. Due to the different radius (R) dependencies of the Zeeman and orbital terms, R and B_z can be chosen such that both $\cos(3\theta)$ terms in Table 2.1 cancel at one Dirac point, provided that $\Delta_{SO} > 0$ [25] (see Fig. 2.3). However, since R cannot be chosen continuously, the cancellation is perfect only for one of the two terms. The Zeeman term can be removed at \mathbf{K} with $B_z = -\mu_B / \beta$, but small gaps will remain at energy $\varepsilon = 0$. On the other hand, if the $\varepsilon = 0$ gaps are to be closed, B_z must be tuned such that $\Delta k_B^t + \Delta k_{cv}^t = 0$. The

small residual Zeeman term $\beta^* = \beta + \mu_B B_z$ ($|\beta^*| \ll |\beta|$) then leads to

$$\varepsilon = \pm \sqrt{(\beta^*)^2 + (eE\xi)^2} \pm \sqrt{(\hbar v_F k)^2 + \alpha^2}, \quad (2.6)$$

and to a small spin-polarization $\langle S^z \rangle \simeq \pm \beta^*/eE\xi$ ($\langle S^x \rangle = 0$ in all cases).

An illustrative example is the (17,14)-CNT with $B_z \simeq 0.81\text{T}$, for which the orbital and Zeeman cancellations work particularly well. At \mathbf{K} the spectrum and the spinor properties $\langle m, k | S^{x,y,z} | m, k \rangle$ of an armchair CNT are restored, while at \mathbf{K}' the curvature-induced gap $\hbar v_F \Delta k_{cv}^t$ is amplified by a factor of 2 (see Fig. 2.3). This amplification is sufficient to remove all states of \mathbf{K}' from the relevant energy range so that only \mathbf{K} contributes a single pair of helical modes at the chemical potential μ_1 .

2.6 Conclusions

We note that as an immediate consequence of the SOI induced gaps the conductance of the CNT is reduced by a factor of two, and by an additional factor of two if the valley degeneracy is lifted. As mentioned, helical modes can be used as spin filters, Cooper pair splitters, and allow for Majorana fermions at the CNT edges if the latter is brought in contact with a superconductor. These properties, together with the all-electric control, make CNTs attractive candidates for spintronic and quantum computing applications.

We acknowledge discussions with D. L. Maslov, and funding from the Swiss NSF, NCCR Nanoscience (Basel), and DARPA QuEST.

Bibliography

- [1] R. Saito, G. Dresselhaus, and M. S. Dresselhaus, *Physical Properties of Carbon Nanotubes*, (Imperial College Press, London, 1998).
- [2] F. Kuemmeth, S. Ilani, D. C. Ralph, and P. L. McEuen, *Nature* **452**, 448 (2008).
- [3] H. O. H. Churchill, A. J. Bestwick, J. W. Harlow, F. Kuemmeth, D. Marcos, C. H. Stwertka, S. K. Watson, and C. M. Marcus, *Nat. Phys.* **5**, 321 (2009).
- [4] G. A. Steele, G. Gotz, and L. P. Kouwenhoven, *Nature Nanotechnology* **4**, 363 (2009).
- [5] H. Aurich, A. Baumgartner, F. Freitag, A. Eichler, J. Trbovic, and C. Schönenberger, *Appl. Phys. Lett.* **97**, 153116 (2010).
- [6] T. Ando, *J. Phys. Soc. Jpn.* **69**, 1757 (2000).
- [7] D. Huertas-Hernando, F. Guinea, and A. Brataas, *Phys. Rev. B* **74**, 155426 (2006).
- [8] J.-S. Jeong and H.-W. Lee, *Phys. Rev. B* **80**, 075409 (2009).
- [9] W. Izumida, K. Sato, and R. Saito, *J. Phys. Soc. Jpn.* **78**, 074707 (2009).
- [10] D. V. Bulaev, B. Trauzettel, and D. Loss, *Phys. Rev. B* **77**, 235301 (2008).
- [11] M. S. Rudner and E. I. Rashba, *Phys. Rev. B* **81**, 125426 (2010).
- [12] K. Flensberg and C. M. Marcus, *Phys. Rev. B* **81**, 195418 (2010).
- [13] A. Pályi and G. Burkard, *Phys. Rev. B* **82**, 155424 (2010).
- [14] B. Braunecker, G. I. Japaridze, J. Klinovaja, and D. Loss, *Phys. Rev. B* **82**, 045127 (2010).
- [15] P. Středa and P. Šeba, *Phys. Rev. Lett.* **90**, 256601 (2003).
- [16] K. Sato, D. Loss, and Y. Tserkovnyak, arXiv:1003.4316.
- [17] R. M. Lutchyn, J. D. Sau, and S. Das Sarma, *Phys. Rev. Lett.* **105**, 077001 (2010); Y. Oreg, G. Refael, F. von Oppen, *ibid.* **105**, 177002 (2010).
- [18] M. Z. Hasan and C. L. Kane, *Rev. Mod. Phys.* **82**, 3045 (2010).
- [19] L. X. Benedict, S. G. Louie, and M. L. Cohen, *Phys. Rev. B* **52**, 8541 (1995).
- [20] D. S. Novikov and L. S. Levitov, *Phys. Rev. Lett.* **96**, 036402 (2006).
- [21] B. Kozinsky and N. Marzari, *Phys. Rev. Lett.* **96**, 166801 (2006).

- [22] M. J. Schmidt and D. Loss, Phys. Rev. B **81**, 165439 (2010).
- [23] H. Min, J. E. Hill, N. A. Sinitsyn, B. R. Sahu, L. Kleinman, and A. H. MacDonald, Phys. Rev. B **74**, 165310 (2006).
- [24] For an electric field in radial direction $H_{\text{SO}}^{\text{el}}$ vanishes [7].
- [25] For $\Delta_{\text{SO}} < 0$, Δk_{cv}^t and $\tau\beta$ have opposite signs, so that either the transverse k -shift or the effective Zeeman field can be canceled by tuning B_z , but not both. However, a calculation based on hydrogenic orbitals and a r^{-1} potential shows that $\Delta_{\text{SO}} > 0$.

Chapter 3

Carbon nanotubes in electric and magnetic fields

We derive an effective low-energy theory for metallic (armchair and non-armchair) single-wall nanotubes in the presence of an electric field perpendicular to the nanotube axis, and in the presence of magnetic fields, taking into account spin-orbit interactions and screening effects on the basis of a microscopic tight binding model. The interplay between electric field and spin-orbit interaction allows us to tune armchair nanotubes into a helical conductor in both Dirac valleys. Metallic non-armchair nanotubes are gapped by the surface curvature, yet helical conduction modes can be restored in one of the valleys by a magnetic field along the nanotube axis. Furthermore, we discuss electric dipole spin resonance in carbon nanotubes, and find that the Rabi frequency shows a pronounced dependence on the momentum along the nanotube.

This chapter has been published in Physical Review B 84, 085452 (2011).

3.1 Introduction

The last two decades have seen remarkable progress in the experimental techniques to fabricate and analyze high purity carbon nanotubes (CNTs).[1, 2, 3, 4, 5, 6, 7] This progress has paved the way for using CNTs for electron and, in particular, electron spin based effects that are of interest for quantum information processing and spintronics.[8, 9, 10, 11, 12, 13, 14, 15, 16, 17, 18, 19, 20, 21, 22, 23] For the latter, the spin-orbit interaction (SOI) plays a significant role as it allows the spin manipulation by electric fields. The purity of CNTs has by now advanced so far that indeed SOI effects can be observed.[9, 10, 11, 12, 13]

In this paper, we investigate the SOI in metallic single-wall CNTs in the presence of external electric and magnetic fields. We provide an extensive discussion of electric field screening in CNTs and of resonant spin transitions via ac electric fields, namely, electric dipole spin resonance (EDSR). Our starting point is a tight binding description including all second shell orbitals of the carbon atoms, from which we derive an effective low-energy band theory.

In the metallic regime, SOI effects by an external electric field can only be expected if the field is applied perpendicularly to the CNT axis. Without the electric field, the SOI in a CNT has been studied before[24, 25, 26, 27, 28, 29] and is the result of the orbital mixing caused by the curvature of the graphene sheet wrapped up into a cylinder. This leads to different geometric conditions than for flat graphene, which has accordingly a different SOI.[30, 31] It is also very different from the SOI found in typical one-dimensional semiconductor wires because of the rotational symmetry of the CNT. In a semiconductor wire, the usual Rashba-SOI with a well-defined spin-precession axis arises from the specific asymmetric electric environment caused by the confining potentials. Such an axis is absent in the rotationally invariant CNT unless it is reintroduced by the application of an external transverse electric field. As we discuss in detail below, this leads indeed to a Rashba-like SOI. However, in contrast to the semiconductors, the CNTs have a hexagonal lattice structure with two carbon atoms per unit cell. The resulting band structure has a nearly vanishing density of states at the charge neutrality point (Dirac point), and roughly a linearly increasing density of states at low energies away from this point. This means, first, that the high energy states affect the low energy properties in a more pronounced way than in a semiconductor. Second, the screening of the external electric field becomes less effective, and the distribution of charges on the tube surface can become complicated. As the screened field affects the low-energy physics as well, it requires specific investigation. It turns out here that for a quantitative understanding we need to start indeed from the full band structure based on the lattice description, and not from the effective low-energy Dirac theory.

The combination of these effects allows us to understand how precisely SOI and especially the SOI parts induced by the external electric field affect the system properties. The larger number of external and internal degrees of freedom as compared to semiconductor wires, such as field strength, sublattice or Dirac valley index, CNT radius, chirality, and

chemical potential, allows for an extensive tunability of the SOI-induced system properties. For instance, in armchair CNTs it allows us to obtain in both Dirac valleys helical, spin-filtered conduction modes, in which opposite spins are transported in opposite directions. Similar helical states occur in SOI-split quantum wires[32, 33, 34, 35, 36, 37, 38, 39] and at the edges of topological insulators,[40] and can be used, for instance, as spin filters[41, 39] or as Cooper-pair splitters.[42] In addition, if such a helical conductor is brought into proximity to a superconductor, it allows for the realization of Majorana end states. This has attracted much attention very recently,[43, 44, 45, 46, 47] mainly because these Majorana states may be used as fundamental quantum states for topological quantum computation.[48]

It should be noted that in semiconductor quantum wires the helical modes are realized only under conditions of an external magnetic field, with the consequence that time-reversal symmetry is broken and the spins at opposite conduction band branches are not truly antiparallel. In contrast, in armchair CNTs the helical modes can be obtained in an all-electric setup, and they are perfectly polarized in the sense that only the spin expectation value S^y in the direction perpendicular to the electric field and the CNT axis is nonzero, even though we generally have $|\langle S^y \rangle| < 1$ within the helical bands.

For metallic but non-armchair CNTs, two more terms appear in the low-energy Hamiltonian. First, an orbital curvature induced term, which opens gaps at the remaining helical zero-energy modes. Second, a SOI term, which plays the role of an effective Zeeman field transverse to the S^y polarization, yet with opposite sign in each Dirac valley. While these two terms primarily destroy the helical conduction modes, their presence can be turned to an advantage: by applying a magnetic field along the CNT axis, the effective Zeeman field in one of the valleys can be suppressed, while it doubles the gap in the other valley. Hence the helical conduction modes are restored to high quality in one of the valleys, while conduction in the other valley is suppressed completely.

To conclude, we provide a microscopic description of electric dipole spin resonance[49, 50, 51, 52, 8, 53] (EDSR) in CNTs. An ac electric field perpendicular to the CNT axis couples to the electronic spin via the SOI. However, this coupling comprises an additional sublattice coupling that is absent in semiconductor setups. It causes a significant momentum dependence of the resonant Rabi frequency of the EDSR experiment. The further application of a static electric field, perpendicular to the CNT axis and to the ac field, lifts the spin degeneracy of the bands in an way analogous to a static Zeeman field. This allows us to propose an all electric realization of Rabi resonance experiments, in which the electric fields replace the static and time-dependent magnetic fields.

The paper is structured as follows. In Sec. 3.2 we introduce the tight-binding model of the hexagonal carbon lattice including SOI and the effect of electric and magnetic fields. The π and σ bands are discussed in Sec. 3.3, and we identify the important $\pi\sigma$ band hybridization couplings that have an impact on the low-energy physics. This allows us to derive the effective low-energy theory for the π bands in Sec. 3.4. The partial screening of the external electric field is investigated in Sec. 3.5, where we discuss in particular the validity of linear response and the influence of the σ bands. The implications of

the effective low-energy theory are analyzed in Sec. 3.6, with special focus on helical modes, valley suppression and the role of further external magnetic fields. Turning to the dynamical response of the CNTs, in Sec. 3.7, we investigate resonant spin transitions by an ac electric field. The final section 3.8 contains our conclusions.

3.2 Model

Our calculations are based on a tight-binding model describing the second shell orbitals of the carbon atoms in CNTs. [54] It takes into account the spin-orbit interaction and external electric and magnetic fields. The Hamiltonian we start from consists of four terms

$$H = H_{\text{hop}} + H_{\text{SO}} + H_E + H_B, \quad (3.1)$$

where H_{hop} describes the hopping between neighboring tight-binding orbitals, H_{SO} describes the on-site spin-orbit interaction, and H_E and H_B describe external electric and magnetic fields, respectively. The Hamiltonian is expressed in second quantization by the electron annihilation operators $c_{\mathbf{n},\zeta,\mu,\lambda}$, where the two-dimensional integer vector $\mathbf{n} = (n_1, n_2)$ labels the unit cells of a honeycomb lattice, $\zeta = \pm 1$ labels the sublattice A/B, and $\lambda = \pm 1$ labels the spin. $\mu = s, p_r, p_t, p_z$ denotes the second shell orbitals with $\mu = s$ the s orbital and $\mu = p_r, p_t, p_z$ the p orbitals. The p_r orbital is perpendicular to the surface of the CNT and essentially constitutes the π band. The $p_{t,z}$ orbitals are tangential (see Figs. 3.1 and 3.2) and, together with the s orbital, build the σ bands. These orbitals span a local coordinate system.

If the cylinder surface on which the carbon atoms are placed in a CNT is projected onto a plane, the graphene lattice with lattice vectors $\mathbf{a}_1 = a(\hat{\mathbf{t}} \cos \theta + \hat{\mathbf{z}} \sin \theta)$ and $\mathbf{a}_2 = a(\hat{\mathbf{t}} \cos(\pi/3 - \theta) - \hat{\mathbf{z}} \sin(\pi/3 - \theta))$ is recovered, where θ is the chiral angle of the nanotube, defined as the angle between the first unit vector \mathbf{a}_1 and the chiral vector C (see Fig. 3.1). In the following, we will also use the collective site index $i = (n_1, n_2, \zeta)$ to label the atom positions. The position of atom i is then $\mathbf{R}_i = n_1 \mathbf{a}_1 + n_2 \mathbf{a}_2 + (1 - \zeta) \mathbf{L}^1 / 2$. The three vectors

$$\mathbf{L}^1 = \frac{a}{\sqrt{3}}(-\hat{\mathbf{t}} \sin \theta + \hat{\mathbf{z}} \cos \theta), \quad (3.2)$$

$$\mathbf{L}^2 = \frac{a}{\sqrt{3}}(\hat{\mathbf{t}} \cos(\pi/6 - \theta) - \hat{\mathbf{z}} \sin(\pi/6 - \theta)), \quad (3.3)$$

$$\mathbf{L}^3 = \frac{a}{\sqrt{3}}(-\hat{\mathbf{t}} \cos(\pi/6 + \theta) - \hat{\mathbf{z}} \sin(\pi/6 + \theta)), \quad (3.4)$$

connect an A site with its three nearest neighbors on the B sublattice. These three B sites will be denoted by $B_{1,2,3}$ in the following. Note that we have chosen to define the model directly in a coordinate system which will be convenient for the subsequent calculations.

In the following, we describe each term in Eq. (3.1) and its derivation in detail.

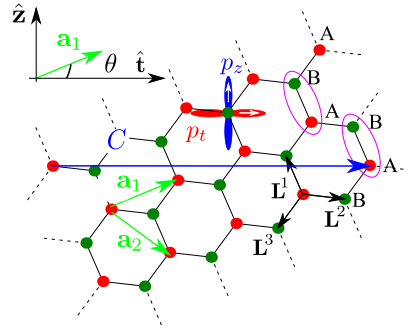


Figure 3.1: Definition of the honeycomb lattice vectors and the direction of the p_z and p_t orbitals. The white arrows in the p orbitals point into the direction where the wave function is positive. The ellipses indicate the unit cells consisting of A and B sublattice atoms. The p orbital alignment is equal on both sublattices. Together with the p_r orbital, which points out of the plane (not shown here), the directions of p_r, p_t, p_z form a right-handed set of vectors.

3.2.1 Hopping Hamiltonian

The term H_{hop} describes the hopping between orbitals on neighboring carbon sites as well as the on-site orbital energies. We only take into account nearest neighbor hopping and assume the orbitals on neighboring carbon atoms to be orthogonal. The hopping Hamiltonian has the form

$$H_{\text{hop}} = \sum_{\langle i,j \rangle} \sum_{\mu,\mu',\lambda} t_{\mu\mu'}^{ij} c_{i\mu\lambda}^\dagger c_{j\mu'\lambda} + \varepsilon_s \sum_{i,\lambda} c_{is\lambda}^\dagger c_{is\lambda}, \quad (3.5)$$

where $\langle i,j \rangle$ runs over nearest neighbor sites, and $\varepsilon_s = -8.9$ eV is the orbital energy of the carbon s orbitals relative to the p orbital energy. The latter is set to zero in this paper. The amplitude $t_{\mu\mu'}^{ij}$ of an electron hopping from the orbital μ' on the j th site to the orbital μ on the i th site is a linear combination of the four fundamental hopping

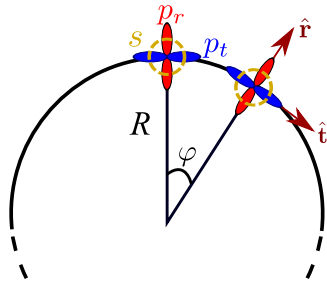


Figure 3.2: Cross section of a CNT. The \hat{z} -direction is along the nanotube axis. The orientation of the orbitals p_r, p_t as well as the local coordinate system \hat{r}, \hat{t} depends on the azimuthal angle φ . The s orbital is indicated by the dashed circles.

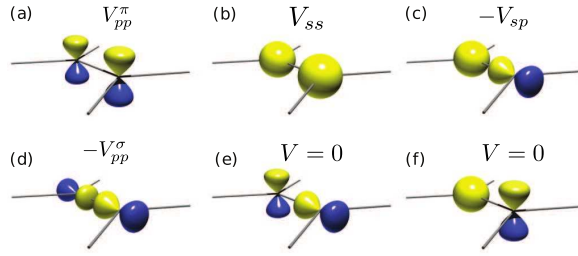


Figure 3.3: Hopping between atomic orbitals of neighboring carbon sites in the graphene limit. (a) - (d) show the orbital combinations with non-zero hopping amplitude. (e), (f) show hoppings which are forbidden by symmetry.

amplitudes [54] $V_{ss} = -6.8$ eV, $V_{sp} = 5.6$ eV, $V_{pp}^\pi = -3.0$ eV, $V_{pp}^\sigma = 5.0$ eV (see Fig. 3.3) with coefficients depending on the relative orientation of the orbitals μ and μ' . [55] For the explicit calculation of $t_{\mu\mu'}^{ij}$, the p orbitals are decomposed into components parallel and perpendicular to the $i - j$ bond. These components can be easily expressed in terms of scalar products (see Fig. 3.4). If the direction of a p orbital on the A atom is \mathbf{p}_μ^A and the direction of a p orbital on the B_n atom is $\mathbf{p}_\nu^{B_n}$, then the projections on the unit vector $\mathbf{l}^n = \mathbf{L}^n / |\mathbf{L}^n|$ in the direction from atom A to atom B_n are

$$\sigma_\perp = (\mathbf{p}_\mu^A \cdot \mathbf{l}^n)(\mathbf{p}_\nu^{B_n} \cdot \mathbf{l}^n), \quad (3.6)$$

$$\sigma_\parallel = \mathbf{p}_\mu^A \cdot \mathbf{p}_\nu^{B_n} - (\mathbf{p}_\mu^A \cdot \mathbf{l}^n)(\mathbf{p}_\nu^{B_n} \cdot \mathbf{l}^n), \quad (3.7)$$

where indices $\{\mu, \nu\} = \{r, t, z\}$ describe p orbitals and $n = \{1, 2, 3\}$ denotes the neighboring B atoms. Therefore, the hopping matrix elements are

$$t_{\mu\nu}^{AB_n} = V_{pp}^\pi (\mathbf{p}_\mu^A \cdot \mathbf{p}_\nu^{B_n} - (\mathbf{p}_\mu^A \cdot \mathbf{l}^n)(\mathbf{p}_\nu^{B_n} \cdot \mathbf{l}^n)) + V_{pp}^\sigma (\mathbf{p}_\mu^A \cdot \mathbf{l}^n)(\mathbf{p}_\nu^{B_n} \cdot \mathbf{l}^n), \quad (3.8)$$

$$t_{\mu s}^{AB_n} = -V_{sp}(\mathbf{p}_\mu^A \cdot \mathbf{l}^n), \quad (3.9)$$

$$t_{s\nu}^{AB_n} = V_{sp}(\mathbf{p}_\nu^{B_n} \cdot \mathbf{l}^n). \quad (3.10)$$

3.2.2 Spin-orbit interaction

The spin-orbit interaction is modeled by projecting the Thomas Hamiltonian for a spherically symmetric atomic potential $V(r)$ [56]

$$H_{SO}^{\text{intr}} = \frac{\hbar}{4m_e^2 c^2} \frac{1}{r} \frac{dV(r)}{dr} \mathbf{L} \cdot \mathbf{S} \quad (3.11)$$

onto the subspace spanned by the second shell orbitals of each individual carbon atom. \mathbf{L} is the electron angular momentum operator and \mathbf{S} is the vector of the spin Pauli matrices with eigenvalues ± 1 .

By symmetry, this projection can be reduced to a form depending on a single parameter only, defining the strength of the intrinsic SOI

$$\Delta_{\text{SO}} = \frac{\hbar^2}{4m_e^2c^2} \langle p_r^A | (\partial_t[\partial_r V] - \partial_r[\partial_t V]) | p_t^A \rangle. \quad (3.12)$$

In the literature one finds a wide spread for the spin-orbit coupling constant Δ_{SO} (see Refs. [57, 31, 58]). Note also that there are different conventions for the spin operators used in the spin-orbit Hamiltonian. In some works, Pauli matrices with eigenvalues ± 1 are used while in other papers, the spin operators have eigenvalues $\pm \frac{1}{2}$. In this paper, we always use Pauli matrices with eigenvalues ± 1 . For the spin-orbit coupling constant one finds values between 3 meV[31] and 20 meV.[58] In this work we follow Ref. [57] and use $\Delta_{\text{SO}} = 6$ meV. The projected spin-orbit Hamiltonian reads

$$H_{\text{SO}} = i\Delta_{\text{SO}} \sum_{\substack{i,\lambda,\lambda' \\ \mu,\nu,\eta}} \varepsilon^{\mu\nu\eta} c_{i\mu\lambda}^\dagger S_{\lambda\lambda'}^\nu c_{i\eta\lambda'}. \quad (3.13)$$

Here, $\mu, \eta = p_r, p_t, p_z$ run over the p orbitals only. $\varepsilon^{\mu\nu\eta}$ is the Levi-Civita symbol. The index $\nu = r, t, z$ labels the spin components in the local coordinate system, i.e., $S^r = S^x \cos \varphi_i + S^y \sin \varphi_i$, $S^t = S^y \cos \varphi_i - S^x \sin \varphi_i$, with φ_i the azimuthal angle of site i (see Fig. 3.2) and $S^{x,y,z}$ the spin Pauli matrices (with eigenvalues ± 1). The spin-orbit energies emerging from H_{SO} and from the curvature effects are found to be much larger than the spin-orbit energies due to the d -orbitals, [59] allowing us to neglect the latter.

3.2.3 Electric fields

In this section we introduce the Hamiltonian describing a homogenous external electric field \mathbf{E} perpendicular to the CNT axis. Due to screening effects, local fields with complicated spatial dependence are generated by the rearrangement of the electron density on the lattice and have to be taken into account in principle. However, it turns out that none of these nontrivial contributions affect the physics in an essential way.

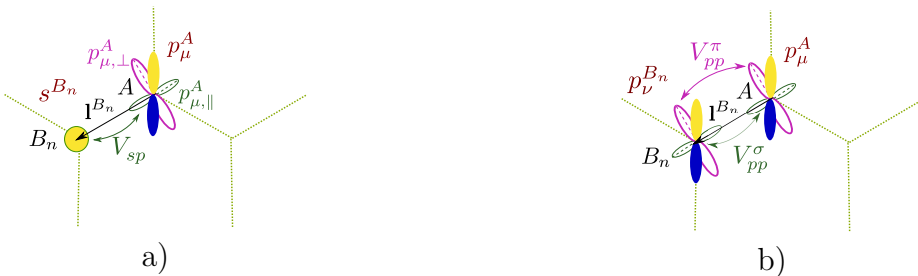


Figure 3.4: The hopping element between a) p_μ^A and s^{B_n} b) p_μ^A and $p_\nu^{B_n}$ can be calculated by the decomposition of the $p_\mu^A(p_\nu^{B_n})$ orbital into two parts: perpendicular to the bond $p_{\mu,\perp}^A(p_{\nu,\perp}^{B_n})$ and parallel to the bond $p_{\mu,\parallel}^A(p_{\nu,\parallel}^{B_n})$.

We start from the most general electrostatic potential $\phi_{\text{tot}}(\mathbf{r}) = \phi_{\text{ext}}(\mathbf{r}) + \phi_{\text{ind}}(\mathbf{r})$, which is the sum of the potential ϕ_{ext} coming from the homogeneous external field and the generally complicated potential ϕ_{ind} from screening effects. The matrix elements $\langle \mu, i | \phi(\mathbf{r}) | \mu', j \rangle$ between the orbitals of two different carbon atoms $i \neq j$ are much smaller than the typical hopping elements ($\sim \text{eV}$) so that we can safely neglect them and consider only on-site effects of the electric potential.

The averaged potential $\phi_{\mu\mu}(\mathbf{R}_i) = \langle \mu, i | \phi_{\text{tot}}(\mathbf{r}) | \mu, i \rangle$ for the μ orbital on site i changes the electrostatic energy of an electron in this orbital. Note that \mathbf{R}_i is the position of the i th carbon atom in three-dimensional space. In the following, we assume that the dependence of $\phi_{\mu\mu}(\mathbf{R}_i)$ on the orbital μ is negligible, i.e., $\phi_{\text{tot}}(\mathbf{R}_i) \simeq \phi_{\mu\mu}(\mathbf{R}_i)$. Furthermore, we show in Sec. 3.5 that even with the induced potential ϕ_{ind} included, ϕ_{tot} essentially depends on the azimuthal angle φ_i similar to the case of a homogeneous field. Therefore, the diagonal matrix elements of the electrostatic potential are $\phi(\mathbf{R}_i) \simeq \phi_{\text{tot}}(\varphi_i) \propto \cos \varphi_i$ and give rise to the Hamiltonian

$$H_E^{(1)} = \sum_{i,\mu,\lambda} \phi_{\text{tot}}(\varphi_i) c_{i\mu\lambda}^\dagger c_{i\mu\lambda}. \quad (3.14)$$

For sufficiently small CNT radii R and electric fields the total potential on the surface of the CNT is well approximated by $\phi_{\text{tot}}(\varphi_i) \simeq eE^*R \cos \varphi_i$, where $E^* < |\mathbf{E}|$ is the screened electric field and e is the electron charge.

We note that, because ϕ varies on the scale of the spatial extent of the orbital wave function and breaks the lattice symmetries, in general, the matrix elements between the different orbitals $\phi_{\mu\mu'}(\mathbf{R}_i) = \langle \mu, i | \phi(\mathbf{r}) | \mu', i \rangle \neq 0$ and transitions between orthogonal orbitals μ, μ' on the same carbon atom are generated. We call this the μ - μ' transitions in the following. The potential of a homogeneous external field alone gives rise to s - p_r and s - p_t transitions. But the complicated additional induced potential $\phi_{\text{ind}}(\mathbf{r})$ gives also rise to coupling between other orbitals. For this work, the s - p_r transition is most important because of two reasons: 1) It is the only transition directly coupling π and σ bands, thus giving rise to a first order effect in the s - p_r coupling strength. 2) Its strength is determined by the unscreened field E and not by the screened $E^* < E$. Indeed, the induced potential ϕ_{ind} drops out, i.e., $\langle p_r | \phi_{\text{ind}}(\mathbf{r}) | s \rangle \simeq 0$, as ϕ_{ind} is approximately an even function in the radial coordinate r about the tube radius $r = R$. The Hamiltonian describing the s - p_r transition is

$$H_E^{(2)} = -eE\xi_0 \cos(\varphi_i) c_{ip_r\lambda}^\dagger c_{is\lambda} + \text{H.c.}, \quad (3.15)$$

with the strength of the transitions being characterized by the integral

$$\xi_0 = - \int d^3\mathbf{r} \psi_{2s}^*(\mathbf{r}) z \psi_{2p_z}(\mathbf{r}) = \frac{3a_B}{Z}, \quad (3.16)$$

where ψ_{2s} and ψ_{2p_z} are the hydrogenic wave functions of the second shell atomic orbitals, a_B is the Bohr radius, and Z is the effective nuclear charge, which for the second shell in carbon is $Z \simeq 3.2$. From this we obtain $\xi_0 \simeq 0.5 \text{ \AA}$. Note that our value for ξ_0 is a rather conservative estimate. It is roughly four times smaller than what has been assumed in Ref. [31].

3.2.4 Magnetic fields

The Zeeman Hamiltonian describing the interaction of the electron spin with the magnetic field is in the tight-binding model written as

$$H_{\text{mag}} = \sum_{i,\mu,v,\lambda,\lambda'} \mu_B B_v c_{i\mu\lambda}^\dagger S_{\lambda\lambda'}^v c_{i\mu\lambda'}, \quad (3.17)$$

where the index μ runs over all orbitals, i labels the position of the atom, and λ, λ' denote the spin. B_v with $v = x, y, z$ are the components of the magnetic field in the global coordinate system, which we choose such that the electric field is always in x direction and the CNT axis is along $\hat{\mathbf{z}}$.

The orbital effect of the magnetic field is usually expressed in terms of Peierls phases, multiplying the hopping amplitudes in the tight-binding Hamiltonian. For a magnetic field along the CNT axis, which will be of most interest in this paper, this will lead to an Aharonov-Bohm shift of the circumferential wave vector, which can be incorporated easily into the effective model, derived subsequently.

3.3 π and σ bands

In general, all four orbitals of the second shell in CNTs are hybridized by the hopping Hamiltonian H_{hop} . However, in the limit $R \rightarrow \infty$, the hopping amplitudes between the p_r orbital and any of the orbitals s, p_t, p_z become zero, and the hopping Hamiltonian becomes equal to the Hamiltonian of flat graphene. The p_r orbitals then form the π band and the remaining three orbitals, which are still strongly hybridized, form the σ bands. For CNTs with finite R , the π band hybridizes with the σ bands due to the CNT curvature, which leads to non-zero hopping amplitudes $t_{ij}^{p_r p_t}, t_{ij}^{p_r p_z}, t_{ij}^{p_r s}$. However, the $\pi\sigma$ hybridization is still small for realistic CNT sizes, so that it is convenient to partition the total Hamiltonian [Eq. (3.1)] as

$$H = H_\pi + H_\sigma + H_{\pi\sigma} + H_{\sigma\pi}. \quad (3.18)$$

The parts H_π contain only electron operators $c_{ip_r\lambda}$ for the p_r orbitals, H_σ contains only operators for the orbitals p_t, p_z, s , and the parts $H_{\pi\sigma}$ ($H_{\sigma\pi}$) contain only the combinations $c_{ip_r\lambda}^\dagger c_{i\mu\lambda}$ ($c_{i\mu\lambda}^\dagger c_{ip_r\lambda}$) with $\mu = p_t, p_z, s$ running only over the σ orbitals. We will use the symbols $H_\pi, H_\sigma, H_{\pi\sigma}, H_{\sigma\pi}$ also for the representation of H in first quantization, i.e., for complex matrices whenever this notation is more convenient.

In the following, we discuss the π -band Hamiltonian H_π and the σ -band Hamiltonian H_σ separately before we take into account the $\pi\sigma$ hybridization. For this, we transform to a k -space representation of the electron operators

$$c_{i\mu\lambda} = \frac{1}{\sqrt{N}} \sum_{\kappa} e^{i\kappa \cdot \mathbf{R}_i} c_{\kappa\zeta\mu\lambda} \quad (3.19)$$

where N is the number of unit cells. The preliminary definition of the momentum $\kappa = \kappa \hat{\mathbf{z}} + \kappa_t \hat{\mathbf{t}}$ has a momentum component κ along the tube and one component κ_t around the tube. Remember that the alignment of the corresponding unit vectors $\hat{\mathbf{z}}, \hat{\mathbf{t}}$ relative to the lattice depends on the chirality of the tube (see Fig. 3.1).

3.3.1 π band hopping Hamiltonian

We start the discussion of the π band with the limit $R \rightarrow \infty$, in which the hopping amplitude between all nearest-neighbor p_r orbitals is V_{pp}^π . The transformation of the hopping terms of the π band Hamiltonian H_{hop}^π to k -space gives

$$H_{\text{hop}}^\pi = V_{pp}^\pi \sum_{\kappa} w(\kappa) c_{\kappa A p_r \lambda}^\dagger c_{\kappa B p_r \lambda} + \text{H.c.}, \quad (3.20)$$

where $w(\kappa) = e^{i\kappa \cdot \mathbf{L}^1} + e^{i\kappa \cdot \mathbf{L}^2} + e^{i\kappa \cdot \mathbf{L}^3}$. The spectrum $\pm V_{pp}^\pi |w(\kappa)|$ of H_{hop}^π is zero at the two Dirac points $\mathbf{K} = 4\pi(\hat{\mathbf{t}} \cos \theta + \hat{\mathbf{z}} \sin \theta)/3a$ and $\mathbf{K}' = -\mathbf{K}$. Since we are interested mainly in the low-energy states, we expand κ about each of the two Dirac points,

$$\kappa = \mathbf{K} + \mathbf{k} \quad \text{or} \quad \kappa = \mathbf{K}' + \mathbf{k}, \quad (3.21)$$

to linear order in $\mathbf{k} = k \hat{\mathbf{z}} + k_t \hat{\mathbf{t}}$. The resulting approximated hopping Hamiltonian for the π band reads

$$H_{\text{hop}}^\pi \simeq \hbar v_F \sum_{\mathbf{k}} e^{i\tau\theta} (\tau k_t - ik) c_{\mathbf{k} A \tau p_r \lambda}^\dagger c_{\mathbf{k} B \tau p_r \lambda} + \text{H.c.}, \quad (3.22)$$

with $\hbar v_F = \sqrt{3}|V_{pp}^\pi|/2a$. The index $\tau = \pm 1$ labels the two valleys \mathbf{K} and \mathbf{K}' , respectively. Finally, to bring (3.22) to a more convenient form, we change the phase of all p_r orbitals on the A sublattice by

$$c_{\mathbf{k} A \tau p_r \lambda} \rightarrow \tau e^{i\tau\theta} c_{\mathbf{k} A \tau p_r \lambda} \quad (3.23)$$

and arrive at the usual first quantized form of the Dirac Hamiltonian

$$H_{\text{hop}}^\pi = \hbar v_F (k_t \sigma_1 + k \tau \sigma_2), \quad (3.24)$$

where the Pauli matrices σ_i operate in the A,B sublattice space. σ_3 equals 1 on the A sublattice and -1 on the B sublattice. Note that, due to the finite circumference of carbon nanotubes, $k_t = (n - \tau \delta/3)/R$ is quantized. $\delta = (N_1 - N_2) \bmod 3$, for a (N_1, N_2) -CNT, is zero for metallic nanotubes, to which we restrict the discussion in this paper.

The deviations of $t_{ij}^{p_r p_r}$ from V_{pp}^π due to the finite radius R leads to an additional contribution to the non-diagonal part of H_π , which is added directly to $t = V_{pp}^\pi w(\mathbf{k})$,

$$\frac{\tau a^2}{64R^2} (4(V_{pp}^\sigma + V_{pp}^\pi) e^{-3i\tau\theta} + e^{3i\tau\theta} (V_{pp}^\pi - V_{pp}^\sigma)). \quad (3.25)$$

This results in a shift of the wave vectors dependent on the chirality and radius along the both axes. The curvature effects also lead to a renormalization of the Fermi velocity,

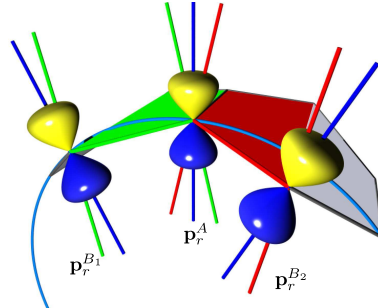


Figure 3.5: Curvature induced σ bonding between p_r orbitals of neighbouring atoms (The corresponding atoms are defined as A, B₁, and B₂). Blue lines are aligned with the corresponding p_r orbital directions and red (green) lines are perpendicular to the red (green) hexagon segment and, therefore, to the red (green) bond between the atoms A and B₂(B₁). Note that all these lines (blue, red, and green) are aligned in graphene. Thus, in graphene, only π bonding (that is due to overlap of orbitals aligned perpendicular to the connecting line between the two atoms) is possible between such orbitals. NT curvature breaks such a symmetry: in curved graphene sheet, p_r orbital direction (shown by blue lines) has perpendicular and parallel components to the line connecting two atoms. The latter component is responsible to a σ bond formation (that is due to overlap of orbitals along the line connecting the two atoms).

which can be obtained if we keep terms up to second order in a/R and first order in k . The correction to H_{hop}^π is

$$\Delta H_{\text{hop}}^\pi = \hbar(\Delta v_F^\perp k_t \sigma_1 + \tau \Delta v_F^\parallel k \sigma_2), \quad (3.26)$$

with

$$\hbar \Delta v_F^\perp = \frac{2(7V_{pp}^\pi + 5V_{pp}^\sigma) + \cos 6\theta(V_{pp}^\pi - V_{pp}^\sigma)}{128\sqrt{3}} \left(\frac{a}{R}\right)^2 \quad (3.27)$$

$$\hbar \Delta v_F^\parallel = \frac{2(V_{pp}^\sigma + 3V_{pp}^\pi) - \cos 6\theta(V_{pp}^\pi - V_{pp}^\sigma)}{128\sqrt{3}} \left(\frac{a}{R}\right)^2. \quad (3.28)$$

Moreover, there is an additional term which couples transverse and longitudinal movements,

$$\Delta H_{t-z}^\pi = \hbar \Delta v_F^{t-z} ((k\sigma_1 + \tau k_t \sigma_2)), \quad (3.29)$$

with

$$\hbar \Delta v_F^{t-z} = \frac{1}{128\sqrt{3}} \left(\frac{a}{R}\right)^2 \sin 6\theta(V_{pp}^\pi - V_{pp}^\sigma). \quad (3.30)$$

It should be emphasized that the corrections to the Hamiltonian given by Eqs. (3.25)–(3.29) are not the only terms responsible for the shifts of the wave vectors and the Fermi velocity renormalization. Further terms leading to effects on the same order of magnitude indeed arise from the π - σ band coupling. Such corrections by the higher energy bands

will be discussed in the next sections. Collecting all terms we obtain the correction to the Fermi velocity

$$\frac{\Delta v_F^\parallel}{v_F} = \gamma \left(\frac{a}{R} \right)^2. \quad (3.31)$$

From Eq. (3.28) we find $\gamma = -0.05$, while the direct numerical solution of Eq. (3.1) gives $\gamma = -0.15$, which indeed reflects the significance of the correction by the energetically higher bands. In any case, the curvature-induced renormalization of the Fermi velocity is small and does not give rise to any significant effect in the regime discussed in this work.

3.3.2 σ band hopping Hamiltonian

The orbitals s, p_t, p_z on the sublattices A and B give rise to six σ bands. For a flat honeycomb lattice (i.e., $R \rightarrow \infty$), there is no hybridization between these σ bands and the π band. For CNTs with finite radii R , finite hopping matrix elements between the σ and the π orbitals cause a small hybridization which will be treated in perturbation theory below. Indeed, one of the small parameters appearing in the perturbation theory is the ratio a/R with a the lattice constant. It is important to understand that, in order to correctly account for the curvature effects to order $(a/R)^2$ in the analytical theory derived in Sec. 3.4, it is sufficient to treat the σ bands in the limit $R \rightarrow \infty$, i.e., in zeroth order in a/R . Any curvature effect in the σ bands of order of a/R would lead to a correction of at least third order.

Furthermore, since the effective theory will be valid only near the Dirac points \mathbf{K}, \mathbf{K}' , we only consider the eigenstates and eigenenergies of the σ bands at the Dirac points, i.e., for $\kappa = \mathbf{K}, \mathbf{K}'$. In k space and in the basis

$$\mathcal{S} = \{|s^A\rangle, |p_t^A\rangle, |p_z^A\rangle, |s^B\rangle, |p_t^B\rangle, |p_z^B\rangle\}, \quad (3.32)$$

the σ band Hamiltonian has the block form

$$H_\sigma = \begin{pmatrix} \mathbf{0} & h_{\sigma,AB} \\ h_{\sigma,AB}^\dagger & \mathbf{0} \end{pmatrix}, \quad (3.33)$$

where $h_{\sigma,AB}$ is given by

$$\frac{3}{4} \begin{pmatrix} 0 & 2iV_{sp} & 2\tau V_{sp} \\ -2iV_{sp} & \tau e^{-3i\tau\theta}(V_{pp}^\pi - V_{pp}^\sigma) & ie^{-3i\tau\theta}(V_{pp}^\pi - V_{pp}^\sigma) \\ -2\tau V_{sp} & ie^{-3i\tau\theta}(V_{pp}^\pi - V_{pp}^\sigma) & -\tau e^{-3i\tau\theta}(V_{pp}^\pi - V_{pp}^\sigma) \end{pmatrix}. \quad (3.34)$$

$\tau = \pm 1$ labels the Dirac point \mathbf{K}, \mathbf{K}' , respectively. H_σ can be diagonalized analytically. We find the energy spectrum of the σ bands at \mathbf{K}, \mathbf{K}'

$$\varepsilon_{pp}^{\sigma(*)} = \pm \frac{3}{2}(V_{pp}^\pi - V_{pp}^\sigma), \quad (3.35)$$

$$\varepsilon_{sp1}^{\sigma(*)} = \frac{1}{2} \left(\varepsilon_s \pm \sqrt{(\varepsilon_s)^2 + 18(V_{sp})^2} \right), \quad (3.36)$$

$$\varepsilon_{sp2}^{\sigma(*)} = \varepsilon_{sp1}^{\sigma(*)}. \quad (3.37)$$

The corresponding eigenvectors are given by

$$|\sigma_{pp}\rangle = \frac{1}{\sqrt{2}}(-\tau e^{-3i\tau\theta}|l^{A,-}\rangle + |l^{B,+}\rangle), \quad (3.38)$$

$$|\sigma_{pp}^*\rangle = \frac{1}{\sqrt{2}}(\tau e^{-3i\tau\theta}|l^{A,-}\rangle + |l^{B,+}\rangle), \quad (3.39)$$

$$|\sigma_{sp1}\rangle = -\tau\eta_-|s^A\rangle + \eta_+|l^{B,-}\rangle, \quad (3.40)$$

$$|\sigma_{sp2}\rangle = \eta_-|s^B\rangle + \tau\eta_+|l^{A,+}\rangle, \quad (3.41)$$

$$|\sigma_{sp1}^*\rangle = \tau\eta_+|s^A\rangle + \eta_-|l^{B,-}\rangle, \quad (3.42)$$

$$|\sigma_{sp2}^*\rangle = \eta_+|s^B\rangle - \tau\eta_-|l^{A,+}\rangle, \quad (3.43)$$

where

$$|l^{j,+}\rangle = \frac{1}{\sqrt{2}}(|p_z^j\rangle + i\tau|p_t^j\rangle), \quad (3.44)$$

$$|l^{j,-}\rangle = \frac{1}{\sqrt{2}}(|p_z^j\rangle - i\tau|p_t^j\rangle), \quad (3.45)$$

$$\eta_{\pm} = \frac{1}{\sqrt{2}}\sqrt{1 \pm \frac{\varepsilon_s}{\sqrt{(\varepsilon_s)^2 + 18(V_{sp})^2}}}. \quad (3.46)$$

3.3.3 $\pi\sigma$ hybridization

In this section we consider different mechanisms which lead to a coupling between π and σ bands. All these couplings are weak compared to the typical energy scales of the π and σ bands, so that we may treat them in perturbation theory. It is therefore convenient to write the Hamiltonian of a carbon nanotube in first quantization in the block form

$$H = \begin{pmatrix} H_\pi & H_{\pi\sigma} \\ H_{\sigma\pi} & H_\sigma \end{pmatrix}, \quad (3.47)$$

where $H_{\pi\sigma}$ is a 2×6 matrix describing the $\pi\sigma$ mixing. It contains three types of contributions, namely from the spin-orbit interaction, from the curvature of the nanotube and from the external electric field, applied to the nanotube. As we want to describe the spin-orbit coupling, we need to explicitly take into account the spin of the electron. Thus, each of the 12 matrix elements of $H_{\pi\sigma}$ is an operator acting on the electronic spin. In the matrices describing curvature and electric field effects, this operator will be the identity, but for the spin-orbit interaction matrices, it will be composed of the spin Pauli matrices S^μ . Also, the matrix elements may contain momentum and position operators.

In the basis $\mathcal{P} \times \mathcal{S}$ with $\mathcal{P} = \{|p_r^A\rangle, |p_r^B\rangle\}$ and $\mathcal{S} = \{|s^A\rangle, |p_t^A\rangle, |p_z^A\rangle, |s^B\rangle, |p_t^B\rangle, |p_z^B\rangle\}$

the total Hamiltonian H is of the form

$$\left(\begin{array}{cc} \boxed{0 & t \\ t^* & 0} & \boxed{\begin{matrix} V_{p_r s}^{AA} & V_{p_r p_t}^{AA} & V_{p_r p_z}^{AA} & V_{p_r s}^{AB} & V_{p_r p_t}^{AB} & V_{p_r p_z}^{AB} \\ V_{p_r s}^{BA} & V_{p_r p_t}^{BA} & V_{p_r p_z}^{BA} & V_{p_r s}^{BB} & V_{p_r p_t}^{BB} & V_{p_r p_z}^{BB} \end{matrix}} \\ \boxed{\begin{matrix} \dots & \dots & \dots & \dots & \dots & \dots \end{matrix}} & \boxed{\begin{matrix} \varepsilon_s & 0 & 0 & H_{ss}^{AB} & H_{sp_t}^{AB} & H_{sp_z}^{AB} \\ \dots & 0 & 0 & -H_{sp_t}^{AB} & H_{p_t p_t}^{AB} & H_{p_t p_z}^{AB} \\ \dots & \dots & 0 & -H_{sp_z}^{AB} & H_{p_t p_z}^{AB} & H_{p_z p_z}^{AB} \\ \dots & \dots & \dots & \varepsilon_s & 0 & 0 \\ \dots & \dots & \dots & \dots & 0 & 0 \\ \dots & \dots & \dots & \dots & \dots & 0 \end{matrix}} \end{array} \right), \quad (3.48)$$

where, as explained above, each matrix element is an operator acting on the electron spin and, furthermore, each matrix element may depend on the crystal momentum κ or on the spatial position \mathbf{r} . It will turn out that the only spatial dependencies we need to deal with are dependencies on the azimuthal angle φ_i of the carbon atoms.

The diagonal blocks correspond to the Hamiltonians of the isolated π and σ bands, as discussed in the two preceding subsections, and the off-diagonal blocks (framed in bold boxes) are the $H_{\pi\sigma}$ and $H_{\sigma\pi} = H_{\pi\sigma}^\dagger$ matrices with entries $V_{uv}^{ij} = \langle u^i | H_{\text{hyb}} | v^j \rangle$ for $i, j \in \{A, B\}$ and $u, v \in \{s, p_t, p_z, p_r\}$. Here H_{hyb} is the part of the Hamiltonian inducing transitions between the π and σ bands. As stated above, it is composed of three different contributions: the hybridization coming from the curvature $H_{\pi\sigma}^{\text{curv}}$, from the spin-orbit $H_{\pi\sigma}^{\text{SO}}$, and from an applied electric field $H_{\pi\sigma}^E$. Each of these contributions will be discussed in the following.

Curvature induced π - σ bond hybridization in nanotubes

Due to the curvature of the nanotube surface, hoppings between orbitals on neighboring carbon atoms, which are symmetry-forbidden in flat graphene, become allowed in CNTs. This is illustrated in Fig. 3.5. We now calculate the corresponding hopping matrix elements in k -space at the Dirac points ($\kappa = \mathbf{K}, \mathbf{K}'$) between the π orbital (p_r) and the σ orbitals (s, p_t, p_z). As the hopping is spin-independent, the hopping matrix is the identity in spin space. Furthermore, since the hopping does not depend on the spatial position of the electron but only on its momentum, the matrix elements will generally be functions of the momentum κ but not of the position operator. Since we are interested only in the physics near the Dirac point, it will be sufficient to consider the Dirac momenta $\kappa = \mathbf{K}, \mathbf{K}'$ only. The neglect of the momentum deviation $\mathbf{k} = \kappa - \mathbf{K}^{(i)}$ from the Dirac momenta in the π *sigma* coupling matrices turns out to be a good approximation; it only gives rise to a small renormalization of the Fermi velocity. \mathbf{k} is only important in the \mathcal{P} subspace, as discussed in Sec. 3.3.1.

It is important to note that, for a curved surface, the vectors \mathbf{L}^n connecting nearest neighbors, not only have tangential components proportional to $\hat{\mathbf{z}}$ and $\hat{\mathbf{t}}$, but also a radial contribution $L_r^n \hat{\mathbf{r}}$. The magnitude L_r^n is of order a/R and thus vanishes in the graphene

limit $R \rightarrow \infty$. The hopping amplitudes $t_{\mu\nu}^{ij}$ must be calculated as described in Eqs. (3.8)–(3.10), and using the above described \mathbf{L}^n vectors with radial contributions. For the transformation to k -space, on the other hand, the radial contributions of \mathbf{L}^n are not needed because $\boldsymbol{\kappa}$ and \mathbf{k} are defined in the two-dimensional tangent space, describing the longitudinal ($\hat{\mathbf{z}}$) and the circumferential or transverse ($\hat{\mathbf{t}}$) direction. Nevertheless, it is convenient to write scalar products between the three-component vectors $\mathbf{L}^n = L_z^n \hat{\mathbf{z}} + L_t^n \hat{\mathbf{t}} + L_r^n \hat{\mathbf{r}}$ and the momentum $\boldsymbol{k} = \kappa \hat{\mathbf{z}} + \kappa_t \hat{\mathbf{t}} + 0 \hat{\mathbf{r}}$.

For a given $\boldsymbol{\kappa}$, the curvature-induced $\pi\sigma$ coupling is defined by

$$H_{\pi\sigma}^{\text{curv}} = \sum_{\substack{n=1,2,3 \\ \mu,\lambda}} \left[e^{i\boldsymbol{\kappa}\cdot\mathbf{L}^n} t_{p_r\mu}^{AB_n} c_{\boldsymbol{\kappa}Ap_r\lambda}^\dagger c_{\boldsymbol{\kappa}B\mu\lambda} + e^{-i\boldsymbol{\kappa}\cdot\mathbf{L}^n} t_{p_r\mu}^{B_nA} c_{\boldsymbol{\kappa}Bp_r\lambda}^\dagger c_{\boldsymbol{\kappa}A\mu\lambda} \right], \quad (3.49)$$

where $\mu = s, p_t, p_z$ runs over the orbitals forming the σ band. As we are finally interested in a low-energy theory for the π band, taking the coupling to the σ band into account in up to second order in the small parameters, one of which is a/R , and since $H_{\pi\sigma}^{\text{curv}}$ will only enter in second order perturbation theory, it is sufficient to keep only the linear a/R order in $H_{\pi\sigma}^{\text{curv}}$. Doing so, we find in the $\mathcal{P} \times \mathcal{S}$ basis

$$H_{\sigma\pi}^{\text{curv}} = \frac{\sqrt{3}a}{16R} \begin{pmatrix} 0 & -2\tau e^{-3i\tau\theta} V_{sp} \\ 0 & i(3V_{pp}^\sigma + 5V_{pp}^\pi) \\ 0 & -\tau(V_{pp}^\pi - V_{pp}^\sigma) \\ -2\tau e^{3i\tau\theta} V_{sp} & 0 \\ i(3V_{pp}^\sigma + 5V_{pp}^\pi) & 0 \\ \tau(V_{pp}^\pi - V_{pp}^\sigma) & 0 \end{pmatrix}. \quad (3.50)$$

Again, $\tau = \pm 1$ labels the Dirac points $\boldsymbol{\kappa} = \mathbf{K}, \mathbf{K}'$, respectively. Furthermore, note that $H_{\sigma\pi}^{\text{curv}}$ is the identity in spin space, so that the matrix in Eq. (3.50) enters the block Hamiltonian twice if the electron spin is taken into account.

Spin-orbit coupling in π bands

For the analysis of the spin-orbit interaction it is important to note that the corresponding Hamiltonian H_{SO} [Eq. (3.13)] is local, i.e., it has no matrix elements connecting orbitals from different lattice sites. Thus, $H_{\sigma\pi}^{\text{SO}}$ can be represented as a $6 \times 2 \times 2$ tensor, corresponding to the six σ orbitals per unit cell, the two π orbitals per unit cell and the two-dimensional spin space. Each matrix element, however, may depend on the unit cell coordinate. It is most convenient to write $H_{\sigma\pi}^{\text{SO}}$ in a local spin basis with spin-components S^r pointing in the radial direction of the nanotube, S^t pointing in the transverse (or circumferential) direction, and S^z pointing along the tube axis. Since the local environment, i.e., the definition of the direction of the p orbitals, are equal for all lattice sites of the

tube, the $\pi\sigma$ coupling matrix due to spin-orbit interaction has a simple form

$$H_{\sigma\pi}^{SO} = i\Delta_{SO} \begin{pmatrix} 0 & 0 \\ S^z & 0 \\ -S^t & 0 \\ 0 & 0 \\ 0 & S^z \\ 0 & -S^t \end{pmatrix}. \quad (3.51)$$

Note that there are no S^r operators in the matrix elements of the SOI between the p_r and the σ orbitals. This is easily seen from the second quantized form of the atomic spin-orbit Hamiltonian Eq. (3.13), in which the Levi Civita symbol forbids the terms in which a spin operator and an orbital in the same direction appear. As a $\pi\sigma$ coupling always involves a p_r orbital, the S^r spin cannot appear.

In Eq. (3.51) the directions of the spin operators are defined in the local basis $\hat{\mathbf{r}}, \hat{\mathbf{t}}, \hat{\mathbf{z}}$. On the other hand, the hopping Hamiltonian does not affect the electron spin. A electron with spin pointing in the global x direction, say, and is hopping around the nanotube has its spin pointing in the global x direction independently of its position. This means that the hopping Hamiltonian is the identity in spin space, but only if the global spin basis $S^{x,y,z}$ is used, rather than the local spin basis $S^{r,t,z}$. Thus, also the spin operators in Eq. (3.51) must be transformed to the global basis. This transformation is given by

$$S^r(\varphi_i) = S^x \cos \varphi_i + S^y \sin \varphi_i \quad (3.52)$$

$$S^t(\varphi_i) = S^y \cos \varphi_i - S^x \sin \varphi_i \quad (3.53)$$

$$S^z = S^z. \quad (3.54)$$

Note that, unlike the hopping matrix $H_{\sigma\pi}^{\text{curv}}$, $H_{\sigma\pi}^{\text{SO}}$ depends not on the momentum but rather on φ_i . This is because the spin-orbit Hamiltonian we started from did not involve hoppings between neighboring carbon atoms but only local terms. Transforming this spatially dependent part of the Hamiltonian to the momentum space leads to non-diagonal matrix elements in \mathbf{k} , coupling the transverse momentum k_t to its neighboring momenta $k_t \pm \frac{1}{R}$. As we are finally interested in a low-energy theory for the lowest π subband, all virtual $+\Delta k_t$ processes must be compensated by a $-\Delta k_t$ process in second order perturbation theory. This will be discussed in detail in Sec. 3.4. For now, we keep the real-space notation of $H_{\sigma\pi}^{\text{SO}}$ and emphasize again that the matrices in Eqs. (3.50) and (3.51) are defined with respect to a different basis (k space and real space, respectively).

Electric field

As discussed in Sec. 3.2.3, there are two significant effects of an electric field applied perpendicular to the carbon nanotube. The orbitally diagonal cosine potential, described by $H_E^{(1)}$, will be discussed in Sec. 3.5; it turns out that $H_E^{(1)}$ is reduced by screening effects and, apart from leading to a small renormalization of the Fermi velocity,[] has no significant effect on the low-energy theory we aim at.

Most important, however, is the $s-p_r$ transition, described by $H_E^{(2)}$. In the basis $\mathcal{P} \times \mathcal{S}$, we find for the contribution of the $s-p_r$ transition to the $\pi\sigma$ coupling

$$H_{\sigma\pi}^E = \begin{pmatrix} -eE_r(\varphi_i)\xi_0 & 0 \\ 0 & 0 \\ 0 & 0 \\ 0 & -eE_r(\varphi_i)\xi_0 \\ 0 & 0 \\ 0 & 0 \end{pmatrix}, \quad (3.55)$$

where $E_r(\varphi_i)$ is the radial component of the electric field. The angular dependence of the electric field in the linear response regime can be approximated by

$$E_r(\varphi_i) = E \cos \varphi_i, \quad (3.56)$$

where E is the magnitude of the applied electric field applied perpendicular to the CNT axis (see also Fig. 1 in Ref. [60]). Again, we note that the matrix elements of $H_{\sigma\pi}^E$ are identities in spin space and do not depend on the momentum but on the azimuthal angle φ_i of the carbon atoms.

3.4 Effective Hamiltonian for the π band

Having defined all parts of the microscopic Hamiltonian, we are now in a position to derive the effective low-energy Hamiltonian of the CNT. This will be done in second order perturbation theory. The small parameters in which we expand are: the surface curvature a/R , the spin-orbit interaction coupling strength $\Delta_{SO} = 6$ meV, and the electric field strength $eE\xi_0 \simeq 50 \cdot E[\text{V/nm}]$ meV. The last two quantities are energy scales and must be compared to the typical σ band eigen energies which are on the order of a few eV. In the derivation of the low-energy theory, we completely neglect the Hamiltonian $H_E^{(1)}$. For the π band this Hamiltonian alone is known to give rise to a Fermi-velocity renormalization of second order in the electric field.[61] The question whether $H_E^{(1)}$ can actually be neglected will be critically discussed in Sec. 3.6.

The effective Hamiltonian for the π band is calculated in second-order perturbation theory as

$$H_\pi^{\text{eff}} \simeq H_\pi + H_{\pi\sigma} \frac{1}{\varepsilon - H_\sigma} H_{\pi\sigma}^\dagger, \quad (3.57)$$

where

$$H_{\pi\sigma} = H_{\pi\sigma}^{\text{curv}} + H_{\pi\sigma}^{SO} + H_{\pi\sigma}^E. \quad (3.58)$$

We proceed by inserting into Eq. (3.57) the unitary matrix U_σ , which diagonalizes H_σ and is constructed from the eigenvectors given by Eqs. (3.38)–(3.43)

$$H_\pi^{\text{eff}} \simeq H_\pi + H_{\pi\sigma} U_\sigma U_\sigma^\dagger \frac{1}{\varepsilon - H_\sigma} U_\sigma U_\sigma^\dagger H_{\pi\sigma}^\dagger, \quad (3.59)$$

so that the inverse operator $(\varepsilon - H_\sigma)^{-1}$ reduces to a diagonal sum of the σ band eigenvalues. Furthermore, since we are interested in energies close to the Dirac point, we set $\varepsilon = 0$. This reduces the complicated 8×8 Hamiltonian matrix, describing π and σ orbitals, to an effective 2×2 Hamiltonian matrix for the π orbitals only. The two-dimensional vector space, the matrix H_π^{eff} is defined in, corresponds to the two sublattices A and B. Note, however, that the matrix elements of H_π^{eff} still contain the momentum operator $\hat{\mathbf{k}} = (\hat{k}_t, \hat{k})$, the position operator $\hat{\varphi}_i$ and spin operators. In particular, we find

$$\begin{aligned} H_\pi^{\text{eff}}(\hat{\varphi}_i, \hat{\mathbf{k}}) = & \hbar v_F [(\hat{k}_t + \Delta k_{\text{cv}}^t)\sigma_1 + \tau(\hat{k} + \Delta k_{\text{cv}}^z)\sigma_2] \\ & + \alpha [S^z\sigma_1 - \tau S^t(\varphi_i)\sigma_2] + \tau\beta_1 [S^z \cos 3\theta - S^t(\varphi_i) \sin 3\theta] \\ & + \tau e E_r(\varphi_i) \xi_2 [S^t(\varphi_i)\sigma_2 - \tau S^z\sigma_1] + \\ & + \gamma_1 \tau S^r(\varphi_i)\sigma_3 + e E_r(\varphi_i)\xi_1, \end{aligned} \quad (3.60)$$

with the coefficients

$$\hbar v_F \begin{pmatrix} \Delta k_{\text{cv}}^t \\ \Delta k_{\text{cv}}^z \end{pmatrix} = \tau \frac{V_{pp}^\pi(V_{pp}^\pi + V_{pp}^\sigma)}{8(V_{pp}^\pi - V_{pp}^\sigma)} \left(\frac{a}{R} \right)^2 \begin{pmatrix} -\cos 3\theta \\ \sin 3\theta \end{pmatrix} \quad (3.61)$$

$$\alpha = \frac{\sqrt{3}\varepsilon_s(V_{pp}^\pi + V_{pp}^\sigma)\Delta_{\text{SO}}}{18V_{sp}^2} \frac{a}{R}, \quad (3.62)$$

$$\beta_1 = -\frac{\sqrt{3}V_{pp}^\pi\Delta_{\text{SO}}}{3(V_{pp}^\pi - V_{pp}^\sigma)} \frac{a}{R}, \quad (3.63)$$

$$\gamma_1 = \frac{2\varepsilon_s\Delta_{\text{SO}}^2}{9V_{sp}^2}, \quad (3.64)$$

$$\xi_1 = -\frac{(V_{pp}^\sigma + V_{pp}^\pi)}{2\sqrt{3}V_{sp}} \frac{a}{R} \xi_0, \quad (3.65)$$

$$\xi_2 = \frac{2\Delta_{\text{SO}}}{3V_{sp}} \xi_0. \quad (3.66)$$

As we aim at an effective theory for the lowest subband, we project $H_\pi^{\text{eff}}(\hat{\varphi}_i, \hat{\mathbf{k}})$ onto the subspace spanned by the wave functions of this subband. These wave functions are plane waves $\propto \exp(ikz)$ which do not depend on φ . Thus, projection means φ -averaging the Hamiltonian and setting $\hat{k}_t = 0$. Furthermore, since there is no operator in $H_\pi^{\text{eff}}(\hat{\varphi}_i, \hat{\mathbf{k}})$ which does not commute with \hat{k} , we may write

$$H_\pi^{\text{eff}}(k) = \int \frac{d\varphi}{2\pi} H_\pi^{\text{eff}}(\varphi, (0, k)). \quad (3.67)$$

Any term in $H_\pi^{\text{eff}}(\varphi, (0, k))$ containing odd powers of sin or cos average to zero. Finally, the resulting effective low-energy theory is given by

$$H_\pi^{\text{eff}} = H_{\text{hop}}^\pi + H_{\text{orb}}^{\text{cv}} + H_{\text{SO}}^{\text{cv}} + H_{\text{SO}}^{\text{el}}. \quad (3.68)$$

$H_{\text{orb}}^{\text{cv}}$ describes the curvature induced k -shift of the Dirac points.[24, 27, 29] For non-armchair metallic CNTs, $\Delta k_{\text{cv}}^t \neq 0$ leads to the opening of a gap at the Dirac point

$$H_{\text{orb}}^{\text{cv}} = \hbar v_F \Delta k_{\text{cv}}^t \sigma_1, \quad (3.69)$$

with

$$\hbar v_F \Delta k_{\text{cv}}^t = -\tau \frac{5.4 \text{ meV}}{R[\text{nm}]^2} \cos 3\theta. \quad (3.70)$$

The k -shift Δk_{cv}^z along the CNT is irrelevant and has been neglected here (see also Ref. [60]).

$H_{\text{SO}}^{\text{cv}}$ contains the curvature induced SOI [28, 27] which does not average out in the φ integration,

$$H_{\text{SO}}^{\text{cv}} = \alpha S^z \sigma_1 + \tau \beta S^z, \quad (3.71)$$

with the parameters

$$\alpha \simeq \frac{-0.08 \text{ meV}}{R[\text{nm}]}, \quad (3.72)$$

$$\beta \simeq \frac{-0.31 \text{ meV}}{R[\text{nm}]} \cos 3\theta. \quad (3.73)$$

This term contains only on the S^z spin operator which is consistent with the rotational symmetry of the nanotube. $H_{\text{SO}}^{\text{cv}}$ is responsible for the breaking of the electron-hole symmetry.[9]

Finally, the electric field induced SOI depends on the product $E(\varphi)S^t(\varphi)$, which does not average out in the φ integral. Indeed, $E(\varphi) \propto \cos \varphi$ while $S^t(\varphi) = S^y \cos \varphi - S^x \sin \varphi$. The $\cos^2 \varphi$ integral leads to a nonvanishing

$$H_{\text{SO}}^{\text{el}} = \tau e E \xi S^y \sigma_2, \quad (3.74)$$

where

$$\xi = \xi_2/2 = \frac{\Delta_{\text{SO}}}{3V_{sp}} \xi_0 \simeq 2 \times 10^{-5} \text{ nm}. \quad (3.75)$$

This term breaks rotational invariance of the CNT and involves the S^y operator for the electric field along the x axis. The fact that the directions of the applied field and the induced spin polarization are perpendicular is typical for the electric field-induced SOI.

3.5 Field screening

An electric field applied perpendicularly to a carbon nanotube induces a rearrangement of the electrons on the tube surface. If the electrons were free to move, as in the case of a

metal cylinder, the field inside the tube would be perfectly screened. However, since the density of states in CNTs at half-filling is small, the electrons rather behave as in half-metals, and thus the field screening is only partial. In the following, we calculate the field screening and its consequences explicitly by two methods: by a linear response calculation and by a direct diagonalization of the full Hamiltonian, including the external field. The analytical linear response calculation will provide us with a simple and intuitive picture of the screening but some uncontrolled approximations such as, for instance, the restriction to the π band, are needed there. The numerical calculation takes into account all bands derived from the second shell orbitals of the carbon atoms and provides a quantitative result, corroborating the linear response calculation.

The task is, therefore, to calculate the charge response of a CNT to the electrostatic potential described by

$$H_E = \phi_{0,\text{tot}} \sum_{\mathbf{n},\zeta} \cos(\varphi_{\mathbf{n},\zeta}) \hat{n}_{\mathbf{n},\zeta} \quad (3.76)$$

with $\phi_{0,\text{tot}}$ the amplitude of the total electrostatic potential acting on the tube surface. $\varphi_{\mathbf{n},\zeta}$ is the azimuthal angle of the carbon atom in unit cell \mathbf{n} and sublattice ζ . The operator $\hat{n}_{\mathbf{n},\zeta} = \sum_{\mu} c_{\mathbf{n},\zeta,\mu}^{\dagger} c_{\mathbf{n},\zeta,\mu}$ counts the electrons on atom (\mathbf{n}, ζ) in all second shell orbitals $\mu = s, p_r, p_t, p_z$. In order to keep the notation simple, we drop the spin index λ in this section and multiply the charge response by a factor of 2.

Note that H_E describes a homogeneous electric field E , which gives rise to the electrostatic potential $\phi_{\text{ext}}(\varphi) = eER \cos \varphi$. E is the field which is applied externally. In the following we will show that the induced electron charges on the tube surface give rise to an induced electrostatic potential $\phi_{\text{ind}}(\mathbf{r})$ which, although it has a rather complicated spatial structure away from the nanotube surface (i.e. for $|\mathbf{r}| \neq R$), reduces to $\phi_{\text{ind}}(\varphi) = \phi_{0,\text{ind}} \cos \varphi$ for $|\mathbf{r}| = R$. Thus, anticipating this result, the total potential $\phi_{\text{tot}}(\varphi) = \phi_{\text{ext}}(\varphi) + \phi_{\text{ind}}(\varphi) = \phi_{0,\text{tot}} \cos \varphi$ is described by the Hamiltonian (3.76). As discussed in Sec. 3.5.4, this additivity property of the amplitudes $\phi_{0,\text{ext}}$ and $\phi_{0,\text{ind}}$ can be interpreted as a linear screening of the electric field inside the nanotube, i.e., $\phi_{0,\text{tot}} = eE^*R$ with the screened field $E^* < E$.

3.5.1 Linear response of the π band

We define the static linear response coefficient $\chi_{\zeta\zeta'}^{\mu\mu'}(\mathbf{n}, \mathbf{n}')$ as the proportionality constant between the density response at site (\mathbf{n}, ζ) in orbital μ and the density perturbation at site (\mathbf{n}', ζ') in orbital μ' described by any Hamiltonian $A c_{\mathbf{n}'\zeta'\mu'}^{\dagger} c_{\mathbf{n}'\zeta'\mu'}$

$$\rho_{\mathbf{n}\zeta\mu} = \delta \left\langle c_{\mathbf{n}\zeta\mu}^{\dagger} c_{\mathbf{n}\zeta\mu} \right\rangle = A \chi_{\zeta\zeta'}^{\mu\mu'}(\mathbf{n}, \mathbf{n}'). \quad (3.77)$$

$\chi_{\zeta\zeta'}^{\mu\mu'}(\mathbf{n}, \mathbf{n}')$ can be calculated by the Kubo formula

$$\begin{aligned}\chi_{\zeta\zeta'}^{\mu\mu'}(\mathbf{n}, \mathbf{n}') = -2i \int_0^\infty dt e^{-\eta t} \\ \times \left\langle \left[c_{\mathbf{n}\zeta\mu}^\dagger(t) c_{\mathbf{n}\zeta\mu}(t), c_{\mathbf{n}'\zeta'\mu'}^\dagger c_{\mathbf{n}'\zeta'\mu'} \right] \right\rangle, \quad (3.78)\end{aligned}$$

where $c_{\mathbf{n},\zeta,\mu}(t) = e^{itH} c_{\mathbf{n},\zeta,\mu} e^{-itH}$ is the Heisenberg representation of the electron annihilation operator and $\eta = 0^+$ ensures the convergence of the time integral. The factor 2 accounts for the spin-degeneracy. The average denotes the expectation value with respect to the ground state of the electronic system. The generalization to finite temperatures is possible but not of interest here.

The linear response of the nanotube to the Hamiltonian defined in Eq. (3.76) is

$$\rho_{\mathbf{n}\zeta\mu} = \phi_0 \sum_{\mathbf{n}',\zeta',\mu'} \cos(\varphi_{\mathbf{n}',\zeta'}) \chi_{\zeta\zeta'}^{\mu\mu'}(\mathbf{n}, \mathbf{n}'). \quad (3.79)$$

In the remainder of this subsection we deal only with the linear response in the π band allowing us to set $\mu = \mu' = p_r$ and suppress the orbital index. The contributions of the σ band will be discussed below on the basis of the numerical calculation. Furthermore, we restrict the calculation to armchair nanotubes.

A straightforward calculation of the charge density induced by the Hamiltonian (3.76) gives rise to two terms in the charge response: a normal response, which has the same cosine modulation as the inducing Hamiltonian [Eq. (3.76)], and an anomalous response, which is staggered on the sublattice level and has a sine modulation,

$$\rho(\varphi_{\mathbf{n},\zeta}) = \phi_{0,\text{tot}} [\chi_n \cos \varphi_{\mathbf{n},\zeta} - \zeta \chi_a \sin \varphi_{\mathbf{n},\zeta}], \quad (3.80)$$

with the normal and anomalous response coefficients

$$\chi_n = \chi_{AA} + \text{Re} \chi_{BA} \cos(\varphi_{AB}) - \text{Im} \chi_{BA} \sin(\varphi_{AB}), \quad (3.81)$$

$$\chi_a = \text{Re} \chi_{BA} \sin(\varphi_{AB}) + \text{Im} \chi_{BA} \cos(\varphi_{AB}). \quad (3.82)$$

Here $\varphi_{AB} = a/\sqrt{3}R$ is the difference of the azimuthal angle between the different sublattice sites within one unit cell and χ_{AA}, χ_{BA} are the k -space susceptibilities, defined by

$$\chi_{\zeta\zeta'} = \chi_{\zeta\zeta'}^{pp_r}(\mathbf{q} = \hat{\mathbf{t}}/R). \quad (3.83)$$

As expected, the relevant susceptibilities for the charge response to a transverse homogeneous field are to be evaluated for zero momentum along the tube and for the smallest possible momentum around the tube.

The charge susceptibilities required for Eq. (3.83) can be expressed as k -space integrals

$$\chi_{\zeta\zeta}(\mathbf{q}) = \frac{1}{N} \sum_{\kappa, a, a'} \frac{\Theta(\varepsilon_F - \varepsilon_a(\boldsymbol{\kappa}))\Theta(\varepsilon_{a'}(\boldsymbol{\kappa} + \mathbf{q}) - \varepsilon_F)}{\varepsilon_a(\boldsymbol{\kappa}) - \varepsilon_{a'}(\boldsymbol{\kappa} + \mathbf{q})} \quad (3.84)$$

$$\begin{aligned} \chi_{-\zeta\zeta}(\mathbf{q}) &= \frac{1}{N} \sum_{\kappa, a, a'} aa' \exp(i\zeta(\phi_{\boldsymbol{\kappa}} - \phi_{\boldsymbol{\kappa}+\mathbf{q}})) \\ &\times \frac{\Theta(\varepsilon_F - \varepsilon_a(\boldsymbol{\kappa}))\Theta(\varepsilon_{a'}(\boldsymbol{\kappa} + \mathbf{q}) - \varepsilon_F)}{\varepsilon_a(\boldsymbol{\kappa}) - \varepsilon_{a'}(\boldsymbol{\kappa} + \mathbf{q})}, \end{aligned} \quad (3.85)$$

where the spin-degeneracy has been taken into account. ε_F is the Fermi energy and $\varepsilon_a(\boldsymbol{\kappa})$ are the energy eigenvalues for the two branches ($a = \pm 1$) of the π band. We assume here that the curvature effects, discussed in Sec. 3.3, do not affect the final charge polarization significantly. This assumption will be tested numerically in the next subsection. Thus, we calculate $\varepsilon_{\pm}(\boldsymbol{\kappa}) = \pm|V_{pp}^{\pi}w(\boldsymbol{\kappa})|$ and $\phi_{\boldsymbol{\kappa}} = \arg w(\boldsymbol{\kappa})$ from the Hamiltonian (3.20).

Furthermore, we restrict the discussion to the charge neutrality point $\varepsilon_F = 0$ so that $a = -1$ and $a' = 1$ and

$$\chi_{\zeta\zeta}(\mathbf{q}) = -\frac{1}{|V_{pp}^{\pi}|N} \sum_{\boldsymbol{\kappa}} \frac{1}{|w(\boldsymbol{\kappa})| + |w(\boldsymbol{\kappa} + \mathbf{q})|} \quad (3.86)$$

$$\chi_{-\zeta\zeta}(\mathbf{q}) = \frac{1}{|V_{pp}^{\pi}|N} \sum_{\boldsymbol{\kappa}} \frac{\exp(i\zeta(\phi_{\boldsymbol{\kappa}} - \phi_{\boldsymbol{\kappa}+\mathbf{q}}))}{|w(\boldsymbol{\kappa})| + |w(\boldsymbol{\kappa} + \mathbf{q})|}. \quad (3.87)$$

Note that for $\mathbf{q} = 0$ we have $\chi_{\zeta\zeta}(0) = -\chi_{-\zeta\zeta}(0)$ so that the linear response to a homogeneous potential is zero in flat graphene. This is a consequence of the vanishing density of states of graphene at the charge neutrality point. For the \mathbf{q} vectors given by Eq. (3.83) and for the k -space grid defined by the circumference and the length of the CNT (we assume periodic boundary conditions in z direction), the k -space summations in Eqs. (3.86) and (3.87) are evaluated numerically. For instance, for a (10,10)-CNT and in the limit of infinitely long tubes we obtain

$$|V_{pp}^{\pi}|\chi_n = -0.0424, \quad |V_{pp}^{\pi}|\chi_a = 0.002. \quad (3.88)$$

In the Dirac approximation of the band structure, i.e., $\varepsilon_{\pm}(\mathbf{k}) = \pm\sqrt{3}|V_{pp}^{\pi}||\mathbf{k}a|/2$, Eqs. (3.86) and (3.87) can be calculated analytically for small $q = |\mathbf{q}|$. For the spin-susceptibility, which is equal to the charge susceptibility for non-interacting systems, this has been done in Refs. [62, 63, 64] with the result

$$\frac{\hbar v_F}{a} \chi_{\zeta\zeta}(q) = -\frac{\Lambda a}{2\pi} + \frac{qa}{16} \quad (3.89)$$

$$\frac{\hbar v_F}{a} \chi_{-\zeta\zeta}(q) = \frac{\Lambda a}{2\pi} - \frac{3qa}{16}, \quad (3.90)$$

where Λ is an ultraviolet cutoff, a is the lattice constant, and $\hbar v_F/a = \sqrt{3}|V_{pp}^\pi|/2$. From this we find the analytical forms for the normal and anomalous response coefficients

$$|V_{pp}^\pi|\chi_n = -\frac{1}{4\sqrt{3}}\frac{a}{R} - \frac{\Lambda a}{6\sqrt{3}\pi} \left(\frac{a}{R}\right)^2 + O((a/R)^3) \quad (3.91)$$

$$|V_{pp}^\pi|\chi_a = \frac{\Lambda a}{3\pi}\frac{a}{R} - \frac{1}{8} \left(\frac{a}{R}\right)^2 + O((a/R)^3). \quad (3.92)$$

The comparison of the analytical result for χ_n with the numerical evaluation of the Kubo integrals in Fig. 3.6 shows that the first term in Eq. (3.91) captures the leading a/R -term qualitatively in a correct way. However, the Dirac approximation leads to a wrong prefactor.

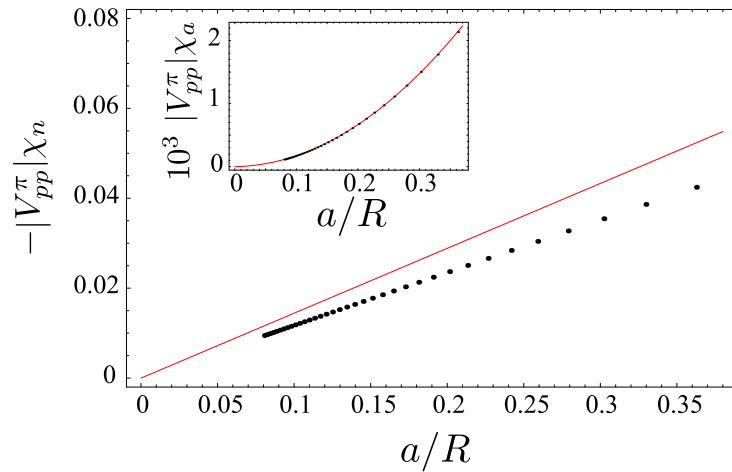


Figure 3.6: The normal response coefficient χ_n of the π band as a function of a/R . The black dots are the exact result from the numerical evaluation of Eqs. (3.86) and (3.87). The solid line shows the linear term in Eq. (3.91). The inset shows the anomalous response coefficient χ_a together with a polynomial fit $\chi_a \simeq 0.016(a/R)^2$.

The analytical form of the anomalous response calculated in the Dirac approximation differs from the exact result. In the next subsection we explain the reason for this and why the evaluation of Kubo formulas within the Dirac approximation is not reliable. However, as we are finally interested in the field screening, the anomalous response, which is staggered on the atomic scale, is irrelevant as it averages out in a continuum approximation of the charge distribution. The staggered potential induced by the anomalous response has a $\sin \varphi$ modulation so that it does not open a gap. We have checked numerically that such an additional term in the Hamiltonian does not change our results.

3.5.2 Analysis of the Kubo integral

It is instructive to study the structure of the Kubo integrals for the charge susceptibilities [Eqs. (3.86) and (3.87)] in more detail, especially in view of their Dirac approximations.

For $\mathbf{q} = 0$ the intra-sublattice susceptibility has the structure

$$\chi_{\zeta\zeta}(\mathbf{q} = 0) \propto \int d\varepsilon \frac{D(\varepsilon)}{\varepsilon}, \quad (3.93)$$

where $D(\varepsilon) = N^{-1} \sum_{\kappa,a} \delta(\varepsilon - \varepsilon_a(\kappa))$ is the density of states. In graphene, $D(\varepsilon)$ is known to be linear in the energy ε near the Dirac point. For carbon nanotubes, which can be viewed as graphene with one confined direction, $D(\varepsilon)$ is constant for $\varepsilon \simeq 0$, but it increases discontinuously with ε as ε crosses more and more transverse subbands. On a coarse grained energy scale $D(\varepsilon) \sim \varepsilon$ for both, CNTs and graphene, as long as $\varepsilon \lesssim 3$ eV. In the Dirac approximation, it is assumed that only electronic states with low energies are important, i.e., that the integral in Eq. (3.93) converges before $\varepsilon \simeq 3$ eV. However, Eq. (3.93) does obviously not converge for $D(\varepsilon) \sim \varepsilon$ so that, strictly speaking, the Dirac approximation is not allowed for Kubo formulas.

This convergence problem is reflected in the cutoff dependence of the first terms in Eqs. (3.89) and (3.90). However, the terms linear in q do not depend on the ultraviolet cutoff, which suggests that only contributions from small energies, where the Dirac approximation is valid, enter the q -dependence. Indeed, one finds that in the high energy regime

$$\chi_{\zeta\zeta}(\mathbf{q}) - \chi_{\zeta\zeta}(0) \sim \int d\varepsilon \frac{D(\varepsilon)}{\varepsilon^5} \quad (3.94)$$

converges quickly.

In order to compare the Kubo integrals of the tight-binding formulation with the Dirac approximation, we consider $\chi_{AA}(\mathbf{q} = 0)$. Eq. (3.86) can be written as

$$-|V_{pp}^\pi|\chi_{\zeta\zeta}(0) = \int_0^\infty d\varepsilon f(\varepsilon), \quad (3.95)$$

with

$$f(\varepsilon) = \frac{1}{N} \sum_{\kappa} \frac{\delta(\varepsilon - |w(\kappa)|)}{2|w(\kappa)|}. \quad (3.96)$$

In the Dirac approximation in which $w(\mathbf{K} + \mathbf{k}) \propto k_x + ik_y$ is assumed (we may drop all the prefactors in this analysis in favor of notational simplicity), $f_{\text{Dirac}}(\varepsilon)$ can be calculated easily. Since $f(\varepsilon) \sim D(\varepsilon)/\varepsilon$, the Dirac approximation $f_{\text{Dirac}}(\varepsilon)$ must be constant.

Calculating $f(\varepsilon)$ numerically for the more complicated tight-binding form of $w(\kappa)$, which can be evaluated only for finite size systems $N < \infty$, is not quite straightforward. We do this by discretizing the energy in $\Delta\varepsilon$ steps and defining

$$\begin{aligned} f_{\text{tb}}(\varepsilon, N) \\ = \frac{1}{N\Delta\varepsilon} \sum_{\kappa} \frac{\Theta[|w(\kappa)| - \varepsilon]\Theta[\varepsilon + \Delta\varepsilon - |w(\kappa)|]}{2|w(\kappa)|}. \end{aligned} \quad (3.97)$$

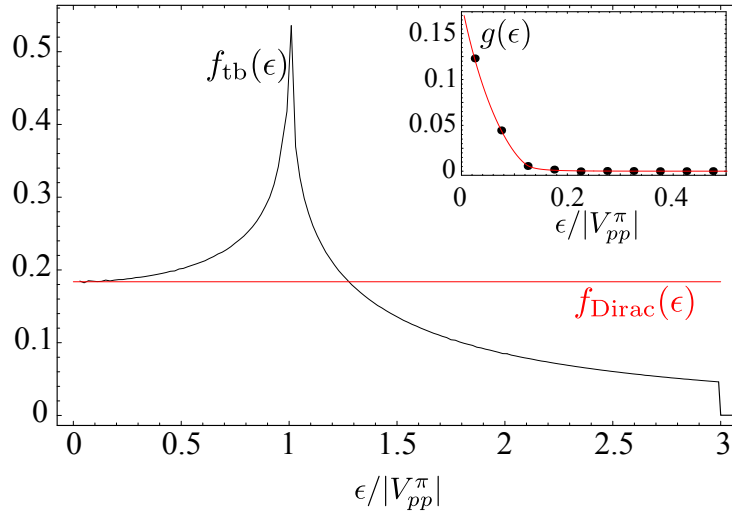


Figure 3.7: The energy-resolved integrand of the Kubo integral $f(\varepsilon)$ for $\chi_{\zeta\zeta}(\mathbf{q} = 0)$. The black line is the integrand calculated from the full tight-binding model $f_{\text{tb}}(\varepsilon)$ (see text). The horizontal gray (red) line shows the integrand in Dirac approximation $f_{\text{Dirac}}(\varepsilon)$. The inset shows the integrand $g(\varepsilon)$ for $\mathbf{q} = 2\pi\hat{\mathbf{t}}/50$. The dots are the results of the tight-binding calculation for a 200×200 k -space grid and the line shows the Dirac approximation of $g(\varepsilon)$.

In the limit $\Delta\varepsilon \rightarrow 0$ and $N \rightarrow \infty$, Eq. (3.97) approaches the actual $f(\varepsilon)$, as defined in Eq. (3.96). However, finite-size effects make f_{tb} look very rugged. In order to obtain a smooth $f(\varepsilon)$, which can be plotted nicely, we define an average over N

$$f_{\text{tb}}(\varepsilon) = \frac{1}{2M} \sum_{m=1}^M \left[f_{\text{tb}}(\varepsilon, (202 + 3m)^2) + f_{\text{tb}}(\varepsilon, (203 + 3m)^2) \right], \quad (3.98)$$

where we have assumed a quadratic k -space grid and we omitted all grids in which a k -space point hits a Dirac point. The choice of the smallest $N = 202^2$ is completely arbitrary, as well as the choice of $M = 82$, as long as M is large enough.

Fig. 3.7 shows $f_{\text{Dirac}}(\varepsilon)$ and $f_{\text{tb}}(\varepsilon)$. Obviously, for small $\varepsilon \ll |V_{pp}^\pi|$ the Dirac approximation coincides with the tight-binding calculation. However, for larger energies they strongly differ. Moreover, while the finite tight-binding bandwidth ($|w(\boldsymbol{\kappa})| \leq 3$) gives a natural high energy cutoff and ensures the convergence of the energy integral, the Dirac model must be replenished by an ultraviolet cutoff Λ in order to ensure the convergence.

For the deviation of the finite \mathbf{q} susceptibility from $\chi_{\zeta\zeta}(0)$

$$-|V_{pp}^\pi|[\chi_{\zeta\zeta}(\mathbf{q}) - \chi_{\zeta\zeta}(\mathbf{q} = 0)] = \int_0^\infty d\varepsilon g(\varepsilon), \quad (3.99)$$

with

$$g(\varepsilon) = \frac{1}{N} \sum_{\kappa} \delta(\varepsilon - |w(\kappa)|) \times \left[\frac{1}{|w(\kappa)| + |w(\kappa + \mathbf{q})|} - \frac{1}{2|w(\kappa)|} \right], \quad (3.100)$$

the integral is convergent for the tight-binding formulation as well as for the Dirac approximation. Furthermore, $g(\varepsilon)$ is only large at low energies, i.e., where the Dirac approximation is valid. Also, the comparison of the Dirac approximation of $g(\varepsilon)$ and the tight-binding calculation in the inset of Fig. 3.7 shows that the integrand $g(\varepsilon)$ is equal in both calculations.

3.5.3 Exact charge response

In order to scrutinize the results of the linear response calculation we diagonalize the Hamiltonian $H_0 + H_E$ numerically and calculate the charge distribution induced by H_E [Eq. (3.76)]. Unlike the linear response method, this calculation is not restricted to small fields E . We start with considering only the π bands in order to be able to check the results of the linear response calculation directly. In a second step, we then take into account all carbon orbitals of the second shell in order to see how the charge response is affected by the σ orbitals.

π band only

Considering only the π band and neglecting all curvature effects, we set $H_0 = H_{\text{hop}}^\pi$. We consider only armchair nanotubes and transform the direction along the nanotube to k -space. For a nanotube with N_c unit cells in circumferential direction, the Hamiltonian is a k -dependent $2N_c \times 2N_c$ matrix, which we diagonalize numerically. From the eigenvalues $\varepsilon_{m,k}$ and the corresponding eigenvectors $\psi_{m,k}(\varphi)$ we calculate the induced charge density (in units of the electron charge e)

$$\rho(\varphi) = \frac{2}{N_z} \sum_{m,k} \Theta(\varepsilon_F - \varepsilon_{m,k}) |\psi_{m,k}(\varphi)|^2 - 1. \quad (3.101)$$

Note that φ must be considered as a discrete variable with $2N_c$ possible values between 0 and 2π corresponding to the A and B sublattice sites in the N_c unit cells in circumferential direction. N_z is the number of unit cells along the tube (z direction). The spin-degeneracy is taken into account in Eq. (3.101).

Fig. 3.8 compares the density response to an external field corresponding to $\phi_{0,\text{tot}} = 0.01V_{pp}^\pi$, calculated from linear response and from the direct solution of the lattice Hamiltonian. Within numerical accuracy, both calculations give the same results for these small potential amplitudes. Also, one can clearly see the anomalous response, which makes the response curve different from a pure cosine shape.

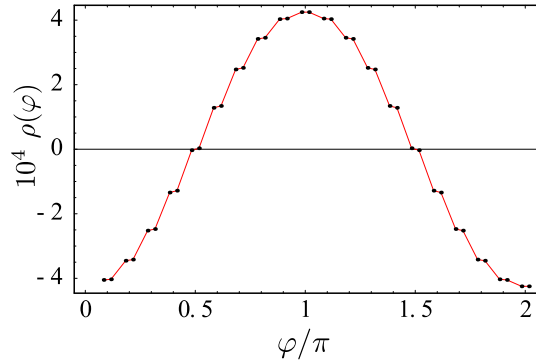


Figure 3.8: The induced π band charge density $\rho(\varphi)$ for in a (10,10)-CNT for $\phi_{0,\text{tot}} = 0.01V_{pp}^\pi$. The black dots show the results of the numerical diagonalization of the π band Hamiltonian. The line (red) is the charge response evaluated in linear response. The linear response data is also discrete. It is joined that it can be distinguished from the numerical results. Actually both calculations give the same result.

The response coefficients χ_n and χ_a can be extracted from the numerical calculations of the induced charge densities $\rho(\varphi)$ by a fit to Eq. (3.80). The normal response coefficients χ_n for larger potentials $\phi_{0,\text{tot}}$ resulting from these fits are shown in Fig. 3.9. For small external potentials, $\chi_n(\phi_{0,\text{tot}})$ is close to its linear response result, Eq. (3.91). For larger potentials, however, there are large deviations. The linear response regime is left if $\phi_{0,\text{tot}}$

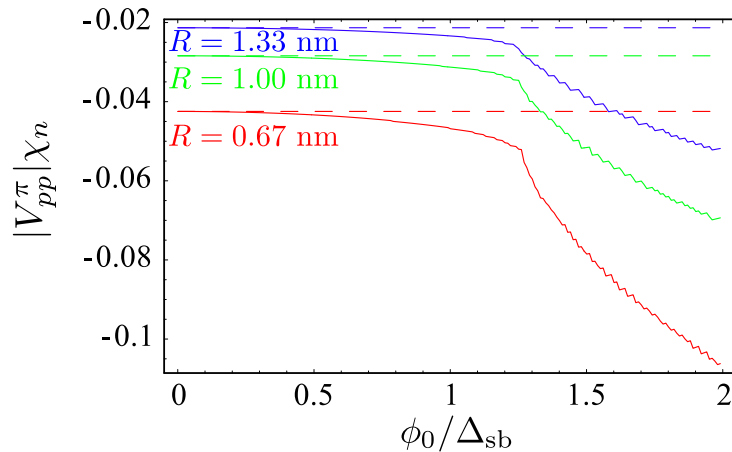


Figure 3.9: Nonlinearities in the normal response coefficient χ_n in the π band. The different curves correspond to different nanotube radii $R = 0.67, 1.00$, and 1.33 nm. The solid lines are the response coefficients fitted to the numerical charge density calculated by Eq. (3.101). The dashed lines indicate the corresponding linear response coefficients. The applied potential (abscissa) is rescaled with the subband splittings of the nanotubes with the different radii. These are $\Delta_{\text{sb}} = (0.31, 0.16, 0.078)|V_{pp}^\pi|$ for the radii $R = 0.67, 1.00$, and 1.33 nm, respectively.

is on the order of the subband splitting Δ_{sb} . This subband splitting depends on the CNT radius and is given in the caption of Fig. 3.9.

σ band contributions

In the analysis of the Kubo integral we have observed that the contributions to the charge susceptibilities from high energies cannot a priori be neglected. Thus, in order to check the stability of the π band calculation of the induced charge density, we calculate the charge redistribution in a tight-binding model containing all second shell orbitals of the carbon atoms, i.e., the π and the σ bands. For this, we numerically diagonalize the Hamiltonian

$$H = H_{\text{hop}} + H_{\text{SO}} + H_E, \quad (3.102)$$

with the individual terms of H defined in Sec. 3.2. The charge density can be separated into a π band part and a σ band part

$$\rho^\pi(\varphi_{\mathbf{n},\zeta}) = \sum_\lambda \left\langle c_{\mathbf{n}\zeta p_r \lambda}^\dagger c_{\mathbf{n}\zeta p_r \lambda} \right\rangle \quad (3.103)$$

$$\rho^\sigma(\varphi_{\mathbf{n},\zeta}) = \sum_\lambda \sum_{\mu=s,p_z,p_t} \left\langle c_{\mathbf{n}\zeta \mu \lambda}^\dagger c_{\mathbf{n}\zeta \mu \lambda} \right\rangle. \quad (3.104)$$

Both terms have the qualitative form found in the linear response theory. Defining the normal and the anomalous response coefficients for the π and σ response separately, we find for the exemplary (10,10)-CNT

$$|V_{pp}^\pi| \chi_n^\pi = -0.050 \quad V_{pp}^\pi \chi_n^\sigma = -0.0077 \quad (3.105)$$

$$V_{pp}^\pi \chi_a^\pi = 0.011 \quad V_{pp}^\pi \chi_a^\sigma = 0.0049 \quad (3.106)$$

Thus, about 87% of the normal charge response, which will be important for the field screening discussed in the next subsection, comes from the π electrons. Note that the field screening, which enters the Hamiltonian of this numerical calculation, has been taken into account self-consistently.

3.5.4 Field screening

As mentioned before, the charge response calculated in the previous subsections is not the actual charge response of the carbon nanotube because electron-electron interactions have not been taken into account. Their effect, however, is important because they reduce the amplitude of the charge rearrangement considerably.

In order to see this, we include the electron-electron interactions with a self-consistent Hartree calculation. In addition to this mean-field approximation, we assume that the charge induced by an external electric field is distributed homogeneously on the carbon

nanotube surface, i.e., we neglect the anomalous response as it is staggered on the sub-lattice level and averages out in the continuum approximation. We therefore assume that the electric field induces the continuous charge distribution

$$\rho^{3D}(\mathbf{r}) = \rho_0 \cos(\varphi) \delta(|\mathbf{r}| - R), \quad (3.107)$$

where R is the radius of the nanotube, φ is the continuous azimuthal angle of the spatial coordinate \mathbf{r} measured from the center of the nanotube, and ρ_0 is the amplitude of the induced charge distribution. ρ_0 is most easily determined by requiring that the total induced charge in the positive half space ($\cos \varphi > 0$) calculated from the continuum approximation Eq. (3.107) and from the lattice-resolved expression Eq. (3.80) are equal,

$$\int d^3\mathbf{r} \Theta(\cos \varphi) \rho^{3D}(\mathbf{r}) = e \sum_{\mathbf{n},\zeta} \Theta(\cos \varphi_{\mathbf{n},\zeta}) \rho(\varphi_{\mathbf{n},\zeta}), \quad (3.108)$$

with $\Theta(x)$ the unit step function and e the electron charge. The anomalous response drops out on the right hand side of Eq. (3.108). Furthermore, for the normal response, the right hand side of Eq. (3.108) is calculated approximately by using

$$\sum_{\mathbf{n},\zeta} f(\varphi_{\mathbf{n},\zeta}) \simeq \frac{L}{a} \frac{1}{\Delta\varphi} \int d\varphi f(\varphi), \quad (3.109)$$

where $\Delta\varphi = \frac{\sqrt{3}a}{4R}$ is the mean azimuthal angle between neighboring lattice sites in the armchair CNT, L is the length of the tube (in z direction) and $f(\varphi)$ is any function. The consequences of the errors, introduced by the above approximation, for the screening properties are much smaller than the consequences of the uncertainties of the hopping parameters. Therefore, we have

$$\rho_0 = \frac{4e}{\sqrt{3}a^2} \chi_n \phi_{0,tot}, \quad (3.110)$$

with $\phi_{0,tot}$ the amplitude of the electrostatic potential at the tube surface, including the contributions from the external and the induced fields. This back action effect is the basis for charge screening and will be calculated in the following.

A charge distribution of the form (3.107) induces an electric potential ϕ_{ind} which can be calculated by

$$\phi_{ind}(\mathbf{r}) = \frac{e}{4\pi\epsilon_0} \int d^3\mathbf{r}' \frac{\rho^{3D}(\mathbf{r}')}{|\mathbf{r} - \mathbf{r}'|}, \quad (3.111)$$

where ϵ_0 is the vacuum dielectric constant. For symmetry reasons, ϕ_{ind} does not depend on the z coordinate (along the tube) but has only a radial (r) and azimuthal (φ) dependence. We find

$$\phi_{ind}(r, \varphi) = \phi_{0,ind} \cos(\varphi) f(r/R). \quad (3.112)$$

with $\phi_{0,ind} = -\Gamma \phi_{0,tot}$ and

$$f(r/R) = \begin{cases} \frac{r}{R} & \text{for } r < R \\ \frac{R}{r} & \text{for } r > R \end{cases}. \quad (3.113)$$

The proportionality constant Γ is given by

$$\Gamma = 356.78R[\text{nm}]|\chi_n|\text{eV} \quad (3.114)$$

The total electrostatic potential $\phi_{\text{tot}}(\mathbf{r})$ felt by the electrons on the tube surface consists of two parts

$$\phi_{\text{tot}}(\mathbf{r}) = \phi_{\text{ext}}(\mathbf{r}) + \phi_{\text{ind}}(\mathbf{r}), \quad (3.115)$$

where $\phi_{\text{ext}}(\mathbf{r})$ comes from the external electric field and $\phi_{\text{ind}}(\mathbf{r})$ is induced by the rearrangement of electron charges at the tube surface.

At the tube surface $|\mathbf{r}| = R$, all terms in Eq. (3.115) have the same functional form ($\sim \cos \varphi$), so that the problem of solving the self-consistency equation reduces to an equation for the amplitudes of the electric potentials at the tube surface

$$\phi_{0,\text{tot}} = \phi_{0,\text{ext}} + \phi_{0,\text{ind}} = \phi_{0,\text{ext}} - \Gamma \phi_{0,\text{tot}} \quad (3.116)$$

and so

$$\phi_{0,\text{tot}} = \phi_{0,\text{ext}}/\gamma, \quad \gamma = 1 + \Gamma. \quad (3.117)$$

Inside the tube ($r < R$), the functional form of $\phi_{\text{tot}}(\mathbf{r})$ is the same as $\phi_{\text{ext}}(\mathbf{r})$, so that the total electric field inside the tube is homogeneous, just as the external field, but is screened by the factor γ . Thus, we may define the screened field

$$E^* = E/\gamma. \quad (3.118)$$

Note, however, that only inside the nanotube, the field is screened homogeneously. Outside the tube, the total electric field is highly inhomogeneous.

The screening factor γ quantifies how free the surface charges are to move. For a metal cylinder $\gamma \rightarrow \infty$, which means that the charges can move freely on the surface. For a cylinder made from an insulating material, the charges are localized and can only form dipoles, which is reflected by $\gamma \gtrsim 1$. A carbon nanotube lies in between the metallic and the insulating limit. For a (10,10)-CNT, for instance, we find $\gamma \simeq 5.6$, where the π and σ bands are taken into account. Note that $\gamma - 1$ depends linearly on the inverse hopping parameters [see, e.g., Eqs. (3.105) and (3.106)], so that the typical error of γ in a tight-binding calculation as performed here can be estimated by the spread of tight-binding parameters found in the literature. Within these error bars of 30%, our result is in agreement with previous works.[65, 66]

3.6 Analysis of the low-energy theory

3.6.1 Spectrum without electric field

In the absence of electric fields, the CNT is invariant under rotations around its axis and the z projection of the spin $s^z = \pm 1$ is a good quantum number. In addition, the

valley index $\tau = \pm 1$ is always a good quantum number, as long as there is no intervalley scattering. The term $\hbar v_F \Delta k_{\text{cv}}^z \sigma_2$ in $H_{\text{orb}}^{\text{cv}}$ shifts the momentum of the Dirac point along the tube. Assuming infinitely long tubes, this shift is irrelevant and can be dropped. Thus, we are left with the Hamiltonian

$$H = \tau s^z \beta + \tau \hbar v_F k \sigma_2 + (\hbar v_F (k_t + \Delta k_{\text{cv}}^t) + \alpha s^z) \sigma_1, \quad (3.119)$$

which is readily diagonalized (see also Ref. [27]). The eigenvalue spectrum has eight branches, given by

$$\varepsilon_{u,s_z}(k) = \tau s^z \beta + \sqrt{(\hbar v_F k)^2 + (\hbar v_F (k^t + \Delta k_{\text{cv}}^t) + \alpha s^z)^2}, \quad (3.120)$$

$$\varepsilon_{d,s_z}(k) = \tau s^z \beta - \sqrt{(\hbar v_F k)^2 + (\hbar v_F (k^t + \Delta k_{\text{cv}}^t) + \alpha s^z)^2}, \quad (3.121)$$

where $\tau = \pm 1$ and $s^z = \pm 1$. In the basis $\{|A\uparrow\rangle, |B\uparrow\rangle, |A\downarrow\rangle, |B\downarrow\rangle\}$, the eigenvectors are given by

$$\frac{1}{\sqrt{2}} \begin{pmatrix} 1 \\ e^{i\vartheta_+} \\ 0 \\ 0 \end{pmatrix}, \frac{1}{\sqrt{2}} \begin{pmatrix} -1 \\ e^{i\vartheta_+} \\ 0 \\ 0 \end{pmatrix}, \frac{1}{\sqrt{2}} \begin{pmatrix} 0 \\ 0 \\ 1 \\ e^{i\vartheta_-} \end{pmatrix}, \frac{1}{\sqrt{2}} \begin{pmatrix} 0 \\ 0 \\ -1 \\ e^{i\vartheta_-} \end{pmatrix}, \quad (3.122)$$

with

$$e^{i\vartheta_{\pm}} = \frac{(\hbar v_F (k^t + \Delta k_{\text{cv}}^t) \pm \alpha) + i\tau \hbar v_F k}{\sqrt{(\hbar v_F (k^t + \Delta k_{\text{cv}}^t) \pm \alpha)^2 + (\hbar v_F k)^2}}. \quad (3.123)$$

In the case of a semiconductor CNT a gap between the two nearest spin-up and spin-down states is

$$\Delta = 2|\alpha \pm \beta|, \quad (3.124)$$

where \pm corresponds to electrons and holes, respectively. In the case of an armchair nanotube, the eigenstates are two-fold spin-degenerate and the gap between holes and electrons is $2|\alpha|$.

An electric field perpendicular to the tube axis gives rise to the spin-orbit term $H_{\text{SO}} \propto S^y$, and so s^z no longer is a good quantum number. In the following we discuss the consequences of such an electric field.

3.6.2 Helical modes

As already discussed in Ref. [60], the interplay of strong electric fields and spin-orbit interaction leads to helical modes. For an armchair CNT the chiral angle is $\theta = \pi/6$ and all terms proportional to $\cos 3\theta$ vanish, i.e., $\Delta k_{\text{cv}}^t = 0$ and $\beta = 0$. Furthermore the longitudinal k -space shift Δk_{cv}^z can be ignored since it can be removed by regauging the phase of the orbitals. This leads to the effective Hamiltonian for the lowest subband in an armchair CNT

$$H^{\text{arm}} = \tau \hbar v_F k \sigma_2 + \alpha S^z \sigma_1 + \tau e E \xi S^y \sigma_2, \quad (3.125)$$

which has four branches of eigenvalues

$$\varepsilon(k) = \pm eE\xi \pm \sqrt{\alpha^2 + (\hbar v_F k)^2} \quad (3.126)$$

for each valley. In the basis $\{|A\uparrow\rangle, |B\uparrow\rangle, |A\downarrow\rangle, |B\downarrow\rangle\}$, the corresponding eigenvectors are given by

$$\frac{1}{2} \begin{pmatrix} -1 \\ e^{i\xi} \\ e^{i\xi} \\ 1 \end{pmatrix}, \frac{1}{2} \begin{pmatrix} 1 \\ -e^{i\xi} \\ e^{i\xi} \\ 1 \end{pmatrix}, \frac{1}{2} \begin{pmatrix} 1 \\ e^{i\xi} \\ -e^{i\xi} \\ 1 \end{pmatrix}, \frac{1}{2} \begin{pmatrix} 1 \\ e^{i\xi} \\ e^{i\xi} \\ -1 \end{pmatrix}, \quad (3.127)$$

with

$$e^{i\xi} = \frac{\alpha + i\tau\hbar v_F k}{\sqrt{\alpha^2 + (\tau\hbar v_F k)^2}}. \quad (3.128)$$

Note that the first two terms in Eq. (3.125) commute with the third term. As a result, this two parts can be diagonalized simultaneously, which leads to eigenvectors that are E -independent. The electric field E only enters the eigenvalues. In the following, we label the four branches for each valley by $n = 1, \dots, 4$. For each k , $n = 1$ corresponds to the highest eigenvalue and $n = 4$ to the lowest.

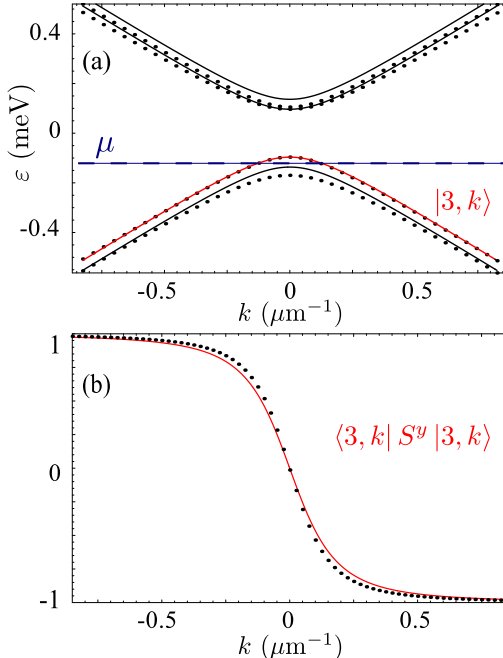


Figure 3.10: (a) Low-energy spectrum for a (10,10)-CNT (armchair) in a field $E = 1$ V/nm. (b) The dependence of y -spin polarization $\langle 3, k | S^y | 3, k \rangle$ on the momentum k along the tube. The solid lines are the results of the analytical low-energy effective theory. The dots correspond to numerical calculations (see text).

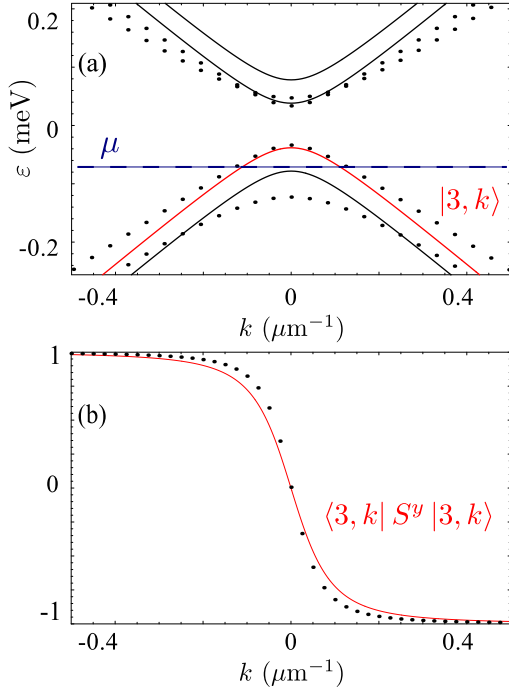


Figure 3.11: a) Low-energy spectrum for armchair CNT (20,20) in a field $E = 1 \text{ V/nm}$. b) The dependence of y -spin polarization $\langle 3, k | S^y | 3, k \rangle$ on a wave vector k . The solid lines are the results of the analytical low-energy effective theory. The dots correspond to numerical calculations (see text).

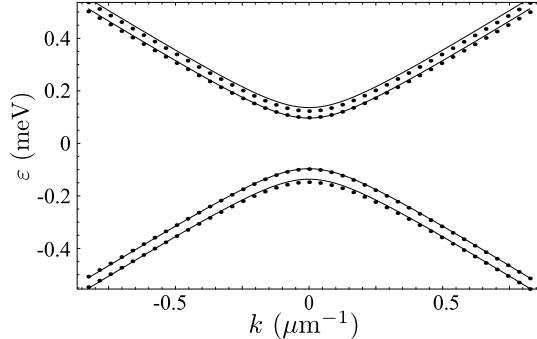


Figure 3.12: Low-energy spectrum for armchair CNT (10,10) in a field $E = 1 \text{ V/nm}$ assuming that the screening factor γ is equal to 20. The solid lines are the results of the analytical low-energy effective theory. The dots correspond to numerical calculations. In this limit we observe a good agreement between two models, which confirms our hypothesis that discrepancies in Fig. 3.10 are caused by the fact that we neglected the change in charge distribution caused by electric field.

In Figs. 3.10(a) and 3.11(a), the spectrum calculated from the analytical low energy theory is compared to the spectrum calculated from the numerical solution of the complete

tight-binding model [Eq. (3.1)]. Obviously, there are significant differences. These are due to the neglect of the Hamiltonian $H_E^{(1)}$ in the derivation of the analytical theory. It is known[61] that $H_E^{(1)}$ alone gives rise to a renormalization of the Fermi velocity on the order of the squared screened electric field $(E^*)^2 = (E/\gamma)^2$. However, the combination of $H_E^{(1)}$ with other parts in the spin-orbit Hamiltonian which depend trigonometrically on φ may give rise to effects of first order in $E^* \sim 1/\gamma$. Thus, the differences of the numerical and analytical spectrum should disappear in the limit of perfect screening, i.e. $\gamma \rightarrow \infty$. In order to check this expectation, we increase the screening parameter γ in the numerical calculation and find that the agreement between numerics and analytics becomes better for larger screening. For $\gamma = 20$, the analytical theory is as good as the numerics, as shown in Fig. 3.12. Better screening can be achieved, for instance, by filling the CNT with a dielectric.

The reason why these effects are important although they are of higher than second order is that the parameter regime we are discussing here is at the border of the applicability of perturbation theory. Nevertheless, as we will argue now, the effective theory is valuable also in this regime because it correctly captures the most important features of the helical modes. Moreover, we will show that the numerical results predict an even better spin-polarization than the analytical theory.

As mentioned above, the actual value of the parameter ξ is unknown. We use here a conservative estimate $\xi = 2 \cdot 10^{-5}$ nm, but exhausting the range of values for ξ_0 , Δ_{SO} , etc., ξ can increase by one order of magnitude.¹ In this case, i.e. for $\xi = 2 \cdot 10^{-4}$ nm, the analytical theory fits much better to the numerical calculations. This is essentially because the spin-splitting generated by $eE\xi S^z \sigma_2$ is sufficiently large so that the higher order terms, causing the deviations from the simple analytical model, are not effective in this case.

Next, we discuss the spin-polarization. The eigenstates given in Eq. (3.127) allow us to calculate the spin-polarization of each branch in the analytical model. It is easily seen that $\langle k, n | S^{x,z} | k, n \rangle = 0$, i.e., the spin is only polarized in the y direction (perpendicular to the CNT axis and to the electric field). In this sense, the spin is perfectly polarized, even though $\langle S^y \rangle$ is smaller than one; the vector $\langle \mathbf{S} \rangle$, with $\mathbf{S} = (S^x, S^y, S^z)$, is perfectly parallel to the y direction and has no components perpendicular to $\hat{\mathbf{y}}$. This y -spin polarization in the analytical model is given by

$$\langle k, n | S^y | k, n \rangle = \pm \frac{k}{\sqrt{k^2 + (\alpha/\hbar v_F)^2}}. \quad (3.129)$$

Note that $\langle k, n | S^y | k, n \rangle$ is odd in k . This means that for Fermi levels as indicated in Figs. 3.10 and 3.11, we have one helical liquid per Dirac point. The sign of the helicity, however, is the same for each Dirac point (this is a consequence of time-reversal invariance), so that a CNT with a properly tuned Fermi level is a perfect spin filter.

¹Note that in Table I of Ref. [60], ξ was given an order of magnitude too big by mistake. However, given the uncertainty of the parameters ξ_0 , Δ_{SO} , etc., and thus of ξ , all results remain valid.

In Figs. 3.10(b) and 3.11(b), the analytical spin-polarizations are compared with the numerical spin-polarizations. They agree well and the analytical spin-polarization is seen to be a lower bound to the numerical result. One should also note that, because of the increased splitting at zero k between states 3 and 4 of the numerical calculation compared to the analytical results, the range of possible Fermi levels for the helical liquid is increased. This leads to a higher maximum $\langle S^y \rangle$ in the more rigorous numerical solution. Also in this sense, the analytical model provides a lower bound on the maximum $\langle S^y \rangle$. For example, in the case of a (10,10)-CNT to which an electric field $E = 1$ V/nm is applied (see Fig. 3.10) one can achieve $\langle S^y \rangle \simeq 90\%$ in the helical phase.

Another well studied effect of the Hamiltonian $H_E^{(1)}$ is a renormalization of the Fermi velocity. We have not taken this renormalization into account in the analytical calculation in Fig. 3.11, but it is accounted for in the numerical calculation. Also this effect allows us to go to larger k_F in the helical regime.

Now that we have understood which features are well captured by the analytical model (e.g., the spin-polarization and the spectrum of the holes), and which are not described correctly (the electron spectrum for large fields), we discuss the case of non-armchair nanotubes on the basis of the analytical model. As mentioned above, the effects leading to deviations from the analytical results can be suppressed by increasing the screening of the externally applied electric field.

For non-armchair, but metallic nanotubes (i.e., $k_t = 0$), the chiral angle is $\theta \neq \pi/6$ and $\cos(3\theta) \neq 0$. This gives rise to two additional terms in the Hamiltonian [see Eq. (3.125)]. One term, $\hbar v_F \Delta k_{cv}^t \sigma_1$, opens an orbital gap. The other term, $\tau \beta S^z$, acts as an effective Zeeman field along the tube axis. For the mechanism of valley suppression, discussed in the next subsection, it is important to note that both additional terms have opposite signs in different valleys \mathbf{K}, \mathbf{K}' .

The most prominent effect of $\theta \neq \pi/6$ is the opening of a large orbital gap in the meV range for reasonable CNT radii R . For a nanotube with $R = 1.44$ nm but different helical angles, the low-energy spectrum is shown in Fig. 3.13. In the armchair CNT, the helical liquid appears on an energy scale of a few hundred μ eV. Thus, it is not a priori clear that the helicity of the left/right movers survives the departure from the pure armchair topology of the lattice. However, a plausibility argument for the stability of the helicity with respect to $\hbar v_F \Delta k_{cv}^t \sigma_1$ can be given: for large $k \gg \Delta k_{cv}^t$, the electronic states are eigenstates of the operator $\sigma_2 S^y$. In this limit the y -spin polarization (i.e., the helicity) becomes 100%. The y -spin polarization changes sign under $k \rightarrow -k$. Furthermore, as long as there is no band crossing, $\langle S^y \rangle$ must be a smooth, odd function of k . This means, as long as $|k_F| \neq 0$, the y -spin polarizations of the second band at $\pm k_F$ must be opposite. The question is only, how large is the amplitude of the polarization.

The orbital gaps are not the only effect of a nontrivial chirality $\theta \neq \pi/6$. The effective Zeeman field $\tau \beta S^z$ leads to an additional spin-polarization in z direction (along the tube). This can be observed in Fig. 3.14. At small k , where the electronic states are not forced into eigenstates of σ_2 , the effect of this effective Zeeman field is largest, i.e., the z polarization is maximal, while, at large $|k|$, the spin tends to be aligned in y direction. This

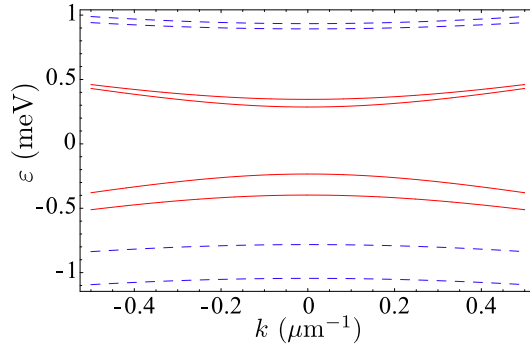


Figure 3.13: Low-energy spectrum for two chiral metallic CNTs with different chiralities but comparable radii. The field strength is 0.5 V/nm. The four bands with smaller absolute energy (red, solid) correspond to a (23,20)-CNT with $R = 1.44$ nm and $\theta = 0.154\pi$. The four bands with larger absolute energy (blue, dashed) are from a (26,17)-CNT with $R = 1.44$ nm and $\theta = 0.128\pi$.

effect reduces the quality of the spin helicity in that the spin alignment is not completely odd in k and not along \hat{y} . Only the y -spin component is odd, but the z -spin is an even function of k .

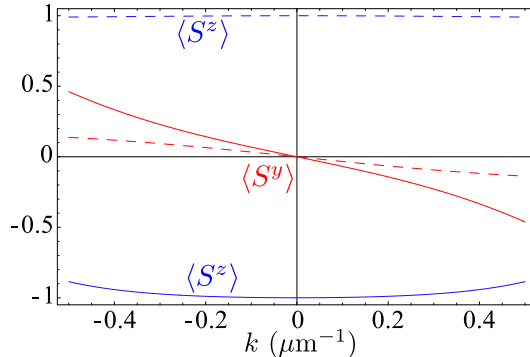


Figure 3.14: Spin-polarizations of the third band in y and z direction in chiral nanotubes as functions of k . The field strength is 0.5 V/nm. The odd functions around $k = 0$ (red) correspond to $\langle S^y \rangle$ and the even functions (blue) to $\langle S^z \rangle$. The solid lines are results from a (23,20)-CNT and the dashed lines from a (26,17)-CNT.

3.6.3 Valley suppression

In the previous section we have seen how the quality of the helicity is reduced in case of a non-armchair chirality of the CNT. This was due to an orbital k -shift $\hbar v_F \Delta k_{cv}^t \sigma_1$ and an effective Zeeman field $\tau \beta S^z$, both of which are consequences of the chiral angle $\theta \neq \pi/6$ deviating from the armchair case. Here, we show that the appearance of these terms can be turned into an advantage: by applying an additional magnetic field along the tube,

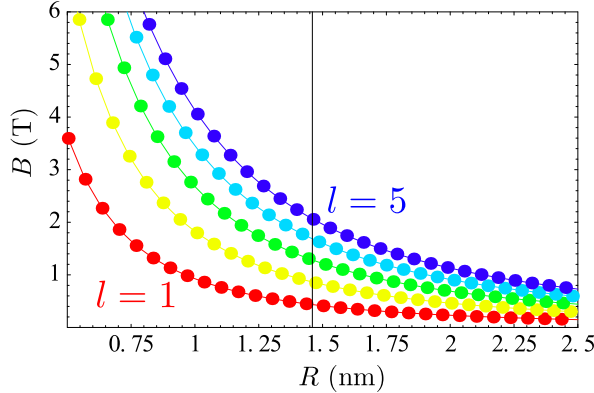


Figure 3.15: Magnetic fields needed for compensating the chirality-induced effective Zeeman term in different $(m + 3l, m)$ -CNTs as a function of CNT radius R . l varies from 1 (lower curves, red) to 5 (upper curves, blue). The dots correspond to the discrete radii and chiralities. The interconnecting lines are guides to the eye. The vertical line shows the optimal CNT radius at which both, the Zeeman term and the orbital shift, are compensated simultaneously.

the perfect helicity can be restored in one valley while all bands of the other valley are removed from the low-energy regime.

First note that both, the orbital k -shift and the effective Zeeman field, can be interpreted as originating from a magnetic field applied along the axis of the CNT. In general, a magnetic field \mathbf{B} has two effects on the electrons. First, it induces a Zeeman energy, described by the Hamiltonian

$$H_Z = \mu_B \mathbf{B} \cdot \mathbf{S}, \quad (3.130)$$

where μ_B is the Bohr magneton and \mathbf{S} is the vector of Pauli matrices for the electron spin (eigenvalues ± 1). Second, if the magnetic field has a component along the CNT axis, i.e., $B_z \neq 0$, the transverse wave function of the electron encloses magnetic flux and this gives rise to a shift in the electron momentum in circumferential direction

$$\Delta k_B^t = \frac{\pi B_z R}{\Phi_0}, \quad (3.131)$$

where $\Phi_0 = h/|e|$ is the magnetic flux quantum. Since Δk_B^t must be added to Δk_{cv}^t , as well as $\mu_B B_z S^z$ must be added to $\tau \beta S^z$, the effect of a non-armchair chirality of the CNT can be compensated for by a magnetic field, at least to a certain degree as explained below. However, since the chirality-induced Δk_{cv}^t and $\tau \beta$ have opposite signs in different valleys, but the real magnetic field terms Δk_B^t and $\mu_B B_z$ have not, this compensation works only in one of the two valleys. In the other valley, instead, the effect of the chirality is even increased.

Note that in general only one of the two chirality effects can be compensated for by a

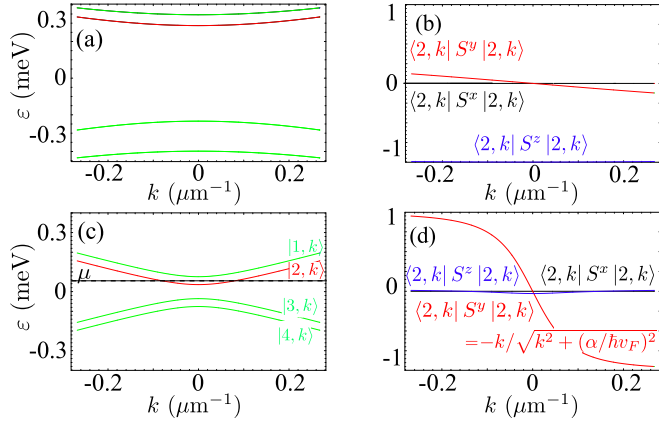


Figure 3.16: Chiral (23,20)-CNT with electric field $E = 1$ V/nm. (a) The spectrum and (b) the spin expectation values at the \mathbf{K}/\mathbf{K}' point for the $|2, k\rangle$ subband and magnetic field $B_z = 0$. For $B_z = 0.46$ T, the bands (c) at \mathbf{K}' (not shown) are gapped, while the spectrum at \mathbf{K} (solid lines) has the same form as in the armchair case [Eq. (3.126)]. The size of the gap is $2|\alpha| = 0.16$ meV. The spin expectation values (d) at \mathbf{K} for $|2, k\rangle$ follow closely the armchair case [see Eq. (3.129)].

magnetic field B_z . Compensating for the orbital gap requires

$$\hbar v_F \frac{\pi B_z R}{\Phi_0} = \tau \frac{5.4 \text{ meV}}{R[\text{nm}]^2} \cos 3\theta, \quad (3.132)$$

while compensating for the effective Zeeman field requires

$$\mu_B B_z = \tau \frac{0.31 \text{ meV}}{R[\text{nm}]} \cos 3\theta. \quad (3.133)$$

In general, Eqs. (3.132) and (3.133) are not compatible.

However, these two conditions have a different dependence on the CNT radius R , so that there exists an optimal radius $R_{\text{opt}} \simeq 1.46$ nm at which Eqs. (3.132) and (3.133) are compatible. For $R = R_{\text{opt}}$, the compensating magnetic field is

$$B_{z,\text{opt}} = 3.67 \text{ T} \cdot \cos 3\theta. \quad (3.134)$$

Of course, the CNT radius is not a continuous variable, but can only take on discrete values. Fig. 3.15 shows the fields needed for compensating the effective Zeeman term for different CNT chiralities. We see in Fig. 3.15 that there are indeed CNTs that have an optimal radius. In fact, the uncertainty in determining the optimal radius of actual CNTs is larger than the spacing of the dots in Fig. 14 so that all dots in the vicinity of the vertical line in the figure can be considered as optimal.

3.6.4 External magnetic fields in armchair CNTs

In this section we discuss the low-energy spectra of armchair carbon nanotubes in strong electric fields and additional magnetic fields \mathbf{B} along the three possible spatial directions.

Magnetic field along the nanotube

A magnetic field along the CNT axis $\mathbf{B} = B_z \hat{\mathbf{z}}$ leads to the shift of the circumferential wave vector, given by Eq. (3.131). Together with the Zeeman term, this leads to the additional term in the Hamiltonian

$$H_{\text{mag}} = \hbar v_F \frac{\pi B_z R}{\Phi_0} \sigma_1 + \mu_B B_z S^z. \quad (3.135)$$

The resulting spectrum of a (20,20)-CNT in a 1 V/nm electric field is shown in Fig. 3.17 for different magnetic field strengths.

As explained above, for the case of a magnetic field along the CNT axis, the additional terms in the Hamiltonian can be accounted for by redefining the parameters β and Δk_{cv}^t , i.e.,

$$\beta^* = \beta + \mu_B B_z, \quad (3.136)$$

$$\Delta k_{\text{cv}}^{t*} = \Delta k_{\text{cv}}^t + \pi B_z R / \Phi_0. \quad (3.137)$$

The energy spectrum at $k = 0$ for a chiral nanotube is given by

$$\varepsilon_{1,3} = -\alpha \pm \sqrt{(eE\xi)^2 + (\beta^* - \hbar v_F \Delta k^{t*})^2}, \quad (3.138)$$

$$\varepsilon_{2,4} = \alpha \pm \sqrt{(eE\xi)^2 + (\beta^* + \hbar v_F \Delta k^{t*})^2}. \quad (3.139)$$

The splitting Δ_1 at $k = 0$ is given, to leading order in the magnetic field B_z and for an armchair nanotube, by

$$\Delta_1 \simeq 2 \left| eE\xi + \frac{(\beta^* + \hbar v_F \Delta k^{t*})^2}{2eE\xi} \right|. \quad (3.140)$$

Magnetic field along the electric field

In case of a magnetic field perpendicular to the CNT axis we take into account only the Zeeman term, as the orbital effect is small for the strengths of the fields considered here. For $\mathbf{B} = B_x \hat{\mathbf{x}}$ parallel to the electric field the additional term in the Hamiltonian reads

$$H_{\text{mag}} = \mu_B B_x S^x. \quad (3.141)$$

For an armchair CNT, the total Hamiltonian can then be diagonalized analytically. We find

$$\begin{aligned} \varepsilon = \pm & \left[(eE\xi)^2 + \alpha^2 + (\mu_B B_x)^2 + (\hbar v_F k)^2 \right. \\ & \left. \pm 2\sqrt{(eE\xi\alpha)^2 + ((eE\xi)^2 + (\mu_B B_x)^2)(\hbar v_F k)^2} \right]^{\frac{1}{2}}. \end{aligned} \quad (3.142)$$

In Fig. 3.18 the spectrum is shown for several values of the magnetic field. B_x decreases the splitting at $k = 0$

$$\Delta_1 \simeq 2 \left| eE\xi \left(1 - \frac{1}{2} \frac{\mu_B^2 B_x^2}{\alpha^2 - (eE\xi)^2} \right) \right|. \quad (3.143)$$

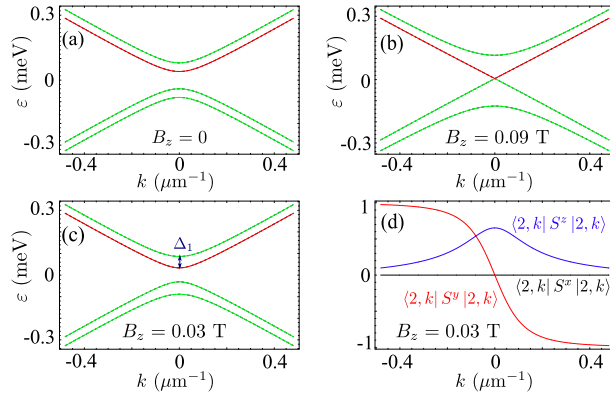


Figure 3.17: Spectrum of a (20,20)-CNT in an electric field $E = 1$ V/nm and different magnetic fields $B_z = 0, 0.09, 0.03$ T (parts a, b, c) along the nanotube axis (z direction). The dependence of the spin-polarization on the wave vector k is shown in part d) for $B_z = 0.03$ T. In the limit of the large magnetic fields the Zeeman term dominates and $\langle S^z \rangle \rightarrow \pm 1$. See Eq. (3.140) for Δ_1 .

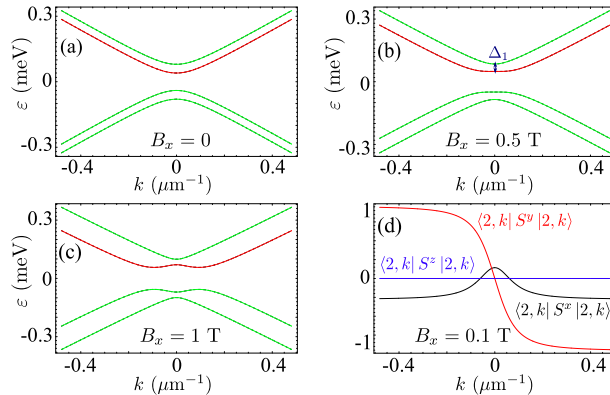


Figure 3.18: The spectrum of a (20,20)-CNT in the electric field $E = 1$ V/nm and different magnetic fields $B_x = 0, 0.5, 1$ T (parts a, b, c) along the electric field (x direction). The dependence of the spin-polarization on the wave vector k is represented on the graph d) for $B_x = 0.1$ T. In the limit of large magnetic fields the Zeeman term dominates and $\langle S^x \rangle \rightarrow \pm 1$. See Eq. (3.143) for Δ_1 .

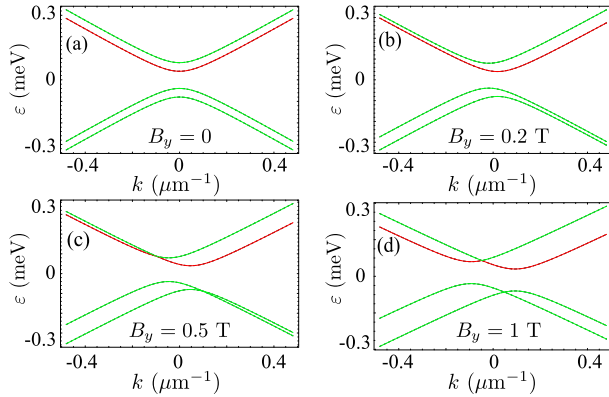


Figure 3.19: The spectrum of the CNT (20,20) in the electric field $E = 1 \text{ V/nm}$ and different magnetic fields $B_y = 0, 0.2, 0.5, 1 \text{ T}$ (parts a, b, c, d) perpendicular to the electric field and to the nanotube axis (y direction). The dependence of the spin-polarization on the wave vector is given by Eq. (3.129) with the shifted wave vector.

Magnetic field perpendicular to the electric field and the nanotube axis

A magnetic field perpendicular to the electric field and to the nanotube axis is described by the Zeeman term

$$H_{mag} = \mu_B B_y S^y. \quad (3.144)$$

In this case the magnetic field tries to polarize the spin in the same direction as the electric field. For an armchair nanotube the Hamiltonian can be diagonalized exactly giving the energy spectrum

$$\varepsilon_{1,2} = -eE\xi \pm \sqrt{\alpha^2 + (\hbar v_F k - \mu_B B_y)^2}, \quad (3.145)$$

$$\varepsilon_{3,4} = eE\xi \pm \sqrt{\alpha^2 + (\hbar v_F k + \mu_B B_y)^2}, \quad (3.146)$$

which is shown in Fig. 3.19. B_y leads to an additional shift $\Delta k = \pm \mu_B B_y / \hbar v_F$ of the momentum along the nanotube axis.

3.7 Resonant spin transitions

The manipulation of the electron spin by time-dependent external fields is most important for quantum computing and spintronics. Traditionally, a time-dependent magnetic field, coupling to the electron spin via the Zeeman energy, is utilized for Rabi flopping.[67] However, the combination of time-dependent electric fields and spin-orbit coupling may give rise to an all-electric control of the electron spin.[49, 50, 51, 52, 53] This effect is called electric dipole spin resonance (EDSR) and it was argued semiclassically[8] that this concept is applicable to CNTs in principle. In the following, we investigate the EDSR effect due to H_{SO}^{el} , which has been derived microscopically in Sec. 3.4.

In a spin resonance experiment one considers a spin which is split by a Zeeman energy E_Z . In order to drive transitions between the spin-up and spin-down states, an external field with frequency $\omega = E_Z/\hbar$ is required. In the case of a CNT, there are two regimes for such transitions, characterized by the frequencies required to drive them. Spin resonance at optical frequencies (THz regime) involve different subbands. They are possible² but not of interest in this work. The intra-subband transitions have characteristic energy scales below 1 meV, which corresponds to frequencies in the GHz regime. AC voltages in the GHz regime can easily be generated electronically, so that this regime is suitable for EDSR.

We now discuss the transitions between electronic states with opposite spins in the lowest subband, induced by a time-dependent electric field

$$\mathbf{E}_{ac}(t) = \mathbf{E}_{ac} \cos \omega t. \quad (3.147)$$

The effective Hamiltonian describing the interaction with a time-dependent field is similar to Eq. (3.74). However, we assume \mathbf{E}_{ac} along the y direction, so that

$$H^{ac}(t) = \tau e E_{ac}(t) \xi S^x \sigma_2. \quad (3.148)$$

This term can be used to implement the EDSR effect. The frequency ω of the field is chosen to fit the energy difference between two eigenstates of H_π^{eff} [Eq. (3.68)], between which the transitions are induced.

Indeed, the form of $H^{ac}(t)$ is typical for the EDSR effect. It has a trigonometric time dependence and is proportional to the spin operator S^x . However, $H^{ac}(t)$ is also proportional to the sublattice operator σ_2 , and this leads to an additional complication compared to a simple spin resonance Hamiltonian of the form $\cos(\omega t)S^x$. This complication disappears in the limit of large k where the term $\tau \hbar v_F k \sigma_2$ dominates in H_π^{eff} and one can assume σ_2 to be a good quantum number, i.e., $\sigma_2 = \pm 1$. In this case the Rabi frequency is given by

$$\omega_R^* = \frac{e E_{ac} \xi}{\hbar}. \quad (3.149)$$

The occurrence of the sublattice operator in the coupling term reduces the Rabi frequency $\omega_R < \omega_R^*$ around $k \simeq 0$.

3.7.1 Without dc electric field

We start with considering non-armchair CNTs with $\theta \neq \pi/6$. In this case, transitions between the states $\varepsilon_{u,+}$ and $\varepsilon_{u,-}$ [see Eq. (3.121)] are driven by $H^{ac}(t)$. For the Rabi

²The electromagnetic field, described by the time-dependent vector potential $\mathbf{A}_{ac}(\mathbf{r}, t) = \mathbf{A}_0 \sin(\omega t - \mathbf{k} \cdot \mathbf{r})$, leads to inter-subband transitions $H^{ind-tr} = v_F e A_0 i(n^+ - n^-)/2c$. The interplay of H^{ind-tr} with the spin-orbit interaction $H_\pi^{\text{SO-tr}} = \gamma_1 \sigma_3 (S^- n^+ + S^+ n^-) + \tau (\beta_1 \sin 3\theta + \alpha \sigma_2) i(S^+ n^- - S^- n^+)$, where the subband transitions come from the angular dependencies of the spin operators in Eq. (3.60), enables the realization of electric dipole spin resonance at optical frequencies. This effect, however, is beyond the scope of this work.

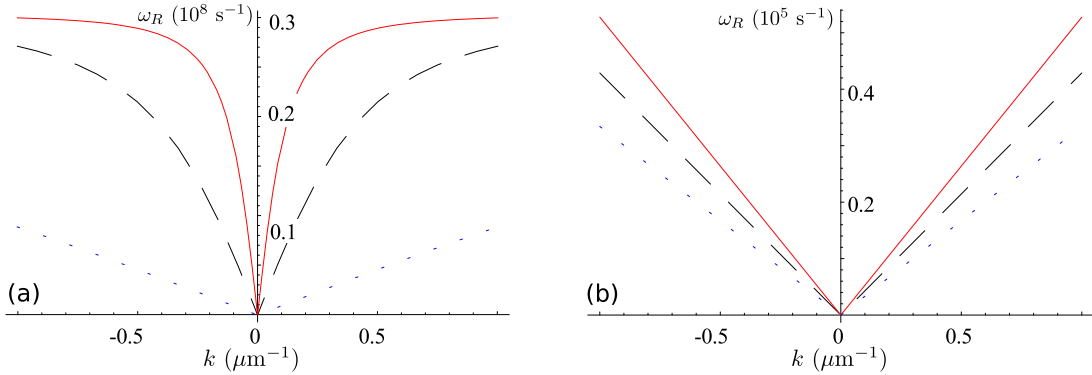


Figure 3.20: The dependence of the Rabi frequency ω_R on the wave vector k along the CNT axis (a) for the metallic nanotubes (13,10)-CNT (dotted), (23,20)-CNT (dashed), and (33,30)-CNT (solid). (b) shows ω_R for semiconducting nanotubes: the CNT (12,10) - dotted, the CNT (18,10) - dashed, the CNT (24,10) - solid. The amplitude of the ac electric field is 1 mV/nm.

frequency we obtain

$$\omega_R = \frac{eE_{ac}\xi}{\hbar} |\sin((\vartheta_+ + \vartheta_-)/2)|, \quad (3.150)$$

where ϑ_{\pm} is defined in Eq. (3.122). In agreement with what was explained above, Eq. (3.150) reduces to ω_R^* in the limit $k \rightarrow \pm\infty$.

For $k = 0$, the wavefunction is an eigenfunction of σ_1 . The states $\varepsilon_{u,+}$ and $\varepsilon_{u,-}$ have opposite spins but the same isospins σ_1 , if $\hbar v_F(k^t + \Delta k_{cv}^t) > \alpha$. The time-dependent electric field [Eq. (3.148)], however, couples spin (S) and isospin (σ) simultaneously. Thus, at $k = 0$ Rabi flopping between $\varepsilon_{u,+}$ and $\varepsilon_{u,-}$ via $H^{ac}(t)$ is not allowed and the Rabi frequency is zero (see Fig. 3.20). Near the Dirac points the Rabi frequency is proportional to k . We find

$$\omega_R \simeq \frac{eE_{ac}\xi}{\hbar} \left| \frac{k}{k^t + \Delta k_{cv}^t} \right|. \quad (3.151)$$

For non-metallic CNTs, k_t is very large and this leads to a strong suppression of the Rabi frequency (see Fig. 3.20).

A magnetic field along the nanotube axis renormalizes the coefficients β and Δk_{cv}^t [see Eqs. (3.136) and (3.137)] and thus allows us to change the Rabi and resonance frequencies. If the magnetic field is chosen such that $k^t + \Delta k_{cv}^{t*} = 0$, i.e., for $B = B_z^{cr}$ [see Eq. (3.132)], with

$$B_z^{cr} = \tau \frac{\Phi_0}{\pi \hbar v_F} \frac{5.4 \text{ meV}}{R[\text{nm}]^3} \cos 3\theta., \quad (3.152)$$

the Rabi frequency is ω_R^* for arbitrary k . Thus, by choosing B_z appropriately, the Rabi frequency can be increased to its upper limit ω_R^* . This effect is stable with respect to small deviations from the optimal B_z , as is shown in Fig. 3.21. Note that for $k = 0$, $\omega_R = \omega_R^*$ for any B_z sufficiently close to B_z^{cr} .

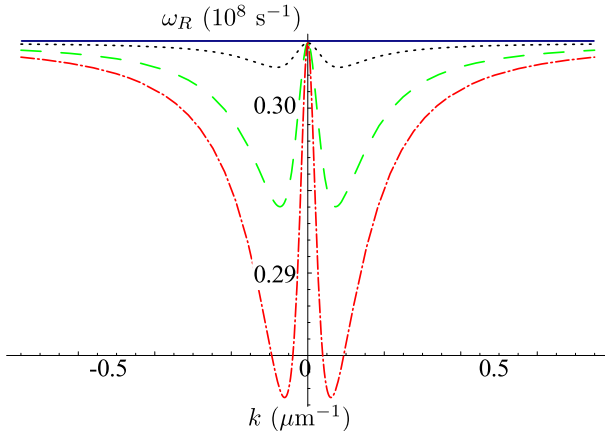


Figure 3.21: The dependence of the Rabi frequency ω_R on the wave vector k along the CNT (26,20) axis. The amplitude of the ac field is 1 mV/nm. The magnetic field along the CNT axis is equal to $B = 0.93B_z^{cr}$ (dash-dotted), $B = 0.95B_z^{cr}$ (dashed), $B = 0.98B_z^{cr}$ (dotted), and $B = B_z^{cr}$ (solid).

As usual, a magnetic field B perpendicular to the nanotube axis aligns the electron spin. An ac electric field along this magnetic field induces Rabi transitions. Assuming that the frequency of the electric field is tuned to the energy of the spin splitting at the Fermi points (the Fermi level is assumed to be tuned into the $k = 0$ splitting), the dependence of the Rabi frequency on the magnetic field is shown in Fig. 3.22.

If a circularly polarized field is applied, one induces the transitions only from the spin-down state at the Fermi level to the state spin-up above the Fermi level

$$H^{circ}(t) = \tau e E_{circ}(t) \xi S^+ \sigma_2, \quad (3.153)$$

with $S^\pm = S^x \pm iS^y$. If the opposite polarization of the field is chosen, the transitions

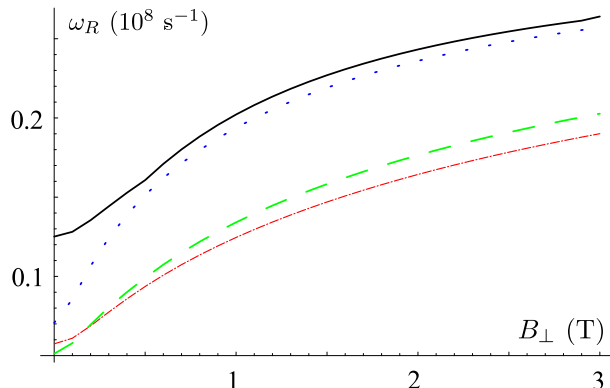


Figure 3.22: The dependence of the Rabi frequency ω_R on the magnetic field B_\perp applied perpendicular to the CNT axis for metallic nanotubes: the CNT (13,10) -dotted, the CNT (23,20) - dashed, the CNT (33,30) - full. The amplitude of the ac field is 1 mV/nm.

occur in the opposite directions.

3.7.2 With static electric field

A static electric field perpendicular to the axis of a nanotube in combination with SOI lifts the spin degeneracy in the spectrum of an armchair nanotube. In contrast to the well-known Rabi resonance method, realized in a static magnetic field and a perpendicular time-dependent magnetic field, we propose an all-electric setup for spin manipulation with two perpendicular electric fields, one of which is static and the other is time-dependent. The static electric field aligns the spin along the y direction, i.e., perpendicular to the CNT axis and perpendicular to the direction of the static electric field. The time-dependent electric field rotates spin around the x direction.

For armchair nanotubes we find that the transitions between states 1 and 2 or between 3 and 4 in the spectrum shown in Fig. 3.10 have the optimal Rabi frequencies ω_R^* . Rabi transitions between these groups (e.g. $1 \leftrightarrow 4$) are not possible.

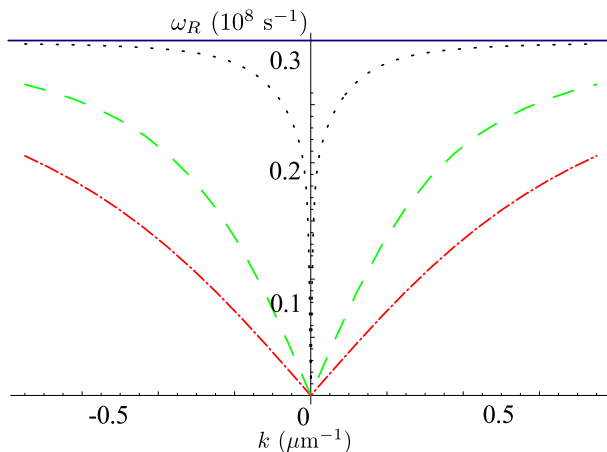


Figure 3.23: The dependence of the Rabi frequency ω_R on the wave vector k along the CNT (26,20) axis. The amplitude of the ac field is $E_{ac} = 1 \text{ mV/nm}$ and $E = 1 \text{ V/nm}$. The magnetic field along the CNT axis is equal to $B = 0$ (dash-dotted), $B = 0.5B_z^{cr}$ (dashed), $B = 0.9B_z^{cr}$ (dotted), and $B = B_z^{cr}$ (solid).

As explained above, for non-armchair but metallic CNTs, the orbital term Δk^{t*} can be compensated by an additional magnetic field $B_z = B_z^{cr}$ along the CNT. Then, as in the case of the armchair nanotube, the Rabi frequency of transitions between states 1 and 2 or between 3 and 4 is ω_R^* , while transitions between states of different groups are not allowed. For $B_z \neq B_z^{cr}$, the Rabi frequencies are smaller than ω_R^* and depend on k , as is shown in Fig. 3.23.

A magnetic field perpendicular to the nanotube axis (see Fig.3.18) breaks the symmetry of the spectrum around the Dirac point. As a result, the resonance frequencies for the right-moving and left-moving modes are different and it is possible to implement the EDSR mechanism for only one of the two modes.

3.8 Conclusions

We have studied the interplay of strong electric fields, magnetic fields and spin-orbit interactions in carbon nanotubes. An approximate effective low-energy theory describing the electrons near the two Dirac points has been derived analytically and this theory has been tested against more sophisticated numerical solutions of the lattice tight-binding Hamiltonian for the second shell π and σ orbitals. We have established that the properties of carbon nanotubes are described well by our analytical model in the limit of large field screening. The latter can be achieved by immersing the CNT into dielectrics.

The central feature of CNTs in electric fields is the appearance of (spin-filtered) helical modes in an all-electric setup. For perfect armchair nanotubes, there are two pairs of helical modes, one for each valley, transporting up-spins in one direction and down-spins in the opposite direction. This helicity is perfect in that the average spin is non-zero only for this one spin component and zero for all others. Thus, the average spin is a perfectly odd function of k for armchair CNTs. For non-armchair chiralities, an additional magnetic field can be used to restore the helical phase in one valley. In the other valley, all electronic states are removed from the low-energy regime so that this valley is suppressed by the combination of non-armchair chirality and magnetic field.

Furthermore, we have shown that the EDSR effect may be implemented by a time-dependent electric field perpendicular to the CNT. The typical Rabi frequencies which can be achieved in this system are in the MHz-GHz range.

We emphasize that the present low-energy theory, which is based on the assumption of structurally perfect infinitely long wires, can be extended to nontrivial geometries and to disordered tubes by adding appropriate terms to the effective Hamiltonian. This low-energy theory reduces the complexity of the modelling significantly because the (large) high-energy (sub) bands have been integrated out already. For instance, spatial potential fluctuations that have sufficiently long ranged correlations, and thus cannot scatter between subbands or valleys, appear as a spatially dependent 4×4 identity matrix in the effective 4×4 real-space Hamiltonian. Thus, the theory derived in this work provides the basis for further investigations of disorder and other effects.

We acknowledge helpful comments by P. Recher and A. Schultes. This work was partially supported by the Swiss NSF, NCCR Nanoscience, NCCR QSIT, and DARPA.

Bibliography

- [1] S. J. Tans, M. H. Devoret, H. Dai, A. Thess, R. E. Smalley, L. J. Geerligs, and C. Dekker, *Nature* **386**, 474 (1997).
- [2] D. H. Cobden and J. Nygård, *Phys. Rev. Lett.* **89**, 046803 (2002).
- [3] W. Liang, M. Bockrath, and H. Park, *Phys. Rev. Lett.* **88**, 126801 (2002).
- [4] E. Minot, Y. Yaish, V. Sazonova, and P. McEuen, *Nature* **428**, 536 (2004).
- [5] P. Jarillo-Herrero, S. Sapmaz, C. Dekker, L. P. Kouwenhoven, and H. S. J. van der Zant, *Nature* **429**, 389 (2004).
- [6] P. Jarillo-Herrero, J. Kong, H. S. J. van der Zant, C. Dekker, L. P. Kouwenhoven, and S. De Franceschi, *Phys. Rev. Lett.* **94**, 156802 (2005).
- [7] M. R. Gräber, W. A. Coish, C. Hoffmann, M. Weiss, J. Furer, S. Oberholzer, D. Loss, and C. Schönenberger, *Phys. Rev. B* **74**, 075427 (2006).
- [8] D. V. Bulaev, B. Trauzettel, and D. Loss, *Phys. Rev. B* **77**, 235301 (2008).
- [9] F. Kuemmeth, S. Ilani, D. C. Ralph, and P. L. McEuen, *Nature* **452**, 448 (2008).
- [10] H. O. H. Churchill, A. J. Bestwick, J. W. Harlow, F. Kuemmeth, D. Marcos, C. H. Stwertka, S. K. Watson, and C. M. Marcus, *Nat. Phys.* **5**, 321 (2009).
- [11] G. A. Steele, G. Gotz, and L. P. Kouwenhoven, *Nat. Nanotechnol.* **4**, 363 (2009).
- [12] H. Aurich, A. Baumgartner, F. Freitag, A. Eichler, J. Trbovic, and C. Schönenberger, *Appl. Phys. Lett.* **97**, 153116 (2010).
- [13] T. S. Jespersen, K. Grove-Rasmussen, J. Paaske, K. Muraki, T. Fujisawa, J. Nygård, and K. Flensberg, *Nat. Phys.* **7**, 348 (2011).
- [14] J. V. Holm, H. I. Jørgensen, K. Grove-Rasmussen, J. Paaske, K. Flensberg, and P. E. Lindelof, *Phys. Rev. B* **77**, 161406 (2008).
- [15] P. Jarillo-Herrero, J. Kong, H. S. van der Zant, C. Dekker, L. P. Kouwenhoven, and S. De Franceschi, *Nature* **434**, 484 (2005).
- [16] S. Sapmaz, P. Jarillo-Herrero, J. Kong, C. Dekker, L. P. Kouwenhoven, and H. S. J. van der Zant, *Phys. Rev. B* **71**, 153402 (2005).
- [17] G. Gunnarsson, J. Trbovic, and C. Schönenberger, *Phys. Rev. B* **77**, 201405 (2008).
- [18] S. Sahoo, T. Kontos, J. Furer, C. Hoffmann, M. Gräber, A. Cottet, and C. Schönenberger, *Nat. Phys.* **1**, 99 (2008).

- [19] F. Kuemmeth, H. Churchill, P. Herring, and C. Marcus, Mater. Today **13**, 18 (2010).
- [20] A. Pályi and G. Burkard, Phys. Rev. B **82**, 155424 (2010).
- [21] M. S. Rudner and E. I. Rashba, Phys. Rev. B **81**, 125426 (2010).
- [22] K. Flensberg and C. M. Marcus, Phys. Rev. B **81**, 195418 (2010).
- [23] S. Weiss, E. I. Rashba, F. Kuemmeth, H. O. H. Churchill, and K. Flensberg, Phys. Rev. B **82**, 165427 (2010).
- [24] T. Ando, J. Phys. Soc. Jpn. **69**, 1757 (2000).
- [25] D. Huertas-Hernando, F. Guinea, and A. Brataas, Phys. Rev. B **74**, 155426 (2006).
- [26] L. Chico, M. P. López-Sancho, and M. C. Muñoz, Phys. Rev. B **79**, 235423 (2009).
- [27] W. Izumida, K. Sato, and R. Saito, J. Phys. Soc. Jpn. **78**, 074707 (2009).
- [28] J.-S. Jeong and H.-W. Lee, Phys. Rev. B **80**, 075409 (2009).
- [29] C. T. White and J. W. Mintmire, J. Phys. Chem. B **109**, 52 (2005).
- [30] C. L. Kane and E. J. Mele, Phys. Rev. Lett. **95**, 226801 (2005).
- [31] H. Min, J. E. Hill, N. A. Sinitsyn, B. R. Sahu, L. Kleinman, and A. H. MacDonald, Phys. Rev. B **74**, 165310 (2006).
- [32] P. Středa and P. Šeba, Phys. Rev. Lett. **90**, 256601 (2003).
- [33] Y. V. Pershin, J. A. Nesteroff, and V. Privman, Phys. Rev. B **69**, 121306(R) (2004).
- [34] P. Devillard, A. Crépieux, K. I. Imura, and T. Martin, Phys. Rev. B **72**, 041309(R) (2005).
- [35] S. Zhang, R. Liang, E. Zhang, L. Zhang, and Y. Liu, Phys. Rev. B **73**, 155316 (2006).
- [36] D. Sánchez, L. Serra, and M.-S. Choi, Phys. Rev. B **77**, 035315 (2008).
- [37] J. E. Birkholz and V. Meden, Phys. Rev. B **79**, 085420 (2009).
- [38] C. H. L. Quay, T. L. Hughes, J. A. Sulpizio, L. N. Pfeiffer, K. W. Baldwin, K. W. West, D. Goldhaber-Gordon, and R. de Picciotto, Nat. Phys. **6**, 336 (2010).
- [39] B. Braunecker, G. I. Japaridze, J. Klinovaja, and D. Loss, Phys. Rev. B **82**, 045127 (2010).
- [40] M. Z. Hasan and C. L. Kane, Rev. Mod. Phys. **82**, 3045 (2010).
- [41] P. Středa and P. Šeba, Phys. Rev. Lett. **90**, 256601 (2003).

- [42] K. Sato, D. Loss, and Y. Tserkovnyak, Phys. Rev. Lett. **105**, 226401 (2010).
- [43] R. M. Lutchyn, J. D. Sau, and S. Das Sarma, Phys. Rev. Lett. **105**, 077001 (2010).
- [44] Y. Oreg, G. Refael, and F. von Oppen, Phys. Rev. Lett. **105**, 177002 (2010).
- [45] A. C. Potter and P. A. Lee, Phys. Rev. B **83**, 094525 (2011).
- [46] J. Alicea, Phys. Rev. B **81**, 125318 (2010).
- [47] S. Gangadharaiah, B. Braunecker, P. Simon, and D. Loss, Phys. Rev. Lett. **107**, 036801 (2011).
- [48] C. Nayak, S. H. Simon, A. Stern, M. Freedman, and S. Das Sarma, Rev. Mod. Phys. **80**, 1083 (2008).
- [49] Y. Kato, R. C. Myers, D. C. Driscoll, A. C. Gossard, J. Levy, and D. D. Awschalom, Science **299**, 1201 (2003).
- [50] V. N. Golovach, M. Borhani, and D. Loss, Phys. Rev. B **74**, 165319 (2006).
- [51] K. C. Nowack, F. H. L. Koppens, Y. V. Nazarov, and L. M. K. Vandersypen, Science **318**, 1430 (2007).
- [52] D. V. Bulaev and D. Loss, Phys. Rev. Lett. **98**, 097202 (2007).
- [53] E. A. Laird, C. Barthel, E. I. Rashba, C. M. Marcus, M. P. Hanson, and A. C. Gossard, Semicond. Sci. Technol. **24**, 064004 (2009).
- [54] R. Saito, G. Dresselhaus, and M. S. Dresselhaus, *Physical Properties of Carbon Nanotubes*, (Imperial College Press1998).
- [55] M. J. Schmidt and D. Loss, Phys. Rev. B **81**, 165439 (2010).
- [56] J. J. Sakurai, *Modern Quantum Mechanics*, (Addison-Wesley1994).
- [57] J. Serrano, M. Cardona, and J. Ruf, Solid State Commun. **113**, 411 (2000).
- [58] F. Guinea, New J. Phys. **12**, 083063 (2010).
- [59] M. Gmitra, S. Konschuh, C. Ertler, C. Ambrosch-Draxl, and J. Fabian, Phys. Rev. B **80**, 235431 (2009).
- [60] J. Klinovaja, M. J. Schmidt, B. Braunecker, and D. Loss, Phys. Rev. Lett. **106**, 156809 (2011).
- [61] D. S. Novikov and L. S. Levitov, Phys. Rev. Lett. **96**, 036402 (2006).
- [62] L. Brey, H. A. Fertig, and S. Das Sarma, Phys. Rev. Lett. **99**, 116802 (2007).

Chapter 3

- [63] A. M. Black-Schaffer, Phys. Rev. B **81**, 205416 (2010).
- [64] S. Saremi, Phys. Rev. B **76**, 184430 (2007).
- [65] L. X. Benedict, S. G. Louie, and M. L. Cohen, Phys. Rev. B **52**, 8541 (1995).
- [66] B. Kozinsky and N. Marzari, Phys. Rev. Lett. **96**, 166801 (2006).
- [67] N. M. Atherton, *Electron Spin Resonance*, (Ellis Horwod Limited, New York1973).

Chapter 4

Electric-Field Induced Majorana Fermions in Carbon Nanotubes

We consider theoretically an armchair Carbon nanotube (CNT) in the presence of an electric field and in contact with an *s*-wave superconductor. We show that the proximity effect opens up superconducting gaps in the CNT of different strengths for the exterior and interior branches of the two Dirac points. For strong proximity induced superconductivity the interior gap can be of the *p*-wave type, while the exterior gap can be tuned by the electric field to be of the *s*-wave type. Such a setup supports a single Majorana bound state at each end of the CNT. In the case of a weak proximity induced superconductivity, the gaps in both branches are of the *p*-wave type. However, the temperature can be chosen in such a way that the smallest gap is effectively closed. Using renormalization group techniques we show that the Majorana bound states exist even after taking into account electron-electron interactions.

This chapter has been published in Physical Review Letters 108, 196804 (2012).

4.1 Introduction

Majorana fermions in solid state systems have attracted considerable attention recently [1, 2, 3, 4, 5, 6, 7, 8, 9, 10]. In particular, the possibility of realizing them as bound states at the ends of semiconducting nanowires in the proximity of an *s*-wave bulk superconductor has led to much activity. Such setups require a Zeeman splitting, typically generated by an external magnetic field [11], that must be larger than the proximity induced gap to induce an effective *p*-wave superconductor in the topological phase. Such a magnetic field, however, tends to destroy the gap in the bulk superconductor itself, and thus a delicate balance must be found [12]. It is therefore very desirable to search for Majorana-scenarios which do not require magnetic fields.

One of the prerequisites for a Majorana bound end state (MBS) is the existence of helical modes, i.e. modes which carry opposite spins in opposite directions. It has been shown recently that such helical states are induced in Carbon nanotubes (CNT) via spin-orbit interaction (SOI) by an external *electric* field E [13, 14]. This mechanism works optimally for a special class of metallic CNTs: armchair CNTs (N, N). This class is characterized by a spin-degenerate low-energy spectrum around the two inequivalent Dirac points, K and K' . This degeneracy can be lifted by E which gives then rise to helical modes.

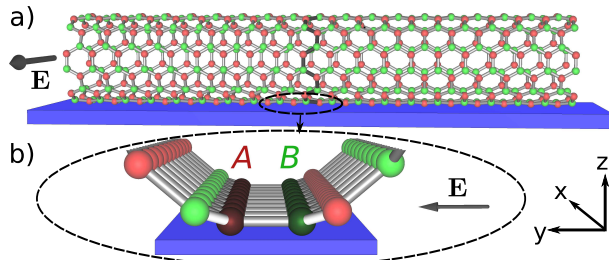


Figure 4.1: (a) An armchair nanotube (cylinder) is placed on top of a superconductor (blue slab). The x -axis points along the nanotube. An electric field E is applied perpendicular to the nanotube, say along y -axis [17]. There are two non-equivalent lattice sites: A (light red) and B (light green). (b) The distances between the superconductor surface and the atoms of sublattice A (dark-red row) and of sublattice B (dark-green row) are assumed the same. Thus, the tunneling amplitudes to the different sublattices are (nearly) equal.

However, when putting the CNT in contact with an *s*-wave superconductor (see Fig. 4.1) with the goal to generate MBS the following problem is encountered. The two Dirac points K and K' are Kramers partners (see Fig. 4.2) and thus the superconducting pairing induced via the proximity effect will involve both of them, *i.e.* left (right)-moving electrons from the branch at K get paired with the right (left)-moving electrons from the branch at K' to form an *s*-wave Cooper pair with zero total momentum.

This results in two superconducting gaps, an ‘exterior’ one, Δ_e , and an ‘interior’ one, Δ_i . Thus, in general, we expect *two* MBS at each end of the CNT (*i.e.* four in total). This,

however, is problematic as the Majorana pair at a given end can combine to form a single fermion by local perturbations. Thus, the question then arises if there exists a regime with only one MBS at each end [15]. As we will show, the answer is affirmative but under rather stringent conditions. One of them requires a comparable tunnel coupling of the A and B sublattices of the CNT to the superconductor, see Fig. 4.1. Using the interference mechanism first described by Le Hur *et al.* [16], we will show that for this particular case Δ_e (Δ_i) gets enhanced (suppressed) due to constructive (destructive) interference in the tunneling process. If $\Delta_{e/i}$ is smaller (larger) than the gap opened by E , then the coupling between the two Dirac points is of p -wave type (s -wave type). This leads to two regimes for MBS. In the first one, only one of two branches has a p -wave gap, thus giving rise to only one MBS at each end of the CNT. In a second regime, where both branches have a potential for p -wave pairing, the temperature T can be chosen to lie between Δ_e and Δ_i , so that only the exterior branches will go fully superconducting, whereas the interior branches stay normal. Again, a single pair of MBS in the CNT emerges. We further investigate the effect of interactions on the MBS. This is particularly important for the second regime due to the presence of gapless states from the interior branches that could be harmful to the MBS. However, using bosonization techniques we will dispel these concerns and show that for screened interactions the MBS remain stable although they can get substantially delocalized similar to the simpler case of Rashba wires [8].

4.2 Armchair nanotube low-energy spectrum

We consider an armchair CNT in the presence of an electric field E applied perpendicular to the CNT axis (see Fig. 4.1)[17]. Taking into account the spin-orbit interaction the low-energy sector is described by an effective Hamiltonian around the Dirac points given by [13]

$$\mathcal{H} = \hbar v_F k \tau_3 \sigma_2 + \tau_3 e E \xi S_z \sigma_2 + \alpha S_x \sigma_1, \quad (4.1)$$

where k is the momentum along the nanotube axis taken from the Dirac point, σ_i is the Pauli matrix on the sublattice space (A, B) associated with the honeycomb unit cell, and S_i is the spin operator with eigenvalues ± 1 . The Pauli matrix τ_i acts on the K, K' -subspace. Here, $v_F \simeq 10^6$ m/s is the Fermi velocity, and the parameter α arises from the interplay between SOI and curvature effects [18, 19, 13]. In the framework of the tight-binding model, $\alpha = -0.08$ meV/ R [nm], where R is the radius of the CNT [13]. The parameter $\xi \simeq 2 \times 10^{-5}$ nm is given by a combination of hopping matrix elements, on-site dipole moment, and SOI [14].

The spectrum given by \mathcal{H} (Eq. 4.1) consists of four branches (see Fig. 4.2), $\varepsilon_n(k) = \pm eE\xi \pm \sqrt{\alpha^2 + (\hbar v_F k)^2}$ for each Dirac point. In the following, we label the four branches by $n = 1, \dots, 4$. For each k , $n = 1$ corresponds to the highest eigenvalue and $n = 4$ to the lowest. The remarkable feature of the spectrum is the existence of helical modes, which carry opposite spins in opposite directions. The average value of the spin along the CNT-axis ($\langle S_x \rangle$) or parallel to E -field ($\langle S_y \rangle$) is equal to zero. The projection of the spin along the

z -direction is equal to $\langle S_z \rangle = \sin \zeta$, where ζ is defined by $\zeta = \arcsin(\hbar v_F k / \sqrt{\alpha^2 + (\hbar v_F k)^2})$ and depends on the wavevector k . Note that the eigenvectors $\psi_{nK}^{e/i}$ and $\psi_{nK'}^{e/i}$ are independent of E . For a (10,10)-CNT and $E = 1\text{V/nm}$, and with a Fermi level μ tuned between the two lowest electronic states polarizations close to 90% can be reached [14].

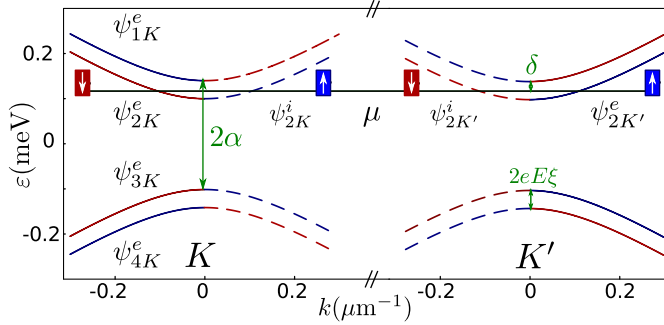


Figure 4.2: The energy spectrum around the Dirac points K, K' for a (10,10)-CNT in an electric field $E = 1\text{ V/nm}$, which consists of exterior (full line) and interior (dashed line) branches. Each branch of the spectrum is characterized by the sign of the spin projection along the z -axis $\langle S_z \rangle$ (red: spin down, blue: spin up). The Fermi level μ lies inside the gap given by $2eE\xi$, and $\delta = eE\xi + \alpha - \mu$.

Proximity induced superconductivity. If a CNT is in contact with an s -wave bulk superconductor, then the proximity effect induces superconductivity also in the CNT which at the BCS mean-field level is described by

$$\sum_{i,j,i',j',s} (\Delta_d c_{ip_r s}^\dagger c_{jp_r \bar{s}}^\dagger + \Delta_n c_{i'p_r s}^\dagger c_{j'p_r \bar{s}}^\dagger) + h.c., \quad (4.2)$$

where we concentrate on the contribution coming from the π -bands formed by the radial p_r -orbitals [20, 13]. Here, $c_{ip_r s}^{(\dagger)}$ are the standard fermionic annihilation (creation) operators, with s and \bar{s} denoting opposite spin states. The sum runs over atoms which are in contact with the bulk superconductor: i and j belong to the same sublattice, whereas i' and j' belong to different sublattices. Generically, the lattice constant of the superconducting material is not commensurate with the one of graphene. The CNT is placed in such a way that the distance from the superconducting surface to the A and B atoms is the same (see Fig. 1), which is satisfied for armchair CNTs. This ensures equal probability amplitude for tunneling to either sublattice. Since the phase of the superconducting order parameter $\Delta_{d/n}$ can be chosen arbitrary, we assume them to be real. The coupling terms in Eq. (4.2) conserve momentum, so they pair Kramers partners from the opposite Dirac cones. The process in which the Cooper pair tunnels from the superconductor to either one of the sublattice σ is written as

$$\Delta_d \sum_{\sigma,s,\kappa} \text{sgn}(\sigma \bar{s}) \psi_{\sigma s \kappa}^\dagger \psi_{\sigma \bar{s} \bar{\kappa}}^\dagger + h.c., \quad (4.3)$$

where the indices κ and $\bar{\kappa}$ denote opposite Dirac points. The operators $\psi_{\sigma s \kappa}$ and $c_{ip_r s}$ are connected via Fourier transformation [14]. The pairing term between electrons in different sublattices are

$$i\Delta_n \sum_{\sigma, s, \kappa} \text{sgn}(\bar{s}) \psi_{\sigma s \kappa}^\dagger \psi_{\bar{\sigma} \bar{s} \bar{\kappa}}^\dagger + h.c. \quad (4.4)$$

To simplify the notation we introduce Pauli matrices η_i which act on the particle-hole subspace, and we work in the basis $\tilde{\Psi} = (\Psi, \Psi^\dagger)$, with

$$\Psi = (\psi_{A\uparrow K}, \psi_{B\uparrow K}, \psi_{A\downarrow K}, \psi_{B\downarrow K}, \psi_{A\uparrow K'}, \psi_{B\uparrow K'}, \psi_{A\downarrow K'}, \psi_{B\downarrow K'}).$$

This allows us to rewrite Eqs. (4.3) and (4.4) in a compact form $H_{sc} = \tilde{\Psi}^\dagger \mathcal{H}_{sc} \tilde{\Psi}$,

$$\mathcal{H}_{sc} = -\eta_2 \tau_1 S_y \Delta_d \sigma_3 + \eta_1 \tau_1 S_y \Delta_n \sigma_1. \quad (4.5)$$

In the same basis, \mathcal{H} in Eq. (4.1) can be rewritten as $\mathcal{H} = \frac{1}{2}(\hbar v_F k \sigma_2 + eE\xi \eta_3 \tau_3 S_z \sigma_2 + \alpha \eta_3 S_x \sigma_1)$. To express the coupling between the different energy states in a canonical form we work in the basis of eigenvectors $\{\psi_{nK}^e, \psi_{nK}^i, \psi_{nK'}^e, \psi_{nK'}^i\}$. For the states at the Fermi level, $n = 2$, H_{sc} becomes

$$\sum_{l=e,i} \Delta_l (\psi_{2K'}^l \psi_{2K}^l - \psi_{2K}^l \psi_{2K'}^l) + h.c., \quad (4.6)$$

with different coupling strengths for the exterior (e) and interior (i) branches,

$$\Delta_{e/i} = \Delta_d \pm \Delta_n |\sin \zeta|. \quad (4.7)$$

We note that the sign reflects the constructive and destructive interference, *resp.*, in the tunneling process from the bulk-superconductor into the CNT [16]. The final effective Hamiltonian for states at the Fermi level (expressed in terms of right- and left-movers, see below) takes the form $\mathcal{H}_{n=2} = \mathcal{H}_e \beta_e + \mathcal{H}_i \beta_i$, where $\mathcal{H}_l = k \tau_3 - \Delta_l \eta_2 \tau_2$, where $\beta_{e/i} = (1 \pm \beta_3)/2$ (with the Pauli matrix β_3) acts on the exterior/interior branch subspace. \mathcal{H}_l describes a one-dimensional p -wave topological superconductor of class DIII, satisfying time reversal, particle-hole, and chirality symmetry [22]. In Eq. (4.6), we neglected a term $\Delta_n \cos \zeta$ characterizing the coupling between $\psi_{2K}^{e/i}$ and $\psi_{4K'}^{e/i}$ which are separated by the particle-hole gap 2α , see Fig. 4.2. In the following we consider the limit of equal diagonal and non-diagonal parameters, *i.e.*, $\Delta_d \approx \Delta_n$ [21]. We note that for $k \gg \alpha/\hbar v_F$ the coupling between the interior branches is close to zero and that between the exterior branches is equal to $2\Delta_d$. We show that this asymmetry in the coupling strengths is crucial for the existence of Majorana bound states in CNTs.

4.3 Majorana bound states

Next, we obtain the MBS following the derivation of Ref. [8]. For illustrative purposes we derive the bound states that arise by considering the exterior branches. The field corresponding to the exterior branch is defined as, $\psi_e(x) = \psi_{2K}^R(x) e^{i(k_F+K)x} + \psi_{2K'}^L(x) e^{-i(k_F+K)x}$,

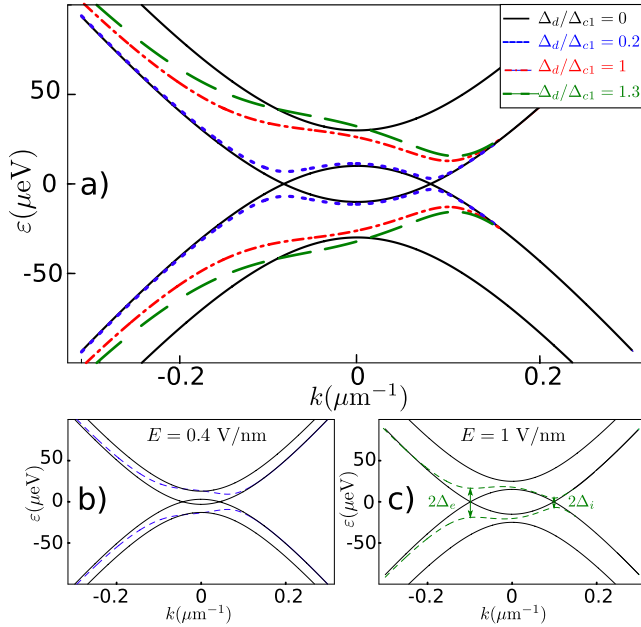


Figure 4.3: The particle-hole spectrum of a CNT (10,10) in the presence of an electric field E with the Fermi level μ tuned inside the energy gap between the two upper branches (solid black lines). All energies are counted from $\mu = 0.11 \text{ meV}$ (see Fig. 4.2). By proximity effect, superconducting gaps $\Delta_{e,i}$ are opened at the Fermi points k_F . (a) Here, the E -field is fixed at 1 V/nm and Δ_d is varied. For $\Delta_d = 5 \mu\text{eV} < \Delta_{c1}$ both branches are in the p -wave phase (dotted blue line). At the critical value $\Delta_d = 23 \mu\text{eV} = \Delta_{c1}$ the gaps induced by the proximity effect and by E are equal (dot-dashed red line). For $\Delta_d = 30 \mu\text{eV} > \Delta_{c1}$ only the interior branch is in the p -wave phase (dashed green line). Keeping Δ_d constant at 11 μeV and changing E , one goes from a regime [dashed blue line in (b)] with $E = 0.4 \text{ V/nm} < E_{c1} = 0.6 \text{ V/nm}$ where only the interior branch is in the p -wave phase to a regime [dashed green line (c)] with $E = 1 \text{ V/nm} > E_{c1} = 0.6 \text{ V/nm}$ where both branches are in the p -wave phase.

where $\psi_{2K}^R(x)$ and $\psi_{2K'}^L(x)$ are the slowly moving right and left components about the K and K' points, *resp.* Denoting the length of the CNT by L , the boundary conditions, $\psi_e(x=0) = \psi_e(x=L) = 0$, yield the restriction $\psi_{2K}^R(x) = -\psi_{2K'}^L(-x)$. Thus, the kinetic term is given by $H_0^{(1)} = -iv_F \int_{-L}^L \psi_{2K}^{R\dagger}(x) \partial_x \psi_{2K}^R(x)$, and the p -wave pairing term between the exterior branches by

$$-\Delta_e \int_{-L}^L dx \operatorname{sgn}(x) [\psi_{2K}^R(x) \psi_{2K}^R(-x) + h.c.] . \quad (4.8)$$

Solving for the zero energy mode localized around $x = 0$, we obtain the MBS $\Psi_e^M(x) \propto \gamma_e \sin[(K + k_F)x] e^{-x/\xi_e}$, where $\gamma_e = \gamma_e^\dagger$, and it is assumed that the localization length, given by $\xi_e = \hbar v_F / 2\Delta_e$, satisfies $\xi_e \ll L$. Similarly for the interior branches, with the index e replaced by i .

In general, the Majorana modes arising from the interior and exterior branches at the same end of the CNT are not protected and can combine into a fermion. To avoid such a scenario one needs to ensure the presence of only one single MBS at each end of the CNT. This can be achieved in two ways.

First, there is a window where the electric field E can be chosen in such a way that the superconductivity in the exterior branch can be tuned into a non-topological s -wave superconductor, while the interior one still remains a topological p -wave superconductor of class DIII [22] (see also above). In this case, only the interior branch supports a MBS at each end of the nanotube, and we refer to this as a topological phase of the CNT (see dashed green line in Fig. 4.3a). Concretely, such a regime is reached for $\Delta_e(k_F) > \delta > \Delta_i(k_F)$, where $k_F \approx \sqrt{(\mu + eE\xi)^2 - \alpha^2/\hbar v_F}$ and $\delta = eE\xi + \alpha - \mu$. With Eq. (4.7) this criterion becomes equivalent to $\Delta_{c2} \gtrsim \Delta_d \gtrsim \Delta_{c1}$, where $\Delta_{c1/c2} = \delta/(1 \pm \sin \zeta)$. For a given value of Δ_d , the experimentally viable approach to drive the system into the topological phase is to tune the electric field E . Indeed, for $E_{c1} \gtrsim E \gtrsim E_{c2}$ (see Fig. 4.3b) the exterior branch is in the s -wave phase, while the interior one is in the p -wave phase. The critical value of the electric field E_{c1} (E_{c2}) is determined by the condition $\delta = \Delta_e(k_F)$ ($\delta = \Delta_i(k_F)$). Similarly, we can tune between the phases by changing the Fermi level. [In passing we note that the gap $eE\xi$, and thus δ , get enhanced by interaction effects around $k = 0$ [23], which is useful for experimental realizations. However, for simplicity we will ignore this feature here.]

Second, in the regime $\Delta_d \lesssim \Delta_{c1}$ (see dotted blue line in Fig. 4.3a) or $E \gtrsim E_{c1}$ (see Fig. 4.3c) both branches are dominated by p -wave pairing. If the temperature is lower than both gaps, *i.e.* $k_B T < \Delta_{e,i}$, then there is an even number of MBS at each end of the nanotube, and the CNT is in the topologically trivial phase. However, in the intermediate regime with $\Delta_e > k_B T > \Delta_i$ [24], the interior gap Δ_i is closed and the Majorana states are removed, yet those from the exterior branches remain, and the CNT is again in the topological phase. In the following we consider this latter scenario and discuss the role of interactions coming from the gapless states of the interior branch.

4.4 Interaction effects

Interactions effects are most conveniently described by linearizing the spectrum of the fermionic fields $\psi_{2K}^{e/i}$ and $\psi_{2K'}^{e/i}$ near the Fermi momentum k_F and expressing them in terms of the bosonized fields. The quadratic part of the bosonized Hamiltonian thus obtained has the following form,

$$H_0 = \frac{1}{2} \sum_{n=\pm} \left\{ v_n K_n (\partial_x \theta_n)^2 + \frac{v_n}{K_n} (\partial_x \phi_n)^2 \right\}, \quad (4.9)$$

where $\partial_x \phi_+$ and $\partial_x \phi_-$ are the sum and difference of densities between the two fermionic bands. The fields conjugate to them are defined as, θ_+ and θ_- , *resp.* The parameters $K_+ \simeq 1 - U_0/\pi v$ and $K_- \simeq 1 + (1 - \langle S_z \rangle^2) U_{2k_F}/2\pi v$ encode information about the interactions and

the renormalized velocities are given as $v_+ \simeq v_F + U_0/\pi$, and $v_- \simeq v_F + b'(1 + \langle S_z \rangle^2)/4\pi$, where the b' -term [25, 26] is due to the backscattering contribution. Here, $U_{0,2k_F}$ denotes the Fourier component of the screened Coulomb interaction. Since $\langle S_z \rangle^2 < 1$ and thus $K_- > 1$, we conclude [27] that the forward scattering term $\propto \int dx d\tau \cos(\sqrt{8\pi}\phi_-)$ scales to zero.

Additional terms induced by the proximity effect lead to a modified Hamiltonian given by

$$H = H_0 + \frac{\Delta_e}{2\pi a} \cos \sqrt{2\pi}(\theta_+ - \phi_-). \quad (4.10)$$

Since we assume here $\Delta_e > k_B T > \Delta_i$, the term due to the interior branches, $\frac{\Delta_i}{2\pi a} \cos \sqrt{2\pi}(\theta_+ + \phi_-)$, is smeared out by temperature effects and will not be considered.

Using standard techniques [27, 28], we derive the following renormalization group (RG) equations,

$$\frac{dK_+}{dl} = \frac{f^2}{4} \left(1 + \frac{4\gamma K_+ K_-}{(1+\gamma)^2} \right), \quad (4.11)$$

$$\frac{dK_-^{-1}}{dl} = \frac{f^2}{4} \left(1 + \frac{4\gamma}{K_- K_+ (1+\gamma)^2} \right), \quad (4.12)$$

$$\frac{d\gamma}{dl} = \frac{f^2}{4} \frac{\gamma(1-\gamma)K_+}{(1+\gamma)(K_+ K_- + 1)}, \quad (4.13)$$

$$\frac{df}{dl} = f \left(2 - \frac{1}{2K_+} - \frac{K_-}{2} \right), \quad (4.14)$$

where the flow parameter $l = \ln[a/a_0]$, $f = 2\Delta_e a$, and γ is the ratio of the velocities v_+/v_- . We note that for the non-interacting case γ is already at its fixed point, $\gamma = 1$, and including interactions (the repulsive interactions are assumed to be well screened) causes only a small deviation from unity [29, 30]. Thus, it is convenient to assume $\gamma = 1$, and under this assumption $K_+ K_-$ is a constant, given in leading order by unity. Above RG equations now acquire the simple form $dR/dl = f^2/2$ and $df/dl = f(2 - 1/R)$, where $R = (1/K_+ + K_-)/2$. These equations are exactly the same as in Ref. [8] derived for interacting spinless fermions in an effective p -wave regime. We conclude that for a CNT whose initial values of the parameters lie in the regime $f_0 > 2\sqrt{2R_0 - \ln(2R_0 e)}$ has its RG flow such that both K_+ and K_- approach the non-interacting value. At this point the problem can be refermionized into a set of decoupled gapped and gapless fermions and for a strongly screened CNT with initial value *e.g.* $K_+ = 0.8$ the localization length ξ_e increases by 25%. Therefore, we conclude that the MBS which arise from gapped fermions remain protected even in the presence of interacting gapless fermions and simply acquire a renormalized ξ_e .

4.5 Conclusions

We have shown that an armchair CNT with helical modes generated by an external electric field is a promising candidate material for Majorana bound states. By placing the CNT on top of an *s*-wave superconductor and tuning the Fermi level and the electric field, one can induce pairing of Kramers partners from opposite Dirac points. This pairing opens up inequivalent gaps for the exterior and the interior branches. The Majorana modes obtained are stabilized by either tuning the electric field such that the exterior gap acquires a predominantly *s*-wave character or by increasing the temperature to remove the pairing in the interior branches.

Acknowledgements We thank Karsten Flensberg for valuable discussions in the initial stage of this work. We also acknowledge helpful discussions with Diego Rainis and Pascal Simon. This work is supported by the Swiss NSF, NCCR Nanoscience and NCCR QSIT, and DARPA.

Bibliography

- [1] L. Fu and C. L. Kane, Phys. Rev. Lett. **100**, 096407 (2008).
- [2] A. R. Akhmerov, J. Nilsson, and C. W. J. Beenakker Phys. Rev. Lett. **102**, 216404 (2009).
- [3] R. M. Lutchyn, J. D. Sau, and S. Das Sarma, Phys. Rev. Lett. **105**, 077001 (2010).
- [4] Y. Oreg, G. Refael, and F. von Oppen, Phys. Rev. Lett. **105**, 177002 (2010).
- [5] A. C. Potter and P. A. Lee, Phys. Rev. B **83**, 094525 (2011).
- [6] J. Alicea, Phys. Rev. B **81**, 125318 (2010).
- [7] X. L. Qi and S. C. Zhang, Rev. Mod. Phys. **83**, 1057 (2011).
- [8] S. Gangadharaiah, B. Braunecker, P. Simon, and D. Loss, Phys. Rev. Lett. **107**, 036801 (2011).
- [9] E. M. Stoudenmire, J. Alicea, O. Starykh, and M.P.A. Fisher, Phys. Rev. B **84**, 014503 (2011).
- [10] R. M. Lutchyn and M.P.A. Fisher, arXiv:1104.2358.
- [11] The Zeeman splitting can also be generated internally e.g. by the Overhauser field coming from the hyperfine interaction between nuclear and electron spins [31].
- [12] T. D. Stanescu, R. M. Lutchyn, and S. Das Sarma, Phys. Rev. B **84**, 144522 (2011).
- [13] J. Klinovaja, M. J. Schmidt, B. Braunecker, and D. Loss, Phys. Rev. Lett. **106**, 156809 (2011).
- [14] J. Klinovaja, M. J. Schmidt, B. Braunecker, and D. Loss, Phys. Rev. B **84**, 085452 (2011).
- [15] A recent proposal for MBS in CNTs focuses on the spectrum around the Γ -point [32] (instead of the K , K' -points with a Dirac spectrum considered here), where this difficulty would be absent in principle. However, the effective Hamiltonian around the Γ -point for a realistic CNT with SOI is not known and needs separate treatment.
- [16] K. Le Hur, S. Vishveshwara, and C. Bena, Phys. Rev. B **77**, 041406 (2008).
- [17] We note that all E -field directions in the yz -plane of Fig. 4.1 are equivalent. Also, by placing metal gates on top and bottom of the CNT, the electric field and the chemical potential can be tuned independently.
- [18] W. Izumida, K. Sato, and R. Saito, J. Phys. Soc. Jpn. **78**, 074707 (2009).

- [19] J.-S. Jeong and H.-W. Lee, Phys. Rev. B **80**, 075409 (2009).
- [20] R. Saito, G. Dresselhaus, and M. S. Dresselhaus, *Physical Properties of Carbon Nanotubes* (Imperial College Press, London, 1998).
- [21] The induced superconductivity matrix elements depend on the probability for the electrons to tunnel on either the A or the B site, which due to the symmetry of the problem (see Fig. 4.1) should be similar. A small difference between Δ_d and Δ_n (Δ_e and Δ_i are still considerably different) would not change our main results.
- [22] S. Ryu, A. P. Schnyder, A. Furusaki, and A. W. W. Ludwig, New Journal of Physics **12**, 065010 (2010).
- [23] B. Braunecker, G. I. Japaridze, J. Klinovaja, and D. Loss, Phys. Rev. B **82**, 045127 (2010).
- [24] For $\Delta_d \sim 5 \mu\text{eV}$, we require $10\text{mK} < T < 100\text{mK}$.
- [25] R. Egger and A. Gogolin, Phys. Rev. Lett. **79**, 5082 (1997); Eur. Phys. J. B **3**, 23 (1998).
- [26] C. Kane, L. Balents, and M.P.A. Fisher, Phys. Rev. Lett. **79**, 5086 (1997).
- [27] T. Giamarchi, *Quantum Physics in One Dimension*, (Clarendon Press, Oxford, 2004).
- [28] A. O. Gogolin, A. A. Nersesyan, and A. M. Tsvelik, *Bosonization and Strongly Correlated Systems*, (University Press, Cambridge, 1998).
- [29] O. A. Starykh, D. L. Maslov, W. Haeusler, and L. I. Glazman, in Lecture Notes in Physics, ed. T. Brandes, vol. 544, p.37, 1999.
- [30] J. Klinovaja, S. Gangadharaiah, and D. Loss, in preparation.
- [31] B. Braunecker, P. Simon, and D. Loss, Phys. Rev. B **80**, 165119 (2009).
- [32] J. D. Sau and S. Tewari, arXiv:1111.5622.

Chapter 4

Chapter 5

Composite Majorana Fermion Wavefunctions in Nanowires

We consider Majorana fermions (MFs) in quasi-one-dimensional nanowire systems containing normal and superconducting sections where the topological phase based on Rashba spin orbit interaction can be tuned by magnetic fields. We derive explicit analytic solutions of the MF wavefunction in the weak and strong spin orbit interaction regimes. We find that the wavefunction for one single MF is a composite object formed by superpositions of different MF wavefunctions which have nearly disjoint supports in momentum space. These contributions are coming from the extrema of the spectrum, one centered around zero momentum and the other around the two Fermi points. As a result, the various MF wavefunctions have different localization lengths in real space and interference among them leads to pronounced oscillations of the MF probability density. For a transparent normal-superconducting junction we find that in the topological phase the MF leaks out from the superconducting into the normal section of the wire and is delocalized over the entire normal section, in agreement with recent numerical results by Chevallier *et al.*.

This chapter has been published in Physical Review B 86, 085423 (2012).

5.1 Introduction

Majorana fermions[1] (MFs), being their own antiparticles, have attracted much attention in recent years in condensed matter physics [2, 3, 4, 5, 6, 7, 8, 12, 9, 10, 13, 15, 14, 16, 17, 11, 18, 19]. Besides being of fundamental interest, these exotic quantum particles have the potential for being used in topological quantum computing due to their non-Abelian statistics[20, 21, 24, 26, 25, 22, 23]. There are a number of systems where to expect MFs, e.g. fractional quantum Hall systems[27, 28], topological insulators[3, 4], optical lattices[5], p -wave superconductors[12], and especially nanowires with strong Rashba spin orbit interaction[7, 8, 9] - the system of interest in this work. There are now several claims for experimental evidence of MFs in topological insulators [29, 30] and, in particular, in semiconducting nanowires of the type considered here[31, 32, 33].

As is well-known[7, 9, 8, 19], an s -wave superconductor brought into contact with a semiconducting nanowire with Rashba spin orbit interaction (SOI) induces effective p -wave superconductivity that gives rise to MFs, one at each end of such a wire. Most studies have analyzed the corresponding model Hamiltonian by direct numerical diagonalization, which provides exact solutions of the Schrödinger equation for essentially all parameter values irrespective of their relative sizes. Less attention, however, has been given to analytical approaches which can provide additional insights into the nature of MFs. As usual, this comes with a price: closed analytic expressions are hard to come by and can be obtained only in special limits. But since these limits turn out to include realistic parameter regimes such an approach is not a mere academic exercise but worthwhile also from a physical point of view.

Motivated by this, we focus in the present work on the spinor-wavefunction for MFs, and derive analytical expressions for various limiting cases, loosely characterized as weak and strong SOI regimes. We find that these solutions are superpositions of states that come, in general, from different extremal points of the energy dispersion, one centered around zero-momentum and the others around the Fermi points. Despite having nearly disjoint support in momentum-space, all such contributions must be taken into account, in general, in order to satisfy the boundary conditions imposed on the spinor-wavefunctions in real space. As a consequence of this composite structure of the MF wavefunctions, there will be more than one localization length that characterizes a single MF. We will see throughout this work that the Schrödinger equation for the systems under consideration allows, in principle, degenerate MF wavefunctions. However, this degeneracy gets completely removed by the boundary conditions considered here, and, consequently, there exists only one single MF wavefunction at a given end of the nanowire. The superposition also gives rise to interference effects that leads to pronounced oscillations of the MF probability density in real space. Quite interestingly, the relative strengths of the different localization lengths as well as of the oscillation periods can be tuned by magnetic fields.

If only a section of the wire is covered with a superconductor, a normal-superconducting (NS) junction is formed. For this case, we find that the MF becomes delocalized over the entire normal section, while still localized in the superconducting section, as noted by sev-

eral groups before[34, 19, 35, 36, 37], and most recently studied in detail in a numerical study by Chevallier *et al.* [38]. Here, we will find analytical solutions for this problem, valid in the weak and strong SOI regime. Depending on the length of the normal section, the support of the MF wavefunction is, again, centered at zero momentum or the Fermi momenta. Also similarly as before, different localization lengths and oscillation periods of the MF in the normal section occur, again tunable by magnetic fields. This could then provide an experimental signature for MFs, e.g. in a tunneling density of states measurement, where a signal that comes from a zero-mode MF will show oscillations along the normal section.

The paper is organized as follows. In Sec. 5.2 we introduce the continuum model of a nanowire including SOI, magnetic field and induced superconductivity. The composite structure of MF in proximity-induced superconducting wire is discussed in Sec. 5.3 for strong and weak SOI. In Sec. 5.4 we investigate an NS junction and show how the type of MF wavefunction oscillates in space and depends on magnetic field. The final Sec. 5.5 contains our conclusions. Some technical details are referred to two Appendices.

5.2 Model

Following earlier work[7, 8, 9, 38, 19], our starting point is a semiconducting nanowire with Rashba SOI (see Fig. 5.1) characterized by a SOI vector α_R that points perpendicularly to the nanowire axis and defines the spin quantization direction z . In addition, a magnetic field \mathbf{B} is applied along the nanowire in x -direction. We imagine that the nanowire (or a section of it) is in tunnel-contact with a conventional bulk s -wave superconductor which leads to proximity-induced superconductivity in the nanowire itself, characterized by the induced s -wave gap Δ_{sc} (see Fig. 5.1). We refer to this part of the nanowire as to the superconducting section (or as to the nanowire being in the superconducting regime), in contrast to the ‘normal’ section of the nanowire that is not in contact with the superconductor and thus in the normal regime.

We describe this nanowire system by a continuum model and our goal is to find the explicit wavefunctions for the MFs in the entire nanowire, including normal and superconducting section. For this, we need to introduce some basic definitions and briefly recall well-known results about the spectrum.

The Hamiltonian $H^0 = H^{kin} + H^{SOI} + H^Z$ for the normal regime [7, 8] consists of the kinetic energy term

$$H^{kin} = \sum_{\sigma} \int dx \Psi_{\sigma}^{\dagger}(x) \left[\frac{(-i\hbar\partial_x)^2}{2m} - \mu \right] \Psi_{\sigma}(x), \quad (5.1)$$

where m is the (effective) electron mass and μ the chemical potential, the SOI term,

$$H^{SOI} = -i\alpha_R \sum_{\sigma,\sigma'} \int dx \Psi_{\sigma}^{\dagger}(x) (\sigma_3)_{\sigma\sigma'} \partial_x \Psi_{\sigma'}(x), \quad (5.2)$$

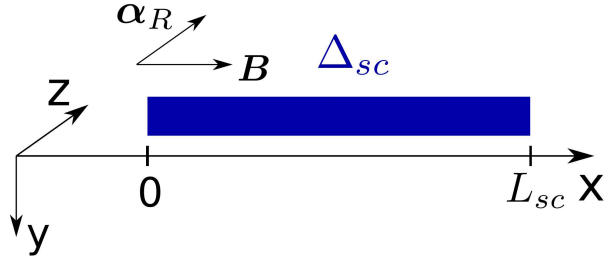


Figure 5.1: Nanowire (blue slab) of length L_{sc} in the superconducting regime with gap Δ_{sc} induced via proximity effect by a bulk s -wave superconductor (not shown). A magnetic field \mathbf{B} is applied along the nanowire in x -direction and perpendicularly to the Rashba SOI vector $\boldsymbol{\alpha}_R$ that points in z -direction.

where, again, the z -axis is chosen along $\boldsymbol{\alpha}_R$, and the Zeeman term corresponding to the magnetic field B along the nanowire (x -axis),

$$H^Z = \Delta_Z \sum_{\sigma, \sigma'} \int dx \Psi_\sigma^\dagger(x) (\sigma_1)_{\sigma\sigma'} \Psi_{\sigma'}(x). \quad (5.3)$$

Here, $\Psi_\sigma^\dagger(x)$ is the creation operator of an electron at position x with spin $\sigma/2 = \pm 1/2$ (along z -axis), and the Pauli matrices $\sigma_{1,2,3}$ act on the spin of the electron. The Zeeman energy is given by $\Delta_Z = g\mu_B B/2$, where g is the g-factor and μ_B the Bohr magneton. It is convenient to introduce the corresponding Hamiltonian density \mathcal{H}^0 ,

$$\begin{aligned} H^0 &= \int dx \psi^\dagger(x) \mathcal{H}^0 \psi(x), \\ \mathcal{H}^0 &= -\hbar^2 \partial_x^2 / 2m - \mu - i\alpha_R \sigma_3 \partial_x + \Delta_Z \sigma_1, \end{aligned} \quad (5.4)$$

which acts on the vector $\psi = (\Psi_\uparrow, \Psi_\downarrow)$. The bulk spectrum of \mathcal{H}^0 (see Fig. 5.2a) consists of two branches and is given by

$$E_\pm^0(k) = \frac{\hbar^2 k^2}{2m} - \mu \pm \sqrt{(\alpha_R k)^2 + \Delta_Z^2}, \quad (5.5)$$

where k is a momentum along the nanowire. By opening a Zeeman gap $2\Delta_Z$, the magnetic field lifts the spin degeneracy at $k = 0$. The chemical potential μ is tuned inside this gap and set to zero. In this case, the Fermi wavevector is determined from $E_-^0(k_F) = 0$ and given by

$$k_F = \sqrt{2k_{so}^2 + \sqrt{4k_{so}^4 + k_Z^4}}, \quad (5.6)$$

where $k_{so} = m\alpha_R/\hbar^2$ and $k_Z = \sqrt{2\Delta_Z m}/\hbar$.

The nanowire in the superconducting regime is described by the Hamiltonian $H^0 + H^{sc}$, where the s -wave BCS Hamiltonian H^{sc} couples states with opposite momenta and spins[7, 8],

$$H^{sc} = \frac{1}{2} \sum_{\sigma, \sigma'} \int dx \Delta_{sc} (\Psi_\sigma(i\sigma_2)_{\sigma\sigma'} \Psi_{\sigma'} + h.c.). \quad (5.7)$$

The proximity-induced superconductivity gap Δ_{sc} is chosen to be real (thereby assuming that we can neglect the flux induced by the B-field, which is the case e.g. for InSb nanowires [31]). The spectrum of $H^0 + H^{sc}$ (see Fig. 5.2b) is then found to be

$$\begin{aligned} E_\pm^2(k) &= \left(\frac{\hbar^2 k^2}{2m} \right)^2 + (\alpha_R k)^2 + \Delta_Z^2 + \Delta_{sc}^2 \\ &\pm 2\sqrt{\Delta_Z^2 \Delta_{sc}^2 + \left(\frac{\hbar^2 k^2}{2m} \right)^2 (\Delta_Z^2 + (\alpha_R k)^2)}. \end{aligned} \quad (5.8)$$

The ‘topological’ gap at $k = 0$ is given by $\Delta_- = \Delta_{sc} - \Delta_Z$, and the closing of this gap marks the transition between nontopological ($\Delta_- > 0$) and topological ($\Delta_- < 0$) phases [5, 7, 8]. In contrast, the gap at k_F , $\Delta_e \equiv 2|E_-(k_F)|$, is always nonzero (see Fig. 5.2b).

5.3 Majorana fermions in the superconducting section

In this section we consider first the simpler case where the superconducting section extends over the entire nanowire from $x = 0$ to $x = L_{sc}$, see Fig. 5.1. In the topological phase there is one MF bound state at each end of the nanowire[7, 8]. In the physically interesting regime, these two MFs should be independent and have negligible spatial overlap. This

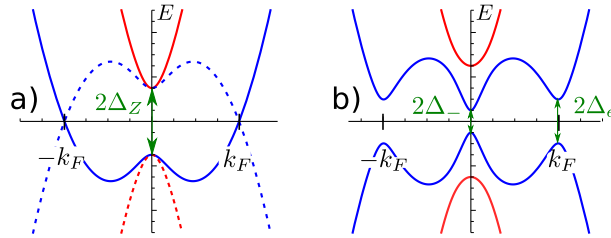


Figure 5.2: Bulk spectrum for extended electron (solid lines) and hole (dashed lines) states in the normal (a) and in the superconducting regime (b). (a) In the normal regime, a Zeeman gap $2\Delta_Z$ is opened at $k = 0$, but the full spectrum is still gapless due to the propagating modes at the Fermi points $\pm k_F$. (b) The proximity-induced superconductivity leads to the opening of a gap Δ_e at the Fermi points $\pm k_F$ and modifies the topological gap $\Delta_- = \Delta_{sc} - \Delta_Z$ at $k = 0$.

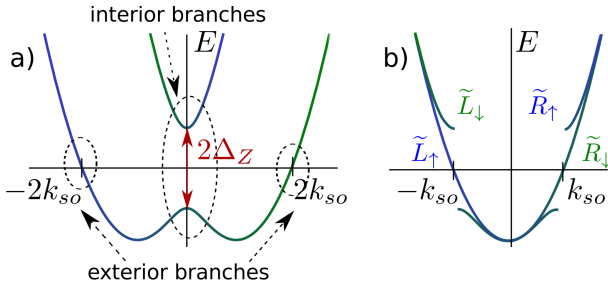


Figure 5.3: (a) Band structure of a nanowire with strong SOI and in a uniform magnetic field B in the lab frame (see also Fig. 5.2) for the normal section. States around $k = 0$ belong to the interior branches and states around $k = k_F = 2k_{so}$ belong to the exterior branches. (b) The same band structure in the rotating frame. The rotating magnetic field $\tilde{\mathbf{B}}(x)$ given by Eq. (5.12) couples \tilde{R}_\uparrow and \tilde{L}_\downarrow that leads to the opening of the Zeeman gap $2\Delta_Z$ but does not affect \tilde{L}_\uparrow and \tilde{R}_\downarrow .

justifies the consideration of a semi-infinite nanowire. In this work we focus on the MF at the left end, $x = 0$.

We will consider two limiting regimes, namely strong ($k_F \simeq 2k_{so}$) and weak ($k_F \simeq k_Z$) SOI. In both regimes, the Hamiltonian can be linearized near the Fermi points and solved analytically. We show that the MF wavefunction has support in k -space from the exterior ($k \simeq \pm k_F$) and the interior ($k \simeq 0$) branches of the spectrum, see Fig. 5.3a. If the system is in some intermediate regime of moderate SOI, the support of the MF wavefunction extends over all momenta from $-k_F$ to k_F , and this case cannot be treated analytically in the linearization approximation considered here.

5.3.1 Regime of strong SOI and rotating frame

The regime of strong SOI is defined by the condition that the SOI energy at the Fermi level is larger than the Zeeman splitting, $\Delta_Z \ll m\alpha_R^2/\hbar^2$ (or $k_F \approx 2k_{so}$), and larger than the proximity gap, $\Delta_{sc} \ll m\alpha_R^2/\hbar^2$. This allows us to treat the magnetic field and the proximity-induced superconductivity as small perturbations.

The spectrum obtained in Eq. (5.5) consists of two parabolas shifted by the SOI momentum $k_{so} = m\alpha_R/\hbar^2$ and with a Zeeman gap opened at $k = 0$ (see Fig. 5.3a). In the strong SOI regime it is more convenient to work in the rotating frame, see Fig. 5.3b. For this we follow Ref. [39] and make use of the following spin-dependent gauge transformation

$$\Psi_\sigma(x) = e^{-i\sigma k_{so}x}\tilde{\Psi}_\sigma(x), \quad (5.9)$$

where tilde refers to the rotating frame. The H^{SOI} term is effectively eliminated ($\tilde{H}^{SOI} = 0$) and the spectrum corresponding to \tilde{H}^{kin} consists of two parabolas centered at $k = 0$, one for spin up and one for spin down. Around the Fermi points, $\pm k_{so}$, the spectrum can be linearized and the electron operators $\tilde{\Psi}_\sigma$ are expressed in terms of slowly-varying right

(\tilde{R}_σ) - and left (\tilde{L}_σ) - movers,

$$\tilde{\Psi}_\sigma(x) = \tilde{R}_\sigma(x)e^{ik_{so}x} + \tilde{L}_\sigma(x)e^{-ik_{so}x}. \quad (5.10)$$

The kinetic energy term in the linearized model is

$$\tilde{H}^{kin} = -i\hbar v_F \int dx [\tilde{R}_\sigma^\dagger(x)\partial_x \tilde{R}_\sigma(x) - \tilde{L}_\sigma^\dagger(x)\partial_x \tilde{L}_\sigma(x)] \quad (5.11)$$

with Fermi velocity $v_F = \alpha_R/\hbar$. Here, we droped all fast oscillating terms, which is justified as long as $\xi \gg 2\pi/k_{so}$, where ξ is a localization length of \tilde{R}_σ and \tilde{L}_σ (see below).

In the rotating frame the B-field becomes helical, rotating in the plane perpendicular to the SOI vector $\boldsymbol{\alpha}_R$,

$$\tilde{\mathbf{B}}(x) = B[\hat{x}\cos(2k_{so}x) - \hat{y}\sin(2k_{so}x)]. \quad (5.12)$$

Here, \hat{x} and \hat{y} are unit vectors in x and y directions, respectively (see Fig. 5.1). This leads to the Zeeman Hamiltonian of the form

$$\begin{aligned} \tilde{H}^Z &= \Delta_Z \int dx \tilde{\Psi}_\sigma^\dagger(x)e^{2i\sigma k_{so}x}\tilde{\Psi}_{-\sigma}(x), \\ &\simeq \Delta_Z \int dx [\tilde{R}_\uparrow^\dagger(x)\tilde{L}_\downarrow(x) + \tilde{L}_\downarrow^\dagger(x)\tilde{R}_\uparrow(x)], \end{aligned} \quad (5.13)$$

where in the second line we used the linearization approximation and, again, droped all fast oscillating terms. We note that only $\tilde{R}_\uparrow(x)$ and $\tilde{L}_\downarrow(x)$ are coupled, which leads to opening of a gap, as shown in Fig. 5.3b. This is similar to the spin-selective Peierls mechanism discovered in Ref. [39] where interaction effects strongly renormalize this gap (here, however, we shall ignore interaction effects).

The superconductivity term [see Eq. (5.7)] in the linearized model becomes

$$\begin{aligned} \tilde{H}^{sc} &= \frac{1}{2} \int dx \Delta_{sc} (\tilde{R}_\uparrow(x)\tilde{L}_\downarrow(x) - \tilde{L}_\downarrow(x)\tilde{R}_\uparrow(x) \\ &\quad + \tilde{L}_\uparrow(x)\tilde{R}_\downarrow(x) - \tilde{R}_\downarrow(x)\tilde{L}_\uparrow(x) + h.c.). \end{aligned} \quad (5.14)$$

We construct two vectors, $\tilde{\phi}^{(i)} = (\tilde{R}_\uparrow, \tilde{L}_\downarrow, \tilde{R}_\uparrow^\dagger, \tilde{L}_\downarrow^\dagger)$ and $\tilde{\phi}^{(e)} = (\tilde{L}_\uparrow, \tilde{R}_\downarrow, \tilde{L}_\uparrow^\dagger, \tilde{R}_\downarrow^\dagger)$, which correspond to the exterior ($k \simeq 2k_{so}$) and interior ($k \simeq 0$) branches of the spectrum in the lab frame (see Fig. 5.3a). The linearized Hamiltonian $\tilde{H}^{kin} + \tilde{H}^Z + \tilde{H}^{sc}$ reduces then to ($l = i, e$)

$$\tilde{H}^{(l)} = \frac{1}{2} \int dx (\tilde{\phi}^{(l)}(x))^\dagger \tilde{\mathcal{H}}^{(l)} \tilde{\phi}^{(l)}(x), \quad (5.15)$$

where the interior branches are described by

$$\tilde{\mathcal{H}}^{(i)} = -i\hbar v_F \sigma_3 \partial_x + \Delta_z \sigma_1 \eta_3 + \Delta_{sc} \sigma_2 \eta_2, \quad (5.16)$$

and the exterior ones by

$$\tilde{\mathcal{H}}^{(e)} = i\hbar v_F \sigma_3 \partial_x + \Delta_{sc} \sigma_2 \eta_2. \quad (5.17)$$

Here, the Pauli matrices $\eta_{1,2,3}$ act on the electron-hole subspace.

The energy spectrum is determined by the Schrödinger equation, $\tilde{\mathcal{H}}^{(l)} \tilde{\varphi}_E^{(l)}(x) = E \tilde{\varphi}_E^{(l)}(x)$, with boundary conditions to be imposed on the eigenfunctions $\tilde{\varphi}_E^{(l)}(x)$ as discussed below. We introduce then the operator $\tilde{\gamma}_E^{(l)} = \int dx \tilde{\varphi}_E^{(l)}(x) \cdot \tilde{\phi}^{(l)}(x)$ and see that it diagonalizes Eq. (5.15), *i.e.*, $\tilde{H}^{(l)} = \sum_E E(\tilde{\gamma}_E^{(l)})^\dagger \tilde{\gamma}_E^{(l)}$. Focusing now on the zero modes, we consider in particular $\tilde{\gamma}^{(l)} \equiv \tilde{\gamma}_{E=0}^{(l)}$ but express it in a more convenient basis,

$$\tilde{\gamma}^{(l)} = \int dx \tilde{\Phi}_{E=0}^{(l)}(x) \cdot \tilde{\Psi}(x), \quad (5.18)$$

where $\tilde{\Psi} = (\tilde{\Psi}_\uparrow, \tilde{\Psi}_\downarrow, \tilde{\Psi}_\uparrow^\dagger, \tilde{\Psi}_\downarrow^\dagger)$ and where fast oscillating terms were dropped. In this new basis $\tilde{\Psi}$, we have reinstalled the phase factors $e^{\pm ik_{so}x}$ (associated with \tilde{R}_σ and \tilde{L}_σ) explicitly in the wavefunctions $\tilde{\Phi}_{E=0}^{(l)}(x)$, so that they are taken automatically into account when we impose the boundary conditions on $\tilde{\Phi}_{E=0}^{(l)}(x)$.

The zero-energy operator $\tilde{\gamma}^{(l)}$ represents a MF, *i.e.*, $(\tilde{\gamma}^{(l)})^\dagger = \tilde{\gamma}^{(l)}$, if and only if the corresponding wavefunction $\tilde{\Phi}_{E=0}^{(l)}(x)$ has the following form

$$\tilde{\Phi}_{E=0}^{(l)}(x) = \begin{pmatrix} f(x) \\ g(x) \\ f^*(x) \\ g^*(x) \end{pmatrix}, \quad (5.19)$$

where the functions f, g are arbitrary up to normalization $\int dx |\tilde{\Phi}_{E=0}^{(l)}(x)|^2 / 2 = \int dx (|f(x)|^2 + |g(x)|^2) = 1$, which, however, will be suppressed in the following.

In infinite space (no boundary conditions), the spectrum of the interior branches [see Eq. (5.16)] is given by $E_\pm^{(i)} = \pm \sqrt{(\hbar v_F \kappa)^2 + \Delta_\pm^2}$, while the one for the exterior branches [see Eq. (5.17)] is given by $E_{1,2}^{(e)} = \pm \sqrt{(\hbar v_F \kappa)^2 + \Delta_e^2}$, where κ is taken from the Fermi point. Here, $\Delta_\pm = \Delta_{sc} \pm \Delta_Z$ and $\Delta_e = \Delta_{sc}$. If Δ_Z and Δ_{sc} become equal, the topological interior gap Δ_- is closed. In contrast, the exterior gap Δ_e is not affected by the magnetic field.

The only normalizable eigenstates of $\tilde{\mathcal{H}}^{(l)}$ at zero energy and at $x > 0$ are two evanescent modes coming from the interior branches, characterized by a decay wavevector $k_\pm^{(i)} = |\Delta_\pm|/\alpha_R$, and two evanescent modes coming from the exterior branches, characterized by a decay wavevector $k^{(e)} = \Delta_{sc}/\alpha_R$. The corresponding zero-energy eigenfunctions $\tilde{\varphi}_{E=0}^{(l)}(x)$ give the four basis wavefunctions, exponentially decaying in the semi-infinite

space $x > 0$,

$$\tilde{\Phi}_-^{(i)} = \begin{pmatrix} -i \operatorname{sgn}(\Delta_-) e^{-ik_{so}x} \\ e^{ik_{so}x} \\ i \operatorname{sgn}(\Delta_-) e^{ik_{so}x} \\ e^{-ik_{so}x} \end{pmatrix} e^{-k_-^{(i)} x}, \quad \tilde{\Phi}_+^{(i)} = \begin{pmatrix} e^{-ik_{so}x} \\ -i e^{ik_{so}x} \\ e^{ik_{so}x} \\ i e^{-ik_{so}x} \end{pmatrix} e^{-k_+^{(i)} x}, \quad (5.20)$$

$$\tilde{\Phi}_1^{(e)} = \begin{pmatrix} i e^{ik_{so}x} \\ e^{-ik_{so}x} \\ -i e^{-ik_{so}x} \\ e^{ik_{so}x} \end{pmatrix} e^{-k^{(e)} x}, \quad \tilde{\Phi}_2^{(e)} = \begin{pmatrix} e^{ik_{so}x} \\ i e^{-ik_{so}x} \\ e^{-ik_{so}x} \\ -i e^{ik_{so}x} \end{pmatrix} e^{-k^{(e)} x}. \quad (5.21)$$

Here we should note that these four degenerate MF wavefunctions are not yet solutions of our problem: they do satisfy the Schrödinger equation but not yet the boundary conditions. Thus, we search now for a linear combination of them, $\tilde{\Phi}_M$, such that the boundary conditions are satisfied. At the left end of the nanowire, the condition on the wavefunction is $\tilde{\Phi}_M(x=0) = 0$. We assume here that the length of the nanowire L_{sc} provides the largest scale, so we can neglect any interplay between the two ends of the nanowire and treat them independently (see also below). The set of vectors $\{\tilde{\Phi}_-^{(i)}, \tilde{\Phi}_+^{(i)}, \tilde{\Phi}_1^{(e)}, \tilde{\Phi}_2^{(e)}\}$ is seen to be linearly independent in the nontopological phase at $x=0$, thus it is impossible to satisfy the boundary conditions and no solution exists at zero energy. In contrast, in the topological phase, $\Delta_Z > \Delta_{sc}$, the two vectors $\tilde{\Phi}_-^{(i)}$ and $\tilde{\Phi}_1^{(e)}$ are ‘collinear’ such that the boundary condition can be satisfied and the zero energy state is a MF given by $\tilde{\Phi}_M = \tilde{\Phi}_-^{(i)} - \tilde{\Phi}_1^{(e)}$ in the rotating frame. Using Eq. (5.9), the MF wavefunction in the lab frame is then given by

$$\Phi_M(x) = \begin{pmatrix} i \\ 1 \\ -i \\ 1 \end{pmatrix} e^{-k_-^{(i)} x} - \begin{pmatrix} i e^{ik_F x} \\ e^{-ik_F x} \\ -i e^{-ik_F x} \\ e^{ik_F x} \end{pmatrix} e^{-k^{(e)} x}, \quad (5.22)$$

with $k_F = 2k_{so}$.

There are a few remarks in order. First, we see that the initial fourfold degeneracy of the MF has been completely removed by the boundary condition and we end up with one single non-degenerate MF wavefunction at the left end of the nanowire, $x=0$ (analogously for the right end, $x=L_{sc}$). This is reminiscent of a well-known fact in elementary quantum mechanics, where for spinless particles in a one-dimensional box the degeneracy also gets removed by vanishing boundary conditions (whereas there is degeneracy for periodic boundary conditions).[40] This non-degeneracy of the MFs is a generic feature which will occur in all cases considered in this work, even in the presence of additional symmetries such as pseudo-time reversal invariance (see Sec. 5.3.2 below and footnote [41]).

Second, we see that the MF wavefunction Φ_M is a ‘composite’ object that is a superposition of two MF wavefunctions with (essentially) disjoint supports in k -space, one

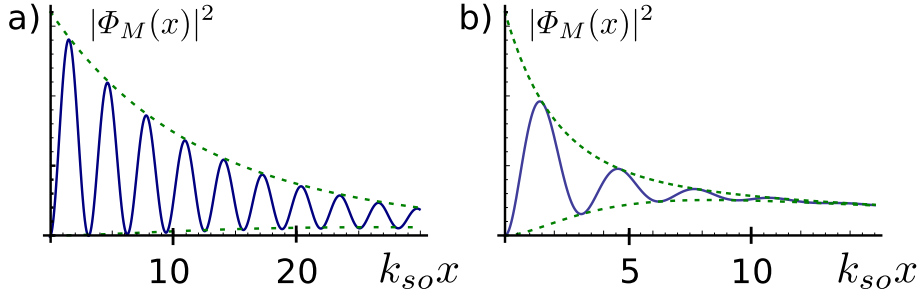


Figure 5.4: The MF probability density $|\Phi_M(x)|^2$, see Eq. (5.22), for a nanowire in the strong SOI regime with $\hbar^2\Delta_{sc}/m\alpha_R^2 = 0.1$. The decaying MF wavefunction Φ_M oscillates with a period π/k_{so} . (a) In the topological phase but still near the transition, $\Delta_Z = 2\Delta_{sc}$, the MF wavefunction undergoes many oscillations due to the interference between $\tilde{\Phi}_-^{(i)}$ and $\tilde{\Phi}_1^{(e)}$. (b) Deep inside the topological phase, $\Delta_Z = 7\Delta_{sc}$, the MF wavefunction from the interior branches decays much faster than the one from the exterior branches. This leads to only a few oscillations of the density and a uniform decay with a decay wavevector $k^{(e)}$ away from the end of the nanowire.

coming from the exterior ($\tilde{\Phi}_1^{(e)}$) and one from interior ($\tilde{\Phi}_-^{(i)}$) branches of the spectrum, respectively. Note that the corresponding wavevectors are extrema of the particle-hole spectrum shown in Fig. 5.2b. As a consequence, these two MF wavefunctions have different localization lengths in real space, $\xi^{(i)} = 1/k_-^{(i)}$ and $\xi^{(e)} = 1/k^{(e)}$, which are inverse proportional to the corresponding gaps, $|\Delta_-|$ and Δ_{sc} . Which one of them determines the localization length of Φ_M depends on the ratio between Δ_Z and Δ_{sc} .

In particular, as the magnetic field is being increased from zero to the critical value $B_c = 2\Delta_{sc}/g\mu_B$, MFs emerge at each end of the nanowire [7, 8, 5]. However, if the localization lengths $\xi^{(i)}$ of these emerging MFs are comparable to the length L_{sc} of the nanowire, then these two MFs are hybridized into a subgap fermion of finite energy (see App. 5.A). This then implies that the MFs in a finite wire can only appear at a magnetic field $B_c^* \simeq B_c(1 + 4\alpha_R/\Delta_{sc}L_{sc})$ that is *larger* than the B_c obtained for a semi-infinite nanowire. If the magnetic field is increased further, the main contribution to the MF bound state comes from the exterior branches.

The composite structure of the MF wavefunction manifests itself in the probability density $|\Phi_M(x)|^2$ along the nanowire. The density of a MF coming only from one of the branches, for example, $\tilde{\Phi}_-^{(i)}$, is just decaying exponentially. In contrast, the density of the composite MF exhibits oscillations (see Fig. 5.4). These oscillations are due to interference and are most pronounced when the contributions of $\tilde{\Phi}_1^{(e)}$ and $\tilde{\Phi}_-^{(i)}$ to $\tilde{\Phi}_M$ are similar, *i.e.*, when both decay lengths, $\xi^{(i)}$ and $\xi^{(e)}$, are close to each other.

The approach of the rotating magnetic field allows us to understand the structure of composite MF wavefunction. However, this approach is valid under the assumption that the SOI at the Fermi level is the largest energy scale. In order to explore the weak SOI regime, we come back to the full quadratic Hamiltonian in the next subsection.

5.3.2 Weak SOI regime: Near the topological phase transition

The regime of weak SOI is defined by the condition that the Zeeman splitting is much larger than the SOI energy at the Fermi level, $\Delta_Z \gg m\alpha_R^2/\hbar^2$ [or $k_F \approx k_Z$, see Eq. (5.6)]. This allows us to treat the SOI as a perturbation [26, 15].

Around the Fermi points, $\pm k_F$, the eigenstates of \mathcal{H}^0 are found from the Schrödinger equation $\mathcal{H}^0(-i\partial_x \rightarrow \pm k_F)\varphi_0^{R/L} = 0$ [see Eq. (5.4)] and given by

$$\varphi_0^{R/L} = \frac{1}{\sqrt{2}} \begin{pmatrix} -1 \pm \frac{k_{so}}{k_F} \\ 1 \pm \frac{k_{so}}{k_F} \end{pmatrix}, \quad (5.23)$$

where $\varphi_0^{R/L}$ denotes the eigenstates at $k = \pm k_F$. In Eq. (5.23) we kept only terms up to first order in k_{so}/k_F . As expected, φ_0^R and φ_0^L are nearly ‘aligned’ along the magnetic field since $\Delta_Z \gg \alpha_R k_F$. In the absence of SOI, φ_0^R and φ_0^L are perfectly aligned along the x -axis and have the same spin, so they cannot be coupled by an ordinary s -wave superconductor. The SOI slightly tilts the spins in the orthogonal direction, which then allows the coupling between these states if the nanowire is brought into the proximity of an s -wave superconductor.

The exterior branches can be treated in the linearized approximation similar to Sec. 5.3.1,

$$\chi(x) = R(x)e^{ik_F x} + L(x)e^{-ik_F x}, \quad (5.24)$$

where, again, R (L) annihilates a right (left) moving electron. These operators are connected to spin-up (Ψ_\uparrow) and spin-down (Ψ_\downarrow) electron operators as $R(x) = \varphi^R(x) \cdot \psi$ and $L(x) = \varphi^L(x) \cdot \psi$, where $\psi = (\Psi_\uparrow, \Psi_\downarrow)$ (with corresponding support for right and left movers). Here, $\varphi^{R/L}(x)$ is given by Eq. (5.23) but where we allow now also for a slowly varying x -dependence.

In this approximation, we find

$$H^0 = -i\hbar v_F \int dx [R^\dagger(x)\partial_x R(x) - L^\dagger(x)\partial_x L(x)], \quad (5.25)$$

where the Fermi velocity is given by $v_F \approx \sqrt{2\Delta_Z/m}$. The proximity-induced superconductivity [see Eq. (5.7)] is described in the linearized model as

$$H^{sc} = \frac{1}{2} \int dx \overline{\Delta}_{sc}(R(x)L(x) - L(x)R(x) + h.c.), \quad (5.26)$$

where the strength of the proximity-induced effective p -wave superconductivity, $\overline{\Delta}_{sc}$, is found from Eqs. (5.7), (5.23), and (5.24),

$$\frac{\overline{\Delta}_{sc}}{\Delta_{sc}} = (\varphi_0^R)^* \cdot i\sigma_2 \varphi_0^L = 2 \frac{k_{so}}{k_F} = \frac{\sqrt{2m}\alpha_R}{\hbar\sqrt{\Delta_Z}} \ll 1. \quad (5.27)$$

The suppression of $\overline{\Delta}_{sc}$ compared to Δ_{sc} can be understood from the fact that two states with opposite momenta at the Fermi level have mostly parallel spins due to the strong

magnetic field and they slightly deviate in the orthogonal direction due to the weak SOI, which then leads to a suppression of Δ_{sc} by a factor k_{so}/k_F .

Again, introducing a vector $\phi^{(e)}(x) = (R, L, R^\dagger, L^\dagger)$, we represent the linearized Hamiltonian $H^{(e)} = H^0 + H^{sc}$ as

$$H^{(e)} = \frac{1}{2} \int dx (\phi^{(e)})^\dagger \mathcal{H}^{(e)} \phi^{(e)},$$

$$\mathcal{H}^{(e)} = -i\hbar v_F \tau_3 \partial_x + \bar{\Delta}_{sc} \tau_2 \eta_2, \quad (5.28)$$

where the Pauli matrices $\tau_{1,2,3}$ act on the right/left-mover subspace.

The spectrum around the Fermi points in infinite space (no boundary conditions) follows from the Schrödinger equation, $\mathcal{H}^{(e)} \varphi^{(e)} = E^{(e)} \varphi^{(e)}$, and is given by $E_{1,2}^{(e)} = \pm \sqrt{(\hbar v_F \kappa)^2 + \Delta_e^2}$, where the momentum κ is again taken from the Fermi points. Here, $2\Delta_e \equiv 2\bar{\Delta}_{sc}$ is the gap induced by superconductivity.

The zero-energy solutions that are normalizable for $x > 0$ are two evanescent modes with wavevector $\bar{k}^{(e)} = \bar{\Delta}_{sc}/\hbar v_F$ determining the localization length. These solutions can be written explicitly as $\varphi_1^{(e)} = (1, -i, 1, i) e^{-\bar{k}^{(e)} x}$ and $\varphi_2^{(e)} = (-i, 1, i, 1) e^{-\bar{k}^{(e)} x}$. Repeating the procedure that led us to Eq. (5.18) in Sec. 5.3.1, we can introduce a new MF operator,

$$\gamma = \int dx \Phi_{E=0}(x) \cdot \Psi(x). \quad (5.29)$$

Here $\Psi = (\Psi_\uparrow, \Psi_\downarrow, \Psi_\uparrow^\dagger, \Psi_\downarrow^\dagger)$. The two corresponding wavefunctions are written as

$$\Phi_j^{(e)} = \begin{pmatrix} f_j(x) \\ i f_j^*(x) \\ f_j^*(x) \\ -i f_j(x) \end{pmatrix} e^{-\bar{k}^{(e)} x}, \quad (5.30)$$

where

$$f_1(x) = i(1 + k_{so}/k_F) e^{ik_F x} - (1 - k_{so}/k_F) e^{-ik_F x},$$

$$f_2(x) = i(1 - k_{so}/k_F) e^{-ik_F x} - (1 + k_{so}/k_F) e^{ik_F x}. \quad (5.31)$$

The effect of the SOI on the states around $k = 0$ is negligible near the topological phase transition if $\hbar^2 |\Delta_-| / 2m\alpha_R^2 \ll 1$. Therefore, the eigenstates for weak and strong SOIs are the same in first order in SOI. This means that we are allowed to take $\tilde{\Phi}_-^{(i)}$ and $\tilde{\Phi}_+^{(i)}$ given by Eq. (5.20) and transform them back into the lab frame,

$$\Phi_-^{(i)} = \begin{pmatrix} -i \operatorname{sgn}(\Delta_-) \\ 1 \\ i \operatorname{sgn}(\Delta_-) \\ 1 \end{pmatrix} e^{-k_-^{(i)} x}, \quad \Phi_+^{(i)} = \begin{pmatrix} 1 \\ -i \\ 1 \\ i \end{pmatrix} e^{-k_+^{(i)} x}. \quad (5.32)$$

After we found four basis wavefunctions $\{\Phi_-^{(i)}, \Phi_+^{(i)}, \Phi_1^{(e)}, \Phi_2^{(e)}\}$, we should impose the boundary conditions on their linear combination $\Phi(x)$. The wavefunction $\Phi(x)$ should vanish at the boundary $x = 0$. One can see that if we neglect the corrections to the wavefunctions $\Phi_1^{(e)}$ and $\Phi_2^{(e)}$ coming from SOI, then we are able to satisfy the boundary conditions. This is a consequence of the fact that in the absence of SOI both states at the Fermi level have the same spin, so that the functions $\Phi_i^{(e)}$, $i = 1, 2$, effectively become spinless objects and the MF always exists and arises only from the exterior branches. For the complete treatment, however, we should also consider contributions from the interior branches. This will be addressed next.

The set of wavefunctions $\{\Phi_-^{(i)}, \Phi_+^{(i)}, \Phi_1^{(e)}, \Phi_2^{(e)}\}$ becomes linearly dependent in the topological regime $\Delta_- < 0$ and the MF wavefunction is given by

$$\Phi_M = \left(1 - \frac{k_{so}}{k_F}\right) \Phi_1^{(e)} - \left(1 - \frac{k_{so}}{k_F}\right) \Phi_2^{(e)} - 4 \frac{k_{so}}{k_F} \Phi_-^{(i)}. \quad (5.33)$$

As in the regime of strong SOI (see Subsec. 5.3.1), the MF wavefunction has its support around wavevectors $k = 0$ (interior branches) and $k = \pm k_F$ (exterior branches). However, in contrast to the previous case, the contribution of the interior branches is suppressed by the small parameter k_{so}/k_F , thus the exterior branches contribute most to the MF wavefunction. At the same time we note that the localization length of MFs is determined by the smallest gap in the system. Near the topological phase transition[7, 8], which corresponds to the closing of the topological (interior) gap, the interior branches determine the localization length as long as $\bar{k}^{(e)} > k_-^{(i)}$. If the magnetic field is increased further, the gap in the system is given by the exterior gap, $2\Delta_e = 2\bar{\Delta}_{sc} \propto 1/\sqrt{B}$ [see Eq. (5.27)]. The localization length is increasing as $\propto B$. As soon as it is comparable to the nanowire length L_{sc} , the wavefunction of the two MFs at opposite ends overlap, and the two zero-energy MF levels are split into one subgap fermion of finite energy.

In the weak SOI regime and sufficiently far away from the topological transition point, $\Delta_Z > \Delta_{sc}(1 + k_{so}/k_F)$, so that the gap is determined by the exterior branches only, we can work in the simplified model[15] given by $\mathcal{H}^{(e)}$ [see Eq. (5.28)]. The explicit MF wavefunction can be found from Eq. (5.33),

$$\Phi_M(x) = \begin{pmatrix} e^{-i\pi/4} \\ ie^{i\pi/4} \\ e^{i\pi/4} \\ -ie^{-i\pi/4} \end{pmatrix} \sin(k_F x) e^{-\bar{k}^{(e)} x}. \quad (5.34)$$

Again, we note that this wavefunction describes a MF with the spin of both, the electron and the hole, pointing in x-direction, again, up to corrections of order of k_{so}/k_F . The MF probability density $|\Phi_M(x)|^2 \propto \sin^2(k_F x) e^{-2\bar{k}^{(e)} x}$ decays oscillating with a period half the Fermi wavelength, $\lambda_F/2 = \pi/k_F$ (see Fig. 5.5).

In passing we remark that $\mathcal{H}^{(e)}$ given in Eq. (5.28) belongs to the topological class DIII according to the classification scheme of Ref. [42] and supports MFs in 1D, in agreement with our result Eq. (5.34) [41].

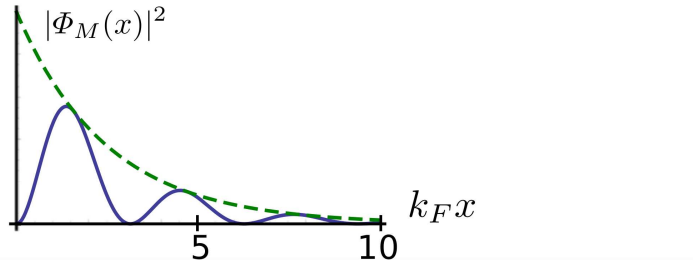


Figure 5.5: The MF probability density $|\Phi_M(x)|^2$ for a nanowire in the weak SOI regime ($m\alpha_R^2/\hbar^2\Delta_{sc} = 0.2$ and $\Delta_Z = 5\Delta_{sc}$) oscillates with period π/k_F due to interference between right- and left-moving contributions [see Eq. (5.30)]. The decay length is given by $1/\bar{k}^{(e)}$.

5.4 Majorana fermions in NS junctions

In this section we consider a nanowire containing a normal-superconducting (NS) junction where the right part is in the superconducting and the left part in the normal regime, see Fig. 5.6. The junction is assumed to be fully transparent. We will show that the MF wavefunction leaks out of the superconducting section and leads to a new MF bound state that extends over the entire normal section. We note that this bound state is different from Andreev bound states [45] known to occur in NS junction systems. Indeed, the existence of the latter at zero energy would be accidental in the presence of a magnetic field since they move away from the Fermi level if the magnetic field is varied. Further, the MFs found in this section always exist in the topological regime and are not sensitive to the length L_n of the normal section, in stark contrast to Andreev bound states that move in energy as function of L_n [45, 46].

We continue to work with the formalism developed in Sec. 5.3 [see Eqs. (5.18) and (5.29)] and represent γ in the basis of electron/hole spin-up/spin-down operators $\Psi(x)$ in

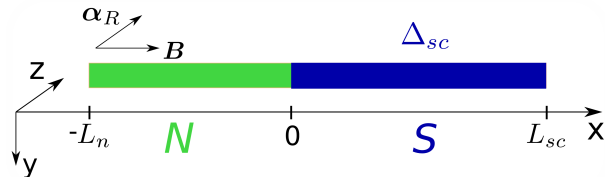


Figure 5.6: NS junction of a nanowire. The right section (blue) of the nanowire from $x = 0$ to $x = L_{sc}$ is brought into contact with a bulk s -wave superconductor (not shown) that induces a gap Δ_{sc} in the nanowire via proximity effect. The left section (green) of the nanowire from $x = -L_n$ to $x = 0$ is in the normal regime. A magnetic field \mathbf{B} is applied along the entire nanowire in x -direction and perpendicularly to the Rashba SOI vector $\boldsymbol{\alpha}_R$, which points in z -direction.

terms of a four-component vector $\Phi(x)$ on which we impose the boundary conditions. As before, the length of the superconducting part of the nanowire L_{sc} is assumed to be much larger than any decay length given by $k_-^{(i)}$, $k_+^{(i)}$, or $k^{(e)}$ ($\bar{k}^{(e)}$). This assumption allows us to treat the nanowire again as semi-infinite with no boundary conditions at $x = L_{sc}$. In contrast, the normal section, $x \in [-L_n, 0]$, is finite. Thus, at $x = 0$ we invoke continuity of the wavefunctions and of their derivatives [44] and at $x = -L_n$ we impose vanishing boundary conditions,

$$\Phi(x = 0^-) = \Phi(x = 0^+), \quad (5.35)$$

$$\partial_x \Phi(x = 0^-) = \partial_x \Phi(x = 0^+), \quad (5.36)$$

$$\Phi(x = -L_n) = 0. \quad (5.37)$$

The analytical form of the functions $\Phi(x)$ can be found in two regimes, again in the weak and strong SOI limits, which we address now in turn.

5.4.1 NS junction in the strong SOI regime

As before, the most convenient way to treat the strong SOI regime is to work in the rotating frame. In Sec. 5.3.1 we already found the four basis wavefunctions at zero energy

$$(\tilde{\Phi}_1^{(sc)}, \tilde{\Phi}_2^{(sc)}, \tilde{\Phi}_3^{(sc)}, \tilde{\Phi}_4^{(sc)}) = (\tilde{\Phi}_-^{(i)}, \tilde{\Phi}_+^{(i)}, \tilde{\Phi}_1^{(e)}, \tilde{\Phi}_2^{(e)}) \quad (5.38)$$

in the superconducting section, for $x \geq 0$ [see Eqs. (5.20) and (5.21)].

The eigenfunctions for the normal section can be found from the linearized Hamiltonians for the interior branches, $\tilde{\mathcal{H}}^{(i)}$ [see Eq. (5.16)], and for the exterior branches, $\tilde{\mathcal{H}}^{(e)}$ [see Eq. (5.17)], with $\Delta_{sc} = 0$. The exterior branches are not gapped leading to the four propagating modes (see Fig. 5.3b) with wavefunctions given by

$$\tilde{\Phi}_1^{(n)} = \begin{pmatrix} -i e^{ik_{so}x} \\ e^{-ik_{so}x} \\ i e^{-ik_{so}x} \\ e^{ik_{so}x} \end{pmatrix}, \quad \tilde{\Phi}_2^{(n)} = \begin{pmatrix} e^{ik_{so}x} \\ i e^{-ik_{so}x} \\ e^{-ik_{so}x} \\ -i e^{ik_{so}x} \end{pmatrix}, \quad \tilde{\Phi}_3^{(n)} = \begin{pmatrix} i e^{ik_{so}x} \\ e^{-ik_{so}x} \\ -i e^{-ik_{so}x} \\ e^{ik_{so}x} \end{pmatrix}, \quad \tilde{\Phi}_4^{(n)} = \begin{pmatrix} e^{ik_{so}x} \\ -i e^{-ik_{so}x} \\ e^{-ik_{so}x} \\ i e^{ik_{so}x} \end{pmatrix}, \quad (5.39)$$

where we choose to represent the wavefunctions in form of MFs, guided by our expectation that the final solution is also a MF. The interior branches are gapped by the magnetic field (see Fig. 5.3b) and the four corresponding wavefunctions describing evanescent modes

are given by

$$\tilde{\Phi}_5^{(n)} = \begin{pmatrix} -i e^{-ik_{so}x} \\ e^{ik_{so}x} \\ i e^{ik_{so}x} \\ e^{-ik_{so}x} \end{pmatrix} e^{k^{(n)}x}, \quad \tilde{\Phi}_6^{(n)} = \begin{pmatrix} e^{-ik_{so}x} \\ i e^{ik_{so}x} \\ e^{ik_{so}x} \\ -i e^{-ik_{so}x} \end{pmatrix} e^{k^{(n)}x}, \quad (5.40)$$

$$\tilde{\Phi}_7^{(n)} = \begin{pmatrix} i e^{-ik_{so}x} \\ e^{ik_{so}x} \\ -i e^{ik_{so}x} \\ e^{-ik_{so}x} \end{pmatrix} e^{-k^{(n)}(L_n+x)}, \quad \tilde{\Phi}_8^{(n)} = \begin{pmatrix} e^{-ik_{so}x} \\ -i e^{ik_{so}x} \\ e^{ik_{so}x} \\ i e^{-ik_{so}x} \end{pmatrix} e^{-k^{(n)}(L_n+x)}, \quad (5.41)$$

with $k^{(n)} = \Delta_Z/\alpha_R$. The modes $\tilde{\Phi}_{5,6}^{(n)}$ decay from their maximum at $x = 0$ to zero for $x \rightarrow -\infty$, while $\tilde{\Phi}_{7,8}^{(n)}$ decay from their maximum at $x = -L_n$ to zero for $x \rightarrow +\infty$.

After having introduced the basis consisting of 12 MF wavefunctions given by Eqs. (5.20), (5.21), (5.39), and (5.41), we search for their linear combination,

$$\tilde{\Phi}_M(x) = \begin{cases} \sum_{j=1}^4 a_j \tilde{\Phi}_j^{(sc)}, & x \geq 0 \\ \sum_{j=1}^8 b_j \tilde{\Phi}_j^{(n)}, & -L_n \leq x \leq 0, \end{cases} \quad (5.42)$$

such that the boundary conditions (5.35)-(5.37) are satisfied. This is, in general, possible only in the topological phase. However, we also find solutions in the nontopological phase, where these solutions exist only if some special relations between the parameters Δ_Z , α_R , Δ_{sc} , and L_n are satisfied. This allows us to identify them as Andreev bound states in an NS junction. Since they are not of interest here, we focus on the solutions in the topological phase only.

It is worth of pointing out that due to the internal symmetry of the MF wavefunctions, five of the coefficients are readily seen to vanish, namely

$$a_2 = b_1 = b_4 = b_5 = b_8 = 0. \quad (5.43)$$

The exact analytical solution is given in App. 5.B and used for the plot in Fig. 5.7. Here, we only discuss the two limiting cases of long and short normal sections L_n .

First, we consider $L_n \gg 1/k^{(n)}$, allowing us to neglect the terms $\tilde{\Phi}_5^{(n)}$ and $\tilde{\Phi}_6^{(n)}$ at $x = -L_n$, and $\tilde{\Phi}_7^{(n)}$ and $\tilde{\Phi}_8^{(n)}$ at $x = 0$. In this case, the sum in Eq. (5.42) is determined by the coefficients

$$\begin{aligned} a_1 &\rightarrow 0, & b_6 &\rightarrow 0, & b_7 &= -1, \\ a_3 &= b_3 = \cos(2k_{so}L_n), & a_4 &= b_2 = -\sin(2k_{so}L_n), \end{aligned} \quad (5.44)$$

leading to the solution of the form

$$\tilde{\Phi}_M(x) = \begin{cases} \tilde{\Phi}_3^{(n)}(2L_n + x) e^{-k^{(e)}x}, & x > 0 \\ \tilde{\Phi}_3^{(n)}(2L_n + x) - \tilde{\Phi}_3^{(n)}(-x) e^{-k^{(n)}(x+L_n)}, & -L_n \leq x < 0. \end{cases} \quad (5.45)$$

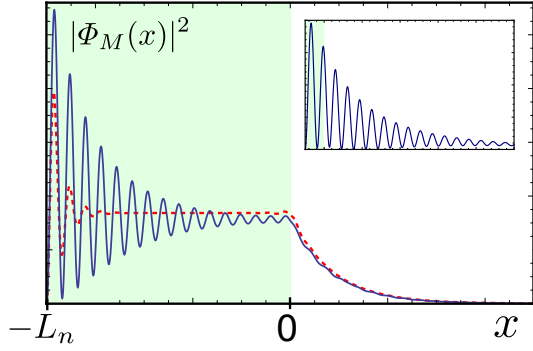


Figure 5.7: The MF probability density $|\Phi_M(x)|^2$ in an NS junction for a nanowire in the strong SOI regime ($\hbar^2 \Delta_{sc}/m\alpha_R^2 = 0.06$). The normal section of length L_n is long compared to the decay length, *i.e.* $k^{(n)} L_n \gg 1$. The MF wavefunction extends over the entire normal section (green) and decays exponentially inside the superconducting section (white). The oscillations with period π/k_{so} result from interference between the three components $\tilde{\Phi}_{2,3,7}^{(n)}$ of Φ_M . In weak magnetic fields ($\Delta_Z = 1.5\Delta_{sc}$, blue full line), $k^{(n)} L_n \sim 1$, and the oscillations extend over the entire normal section. In contrast, in strong magnetic fields ($\Delta_Z = 7\Delta_{sc}$, red dashed line), the oscillations are strongly suppressed. Inset: $|\Phi_M(x)|^2$ as function of x for a short normal section, $k^{(n)} L_n \ll 1$. Similarly to the case of the superconducting wire (see Fig. 5.4), $|\Phi_M(x)|^2$ decays oscillating.

Thus, we see that the MF wavefunction in the lab frame, $\Phi_M(x)$, decays monotonically in the superconducting section while it oscillates in the normal one (see Fig. 5.7). In weak magnetic fields the MF probability density $|\Phi_M(x)|^2$ oscillates over the entire normal section, in contrast to the near absence of oscillations in strong magnetic fields.

We note that a long normal section serves as a ‘momentum filter’. As shown in Subsec. 5.3.1, a MF has equal support from the exterior and interior branches [see Eq. (5.22)] if the entire nanowire is in the superconducting regime. In contrast to that, if a significant portion of the nanowire is in the normal regime, the MF has support mostly from the exterior branches with momenta $k \simeq \pm k_F$. The contributions from the interior branches with momenta $k \simeq 0$ are negligibly small, $a_1 \rightarrow 0$ and $a_2 = 0$. This behavior can be understood in terms of momentum mismatch: the normal section does not have propagating modes with $k = 0$ (in the lab frame). Thus, while such $k = 0$ modes exist in the superconducting section, they cannot propagate into the normal section.

Second, we consider the opposite limit $L_n \ll 1/k^{(n)}$. Here, we can treat the decaying solutions, $\tilde{\Phi}_j^{(n)}$, $j = 5, 6, 7, 8$, as being constant over L_n . The MF wavefunction $\tilde{\Phi}_M(x)$ is constructed from seven basis MF wavefunctions with the same coefficients as in Eq. (5.44) with the only difference that now $a_1 = -1$. For short normal sections, the form of the MF probability density $|\Phi_M(x)|^2$ is very similar to the one of a superconducting nanowire (compare inset of Fig. 5.7 with Fig. 5.4a). Again, the interference between $\tilde{\Phi}_-^{(i)}$, $\tilde{\Phi}_1^{(e)}$, and $\tilde{\Phi}_2^{(e)}$ leads to oscillations in the superconducting section.

In both limits of short and long normal sections, $|\Phi_M(x)|^2$ has its maximum in the normal section while it decays in the superconducting one. This opens the possibility of measuring the presence of a MF state spectroscopically in the normal section. The amplitude and period of oscillations of the MF probability density is sensitive to magnetic fields and to the nanowire length, controlled e.g. by an infinite barrier on the left end. Moreover, by shifting such a barrier via gates, we can change the type of MF from $\tilde{\Phi}_1^{(e)}$ to $\tilde{\Phi}_2^{(e)}$ [see Eqs. (5.38), (5.42), and (5.44)]. This amounts to change a given MF state from a ‘real part’ type, $\psi + \psi^\dagger$, to an ‘imaginary part’ type, $i(\psi - \psi^\dagger)$.

5.4.2 NS junction in the weak SOI regime

As before, we first identify basis wavefunctions in the superconducting section and in the normal section. Then, we search for a linear combination of them such that the boundary conditions given by Eqs. (5.35)-(5.37) are satisfied.

As shown in Sec. 5.3.2, the MF wavefunction Φ_M has predominantly support from the exterior branches. The correction to the MF wavefunction from the interior branches is suppressed by a factor k_{so}/k_F [see Eq. (5.33)]. If we focus on the regime away from the topological phase transition where the exterior gap is smaller than the interior one, then, as in Eq. (5.30), the MF wavefunction can be constructed to first order in k_{so}/k_F from the exterior wavefunctions $\Phi_{j=1,2}^{(e)}$ alone,

$$\Phi_j^{(sc)} = \begin{pmatrix} g_j(x) \\ ig_j^*(x) \\ g_j^*(x) \\ -ig_j(x) \end{pmatrix} e^{-\bar{k}^{(e)}x},$$

$$g_1 = e^{-i\pi/4} \sin(k_F x), \quad g_2 = e^{-i\pi/4} \cos(k_F x). \quad (5.46)$$

The propagating electron modes φ^R and φ^L of Eq. (5.23) in the normal section described by H^0 (without H^{sc}) were considered before [see Eq. (5.29)] and given by

$$\Phi_1^{(n)} = \begin{pmatrix} e^{-ik_F x} \\ -e^{-ik_F x} \\ e^{ik_F x} \\ -e^{ik_F x} \end{pmatrix}, \quad \Phi_2^{(n)} = \begin{pmatrix} e^{ik_F x} \\ -e^{ik_F x} \\ e^{-ik_F x} \\ -e^{-ik_F x} \end{pmatrix}, \quad \Phi_3^{(n)} = \begin{pmatrix} ie^{-ik_F x} \\ -ie^{-ik_F x} \\ -ie^{ik_F x} \\ ie^{ik_F x} \end{pmatrix}, \quad \Phi_4^{(n)} = \begin{pmatrix} ie^{ik_F x} \\ -ie^{ik_F x} \\ -ie^{-ik_F x} \\ ie^{-ik_F x} \end{pmatrix}. \quad (5.47)$$

The ansatz for the wavefunction in both sections is

$$\Phi(x) = \begin{cases} \sum_{j=1}^2 a_j \Phi_j^{(sc)}, & x \geq 0 \\ \sum_{j=1}^4 b_j \Phi_j^{(n)}, & -L_n \leq x \leq 0. \end{cases} \quad (5.48)$$

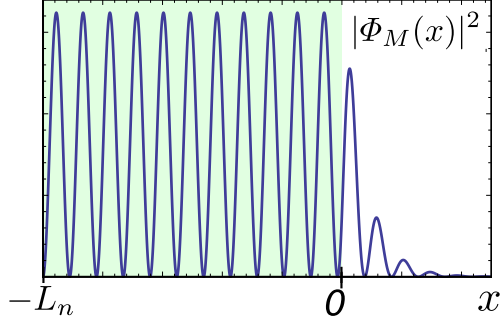


Figure 5.8: The MF probability density $|\Phi_M(x)|^2$ in an NS junction for a nanowire in the weak SOI regime ($m\alpha_R^2/\hbar^2\Delta_{sc} = 0.2$ and $\Delta_Z = 5\Delta_{sc}$). The MF wavefunction extends over the entire normal section of length L_n (green) and decays rapidly inside the superconducting section (white).

The coefficients a_j and b_j can then be found from the boundary conditions (5.35)-(5.37),

$$\begin{aligned} a_1 &= 2[\bar{k}^{(e)} \sin(k_F L_n) + k_F \cos(k_F L_n)], \\ a_2 &= 2k_F \sin(k_F L_n), \\ b_1 &= -b_4 = k_F \cos(k_F L_n - \pi/4), \\ b_2 &= -b_3 = -k_F \cos(k_F L_n + \pi/4), \end{aligned} \quad (5.49)$$

leading finally to the MF wavefunction of the form

$$\Phi_M(x) = f(x) \begin{pmatrix} e^{-i\pi/4} \\ -e^{-i\pi/4} \\ e^{i\pi/4} \\ -e^{i\pi/4} \end{pmatrix}, \quad (5.50)$$

where

$$f(x) = \begin{cases} k_F \sin(k_F[x + L_n]), & -L_n \leq x \leq 0 \\ e^{-\bar{k}^e x} [k_F \sin(k_F[x + L_n]) \\ + \bar{k}^e \sin(k_F x) \sin(k_F L_n)], & x \geq 0. \end{cases} \quad (5.51)$$

The corresponding MF probability density $|\Phi_M(x)|^2$ is shown in Fig. 5.8. The MF wavefunction extends over the entire normal section. In this section, we considered as basis functions only propagating modes, $\Phi_j^{(n)}$, leading to a purely oscillatory solution with the period given by half the Fermi wavelength $\lambda_F/2 = \pi/k_F$. In contrast, in the superconducting section, the MF wavefunction decays on a short distance. In other words, the MF is mostly delocalized over the entire normal section and is strongly localized in the superconducting section, in agreement with recent numerical results[38]. This might simplify the detection of MFs by local density measurements since the normal section is freely accessible to tunnel contacts, in contrast to the superconducting section which needs to be covered by a bulk *s*-wave superconductor.

5.5 Conclusions

In this work, we have focused on the wavefunction properties of Majorana fermions occurring in superconducting nanowires and in nanowires with an NS junction. The superconducting phase is effectively p -wave and is based on an interplay of s -wave proximity effect, spin orbit interaction, and magnetic fields. We have derived explicit results for the MF wavefunctions in the regime of strong and weak SOI and shown that the wavefunctions are composite objects, being superpositions of contributions coming from the interior (around $k = 0$) and exterior (around $\pm k_F$) branches of the spectrum in momentum space. While the underlying Hamiltonians considered in this work allow degenerate MF wavefunctions, the boundary conditions at hand completely lift this degeneracy and we are left with only one single MF state at a given end of the nanowire (*i.e.* in total there are two MF states for the entire nanowire).

In the strong SOI regime of a superconducting nanowire both branches contribute equally. However, the decay length of the MF is determined by the branch that also defines the smallest gap in the system. Moreover, the oscillations in the MF probability density with period of the Fermi wavelength are decaying on the scale given by the largest gap in the system. In the weak SOI regime, the exterior branches mostly contribute to the MF wavefunction. The contributions of the interior branch is suppressed by the small factor $k_{so}/k_F \ll 1$ and only close to the topological phase transition this branch determines the localization length of the MF. The interference between modes from k_F and $-k_F$ leads to oscillations of the probability density of the MF with an exponentially decaying envelope.

For a nanowire with an NS junction we find that the MF wavefunction becomes delocalized over the entire normal section, while still being localized in the superconducting section, in agreement with recent numerical results.[38] Again, we obtain analytical results for the weak and strong SOI regimes. Depending on the length of the normal section, the support of the MF wavefunction is centered at zero momentum or at the Fermi points. Again, we find different localization lengths and oscillation periods of the MF in the normal section that are tunable by magnetic fields. Based on this insight, we expect that in a tunneling density of states measurement the tunneling current at zero bias exhibits oscillations as a function of position along the normal section due to the presence of the MF in the normal section.

Finally, we remark that in this work we have focused on single particle properties and ignored, in particular, interaction effects. It would be interesting to extend the present analysis to interacting Luttinger liquids, in particular for the SOI nanowire with an NS junction, combining the approaches developed in Refs. [47, 39, 15, 14].

Acknowledgements. We acknowledge fruitful discussions with Karsten Flensberg, Diego Rainis, and Luka Trifunovic. This work is supported by the Swiss NSF, NCCR Nanoscience and NCCR QSIT, and DARPA.

5.A Finite nanowire

In this Appendix we address the problem of a finite superconducting section of length L_{sc} . In this case, the decaying modes $\tilde{\Phi}_0 = \{\tilde{\Phi}_-^{(i)}, \tilde{\Phi}_+^{(i)}, \tilde{\Phi}_1^{(e)}, \tilde{\Phi}_2^{(e)}\}$ with maximum at $x = 0$ are given by Eqs. (5.20) and (5.21). Now we should also take into account the four evanescent modes with maximum at $x = L_{sc}$. These modes, $\tilde{\Phi}_{L_{sc}} = \{\tilde{\Phi}_-^{(i)}, \tilde{\Phi}_+^{(i)}, \tilde{\Phi}_1^{(e)}, \tilde{\Phi}_2^{(e)}\}$, are found from Eqs. (5.16), (5.17) and are similar by their structure to $\tilde{\Phi}_0$,

$$\begin{aligned} \tilde{\Phi}_-^{(i)} &= \begin{pmatrix} i \operatorname{sgn}(\Delta_-) e^{-ik_{so}x} \\ e^{ik_{so}x} \\ -i \operatorname{sgn}(\Delta_-) e^{ik_{so}x} \\ e^{-ik_{so}x} \end{pmatrix} e^{k_-^{(i)}(x-L_{sc})}, & \tilde{\Phi}_+^{(i)} &= \begin{pmatrix} e^{-ik_{so}x} \\ i e^{ik_{so}x} \\ e^{ik_{so}x} \\ -i e^{-ik_{so}x} \end{pmatrix} e^{-k_+^{(i)}(x-L_{sc})}, \\ \tilde{\Phi}_1^{(e)} &= \begin{pmatrix} -i e^{ik_{so}x} \\ e^{-ik_{so}x} \\ i e^{-ik_{so}x} \\ e^{ik_{so}x} \end{pmatrix} e^{-k^{(e)}(x-L_{sc})}, & \tilde{\Phi}_2^{(e)} &= \begin{pmatrix} e^{ik_{so}x} \\ -i e^{-ik_{so}x} \\ e^{-ik_{so}x} \\ i e^{ik_{so}x} \end{pmatrix} e^{-k^{(e)}(x-L_{sc})}. \end{aligned} \quad (5.52)$$

We construct a 8×4 matrix $\tilde{\omega}(x)$ from the eight basis wavefunctions. The zero-energy solution can then be compactly written as

$$\tilde{\Phi}(x) = \mathbf{a} \cdot \tilde{\Phi}_0(x) + \mathbf{b} \cdot \tilde{\Phi}_{L_{sc}}(x) \equiv \tilde{\omega}(x) \begin{pmatrix} \mathbf{a} \\ \mathbf{b} \end{pmatrix}, \quad (5.53)$$

where $\mathbf{a} = (a_1, a_2, a_3, a_4)$ and $\mathbf{b} = (b_1, b_2, b_3, b_4)$ are coefficients that should be determined from the boundary conditions,

$$\tilde{\Phi}(x = 0, L_{sc}) = 0, \quad (5.54)$$

which can be rewritten as a matrix equation in terms of a 8×8 matrix $\tilde{\Omega}$,

$$\tilde{\Omega} \begin{pmatrix} \mathbf{a} \\ \mathbf{b} \end{pmatrix} = (\tilde{\omega}(0) \ \tilde{\omega}(L_{sc})) \begin{pmatrix} \mathbf{a} \\ \mathbf{b} \end{pmatrix} = 0. \quad (5.55)$$

The determinant of the matrix $\tilde{\Omega}$ is nonzero, so the solution of the matrix equation is unique and trivial, $(\mathbf{a}, \mathbf{b}) = 0$. This means that, strictly speaking, MFs cannot emerge in a finite-size nanowire. MFs exist only under the assumption that the overlap of the two MF wavefunctions (localized at each end of the nanowire and derived in a semi-infinite nanowire model) can be neglected. Otherwise, the two MFs are hybridized into a subgap fermion of finite energy.

5.B Exact solution in strong SOI regime

Here, we present the exact solution for the MF wavefunction $\tilde{\Phi}(x)$ composed of seven different basis MFs wavefunctions [see Eq. (5.42)] and satisfying the boundary conditions (5.35)-(5.37). We find

$$\begin{aligned}
 a_2 &= b_1 = b_4 = b_5 = b_8 = 0, \\
 a_1 &= 4k_{so}^2 + 4k_{so}k^{(e)} \cosh(k^{(n)}L) \sin(2k_{so}L_n) - 2k^{(e)} \cos(2k_{so}L_n)[k^{(e)} \cosh(k^{(n)}L_n) + k^{(n)} \sinh(k^{(n)}L_n)], \\
 a_3 &= e^{-k^{(n)}L_n} [e^{k^{(n)}L_n} (k^{(e)}[k^{(n)} - 2k_-^{(i)}] + k^{(n)}[k^{(n)} - k_-^{(i)}]) - 4k_{so}^2 e^{2k^{(n)}L_n} \cos(2k_{so}L_n) \\
 &\quad - 2k_{so}(e^{2k^{(n)}L_n} k^{(e)} + k_-^{(i)} - k^{(n)}) \sin(2k_{so}L_n)], \\
 a_4 &= -e^{-k^{(n)}L_n} [2e^{k^{(n)}L_n} k_{so}(k^{(n)} - k_-^{(i)} - k^{(e)}) + 2k_{so}(e^{2k^{(n)}L_n} k^{(e)} + k_-^{(i)} - k^{(n)}) \cos(2k_{so}L_n) \\
 &\quad - e^{2k^{(n)}L_n} 4k_{so}^2 \sin(2k_{so}L_n)], \\
 b_2 &= -e^{-k^{(n)}L_n} (-2e^{k^{(n)}L_n} k_{so}k^{(e)} + 2k_{so}(k_-^{(i)} - k^{(n)}) \cos(2k_{so}L_n) - 4k_{so}^2 e^{2k^{(n)}L_n} \sin(2k_{so}L_n)), \\
 b_3 &= e^{-k^{(n)}L_n} (e^{k^{(n)}L_n} k^{(e)}[k^{(e)} - k_-^{(i)}] - 4k_{so}^2 e^{2k^{(n)}L_n} \cos(2k_{so}L_n) + 2k_{so}(k^{(n)} - k_-^{(i)}) \sin(2k_{so}L_n)), \\
 b_6 &= -2k_{so}(k^{(n)} - k_-^{(i)}) - e^{k^{(n)}L_n} k^{(e)}[2k_{so} \cos(2k_{so}L_n) + (k^{(e)} - k_-^{(i)}) \sin(2k_{so}L_n)], \\
 b_7 &= 4k_{so}^2 e^{k^{(n)}L_n}.
 \end{aligned} \tag{5.56}$$

Bibliography

- [1] E. Majorana, Nuovo Cimento **14**, 171 (1937).
- [2] A. Y. Kitaev, Physics-Uspekhi **44**, 131 (2001).
- [3] L. Fu and C. L. Kane, Phys. Rev. Lett. **100**, 096407 (2008).
- [4] Y. Tanaka, T. Yokoyama, and N. Nagaosa, Phys. Rev. Lett. **103**, 107002 (2009).
- [5] M. Sato and S. Fujimoto, Phys. Rev. B **79**, 094504 (2009).
- [6] A. R. Akhmerov, J. Nilsson, and C. W. J. Beenakker, Phys. Rev. Lett. **102**, 216404 (2009).
- [7] R. M. Lutchyn, J. D. Sau, and S. Das Sarma, Phys. Rev. Lett. **105**, 077001 (2010).
- [8] Y. Oreg, G. Refael, and F. von Oppen, Phys. Rev. Lett. **105**, 177002 (2010).
- [9] J. Alicea, Phys. Rev. B **81**, 125318 (2010).
- [10] K. Flensberg, Phys. Rev. B **82**, 180516 (2010).
- [11] M. Duckheim and P. W. Brouwer, Phys. Rev. B **83**, 054513 (2011).
- [12] A. C. Potter and P. A. Lee, Phys. Rev. B **83**, 094525 (2011).
- [13] X. L. Qi and S. C. Zhang, Rev. Mod. Phys. **83**, 1057 (2011).
- [14] E. M. Stoudenmire, J. Alicea, O. Starykh, and M.P.A. Fisher, Phys. Rev. B **84**, 014503 (2011).
- [15] S. Gangadharaiah, B. Braunecker, P. Simon, and D. Loss, Phys. Rev. Lett. **107**, 036801 (2011).
- [16] R. M. Lutchyn and M.P.A. Fisher, Phys. Rev. B **84**, 214528 (2011).
- [17] J. Klinovaja, S. Gangadharaiah, and D. Loss, Phys. Rev. Lett. **108**, 196804 (2012).
- [18] J. S. Lim, L. Serra, R. Lopez, and R. Aguado, arXiv:1202.5057.
- [19] For a recent comprehensive review, see J. Alicea, arXiv:1202.1293.
- [20] A. Kitaev, Ann. Phys. **303**, 2 (2003).
- [21] M. H. Freedman, A. Kitaev, M. J. Larsen, and Z. Wang, Bull. Amer. Math. Soc. **40**, 31 (2003).
- [22] S. Bravyi and A. Kitaev, Phys. Rev. A **71**, 022316 (2005).

- [23] S. Bravyi, Phys. Rev. A **73**, 042313 (2006).
- [24] C. Nayak, S. H. Simon, A. Stern, M. Freedman, and S. Das Sarma, Rev. Mod. Phys. **80**, 1083 (2008).
- [25] P. Bonderson, M. Freedman, and C. Nayak, Phys. Rev. Lett. **101**, 010501 (2008).
- [26] J. Alicea, Y. Oreg, G. Refael, F. von Oppen, and M.P.A. Fisher, Nat. Phys. **7**, 412 (2011).
- [27] N. Read and D. Green, Phys. Rev. B **61**, 10267 (2000).
- [28] C. Nayak, S. H. Simon, A. Stern, M. Freedman, and S. Das Sarma, Rev. Mod. Phys. **80**, 1083 (2008).
- [29] S. Sasaki, M. Kriener, K. Segawa, K. Yada, Y. Tanaka, M. Sato, and Y. Ando, Phys. Rev. Lett. **107**, 217001 (2011).
- [30] J. R. Williams, A. J. Bestwick, P. Gallagher, Seung Sae Hong, Y. Cui, Andrew S. Bleich, J. G. Analytis, I. R. Fisher, and D. Goldhaber-Gordon, arXiv:1202.2323.
- [31] V. Mourik, K. Zuo, S. M. Frolov, S. R. Plissard, E. P. A. M. Bakkers, and L. P. Kouwenhoven, Science **336**, 1003 (2012).
- [32] M. T. Deng, C. L. Yu, G. Y. Huang, M. Larsson, P. Caroff, and H. Q. Xu, arXiv:1204.4130.
- [33] L. P. Rokhinson, X. Liu, and J. K. Furdyna, arXiv:1204.4212.
- [34] H-J. Kwon, K. Sengupta, V. M. Yakovenko, Eur. Phys. J. **37**, 349 (2004); J. Low Temp. Phys. **30**, 613 (2004).
- [35] D. Sticlet, C. Bena, and P. Simon, Phys. Rev. Lett. **108**, 096802 (2012).
- [36] J. D. Sau, C. H. Lin, H.-Y. Hui, and S. Das Sarma, Phys. Rev. Lett. **108**, 067001 (2012).
- [37] M. Cheng, and R. M. Lutchyn, arXiv:1201.1918.
- [38] D. Chevallier, D. Sticlet, P. Simon, and C. Bena, arXiv:1203.2643.
- [39] B. Braunecker, G.I. Japaridze, J. Klinovaja, and D. Loss, Phys. Rev. B **82**, 045127 (2010).
- [40] L. D. Landau and E. M. Lifshitz, Quantum Mechanics (Non-Relativistic Theory), vol. 3, (Pergamon Press, New York, 1977), p 60; S. De Vincenzo, Braz. J. of Phys. **38**, 355 (2008).

- [41] We note that $\mathcal{H}^{(e)}$ given in Eq. (5.28) is invariant under the (pseudo-) time reversal operation \mathcal{T} , defined[42] by $U_T^\dagger(\mathcal{H}^{(e)})^*U_T = +\mathcal{H}^{(e)}$. Indeed, choosing $U_T = -i\tau_2 \otimes \eta_0$, we see that the former relation is satisfied. Similarly for the particle-hole symmetry \mathcal{C} , defined[42] by $U_C^\dagger(\mathcal{H}^{(e)})^*U_C = -\mathcal{H}^{(e)}$, which is satisfied for $U_C = \tau_0 \otimes \eta_1$. Thus, since $\mathcal{T}^2 = -1$ and $\mathcal{C}^2 = 1$, $\mathcal{H}^{(e)}$ belongs to the topological class DIII.[42] In the right/left basis $\phi^{(e)} = (R, L, R^\dagger, L^\dagger)$ the MF wavefunction $\Phi_M(x)$ that vanishes at the boundary [see Eqs. (5.34),(5.29)] becomes $\varphi_M = \varphi_1^{(e)} - \varphi_2^{(e)}$. Its degenerate time-reversed partner, $\mathcal{T}\varphi_M = \varphi_1^{(e)} + \varphi_2^{(e)}$, also solves the Schrödinger equation but does not satisfy the boundary condition and therefore is not a solution. In other words, \mathcal{T} -invariance alone is only a *necessary* condition for degeneracy: the latter can be removed by boundary conditions. For an alternative classification of $\mathcal{H}^{(e)}$ see Ref. [43].
- [42] S. Ryu, A. P. Schnyder, A. Furusaki, and A. W. W. Ludwig, New J. of Phys. **12**, 065010 (2010).
- [43] S. Tewari and J. D. Sau, arXiv:1111.6592 (2011).
- [44] We note that we search for solutions of the original Hamiltonian with quadratic dispersion and thus the wavefunctions and their derivatives have to be continuous everywhere.
- [45] A.F. Andreev, Sov. Phys. JETP **19**, 1228 (1964).
- [46] R. A. Riedel and P. F. Bagwell, Phys. Rev. B **48**, 15198 (1993).
- [47] D. L. Maslov, M. Stone, P. M. Goldbart, and D. Loss, Phys. Rev. B **53**, 1548 (1996).

Chapter 5

Chapter 6

Transition from fractional to Majorana fermions in Rashba nanowires

We study hybrid superconducting-semiconducting nanowires in the presence of Rashba spin-orbit interaction (SOI) as well as helical magnetic fields. We show that the interplay between them leads to a competition of phases with two topological gaps closing and reopening, resulting in unexpected reentrance behavior. Besides the topological phase with localized Majorana fermions (MFs) we find new phases characterized by fractionally charged fermion (FF) bound states of Jackiw-Rebbi type. The system can be fully gapped by the magnetic fields alone, giving rise to FFs that transmute into MFs upon turning on superconductivity. We find explicit analytical solutions for MF and FF bound states and determine the phase diagram numerically by determining the corresponding Wronskian null space. We show by renormalization group arguments that electron-electron interactions enhance the Zeeman gaps opened by the fields.

This chapter has been published as Phys. Rev. Lett. **109**, 236801 (2012).

6.1 Introduction

Majorana fermions [1] (MF) in condensed matter systems [2], interesting from a fundamental point of view as well as for potential applications in topological quantum computing, have attracted wide interest, both in theory [3, 4, 5, 6, 7, 8, 9, 10, 11, 12, 13, 14, 15, 16] and experiment [17, 18, 19]. One of the most promising candidate systems for MFs are semiconducting nanowires with Rashba spin-orbit interaction (SOI) brought into proximity with a superconductor [7, 8, 9]. In such hybrid systems a topological phase with a MF at each end of the nanowire is predicted to emerge once an applied uniform magnetic field exceeds a critical value [6, 7, 8, 9]. As pointed out recently [20], the Rashba SOI in such wires is equivalent to a helical Zeeman term, and thus the same topological phase with MFs is predicted to occur in hybrid systems in the presence of a helical field but without SOI [21, 22].

Here, we go a decisive step further and address the question, what happens when *both* fields are present, an internal Rashba SOI field as well as a helical—or more generally—a spatially varying magnetic field. Quite remarkably, we discover that due to the interference between the two mechanisms the phase diagram becomes surprisingly rich, with reentrance behavior of MFs and new phases characterized by fractionally charged fermions (FF), analogously to Jackiw-Rebbi fermion bound states [23]. Since the system is fully gapped by the magnetic fields at certain Rashba SOI strengths (in the absence of superconductivity), these FFs act as precursors of MFs into which they transmute by turning on superconductivity.

The main part of this work aims at characterizing the mentioned phase diagram. For this we find explicit solutions for the various bound states, which allows us to derive analytical conditions for the boundaries of the topological phases. We also perform an independent numerical search of the phases and present results illustrating them. We show that the phases can be controlled with experimentally accessible parameters, such as the uniform field or the chemical potential. We formulate the topological criterion as a condition local in momentum space via the kernel dimension of the Wronskian, which does not require the knowledge of the spectrum in the entire Brillouin zone. We also address interaction effects and show that they increase all Zeeman gaps and thereby the stability of the topological phase.

6.2 Model

We consider a system consisting of a semiconducting nanowire with Rashba SOI in proximity with an *s*-wave bulk superconductor and in the presence of magnetic fields which contain uniform and spatially varying components, see Fig. 6.1. The Rashba spin-orbit interaction is characterized by a SOI vector α pointing along, say, the z -axis. The effective continuum Hamiltonian for the nanowire is in Nambu representation given by

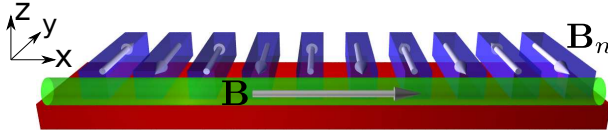


Figure 6.1: Schematics of the hybrid semiconducting-superconducting system, consisting of a finite Rashba nanowire (green cylinder) on top of an s-wave bulk superconductor (red slab) in the presence of a uniform magnetic field \mathbf{B} (grey arrow) applied along the nanowire in x-direction. Periodically arranged nanomagnets (blue bars) produce a spatially varying magnetic field $\mathbf{B}_n(x)$ (grey arrows). We note that $\mathbf{B}_n(x)$ can also be generated intrinsically e.g. by a helical hyperfine field of nuclear spins inside the nanowire [24].

$$H_0 = \frac{1}{2} \int dx \psi^\dagger(x) \mathcal{H}_0 \psi(x) \text{ with}$$

$$\mathcal{H}_0 = (-\hbar^2 \partial_x^2 / 2m - \mu) \eta_3 - i\alpha \eta_3 \sigma_3 \partial_x, \quad (6.1)$$

where m is the electron mass. Here, $\psi = (\Psi_\uparrow, \Psi_\downarrow, \Psi_\uparrow^\dagger, \Psi_\downarrow^\dagger)$, and $\Psi_\sigma^{(\dagger)}(x)$, with $\sigma = \uparrow / \downarrow$, is the annihilation (creation) operator for a spin up/down electron at position x . The Pauli matrix σ_i (η_i) acts in the spin (electron-hole) space. The spectrum of \mathcal{H}_0 consists of four parabolas centered at the Rashba momentum $\pm k_{so} = \pm m\alpha/\hbar^2$, see Fig. 6.2. The chemical potential μ is chosen to be zero at the crossing of the Rashba branches at $k = 0$.

The uniform (\mathbf{B}) and spatially varying (\mathbf{B}_n) magnetic fields lead to the Zeeman term,

$$\mathcal{H}_z = g\mu_B [\mathbf{B} + \mathbf{B}_n(x)] \cdot \boldsymbol{\sigma} \eta_3 / 2, \quad (6.2)$$

where g is the g-factor and μ_B the Bohr magneton. The proximity-induced superconductivity couples states of opposite momenta and spins and is described by $\mathcal{H}_s = \Delta_s \sigma_2 \eta_2$, where the effective pairing amplitude Δ_s can be assumed to be non-negative.

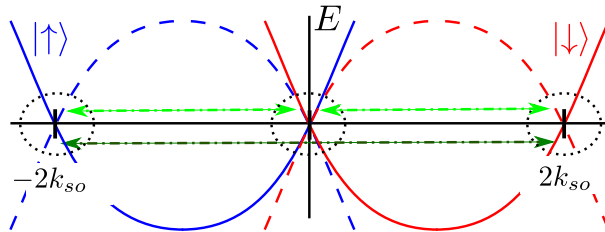


Figure 6.2: The spectrum of Rashba nanowire consists of parabolas shifted by $\pm k_{so}$: solid and dashed lines correspond to the electron and hole spectrum, respectively. The outer circles (dotted) mark the exterior branches and the inner circle (dotted) marks the interior branches. A spatially varying magnetic field with period $4k_{so}$ (dark green arrow) couples the exterior branches. Similarly, a uniform magnetic field couples the interior branches at $k = 0$ (not indicated). A spatially varying magnetic field with period $2k_{so}$ (light green arrow) mixes exterior with interior branches.

From now on, we assume that the SOI energy $m\alpha^2/\hbar^2$ is the largest energy scale at the Fermi level in the problem. In this strong SOI regime, we can treat the B -fields and Δ_s as small perturbations. This allows us to linearize the full Hamiltonian $\mathcal{H}_0 + \mathcal{H}_z + \mathcal{H}_s$ around $k = 0$ (referred to as interior branches) and $k = \pm 2k_{so}$ (referred to as exterior branches), see Fig. 6.2. This entails that we can use the ansatz

$$\Psi(x) = R_\uparrow + L_\downarrow + L_\uparrow e^{-2ik_{so}x} + R_\downarrow e^{2ik_{so}x}, \quad (6.3)$$

where the right mover $R_\sigma(x)$ and the left mover $L_\sigma(x)$ are slowly-varying fields. For a uniform magnetic field alone (chosen along the x -axis) the full Hamiltonian becomes $H = \frac{1}{2} \int dx \tilde{\psi}(x)^\dagger \mathcal{H} \tilde{\psi}(x)$ with

$$\mathcal{H} = -i\hbar v_F \sigma_3 \tau_3 \partial_x + \Delta_z \eta_3 \sigma_1 (1 + \tau_3)/2 + \Delta_s \eta_2 \sigma_2, \quad (6.4)$$

where the Pauli matrix τ_i acts in the interior-exterior branch space, and

$$\tilde{\psi} = (R_\uparrow, L_\downarrow, R_\uparrow^\dagger, L_\downarrow^\dagger, L_\uparrow, R_\downarrow, L_\uparrow^\dagger, R_\downarrow^\dagger). \quad (6.5)$$

The Fermi velocity is given by $v_F = \alpha/\hbar$ and the Zeeman energy by $\Delta_z = g\mu_B B/2$. Next, we include the spatially varying magnetic field, and assume that it has a substantial Fourier component either at $4k_{so}$ (case I) or at $2k_{so}$ (case II), leading to additional couplings between all branches of the spectrum, see Fig. 6.2. We treat now the two cases in turn and will see that the interplay of Rashba and magnetic fields leads to a surprisingly rich diagram of topological phases.

6.3 Case I - period $4k_{so}$

Here, we consider $\mathbf{B}_n(x)$ with period $4k_{so}$ and perpendicular to $\boldsymbol{\alpha}$. For a field with oscillating amplitude only, we consider two geometries, $\mathbf{B}_{n,x} = \hat{x}B_n \cos(4k_{so}x + \theta)$ and $\mathbf{B}_{n,y} = \hat{y}B_n \sin(4k_{so}x + \theta)$, with arbitrary phase shift θ , while for a helical field we consider a field with anticlockwise rotation, $(\mathbf{B}_{n,x} + \mathbf{B}_{n,y})/2$. (clockwise rotation does not lead to coupling). We note that $\mathbf{B}_n(x)$ can also be generated intrinsically e.g. by the hyperfine field of ordered nuclear spins inside the nanowire [24]. All geometries lead to identical results: they affect only the exterior branches (see Fig. 6.2) and the corresponding Hamiltonian remains block-diagonal in τ -space. The full Hamiltonian becomes $\mathcal{H}_{4k_{so}} = \mathcal{H} + \Delta_n(\sigma_1 \cos \theta - \sigma_2 \sin \theta)\eta_3(1 - \tau_3)/2$, where $\Delta_n = g\mu_B B_n/4$. The spectrum for the exterior ($l = e$) and interior ($l = i$) branches is given by

$$E_l^2 = (\hbar v_F k)^2 + \Delta_s^2 + \Delta_l^2 + \mu^2 \pm 2\sqrt{\Delta_s^2 \Delta_l^2 + \mu^2[(\hbar v_F k)^2 + \Delta_l^2]}, \quad (6.6)$$

where $\Delta_{e/i} = \Delta_{n/z}$. We note the equivalence of effects of a uniform field on the interior branches and of a periodic field on the exterior branches. The spectrum is fully gapped except for two special cases, $\Delta_{n/z}^2 = \Delta_s^2 + \mu^2$. This suggests that there will be transitions between different non-trivial phases.

We identify these phases by the presence or absence of bound states inside the gap. For this it is most convenient to study the Wronskian corresponding to the four decaying fundamental solutions [25]. Here, we consider a semi-infinite nanowire, with boundary at $x = 0$, and assume that all decay lengths will be shorter than the system length. For fixed parameters (including the energy E), we find the four decaying eigenstates of $\mathcal{H}_{4k_{so}}$ for the left and right movers. Using Eq. (6.3), we express them in the basis of the original fermionic fields ψ , leading to four four-spinor solutions Φ^j with $j = 1, \dots, 4$, and construct a 4×4 Wronskian matrix $W_{ij}(x) = [\Phi^j(x)]_i$. The dimension d of the null space of $W(0)$ determines the system phase: $d = 0$ corresponds to a phase with no bound states (trivial phase), $d = 1$ at $E = 0$ to a phase with one single Majorana fermion (MF) (topological phase), $d = 2$ at $E = 0$ or $d = 1$ at $E \neq 0$ to a phase with one localized fermion of fractional charge (FF, see below) (fermion phase). We refer to the trivial and fermion phases as non-topological. Finally, the knowledge of the $W(0)$ null space allows us to construct the bound state wave functions, expressed in terms of linearly dependent combinations of Φ^j fulfilling the Dirichlet boundary condition at $x = 0$. In the Appendix 6.A we list the analytical solutions for the MF bound states, from which we see explicitly that these solutions are robust against any parameter variations (topologically stable) as long as the topological gap remains open.

For case I, we find that the system is in the topological phase if one of the following inequalities is satisfied,

$$(IA) \quad \Re\sqrt{\Delta_n^2 - \mu^2} < \Delta_s < \Re\sqrt{\Delta_z^2 - \mu^2} \quad (6.7)$$

$$(IB) \quad \Re\sqrt{\Delta_z^2 - \mu^2} < \Delta_s < \Re\sqrt{\Delta_n^2 - \mu^2}, \quad (6.8)$$

with the corresponding MF wave functions given in the Appendix 6.A. Case IA goes into IB upon interchange $\Delta_z \leftrightarrow \Delta_n$. As anticipated after Eq. (6.6), the boundaries of the topological phase correspond to the system being gapless. In the absence of \mathbf{B}_n , there is only one topological gap, which arises from the interior branches [7, 8]. In this case, only condition IA can be satisfied, and a MF emerges when the uniform B -field exceeds a critical value. However, in the presence of \mathbf{B}_n , the exterior gap is also topological. As shown in Fig. 6.3, the interplay between the two gaps leads to a rich phase diagram with reentrance behaviour. For instance, if $|\Delta_l| > |\mu|$ and $\Delta_s = 0$, the system is in the non-topological phase but still fully gapped by the magnetic fields. With increasing Δ_s , first the exterior (interior) gap closes and reopens, bringing the system into the topological phase. Then, upon further increase of Δ_s , the interior (exterior) gap closes and reopens, bringing the system back into the non-topological phase.

We note that case IB allows the presence of a MF in weaker uniform magnetic fields, see Fig. 6.3. If the nanomagnets generating \mathbf{B}_n can be arranged such that the field penetration into the bulk-superconductor is minimized, as illustrated in Fig. 6.1, much stronger oscillating than uniform fields can be applied, opening up the possibility to generate MFs in systems with small g -factors.

The system is in the fermion phase, if

$$\theta = \pi + \phi_n + \phi_z, \text{ and} \\ \Delta_s < \min\{\Re\sqrt{\Delta_z^2 - \mu^2}, \Re\sqrt{\Delta_n^2 - \mu^2}\}, \quad (6.9)$$

where the phases $\phi_{z,n}$ are defined by $e^{i\phi_{z,n}} = (\sqrt{\Delta_{z,n}^2 - \mu^2} + i\mu) / \Delta_{z,n}$. The corresponding wave functions are listed in the Appendix 6.A. In this regime, two MFs (both localized at $x = 0$) fuse to one fermion bound state. Such bound state fermions are known to have fractional charge $e/2$ [26, 27, 28, 29], as first discovered in the Jackiw-Rebbi model [23, 30]. We note that such FFs appear also in the Su-Schrieffer-Heeger model [26], where they arise as a purely orbital effect due to site-dependent hoppings. In contrast, the FFs found here are a spin effect and arise from Zeeman interactions with non-uniform magnetic fields. If neither of the inequalities (6.7)-(6.9) is satisfied, the system is in the trivial phase without any bound state at zero energy.

Detuning from the conditions in Eq. (6.9), the two zero-energy solutions are usually split, becoming a fermion-antifermion pair at energies $\pm E$. Importantly, FFs do not require the presence of superconductivity. For example, if $\Delta_s = 0$ and $\mu = 0$, the two bound states have energy

$$E_{FF} = \pm \frac{\Delta_z \Delta_n \sin \theta}{\sqrt{\Delta_z^2 + \Delta_n^2 - 2\Delta_z \Delta_n \cos \theta}}. \quad (6.10)$$

We note that the splitting vanishes at $\theta = n\pi$, n integer, due to the chiral symmetry of $\mathcal{H}_{4k_{so}}$ at these special values [30]. In contrast, the MF remains at zero energy for all values of θ , which is a direct manifestation of the stability of the bound state within the topological phase (despite the fact that the MF wave function depends on θ , see Appendix 6.A).

To determine the full phase diagram we have performed a systematic numerical search for all bound state solutions with energies inside the gap and determined the null space of the Wronskian. The results are plotted in Fig. 6.3. The bright yellow lines inside the colored area in Fig. 6.3 correspond to zero-energy FFs satisfying Eq. (6.9). At the point where the lines touch the topological phase (shown in green), the gap closes and reopens and *the zero-energy FF transmutes into a MF*. In the fermion phase away from the zero-energy line the two solutions split (the bigger the splitting the darker the color), until they finally reach the gap (black boundaries) and disappear. The fermion phase exists only for certain values of the phase shift θ , in contrast to the topological phase, which, again, is not sensitive to θ , see Fig. 6.3c. Moreover, the fermion phase is also sensitive to the relative orientation of \mathbf{B} and \mathbf{B}_n , see Fig. 6.3d. In the same panel, we see that outwards regions are more suitable for a fractional charge observation than the central region, where energies of the bound states are very close to the gap edge.

The FF could be detected by comparing the local charge density at, say, the left end of the nanowire for two different phases, where one phase supports FFs while the other one does not. This difference should then reveal the fractional charge $e/2$ of the left FF.

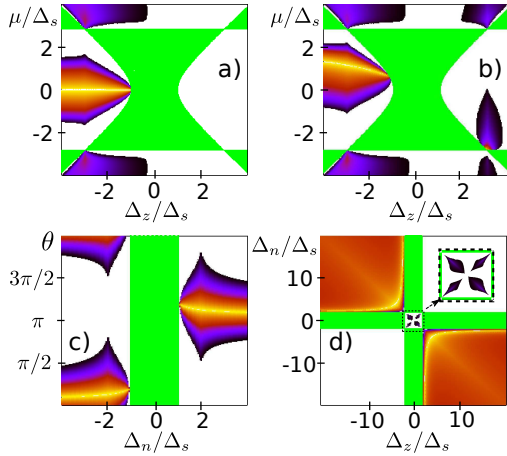


Figure 6.3: Phase diagram for case I supporting three phases: the trivial phase with no bound states (white area), the topological phase with one MF (green area), and the fermion phase with two FFs (colored area). The color in the fermion phase encodes the ratio of the fermion energy to the system gap, which varies from zero (bright yellow) to one (black). Note that the central region of the topological phase corresponds to case IA, while the four corner regions to case IB. Here, (a) $\Delta_n/\Delta_s = 3$, $\theta = 0$, while (b) $\Delta_n/\Delta_s = 3$, $\theta = \pi/4$. Note that $\Delta_z < 0$ and θ corresponds to $\Delta_z > 0$ and $\theta + \pi$. By comparing (a) with (b) and by calculating the dependence on θ [(c) $\mu/\Delta_s = 0.4$, $\Delta_z/\Delta_s = 2$], we note that the topological phase is insensitive to θ in contrast to the fermion phase. The position of a zero-energy FF depends not only on θ and μ [see (a)-(c)] but also on Δ_z and Δ_n [(d) $\mu/\Delta_s = 1.5$, $\theta = \pi/4$] in agreement with Eq. (6.9).

In particular, in the absence of superconductivity, one can compare the phase with $\theta = 0$ (FF present) to the one with $\theta = \pi/2$ (no FF). In the presence of superconductivity, the local charges of the system in the fermion phase (FF present) and in the trivial phase (no bound states) can be compared. E.g., changing the sign of the uniform field transfers the system between the two phases (see Fig. 3a).

6.4 Case II - period $2k_{so}$

6.4.1 Case IIa - $\mathbf{B}_n \perp \boldsymbol{\alpha}$

We now shortly comment on two additional geometries with a spatially varying magnetic field with a period $2k_{so}$. To keep the following discussion concise, we set $\mu = 0$ and state the results for $E = 0$ bound states only. We begin with a field perpendicular to the SOI vector $\boldsymbol{\alpha}$ and given by $\mathbf{B}_{n,x} = \hat{x}B_n \cos(2k_{so}x)$ or $\mathbf{B}_{n,y} = \hat{y}B_n \sin(2k_{so}x)$ (an oscillating field) or $(\mathbf{B}_{n,x} + \mathbf{B}_{n,y})/2$ (a helical field). Such a field mixes the exterior and interior branches, see Fig. 6.2. The corresponding Hamiltonian is $\mathcal{H}_{2k_{so}}^\perp = \mathcal{H} + \Delta_n \eta_3 \sigma_1 \tau_1$. The

spectrum is given by

$$E_{\perp}^2 = (\hbar v_F k)^2 + [\Delta_n^2 + \Delta_z^2/4] + (\Delta_s \pm \Delta_z/2)^2 \pm 2\sqrt{(\hbar v_F k)^2 \Delta_n^2 + [\Delta_n^2 + \Delta_z^2/4](\Delta_s \pm \Delta_z/2)^2}. \quad (6.11)$$

Repeating the procedure used above, we derive the condition for the topological phase as

$$\Delta_z > \Delta_s |1 - \Delta_n^2/\Delta_s^2|. \quad (6.12)$$

Again, the phase boundary to the topological phase corresponds to the parameters at which the system is gapless, i.e. $\Delta_z = \Delta_s |1 - \Delta_n^2/\Delta_s^2|$. We note that in the presence of a spatially periodic magnetic field MFs may emerge at substantially weaker uniform magnetic fields. The fermion phase occurs if

$$|\Delta_n| > \Delta_s \text{ and } \Delta_z < \Delta_s (\Delta_n^2/\Delta_s^2 - 1). \quad (6.13)$$

The rest of the parameter space corresponds to the non-topological phase. The corresponding wave functions for MFs and FFs are given in the Appendix 6.A.

6.4.2 Case IIb - $\mathbf{B}_n \parallel \boldsymbol{\alpha}$

Finally, we comment on an oscillating field aligned with the SOI vector $\boldsymbol{\alpha}$ and given by $\mathbf{B}_n = \hat{z}B_n \cos(2k_{so}x + \theta)$. This field couples the interior and exterior branches (see Fig. 6.2). The corresponding Hamiltonian is $\mathcal{H}_{2k_{so}}^{\parallel} = \mathcal{H} + \Delta_n(\eta_3\sigma_3\tau_1 \cos\theta - \tau_2 \sin\theta)$, with the spectrum given by

$$E_{\parallel}^2 = (\hbar v_F k)^2 + \left[\sqrt{\Delta_n^2 + \frac{\Delta_z^2}{4}} \pm \left(\frac{\Delta_z}{2} \pm \Delta_s \right) \right]^2. \quad (6.14)$$

The topological phase is determined, again, by Eq. (6.12) and the corresponding MF wave functions are given in the Appendix 6.A. We note once more that MFs can be observed in weaker uniform magnetic fields. Interestingly, in this configuration the fermion phase is absent, demonstrating the sensitivity of the FFs to the B -field orientation.

6.5 Electron-electron interactions

Electron interactions play an important role in one-dimensional systems [31] and, in particular, for MFs [21, 32]. E.g., the interior gap opened by a uniform magnetic field is strongly enhanced by interactions [20]; and so we expect the same renormalization to occur here for both gaps. This is indeed the case, as we show next. For this, we perform a renormalization group analysis for both the uniform and the periodic field. Following

Ref. [24] we arrive at the effective Hamiltonian $H = \sum_l \int \frac{dx}{2\pi} H_l(x)$ in terms of conjugate boson fields, $\phi_{e,i}$ and $\theta_{e,i}$, with

$$H_l = v[(\nabla\phi_l)^2 + (\nabla\theta_l)^2] + \frac{\Delta_l}{a} \cos(2\sqrt{K}\phi_l), \quad (6.15)$$

where we have suppressed quadratic off-diagonal terms being less relevant compared to the cosine terms. The index $l = e/i$ denotes the exterior/interior branch, a the lattice constant, $K^2 = (v_s/K_s + v_c K_c)/(v_c/K_c + v_s K_s)$ and $v = \sqrt{(v_c/K_c + v_s K_s)(v_s/K_s + v_c K_c)}/2$. Here, $v_{c,s}$ are the charge (c) and spin (s) velocities and $K_{c,s}$ the corresponding Luttinger liquid parameters [31]. The gaps Δ_l opened by magnetic fields are renormalized upwards by interactions and given by $\tilde{\Delta}_l = \Delta_l(\pi\hbar v_F/\Delta_l a)^{(1-K)/(2-K)}$. For GaAs (InAs) nanowires [24, 21], we estimate an increase by about a factor of 2 (4). The enhanced Zeeman gaps allows the use, again, of materials with lower g -factors.

6.6 Conclusions

The interplay between spatially varying magnetic fields and Rashba SOI in a hybrid nanowire system leads to a rich phase diagram with reentrance behavior and with fractionally charged fermions that get transmuted into Majorana fermions at the reopening of the topological gap.

We acknowledge useful discussions with Claudio Chamon. This work is supported by the Swiss NSF, NCCR Nanoscience, and NCCR QSIT.

6.A MF and FF wavefunctions for different regimes

Here we present the analytical solutions of the Majorana fermion (MF) and fractional fermion (FF) wave functions for different regimes discussed in the main text. Every MF wave function has the four-spinor form $\Phi_{MF}(x) = (f(x), g(x), f^*(x), g^*(x))$ with normalization condition $\int dx |\Phi_{MF}(x)|^2 = 2$ (below we omit the normalization factors). For zero energy $E = 0$, the functions $f(x)$ and $g(x)$ are listed in Table 6.1, together with the regime of validity corresponding to the cases I and II defined in the main text.

We use the notations $e^{i\phi_z} = (\sqrt{\Delta_z^2 - \mu^2} + i\mu)/\Delta_z$, $e^{i\phi_n} = (\sqrt{\Delta_n^2 - \mu^2} + i\mu)/\Delta_n$, and $\phi_{\pm} = (\theta \pm \phi_n - \phi_z)/2$. In row IIa-FF of Table 6.1, only one MF wave function is given, a second one needs to be added from row IIa-MF, depending on whether $(\Delta_s - \Delta_z/2)^2 > \Delta_n^2$ or $(\Delta_s - \Delta_z/2)^2 < \Delta_n^2$.

If $\Delta_s = 0$ and $\mu = 0$, there is one fractional fermion (at one end of the wire) with energy

$$E_{FF} = \Delta_z \Delta_n \sin \theta / \sqrt{\Delta_z^2 + \Delta_n^2 - 2\Delta_z \Delta_n \cos \theta}, \quad (6.16)$$

and the corresponding wave function is given by

$$\Phi_F = \begin{pmatrix} \Phi_{\uparrow} \\ \Phi_{\downarrow} \end{pmatrix} = \begin{pmatrix} e^{i\phi^F} \\ 1 \end{pmatrix} \left(e^{2ik_{so}x - x/\xi_2^F} - e^{-x/\xi_1^F} \right), \quad (6.17)$$

where $\cos \phi^F = E_{FF}/\Delta_z$, $\xi_1^F = \alpha/\sqrt{\Delta_z^2 - E_{FF}^2}$, and $\xi_2^F = \alpha/\sqrt{\Delta_n^2 - E_{FF}^2}$. We note that this fermion has an anti-fermion partner of opposite energy in the Nambu representation.

Table 6.1: Wave functions of MFs and FFs for different regimes at zero energy.

	$\sqrt{\Delta_n^2 - \mu^2} < \Delta_s < \sqrt{\Delta_z^2 - \mu^2}, \Delta_{z,n} > \mu $ $f = ig^* = ie^{-x/\xi_1^{(e)} + i(2k_{so}x + \phi_+ + \phi_z/2)} \cos \phi_- + e^{-x/\xi_3^{(e)} + i(2k_{so}x + \phi_- + \phi_z/2)} \sin \phi_+ - ie^{-x/\xi_2^{(i)} + i\phi_z/2} \cos \phi_n$ $\xi_1^{(e)} = \alpha/(\Delta_s - \sqrt{\Delta_n^2 - \mu^2}), \xi_3^{(e)} = \alpha/(\Delta_s + \sqrt{\Delta_n^2 - \mu^2}), \xi_2^{(i)} = \alpha/(\sqrt{\Delta_z^2 - \mu^2} - \Delta_s)$
(IA)	$0 < \Delta_s < \sqrt{\Delta_z^2 - \mu^2}, \Delta_n = \mu , \Delta_z > \mu $ $f = e^{-\Delta_s x/\alpha + i2k_{so}x} (-ie^{i\phi_z/2} + (2x\mu/\alpha)e^{-i(\theta/2 + \pi/4)} \sin[(\theta - \phi_z)/2 + \pi/4]) + ie^{-x/\xi_2^{(i)} + i\phi_z/2}$ $g = e^{-\Delta_s x/\alpha - i2k_{so}x} (-e^{-i\phi_z/2} + (2x\mu/\alpha)e^{i(\theta/2 + 3\pi/4)} \sin[(\theta - \phi_z)/2 + \pi/4]) + e^{-x/\xi_2^{(i)} - i\phi_z/2}$
MF	$0 < \Delta_s < \sqrt{\Delta_z^2 - \mu^2}, \Delta_n < \mu , \Delta_z > \mu ; k_m = \sqrt{\mu^2 - \Delta_n^2}/\alpha$ $f = ig^* = ie^{-x/\xi_2^{(i)} + i\phi_z/2} - ie^{-\Delta_s x/\alpha + i(2k_{so}x + \phi_z/2)} (\cos(k_m x) + \sin(k_m x) [i\mu + \Delta_n e^{i(\theta - \phi_z)}]) / \sqrt{\mu^2 - \Delta_n^2}$
(IB)	$\sqrt{\Delta_z^2 - \mu^2} < \Delta_s < \sqrt{\Delta_n^2 - \mu^2}, \Delta_{z,n} > \mu $ $f = -ig^* = -ie^{-x/\xi_1^{(i)} - i\phi_z/2} \cos \phi_- + e^{-x/\xi_3^{(i)} + i\phi_z/2} \sin[(\theta - \phi_n + \phi_z)/2] + ie^{-x/\xi_2^{(e)} + i(2k_{so}x + \phi_- + \phi_z/2)} \cos \phi_z$ $\xi_1^{(i)} = \alpha/(\Delta_s - \sqrt{\Delta_z^2 - \mu^2}), \xi_3^{(i)} = \alpha/(\Delta_s + \sqrt{\Delta_z^2 - \mu^2}), \xi_2^{(e)} = \alpha/(\sqrt{\Delta_n^2 - \mu^2} - \Delta_s)$
MF	$\Delta_s < \sqrt{\Delta_n^2 - \mu^2}, \Delta_z = \mu , \Delta_n > \mu $ $f = e^{-\Delta_s x/\alpha} (ie^{i(\theta - \phi_n)/2} - (2x\mu/\alpha)e^{i\pi/4} \sin[(\phi_n - \theta)/2 - \pi/4]) - ie^{-x/\xi_2^{(e)} + i(4k_{so}x + \theta - \phi_n)/2}$ $g = e^{-\Delta_s x/\alpha} (-e^{-i(\theta - \phi_n)/2} + (2x\mu/\alpha)e^{i\pi/4} \sin[(\phi_n - \theta)/2 - \pi/4]) + e^{-x/\xi_2^{(e)} + i(4k_{so}x - \theta + \phi_n)/2}$
	$\Delta_s < \sqrt{\Delta_n^2 - \mu^2}, \Delta_z < \mu , \Delta_n > \mu ; k_m = \sqrt{\mu^2 - \Delta_z^2}/\alpha$ $f = -ig^* = e^{i(\theta - \phi_n)/2} [ie^{-x/\xi_2^{(e)} + i2k_{so}x} - ie^{-\Delta_s x/\alpha} (\cos(k_m x) + \sin(k_m x) [\Delta_z e^{i(\phi_n - \theta)} - i\mu]) / \sqrt{\mu^2 - \Delta_z^2}]$
(I)	$\theta = \pi + \phi_n + \phi_z, 0 \leq \Delta_s < \min\{\Re\sqrt{\Delta_z^2 - \mu^2}, \Re\sqrt{\Delta_n^2 - \mu^2}\}, E_{FF} = 0$
FF	$f_1 = ig_1^* = ie^{i\phi/2} (e^{2ik_{so}x - x/\xi_3^{(e)}} - e^{-x/\xi_2^{(i)}}), f_2 = -ig_2^* = e^{i\phi/2} (e^{2ik_{so}x - x/\xi_2^{(e)}} - e^{-x/\xi_3^{(i)}})$
(IIa)	$\Delta_z > \Delta_s 1 - \Delta_n^2/\Delta_s^2 \text{ and } (\Delta_s - \Delta_z/2)^2 > \Delta_n^2; \xi_\pm = \alpha/(\Delta_z/2 \pm \sqrt{(\Delta_s - \Delta_z/2)^2 - \Delta_n^2})$ $f = ig^* = ie^{2ik_{so}x} (e^{-x/\xi_- - \Delta_n} + e^{-x/\xi_+} A) - ie^{-x/\xi_+} \Delta_n - ie^{-x/\xi_-} A, A = \alpha/\xi_- - \Delta_s$
MF	$\Delta_z > \Delta_s 1 - \Delta_n^2/\Delta_s^2 \text{ and } (\Delta_s - \Delta_z/2)^2 \leq \Delta_n^2; \cos \phi = (\Delta_z/2 - \Delta_s)/\Delta_n, k_m = \sqrt{\Delta_n^2 - (\Delta_s - \Delta_z/2)^2}/\alpha$ $f = ig^* = [ie^{2ik_{so}x} \cos(k_m x + \phi/2) - i \cos(k_m x - \phi/2)] e^{-\Delta_z x/2\alpha}$
(IIa)	$ \Delta_n > \Delta_s, \Delta_z < \Delta_s (\Delta_n^2/\Delta_s^2 - 1), \text{ and } (\Delta_s + \Delta_z/2)^2 > \Delta_n^2; \tilde{\xi}_\pm = \alpha/(\Delta_z/2 \pm \sqrt{(\Delta_s + \Delta_z/2)^2 - \Delta_n^2})$ $f = -ig^* = e^{2ik_{so}x} (e^{-x/\tilde{\xi}_- - \Delta_n} + e^{-x/\tilde{\xi}_+} B) - ie^{-x/\tilde{\xi}_+} \Delta_n - ie^{-x/\tilde{\xi}_-} B, B = \alpha/\tilde{\xi}_- + \Delta_s$
FF	$ \Delta_n > \Delta_s, \Delta_z < \Delta_s (\Delta_n^2/\Delta_s^2 - 1), \text{ and } (\Delta_s + \Delta_z/2)^2 \leq \Delta_n^2; \cos \phi = (\Delta_z/2 + \Delta_s)/\Delta_n, k_m = \sqrt{\Delta_n^2 - (\Delta_s + \Delta_z/2)^2}$ $f = -ig^* = [\cos(k_m x - \phi/2) - ie^{i2k_{so}x} \cos(k_m x + \phi/2)] e^{-\Delta_z x/2\alpha - i\phi/2}$
(IIb)	$\Delta_z > \Delta_s \Delta_n^2/\Delta_s^2 - 1 $ $f = \Delta_n [e^{-x/\xi_2} \cos \theta - ie^{-x/\xi_4} \sin \theta - e^{-x/\xi_3 + i(2k_{so}x - \theta)}]$ $+ i[\Delta_z/2 + \sqrt{\Delta_n^2 + \Delta_z^2/4}] (e^{i(2k_{so}x - \theta)} (e^{-x/\xi_2} \cos \theta + ie^{-x/\xi_4} \sin \theta) - e^{-x/\xi_3})$ $g = -i\Delta_n [e^{-x/\xi_2} \cos \theta + ie^{-x/\xi_4} \sin \theta - e^{-x/\xi_3 - i(2k_{so}x - \theta)}]$ $+ [\Delta_z/2 + \sqrt{\Delta_n^2 + \Delta_z^2/4}] (e^{-i(2k_{so}x - \theta)} (e^{-x/\xi_2} \cos \theta - ie^{-x/\xi_4} \sin \theta) - e^{-x/\xi_3})$ $\xi_2 = \alpha/(\Delta_z/2 + \Delta_s - \sqrt{\Delta_n^2 + \Delta_z^2/4}), \xi_3 = \alpha/(\Delta_z/2 - \Delta_s + \sqrt{\Delta_n^2 + \Delta_z^2/4}), \xi_4 = \alpha/(\Delta_s + \sqrt{\Delta_n^2 + \Delta_z^2/4} - \Delta_z/2)$

Bibliography

- [1] E. Majorana, Nuovo Cimento **14**, 171 (1937).
- [2] J. Alicea, Rep. Prog. Phys. **75**, 076501 (2012).
- [3] A. Y. Kitaev, Physics-Uspekhi **44**, 131 (2001).
- [4] L. Fu and C. L. Kane, Phys. Rev. Lett. **100**, 096407 (2008).
- [5] Y. Tanaka, T. Yokoyama, and N. Nagaosa, Phys. Rev. Lett. **103**, 107002 (2009).
- [6] M. Sato and S. Fujimoto, Phys. Rev. B **79**, 094504 (2009).
- [7] R. M. Lutchyn, J. D. Sau, and S. Das Sarma, Phys. Rev. Lett. **105**, 077001 (2010).
- [8] Y. Oreg, G. Refael, and F. von Oppen, Phys. Rev. Lett. **105**, 177002 (2010).
- [9] J. Alicea, Phys. Rev. B **81**, 125318 (2010).
- [10] A. R. Akhmerov, J. Nilsson, and C. W. J. Beenakker, Phys. Rev. Lett. **102**, 216404 (2009).
- [11] X. L. Qi and S. C. Zhang, Rev. Mod. Phys. **83**, 1057 (2011).
- [12] A. C. Potter and P. A. Lee, Phys. Rev. B **83**, 094525 (2011).
- [13] J. Alicea, Y. Oreg, G. Refael, F. von Oppen, and M. P. A. Fisher, Nat. Phys. **7**, 412 (2011).
- [14] P. W. Brouwer, M. Duckheim, A. Romito, F. von Oppen, Phys. Rev. B **84**, 144526 (2011).
- [15] J. Klinovaja, S. Gangadharaiah, and D. Loss, Phys. Rev. Lett. **108**, 196804 (2012).
- [16] D. Chevallier, D. Sticlet, P. Simon, and C. Bena, Phys. Rev. B **85**, 235307 (2012).
- [17] V. Mourik, K. Zuo, S. M. Frolov, S. R. Plissard, E. P. A. M. Bakkers, L. P. Kouwenhoven, Science, **336**, 1003 (2012).
- [18] M. T. Deng, C. L. Yu, G. Y. Huang, M. Larsson, P. Caroff, and H. Q. Xu, arXiv:1204.4130 (2012).
- [19] A. Das, Y. Ronen, Y. Most, Y. Oreg, M. Heiblum, H. Shtrikman, arXiv:1205.7073 (2012).
- [20] B. Braunecker, G. I. Japaridze, J. Klinovaja, and D. Loss, Phys. Rev. B **82**, 045127 (2010).

- [21] S. Gangadharaiah, B. Braunecker, P. Simon, and D. Loss, Phys. Rev. Lett. **107**, 036801 (2011).
- [22] M. Kjaergaard, K. Wolms, and K. Flensberg, Phys. Rev. B **85**, 020503(R) (2012).
- [23] R. Jackiw and C. Rebbi, Phys. Rev. D **13**, 3398 (1976).
- [24] B. Braunecker, P. Simon, and D. Loss, Phys. Rev. B **80**, 165119 (2009).
- [25] J. Klinovaja and D. Loss, Phys. Rev. B **86**, 085408 (2012).
- [26] W. P. Su, J. R. Schrieffer, and A. J. Heeger, Phys. Rev. Lett. **42**, 1698 (1979).
- [27] S. Kivelson and J. R. Schrieffer, Phys. Rev. B **25**, 6447, (1982).
- [28] R. Rajaraman and J. S. Bell, Phys. Lett. **116B**, 151 (1982).
- [29] L. Santos, Y. Nishida, C. Chamon, and C. Mudry, Phys. Rev. B **83**, 104522 (2011).
- [30] S. Gangadharaiah, L. Trifunovic, and D. Loss, Phys. Rev. Lett. **108**, 136803 (2012).
- [31] T. Giamarchi, *Quantum Physics in One Dimension*, (Clarendon Press, Oxford, 2004).
- [32] E. M. Stoudenmire, J. Alicea, O. Starykh, and M. P. A. Fisher, Phys. Rev. B **84**, 014503 (2011).

Chapter 6

Chapter 7

Helical States in Curved Bilayer Graphene

We study spin effects of quantum wires formed in bilayer graphene by electrostatic confinement. With a proper choice of the confinement direction, we show that in the presence of magnetic field, spin-orbit interaction induced by curvature, and intervalley scattering, bound states emerge that are helical. The localization length of these helical states can be modulated by the gate voltage which enables the control of the tunnel coupling between two parallel wires. Allowing for proximity effect via an *s*-wave superconductor, we show that the helical modes give rise to Majorana fermions in bilayer graphene.

This chapter has been published as Phys. Rev. B **86**, 235416 (2012) (2012).

7.1 Introduction

Graphene and its derivatives [1, 2, 3, 4], such as bilayer graphene (BLG) and carbon nanotubes (CNT), have attracted wide interest due to its peculiar bandstructure with low energy excitations described by Dirac-like Hamiltonians. Moreover, these materials are usually placed on substrates, which allows high control of its geometry, doping, and placement of metallic gates [5, 6, 7, 8, 9]. Topological insulators were predicted for graphene [10], but later it was found that the intrinsic spin-orbit interaction (SOI) is too weak [11, 12]. For BLG, first-principle calculations also show weak SOI [13, 14]. In an other proposal, topologically confined bound states were predicted to occur in BLG where a gap and band inversion is enforced by gates [15]. Quite remarkably, these states are localized in the region where the voltage changes sign, are independent of the edges of the sample, and propagate along the direction of the gates, thus forming effectively a quantum wire [15, 16, 17]. At any fixed energy, the spectrum inside the gap is topologically equivalent to four Dirac cones, each cone consisting of a pair of states with opposite momenta.

The spin degrees of freedom in such BLG wires, however, have not been addressed yet. It is the goal of this work to include them and to show that they give rise to striking effects. In particular, we uncover a mechanism enabling *helical modes* propagating along the wires. In analogy to Rashba nanowires [18], topological insulators [19], and CNTs [20, 21], such modes provide the platform for a number of interesting effects such as spin-filtering and Majorana fermions [22]. Here, the SOI plays a critical role, and in order to substantially enhance it, we consider a BLG sheet with local curvature as shown in Fig. 7.1. Two pairs of top and bottom gates define the direction of the quantum wire which is chosen in such a way that it corresponds to a ‘semi-CNT’ of zigzag type. In this geometry, the energy levels of the mid-gap states cross in the center of the Brillouin zone. A magnetic field transverse to the wire in combination with intervalley scattering leads to an opening of a gap, $2\Delta_g$, between two Kramers partners at zero momentum, see Fig. 7.2. As a result, the number of Dirac cones changes from even (four) to odd (three), and the wire becomes helical with opposite spins being transported into opposite directions. In the following we derive the spectrum and its characteristics analytically and confirm these results by independent numerics. We also address the physics of Majorana fermions which emerge when the wire is in proximity contact to an *s*-wave superconductor.

7.2 Curved bilayer graphene with SOI

We consider a gated curved bilayer graphene with a magnetic field \mathbf{B} (along the x' -axis) applied perpendicular to the direction of the fold (along the z -axis), see Fig. 7.1. We begin with a description of the bilayer graphene in the framework of the tight-binding model [3, 4]. Each layer is a honeycomb lattice composed of two types of non-equivalent atoms A_1 (A_2) and B_1 (B_2) and defined by two lattice vectors \mathbf{a}_1 and \mathbf{a}_2 . We focus here

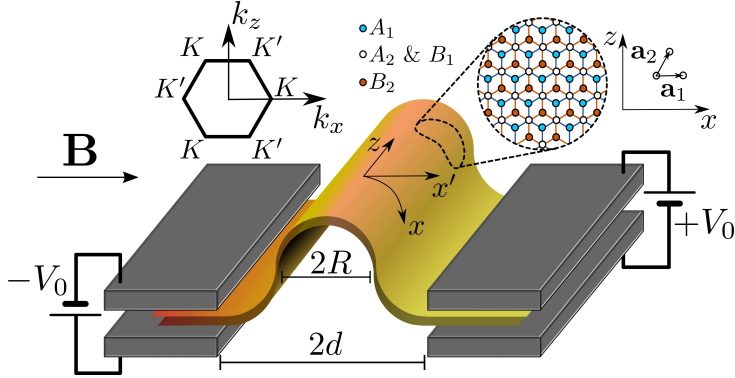


Figure 7.1: A bilayer graphene (BLG) sheet with a fold at $x = 0$ along the z -axis is placed between two pairs of gates that are set to opposite polarities $\pm V_0/2$, inducing the bulk gap. There are mid-gap bound states, localized in transverse x -direction around $x = 0$. At the same time, they freely propagate along the z -direction, forming an effective quantum wire [15]. An externally applied magnetic field $\mathbf{B} = B\mathbf{e}_{x'}$ breaks time-reversal symmetry. The spin-orbit interaction β is induced by the curvature of the wire, which is characterized by the radius R . In the insets we show the BLG structure in momentum (left) and real (right) space for a chosen chirality $\theta = 0$. The edges of the BLG sheet can be arbitrary.

on AB stacked bilayer, in which two layers are coupled only via atoms A_2 and B_1 (see Fig. 7.1) with a hopping matrix element t_\perp ($t_\perp \approx 0.34$ eV). By analogy with CNTs [3], we introduce a chiral angle θ as the angle between \mathbf{a}_1 and the x -axis.

The low-energy physics is determined by two valleys defined as

$$\mathbf{K} = -\mathbf{K}' = (4\pi/3a)(\cos \theta, \sin \theta),$$

where $a = |\mathbf{a}_1|$. The corresponding Hamiltonian in momentum space is written as

$$H_0 = \hbar v_F (k_x \sigma_1 + \tau_3 k_z \sigma_2) + \frac{t_\perp}{2} (\sigma_1 \eta_1 + \sigma_2 \eta_2) - V \eta_3, \quad (7.1)$$

where the Pauli matrices σ_i (η_i) act in the sublattice (layer) space, and the Pauli matrices τ_i act in the valley space. Here, $v_F = \sqrt{3}ta/2\hbar$ is the Fermi velocity ($v_F \approx 10^8$ cm/s), with $t \approx 2.7$ eV being the intralayer hopping matrix element. The k_x (k_z) is the transversal (longitudinal) momentum calculated from the points \mathbf{K} and \mathbf{K}' . The potential difference between the layers opens up a gap $2|V|$ in the bulk spectrum, while a spatial modulation, i.e. $V \rightarrow V(x)$, breaks the translation invariance along the x -direction, thus only the total longitudinal momentum $\mathbf{K}_z^{(\prime)} + k_z$ remains a good quantum number.

The Hamiltonian H_0 can be simplified for small voltages, $|V| \ll t_\perp$, by integrating out the A_2 and B_1 degrees of freedom, which correspond to much higher energies $E \approx t_\perp$. The effective Hamiltonian becomes

$$\tilde{H}_0 = -V \gamma_3 - \frac{\hbar^2 v_F^2}{t_\perp} (k_x^2 - k_z^2) \gamma_1 - \frac{2\hbar^2 v_F^2}{t_\perp} k_x k_z \tau_3 \gamma_2, \quad (7.2)$$

where the Pauli matrices γ_i act in the space of A_1 and B_2 atoms. If the voltage changes sign at $x = 0$ [for example, $V(x) = -V(-x)$], this results in the closing and reopening of the gap. As a consequence, bound states, localized around $x = 0$, emerge within the bulk gap [15]. The eigenstates of \tilde{H}_0 are characterized by k_z and the valley degree of freedom $\tau = \pm 1$. For a step-like kink potential $V(x) = (V_0/2) \operatorname{sgn}(x)$ the energy spectrum is shown in the inset of Fig. 7.2.

Now we include spin and aim at the realization of helical modes in BLG, which requires an analysis of the spin-full mid-gap states. At any fixed energy in the bulk gap, there are 2×4 states, where the factor 2 arises from spin-degeneracy. This means that the spectrum is topologically equivalent to four Dirac cones, each cone consisting of a pair of states with opposite momenta. On the other hand, helical modes are typical for systems with an odd number of Dirac cones. To effectively eliminate one Dirac cone at given chemical potential, the spin-degeneracy should be lifted by a magnetic field B , giving rise to a new gap. Obviously, the opening of such a gap is possible only if there is level crossing in the system. The spectrum of the mid-gap states has support around K and K' . Therefore, if these points, projected onto the k_z -axis, are separated from each other,

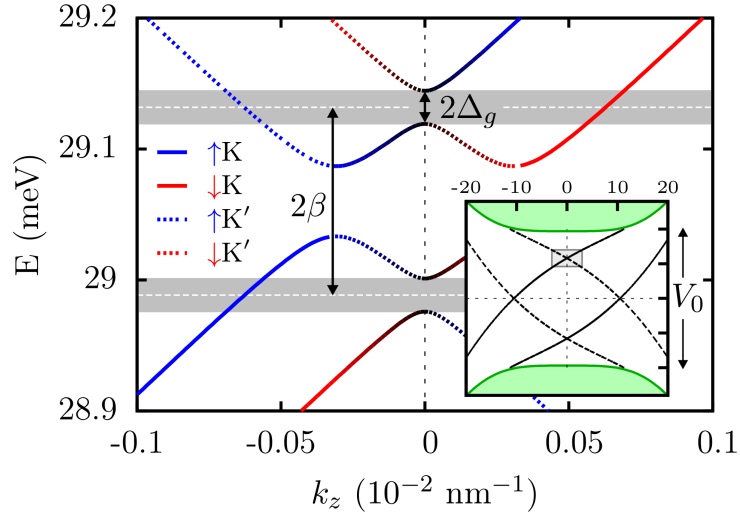


Figure 7.2: The spectrum of the BLG structure for $V_0/2 = 50$ meV and chirality $\theta = 0$. The green area in the inset corresponds to the bulk spectrum. The mid-gap bound states for valleys K (full line) and K' (dashed line) have opposite velocities. The main figure shows the details of K - K' crossing region (shaded region in the inset). The curvature induced SOI shifts spin-up and spin-down levels in opposite directions by the SOI parameter β . A magnetic field \mathbf{B} assisted by intervalley scattering $\Delta_{KK'}$ results in the anti-crossing gap $2\Delta_g$ of two Kramers partners at $k_z = 0$. If the chemical potential μ is tuned inside the gap [shaded area with $\mu \approx (V_0/2\sqrt{2}) \pm \beta$], the system is equivalent to three Dirac cones (only one is shown in the main Figure), resulting in the helical mode regime. Here, $\beta \approx 60$ μeV ($R = 5$ nm), $\Delta_{KK'} = 30$ μeV , and $\Delta_Z = 30$ μeV , so the opened gap is $2\Delta_g \approx 30$ $\mu\text{eV} \approx 300$ mK.

no crossing can occur. We thus see that the chiral angle θ is of a crucial importance for our purpose and the optimal choice is $\theta = 0$ (or very close to it). In this case, $\mathbf{K}_z = \mathbf{K}'_z = 0$, and the level crossing occurs in the center of the Brillouin zone, at $k_z = 0$, see inset of Fig. 7.2. We emphasize that in contrast to nanoribbons [16] the form of the edges of the BLG sheet does not matter provided the distance between edges and wire-axis is much larger than the localization length ξ of the bound state.

Next, we allow also for spin-orbit interaction in our model. While the intrinsic SOI is known to be weak for graphene [11, 12], the strength of SOI in CNT is enhanced by curvature [23, 24, 20, 25]. To take advantage of this enhancement, we consider a folded BLG which is analogous to a zigzag semi-CNT with $\theta = 0$. All SOI terms that can be generated in second-order perturbation theory are listed in Table I of Refs. [20, 25]. From these terms only $H_{so} = \beta\tau_3 s_z$ is relevant for our problem; first, it is the largest term by magnitude, and second, it is the only term which acts directly in the A_1 - B_2 space. Here, s_i is the Pauli matrix acting on the electron spin, and $i = x, y, z$. The value of the effective SOI strength β depends on the curvature, defined by the radius R , and is given by $\beta \approx 0.31 \text{ meV}/R[\text{nm}]$ [20].

In the presence of SOI, the states can still be characterized by the momentum k_z , valley index $\tau = \pm 1$, and spin projection $s = \pm 1$ on the z -axis. The spectrum of $\tilde{H}_0 + H_{so}$ can be obtained from the one of \tilde{H}_0 by simply shifting $E \rightarrow E - \beta\tau s$. This transformation goes through the calculation straightforwardly, and the spectrum in the presence of the SOI becomes

$$E = \beta\tau s \pm \left(\frac{\hbar v_F k_z \tau}{2\sqrt{t_\perp}} \pm \sqrt{\frac{(\hbar v_F k_z)^2}{4t_\perp} + \frac{V_0}{2\sqrt{2}}} \right)^2 \mp \frac{V_0}{\sqrt{2}}. \quad (7.3)$$

The spin degeneracy is lifted by the SOI, giving a splitting 2β . As shown in Fig. 7.2, the level crossings occur between two Kramers partners at $k_z = 0$: $|K, \uparrow\rangle$ crosses with $|K', \downarrow\rangle$, and $|K, \downarrow\rangle$ crosses with $|K', \uparrow\rangle$. The KK' -crossing can occur provided $|\theta| < \sqrt{3(1 + \sqrt{2})t_\perp V_0}/4\pi t$. For the values from Fig. 7.2, we estimate this bound to be about 1° . As mentioned before, to open a gap at $k_z = 0$, one needs first a magnetic field perpendicular to the SOI axis to mix the spin states, and second a K - K' scattering to mix the two valleys. Such valley scattering is described by the Hamiltonian $H_{sc} = \Delta_{KK'}^s \tau_1 + \Delta_{KK'}^a \tau_1 \gamma_3$, where $\Delta_{KK'}^s + \Delta_{KK'}^a$ ($\Delta_{KK'}^s - \Delta_{KK'}^a$) is the scattering parameter for the bottom (top) layer of the BLG. The Zeeman Hamiltonian for a magnetic field \mathbf{B} applied along the x' -direction is given by $H_Z = \Delta_Z s_x$, with $\Delta_Z = g^* \mu_B B / 2$, where μ_B the Bohr magneton. Here, g^* is an effective g -factor due to the curvature of the fold and the localization of the bound state. Since $s_{x'} = s_x \cos \varphi + s_y \sin \varphi$ depends on x via the azimuthal angle $\varphi(x)$ of the fold, we replace $s_{x'}$ by an average over the orbital part of the bound state wave function. This results in $2/\pi < g^*/g < 1$, the precise value being dependent on the localization length, where g is the bare g -factor of graphene.

Using second order perturbation theory for $\beta > \Delta_{KK'}^s, \Delta_Z$, we find that the gap

opened at $k_z = 0$ is given by

$$\Delta_g = \frac{\Delta_{KK'}^s \Delta_Z}{\beta}, \quad (7.4)$$

see Fig. 7.2, which also contains numerical estimates for realistic parameters. We note that Δ_g is enhanced by electron-electron interactions [26], however, we neglect this supportive effect herein. If the chemical potential is tuned inside the gap $2\Delta_g$ [$\mu \approx (V_0/2\sqrt{2}) \pm \beta$], there are three right- and three left-propagating modes. Four states at finite momentum (two left-moving and two right-moving states) are only slightly affected by the magnetic field and thus can still be considered to carry opposite spins, meaning that the total spin transfer is close to zero and these modes are not contributing to spin-filtering. In contrast to that, the two modes with $k_z \approx 0$ are *helical modes*: they have opposite velocities and opposite spins. Thus, similar to Rashba nanowires [18], the BLG quantum wire can be used as a spin filter device.

Moreover, if the BLG is brought into proximity to an *s*-wave superconductor, the states with opposite momenta and spins get paired. Working in the linearized model of left-right movers [27], we obtain the effective Bogoliubov-de Gennes Hamiltonian for each of the three pairs, $j = 1, 2, 3$, written in Nambu space,

$$H_s^j = \hbar v_j k_j \chi_3 + \Delta_s \omega_2 \chi_2, \quad (7.5)$$

where v_j is the velocity for the j th pair at the Fermi level and Δ_s is the strength of the proximity-induced superconductivity, and the Pauli matrices χ_i (ω_i) act in the left-right mover (electron-hole) space. We note that we are in the regime corresponding to strong SOI where we keep only the slowest decaying contributions of the wave functions [27]. To determine the potential existence of MFs in the system, one can study the topological class of H_s^j [28]. This Hamiltonian belongs to the topological class BDI. However, by analogy with multi-band nanowires [29], additional scattering between states would bring the system into the D class. An alternative way of classification, which determines explicitly the number of MF bound states, is to study the null-space of the Wronskian associated with the Schrödinger equation [30]. In our case, we find three MFs at each wire end in the topological phase defined by $\Delta_g^2 \geq \Delta_s^2 + \delta\mu^2$, where $\delta\mu$ is the chemical potential counted from the mid-gap level Δ_g . These MFs are generically hybridized into one MF and one non-zero energy fermion by perturbations such as electron-electron interactions and interband scattering.

7.3 Numerical calculation

Above we have studied the system analytically, assuming a step-like potential. In this section we compare our results with the numerical solution of the Schrödinger equation for the effective Hamiltonian $\tilde{H}_0 + H_{so} + H_{sc} + H_Z$, with a more realistic (smooth) potential, $V(x) = (V_0/2) \tanh(x/d)$, where d is the distance between the gates. The spin-orbit interaction $\beta(x)$ is finite only within the curved region of the BLG sheet. Along the

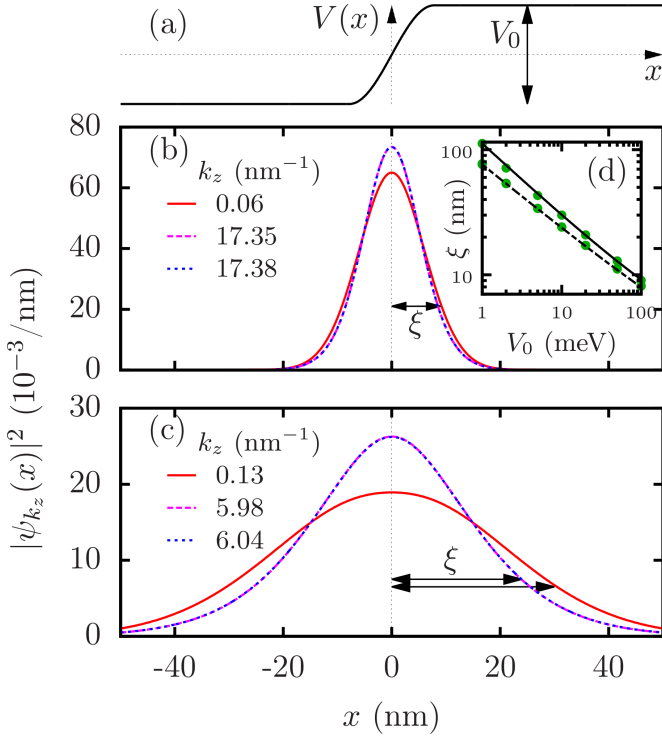


Figure 7.3: (a) The profile of the gate potential $V(x)$ along the curved BLG. The reversed polarity at the two ends gives rise to mid-gap states, localized in x -direction. The density profile of three right-moving states, whose energy E is inside the gap Δ_g , allows us to estimate the localization lengths ξ : (b) $V_0 = 100$ meV, $E = 29.13$ meV, $d = R$ (dashed white line in Fig. 7.2), $\xi \approx 9$ and 8 nm, and (c) $V_0 = 10$ meV, $E = 3.49$ meV, $d = R$, $\xi \approx 30$ and 24 nm. We note that states with larger momenta have shorter localization lengths. (d) The localization length follows approximately $\tilde{\xi} = \xi - \xi_0 \propto 1/\sqrt{V_0}$. The circles are extracted from our numerical calculations, $\xi = \langle x^2 \rangle$, for energies in the middle of the gap Δ_g , equivalent to the white dashed line in Fig. 7.2. The lines are fits, $\tilde{\xi} \propto 1/V_0^p$, for the states at large k_z ($p = 0.59$), shown as dashed lines, and for the states near $k_z = 0$ ($p = 0.52$), shown as full lines.

z -direction, the system is translationally invariant, so the envelope function is given by $\Psi(x, z) = e^{ik_z z} \psi_{k_z}(x)$. The profile of $\psi_{k_z}(x)$ is presented in Fig. 7.3. The localization length follows a power law $\xi - \xi_0 \propto 1/V_0^p$, with $p \approx 1/2$, and the shift $\xi_0 < d$ is due to the finite distance between gates. In the limit $d \rightarrow 0$, where the analytical solution is applicable, the localization length is essentially given by $\xi = 2^{5/4} \hbar v_F / \sqrt{V_0 t_\perp}$ [15], since corrections due to SOI are of negligible higher order in β .

Tunnel junction. The dependence of ξ on the potential V_0 can be exploited to couple parallel wires. For instance, consider two similar quantum wires, running parallel to each

other at a distance D . If $\xi \ll D$ for each wire, then they are completely decoupled. However, lowering the potential in both wires *locally* around a point z_0 on the z -axis, such that $\xi_0 \approx D$, we can enforce wavefunction overlap, leading to a transverse tunnel junction between the two wires at z_0 . In this way, an entire network of helical wires can be envisaged. We mention that such networks could provide a platform for implementing braiding schemes for MFs [31].

7.4 Conclusions

The confinement of states in BLG into an effective quantum wire is achieved by pairs of gates with opposite polarities, leading to eight propagating modes [15]. If the direction of the wire is chosen such that the chiral angle vanishes, both valleys K and K' are projected onto zero momentum k_z . The SOI, substantially enhanced by curvature, defines a spin quantization axis and splits spin-up and spin-down states. A magnetic field assisted by intervalley scattering opens up a gap at the center of the Brillouin zone. If the chemical potential is tuned inside the gap, three right- and three left-propagating modes emerge, so that the system possesses helical modes, which are of potential use for spin-filtering. In the proximity to an s -wave superconductor, the BLG wire hosts Majorana fermions arising from the helical modes. By locally changing the confinement potential and thus the localization lengths, parallel wires can be tunnel coupled. This mechanism can be used to implement braiding of MFs in bilayer graphene.

This work is supported by the Swiss NSF, NCCR Nanoscience, and NCCR QSIT.

Bibliography

- [1] K. S. Novoselov, A. K. Geim, S. V. Morozov, D. Jiang, M. I. Katsnelson, I. V. Grigorieva, S. V. Dubonos, and A. A. Firsov, *Nature (London)* **438**, 197 (2005).
- [2] A. H. Castro Neto, F. Guinea, N. M. R. Peres, K. S. Novoselov, and A. K. Geim, *Rev. Mod. Phys.* **81**, 109 (2009).
- [3] R. Saito, G. Dresselhaus, and M. S. Dresselhaus, *Physical Properties of Carbon Nanotubes*, (Imperial College Press) 1998).
- [4] E. McCann, arXiv: 1205.4849.
- [5] A. K. Geim and K. S. Novoselov, *Nature Materials* **6**, 183 (2007).
- [6] R. T. Weitz, M. T. Allen, B. E. Feldman, J. Martin, and A. Yacoby, *Science* **330**, 812 (2010).
- [7] J. R. Williams, T. Low, M. S. Lundstrom, and C. M. Marcus, *Nature Nanotechnology* **6**, 222 (2011).
- [8] M. T. Allen, J. Martin, and A. Yacoby, *Nature Communications* **3**, 934 (2012).
- [9] A. S. M. Goossens, S. C. Driessens, T. A. Baart, K. Watanabe, T. Taniguchi, and L. M. Vandersypen, arXiv: 1205.5825.
- [10] C. L. Kane and E. J. Mele, *Phys. Rev. Lett.* **95**, 226801 (2005).
- [11] H. Min, J. E. Hill, N. A. Sinitzyn, B. R. Sahu, L. Kleinman, and A. H. MacDonald, *Phys. Rev. B* **74**, 165310 (2006).
- [12] M. Gmitra, S. Konschuh, C. Ertler, C. Ambrosch-Draxl, and J. Fabian, *Phys. Rev. B* **80**, 235431 (2009).
- [13] S. Konschuh, M. Gmitra, D. Kochan, and J. Fabian, *Phys. Rev. B* **85**, 115423 (2012).
- [14] F. Mireles and J. Schliemann, arXiv: 1203.1094.
- [15] I. Martin, Y. M. Blanter, and A. F. Morpurgo, *Phys. Rev. Lett.* **100**, 036804 (2008).
- [16] Z. Qiao, J. Jung, Q. Niu, and A. H. MacDonald, *Nano Letters* **11**, 3453 (2011).
- [17] M. Zarenia, J. M. Pereira, G. A. Farias, and F. M. Peeters, *Phys. Rev. B* **84**, 125451 (2011).
- [18] P. Středa and P. Šeba, *Phys. Rev. Lett.* **90**, 256601 (2003).
- [19] M. Z. Hasan and C. L. Kane, *Rev. Mod. Phys.* **82**, 3045 (2010).

- [20] J. Klinovaja, M. J. Schmidt, B. Braunecker, and D. Loss, Phys. Rev. Lett. **106**, 156809 (2011).
- [21] J. Klinovaja, S. Gangadharaiah, and D. Loss, Phys. Rev. Lett. **108**, 196804 (2012).
- [22] J. Alicea, Rep. Prog. Phys. **75**, 076501 (2012).
- [23] F. Kuemmeth, S. Ilani, D. C. Ralph, and P. L. McEuen, Nature **452**, 448 (2008).
- [24] W. Izumida, K. Sato, and R. Saito, J. Phys. Soc. Jpn. **78**, 074707 (2009).
- [25] J. Klinovaja, M. J. Schmidt, B. Braunecker, and D. Loss, Phys. Rev. B **84**, 085452 (2011).
- [26] B. Braunecker, G. I. Japaridze, J. Klinovaja, and D. Loss, Phys. Rev. B **82**, 045127 (2010).
- [27] J. Klinovaja and D. Loss, Phys. Rev. B **86**, 085408 (2012).
- [28] S. Ryu, A. P. Schnyder, A. Furusaki, and A. W. W. Ludwig, New Journal of Physics **12**, 065010 (2010).
- [29] S. Tewari and J. D. Sau, arXiv: 1111.6592.
- [30] J. Klinovaja, P. Stano, and D. Loss, arXiv: 1207.7322.
- [31] J. Alicea, Y. Oreg, G. Refael, F. von Oppen, and M. P. A. Fisher, Nature Physics **7**, 412 (2011).

Chapter 8

Giant SOI due to rotating magnetic fields in graphene nanoribbons

We theoretically study graphene nanoribbons in the presence of spatially varying magnetic fields produced e.g. by nanomagnets. We show both analytically and numerically that an exceptionally large Rashba spin orbit interaction (SOI) of the order of 10 meV can be produced by the non-uniform magnetic field. As a consequence, helical modes exist in armchair nanoribbons that exhibit nearly perfect spin polarization and are robust against boundary defects. This paves the way to realizing spin filter devices in graphene nanoribbons in the temperature regime of a few Kelvins. If a nanoribbon in the helical regime is in proximity contact to an *s*-wave superconductor, the nanoribbon can be tuned into a topological phase sustaining Majorana fermions.

8.1 Introduction

The last decade has seen remarkable progress in the physics and fabrication of graphene-based systems [1, 2]. The recent advances in producing graphene nanoribbons (GNRs) enable to assemble them with well-defined edges, in particular of armchair type [3, 4]. Moreover, it has been shown that the presence of adatoms can significantly increase the strength of the spin orbit interaction (SOI) of Rashba type [5]. All this together makes nanoribbons promising candidates for spintronics effects. In particular, generation of helical states, modes which transport opposite spins in opposite directions, is of great interest. Such modes were proposed in semiconducting nanowires [6], carbon nanotubes [7, 8], bilayer graphene [9], and experimentally reported for quantum wires in GaAs hole gases [10]. They find applications in spin-filters [6], Cooper pair splitters [11], and, in contact with an *s*-wave superconductor, they provide a platform for Majorana fermions with non-abelian braiding statistics [12].

In the present work we propose a novel way to generate a giant effective SOI in GNRs by spatially varying magnetic fields that can be produced by nanomagnets [13]. This approach has an advantage over using adatoms because the surface of graphene is not in tunnel-contact with other atoms, which usually leads to high disorder with strong intervalley scattering. As we will see, large values of SOI result in helical modes of nearly perfect polarization. Moreover, nanoribbons, in stark contrast to semiconducting nanowires, have considerably larger subband splittings, allowing for a superior control of the number of propagating modes and of the gaps that are characteristic for the helical regime.

Further, our proposal is a next step in bringing topological features to graphene systems. Topological states proposed by Kane and Mele [14] turned out to be experimentally undetectable due to the small intrinsic SOI of graphene. In contrast, we show here that if a GNR in the helical regime is brought into proximity to an *s*-wave superconductor, the system can be tuned into a topological phase that supports Majorana fermions. This opens up the possibility to use GNR for topological quantum computing.

The low-energy physics of armchair GNRs is characterized by broken valley degeneracy enforced by the boundary effects [15]. To generate helical states we also need to lift the spin degeneracy. This can be achieved by magnetic fields in two ways: by a uniform magnetic field and Rashba SOI or by a spatially varying magnetic field. The chemical potential should be tuned inside the gap opened, leading to a helical regime. We will study these two scenarios both analytically and numerically. Moreover, we will show numerically that the presence of helical states is robust against small non-idealities of the GNR edges. This shows that our proposal is realistic and experimentally feasible.

8.2 Graphene nanoribbon

GNRs are strips of graphene, a honeycomb lattice defined by translation vectors \mathbf{a}_1 and \mathbf{a}_2 and composed of two types of atoms, A and B , see Fig. 8.1. The GNR axis is chosen along the z -axis and has a finite width in x direction. GNRs are usually characterized by a width W and a chiral angle θ , the angle between the GNR axis and \mathbf{a}_1 . We only consider armchair nanoribbons for which θ is equal to $\pi/2$.

Graphene can be analyzed in the framework of the tight-binding approach. The effective Hamiltonian includes hoppings of electrons between neighboring sites,

$$\bar{H}_0 = \sum_{\langle ij \rangle, \lambda, \lambda'} t_{ij, \lambda \lambda'} c_i^\dagger c_j \lambda'. \quad (8.1)$$

Here, $c_{i\lambda}$ are the standard electron operators, i and j are nearest-neighbor sites, and λ, λ' are spin projections on the z -axis. Without SOI, the spin is conserved and the hopping amplitude becomes $t_{ij, \lambda \lambda'} = t_{ij} \delta_{\lambda \lambda'}$, where t_{ij} is spin-independent. It is more convenient to treat \bar{H}_0 in momentum space (k_x, k_z) . The low-energy physics of graphene is determined by two valleys around $\mathbf{K} = -\mathbf{K}' = (4\pi/3a, 0)$, where $a = |\mathbf{a}_1|$ is the lattice constant. Wavefunctions can be represented in the form $\psi = \sum_{\tau\sigma} \phi_{\sigma\tau} e^{i\tau K_x x}$, where $\tau = \pm 1$ corresponds to K/K' and $\sigma = \pm 1$ to the A/B sublattice. The Hamiltonian for the slowly-varying wavefunctions $\phi_{\sigma\tau}(x, z)$ is written in terms of the Pauli matrices σ_i (τ_i), acting on the sublattice (valley) degrees of freedom, as

$$H_0 = \hbar v_F (\tau_3 k_x \sigma_1 + k_z \sigma_2). \quad (8.2)$$

Here, k_z (k_x) is the longitudinal (transverse) momentum calculated from a Dirac point, and v_F is the Fermi velocity. From now on we work in the basis $\Phi = (\phi_{AK}, \phi_{BK}, \phi_{AK'}, \phi_{BK'})$.

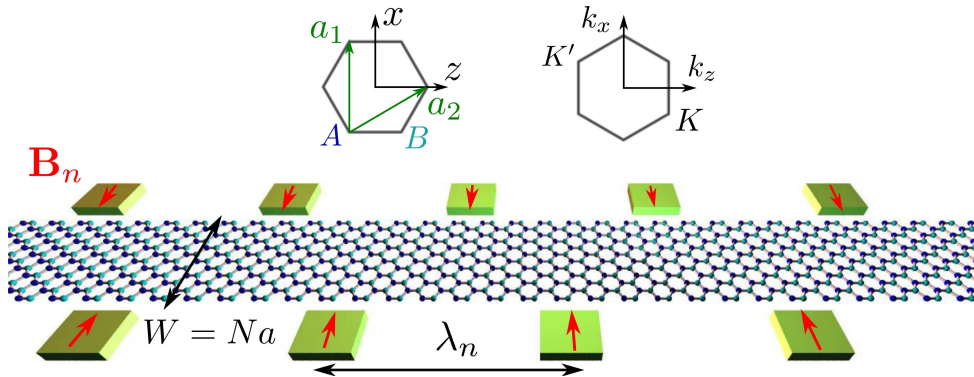


Figure 8.1: An armchair GNR formed by a finite strip of graphene aligned along the z -axis and of width W in x -direction. The GNR is composed of two types of atoms A (blue dot) and B (green dot) and is characterized by hexagons in real space with translation vectors \mathbf{a}_1 and \mathbf{a}_2 . The low-energy physics is determined by the momenta $\mathbf{k} = (k_x, k_z)$ around the two valleys $\mathbf{K} = -\mathbf{K}' = (4\pi/3a, 0)$. Nanomagnets (green slabs) placed with period λ_n on the sides of the GNR provide a spatially varying magnetic field \mathbf{B}_n (red arrows).

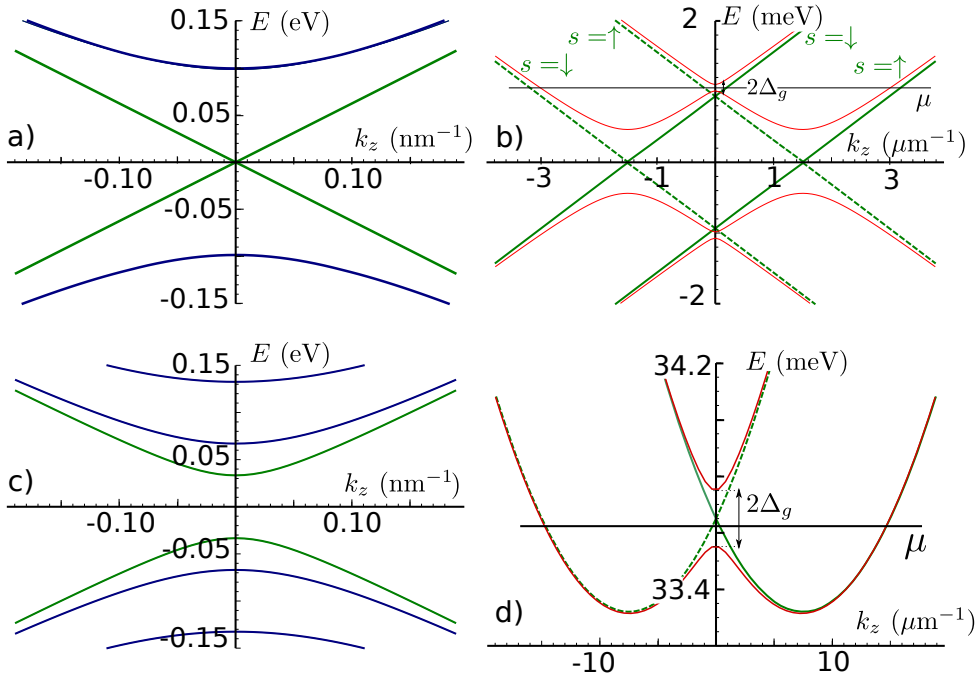


Figure 8.2: The spectrum of an armchair GNR obtained by numerical diagonalization of the tight-binding Hamiltonian $\bar{H}_0 + \bar{H}_{so} + \bar{H}_z$. The low-energy spectrum is linear for metallic [(a,b) with $N = 82$] and quadratic for semiconducting [(c,d) with $N = 81$] GNRs. The SOI [(b) $\Delta_{so} = 1$ meV and (d) $\Delta_{so} = 5$ meV] lifts the spin degeneracy, so the spectrum consists of (b) two Dirac cones or (c) two parabolas shifted by k_{so} from zero (shown by green lines). For a metallic GNR each branch is characterized not only by the spin projection s but also by the isospin γ . The solid (dashed) lines correspond to $\gamma = 1$ ($\gamma = -1$), see (b). While for a semiconducting GNR a magnetic field, $\Delta_Z = 0.1$ meV, alone opens a gap $2\Delta_g$ [(d)], we also need to include intervalley scattering (modeled by fluctuations in on-site energies) for the metallic GNR [(b)]. If the chemical potential μ is tuned inside the gap, the system is in the helical regime with nearly perfect polarization, $\langle s_x \rangle \approx 0.99$, in both cases.

A GNR, in contrast to a graphene sheet, is of finite width W leading to well-gapped subbands. In order to impose open boundary conditions on a GNR consisting of N unit cells in transverse direction, we effectively extend the GNR by two unit cells, so that the width is equal to $W' = (N + 2)a$ and impose vanishing boundary conditions on these virtual sites, $\psi(0, z) = 0$ and $\psi(W', z) = 0$ [15]. This leads to quantization of the transverse momentum k_x , $K_x + k_x = \pi n/W'$, where n is an integer.

If the width of the GNR is such that $N = 3M + 1$, where M is a positive integer, the GNR is metallic [15]. The low-energy spectrum is linear and given by $E_\sigma = \gamma \hbar v_F k_z$, where the isospin $\gamma \pm 1$, corresponding to the eigenvalues of the Pauli matrix σ_2 . The higher levels are two-fold degenerate (apart from spin, see below) and gapped by $\pi \hbar v_F / 3(M+1)a$ (see Fig. 8.2a).

If the GNR width is such that $N = 3M$ (or $N = 3M + 2$), where M is a positive integer, the GNR is semiconducting [15]. The gap at $k_z = 0$ is given by $2\hbar v_F |k_x^{min}|$, with $|k_x^{min}| = \pi/3(N + 2)a$. In case of a semiconducting GNR all orbital states are non-degenerate (see Fig. 8.2c). This means that the boundaries induce intervalley coupling and break the valley degeneracy [16, 15, 17].

If the chemical potential μ crosses only the lowest level of the spectrum, there are two states propagating in opposite directions with opposite isospins σ . However, so far we have not taken spin into account, which will lead to four states at the Fermi level in total. As we will see next, this degeneracy can also be lifted if we include Rashba SOI and a uniform magnetic field or, equivalently, a spatially varying magnetic field.

8.3 Rashba spin orbit interaction

The Rashba SOI arises from breaking inversion symmetry. This can be caused by an electric field E_{ext} applied perpendicular to the GNR plane, or alternatively, by adatoms, which produce local electric fields. In the first case, the SOI is quite small, $\Delta_{so} = eE_{ext}\xi$ with $\xi = 4 \times 10^{-5}$ nm [18, 19] for realistic fields $E_{ext} \sim 1$ V/ μ m. In the second case, the strength of the SOI is significantly increased by doping, and values for Δ_{so} of 10–100 meV have been observed [5]. The general form of the Rashba SOI Hamiltonian can be obtained from symmetry considerations [14],

$$H_{so} = \Delta_{so}(\tau_3 s_z \sigma_1 - s_x \sigma_2), \quad (8.3)$$

where the Pauli matrices s_i act on the spin.

8.4 Rotating magnetic field

An alternative approach to generate helical modes is to apply a spatially varying magnetic field [20, 21, 22]. Such a field can be produced by nanomagnets [13] or by vortices of a superconductor. We emphasize that this scheme requires not perfect periodicity of the field but just a substantial weight of the Fourier component at twice the Fermi wavevector. Moreover, this mechanism is valid for both, rotating and linearly oscillating fields. For simplicity we assume in this section that the Rashba SOI discussed above is negligible. The case when both, a spatially varying magnetic field and Rashba SOI, are present was discussed recently in the context of nanowires [22] and shown to lead to a number of striking effects such as fractionally charged fermions [22].

First, we consider a field rotating in a plane perpendicular to the GNR, leading to the Zeeman term

$$H_n^\perp = \Delta_Z [s_y \cos(k_n z) + s_z \sin(k_n z)], \quad (8.4)$$

where $\Delta_z = g\mu_B B/2$, μ_B is the Bohr magneton, g the g -factor, and $\lambda_n = 2\pi/k_n$ the period of the rotating field. It is convenient to analyze the position-dependent Hamiltonian

$H_0 + H_n^\perp$ in the spin-dependent rotating basis [24, 20]. The unitary transformation $U_n = \exp(ik_n z s_x / 2)$ brings the Hamiltonian back to a GNR with in-plane Rashba SOI and uniform field perpendicular to the GNR,

$$H^\perp = U_n^\dagger (H_0 + H_n^\perp) U_n = H_0 + \Delta_Z s_y + \Delta_{so}^n s_x \sigma_2. \quad (8.5)$$

In a similar way, a field rotating in the plane of a GNR,

$$H_n^\parallel = \Delta_Z [s_x \cos(k_n z) + s_z \sin(k_n z)], \quad (8.6)$$

is equivalent to a GNR with out-of-plane Rashba SOI together with a uniform field along the x -axis,

$$H^\parallel = U_n^\dagger (H_0 + H_n^\parallel) U_n = H_0 + \Delta_Z s_x + \Delta_{so}^n s_y \sigma_2. \quad (8.7)$$

The induced SOI favors the direction of spin perpendicular to the applied rotating magnetic field, and its strength is given by $\Delta_{so}^n = \hbar v_F k_n / 2$, independent of the amplitude Δ_Z . For example, Δ_{so}^n is equal to 10 meV for nanomagnets placed with a period of 200 nm.

8.5 Helical modes

The spectrum of H^\perp (or by analogy of H^\parallel) can be easily found using perturbation theory. Taking into account that realistically $\Delta_Z \ll \Delta_{so}^n$, we treat the Zeeman term as a small perturbation. The induced SOI, given by $\Delta_{so}^n s_x \sigma_2$, leads to spin-dependent shifts of the k_z -momenta by $k_{so} = \Delta_{so}^n / \hbar v_F = k_n / 2$, both for the metallic and the semiconducting GNRs, see Figs. 8.2b and 8.2d. Every level is characterized by the spin projection $s = \pm 1$ on the x -axis, so the spin part of the wavefunctions, $|s\rangle$, is an eigenstate of the Pauli matrix s_x . The corresponding spectrum and wavefunctions that satisfy the vanishing boundary conditions (for ψ) are given by

$$\Phi_{\gamma,s}^{E,k_z} = e^{iz(k_z + sk_{so})} (-i\gamma, 1, i\gamma, -1) |s\rangle, \quad (8.8)$$

$$E_{\gamma,s} = \gamma \hbar v_F (k_z + sk_{so}) \quad (8.9)$$

for a metallic GNR and

$$\begin{aligned} \Phi_{\pm,s}^{E,k_z} &= e^{iz(k_z + sk_{so})} (\pm e^{i\varphi_s + ixk_x^{min}}, e^{ixk_x^{min}}, \\ &\quad \mp e^{i\varphi_s - ixk_x^{min}}, -e^{-ixk_x^{min}}) |s\rangle, \end{aligned} \quad (8.10)$$

$$E_{\pm,s} = \pm \hbar v_F \sqrt{(k_x^{min})^2 + (k_z + sk_{so})^2} \quad (8.11)$$

for a semiconducting GNR. Here we use the notation

$$e^{i\varphi_s} = [k_x^{min} - i(k_z + sk_{so})] / \sqrt{(k_x^{min})^2 + (k_z + sk_{so})^2}.$$

A uniform magnetic field that is perpendicular to the spin-quantization axis defined by the SOI results in the opening of a gap $2\Delta_g$ at $k_z = 0$. Using the wavefunctions given by Eq. (8.10), we can show that $\Delta_g = \Delta_Z k_x^{\min} / \sqrt{(k_x^{\min})^2 + k_{so}^2} \approx \Delta_Z$ for a semiconducting GNR. The spin polarization in this state is given by $|\langle s_x \rangle| \approx 1 - (\Delta_Z k_x^{\min} / 4\hbar v_F k_{so}^2)^2$. In contrast to that, a metallic GNR possesses an additional symmetry. Each branch is characterized not only by spin ($s = \pm 1$) but also by isospin ($\sigma = \pm 1$), see Fig. 8.2b. Thus, a magnetic field alone cannot lift the degeneracy at $k_z = 0$. However, if we include also terms breaking the sublattice symmetry, such as intervalley scattering described by $H_{KK'} = \Delta_{KK'} \tau_1$, a gap will be opened. Here, $\Delta_{KK'}$ is the strength of the intervalley scattering, which can be caused by impurities or fluctuations in the on-site potential. Assuming $\Delta_Z, \Delta_{KK'} \ll \Delta_{so}$, the gap becomes $2\Delta_g = 2\Delta_{KK'} \Delta_Z / \Delta_{so}$ in leading order. The spin polarization of the helical states is given by $|\langle s_x \rangle| \approx 1 - (\Delta_Z / \Delta_{so})^2$. We note that for both semiconducting and metallic GNR, Δ_Z limits the size of the gap Δ_g .

We note that H^\perp is equivalent to the Hamiltonian describing a GNR in the presence of Rashba SOI and a uniform magnetic field applied in perpendicular y -direction, $H_{tot} = H_0 + H_{so} + H_Z$ [see Eqs. (8.2) and (8.3)] in first order perturbation theory in the SOI. Here, the Zeeman term is given by $H_Z = \Delta_Z s_y$. The wavefunctions given by Eqs. (8.8) and (8.10) are eigenstates of the Pauli matrix τ_1 , so the diagonal matrix element of τ_3 is zero. This leads to the result that the term $\tau_3 s_z \sigma_1$ in the Rashba Hamiltonian H_{so} averages out in first order perturbation theory, and H_{tot} is indeed equivalent to H^\perp . This means that the effect of the SOI is a spin-dependent shift of k_z by $k_{so} = \Delta_{so} / \hbar v_F$. Similarly, the uniform magnetic field opens a gap at $k_z = 0$, which can be as big as 10 K for a field of about 10 T.

An alternative approach to above perturbation theory is to analyze the GNR with Rashba SOI analytically. For graphene the spectrum of the effective Hamiltonian $H_0 + H_{so}$ is given by $E_{j,\pm} = \pm \left(\Delta_{so} + j \sqrt{(\hbar v_F k_x)^2 + (\hbar v_F k_z)^2 + \Delta_{so}^2} \right)$, where the index j is equal to 1 (-1) for the highest (lowest) electron level, and the \pm sign distinguishes between electrons and holes. The SOI lifts the spin degeneracy, however, the valley degeneracy is maintained, and τ_3 is a good quantum number. Analogously to Ref. [15], we search for a sum over the eigenstates $\psi_{\tau,q}(x)$ of $H_0 + H_{so}$, $\psi^{E,k_z}(x,z) = \sum_{\tau,q} b_{\tau,q} \psi_{\tau,q}^{E,k_z}(x)$, such that the boundary conditions are satisfied. The index $q = (j, \pm)$ distinguishes between four wavevectors satisfying $E_{j,\pm}(k_x = \pm k_j) = E$, $\hbar v_F k_{1,2} = \sqrt{E^2 - (\hbar v_F k_z)^2 \pm 2E\Delta_{so}}$. We also introduce new variables θ and γ , via $\cos \theta = \hbar v_F k_z / E$ and $\sqrt{2} \sin \theta \sin \gamma = \hbar v_F k_1 / E$. We allow for real as well as imaginary values of $k_{1,2}$, θ , and γ . The spectrum of a metallic GNR is then given implicitly by

$$\begin{aligned} \tan^2 \theta & \left(\sin \left(\frac{k_1 W}{2} \right) \cos \left(\frac{k_2 W}{2} \right) + \cos \left(\frac{k_1 W}{2} \right) \sin \left(\frac{k_2 W}{2} \right) \sin(2\gamma) \right)^2 \\ & = -\sin(k_1 W) \sin(k_2 W) \sin(2\gamma). \end{aligned} \quad (8.12)$$

The exact solution defined by Eq. (8.12) can be analyzed analytically by means of Tailor expansion. For example, if $\Delta_{so} \ll \hbar v_F k_z$, we get $E = \pm \hbar v_F k_z \pm \Delta_{so}$, which is in agreement with previous perturbative calculations.

8.6 Numerics

To check our analytical results numerically, we extend the tight-binding Hamiltonian \bar{H}_0 by allowing for hoppings with spin-flip,

$$\bar{H}_{so} = \sum_{\langle ij \rangle, \lambda, \lambda'} i c_{i\lambda}^\dagger \mathbf{u}_{ij} \cdot \mathbf{s}_{\lambda\lambda'} c_{j\lambda'} + \text{H.c.}, \quad (8.13)$$

in such a way that \bar{H}_{so} is equivalent to the Rashba SOI in the low-energy sector. Here, $\mathbf{s}_{\lambda\lambda'}$ is a vector composed of the Pauli matrices, and spin-dependent hopping elements are defined as $\mathbf{u}_{ij} = -(3\Delta_{so}/4)\mathbf{z} \times \mathbf{e}_{ij}$. A unit vector \mathbf{e}_{ij} points along the bond between two sites i and j . The results of the numerical diagonalization of the Hamiltonian $\bar{H}_0 + \bar{H}_{so} + \bar{H}_Z$ are presented in Fig. 8.2, where the Zeeman term corresponding to a magnetic field \mathbf{B} is modeled as

$$\bar{H}_Z = \sum_{i, \lambda, \lambda'} c_{i\lambda}^\dagger \mathbf{B} \cdot \mathbf{s}_{\lambda\lambda'} c_{i\lambda'}. \quad (8.14)$$

As shown in Fig. 8.2, the numerical results fully confirm the analytical calculations.

8.7 Stability against edge defects.

The spectrum of GNRs is known to be sensitive to the specific form of the edges. For example, the linear spectrum of a metallic GNR becomes parabolic for non-ideal armchair boundaries (see Fig. 8.3). In contrast to that, subband gaps are only slightly modified for semiconducting GNRs. We conclude that the valley degeneracy, in general, is lifted due to strong intervalley mixing induced by the boundaries and this is a property of all armchair GNRs [17, 16]. We emphasize that for the scenario of helical modes developed above we do not need any specific symmetries. Thus, our proposal is robust against edge defects.

The scenario with a rotating magnetic field is even more universal. The only criterion is that the Fermi wavevector k_F is not too large, typically k_F/K_x should be smaller than 10^{-2} . This is a natural limit resulting from the fact that the period of rotation of a magnetic field should be much larger than the lattice constant.

8.8 Majorana fermions.

Next, we consider GNRs in the helical regime brought near to a superconductor. If μ is tuned inside the gap opened by the field, the two propagating modes are helical. The proximity-induced superconductivity in the GNR leads to the coupling between such states and gaps the spectrum. The system can be effectively described in the linearized model for the exterior ($\chi = e$, states with momenta close to the Fermi momentum, $k_e = k_F$) and the interior branches ($\chi = i$, states with nearly zero momenta, $k_i = 0$) [23]. The

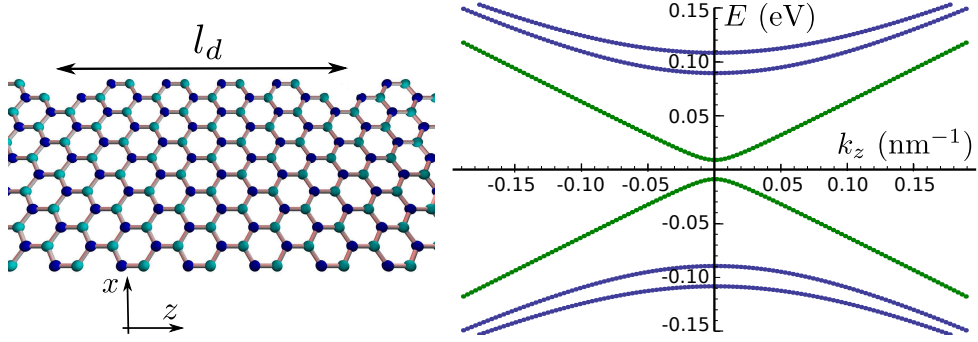


Figure 8.3: Defects on the edges of a metallic armchair GNR ($N = 82$) result in opening of a gap at zero energy. In the numerical diagonalization, the defects were modeled by omitting two atoms on the edges, which was assumed to be periodic with period $l_d = 5\sqrt{3}a$. We see that the spectrum changes only little and the qualitative features of a metallic armchair GNR are maintained.

electron operator is represented as $\Psi(z) = \sum_{\rho=\pm 1, \chi=e,i} e^{i\rho k_\chi z} \Psi_{\rho\chi}$, where the sum runs over the right (R , $\rho = +1$) and left (L , $\rho = -1$) movers. The effective Hamiltonian becomes

$$H = -i\hbar v_F \rho_3 \chi_3 \partial_x + \frac{\Delta_g}{4} \eta_3 \rho_1 (1 + \chi_3) + \Delta_s \eta_2 \rho_2, \quad (8.15)$$

where the Pauli matrices χ_i (η_i) act in the interior-exterior branch (electron-hole) space, and $\tilde{\Psi} = (\Psi_{Re}, \Psi_{Le}, \Psi_{Re}^\dagger, \Psi_{Le}^\dagger, \Psi_{Li}, \Psi_{Ri}, \Psi_{Li}^\dagger, \Psi_{Ri}^\dagger)$. Following Refs. [23, 22], we find that the criterion for the topological phase transition is given by $\Delta_g > \sqrt{\mu^2 + \Delta_s^2}$. In terms of Zeeman energy this gives $\Delta_Z > \Delta_{so} \sqrt{\mu^2 + \Delta_s^2} / \Delta_{KK'}$ ($\Delta_Z > \sqrt{\mu^2 + \Delta_s^2} \sqrt{(k_x^{min})^2 + k_{so}^2} / k_x^{min}$) for a metallic (semiconducting) GNR.

8.9 Conclusions.

We have shown that helical modes can be generated in graphene nanoribbons by a spatially varying magnetic field or by Rashba spin orbit interaction with a uniform magnetic field. We have demonstrated that the opening of the gap is universal for both semiconducting and metallic graphene armchair nanoribbons independent of the mechanism that induces the spin orbit interaction, leading to a helical regime with nearly perfect spin polarization. Moreover, we have checked numerically that the helical regime is robust against boundary defects. All this makes graphene nanoribbons promising candidates for spin effects and spintronics applications.

This work is supported by the Swiss NSF, NCCR Nanoscience, and NCCR QSIT.

Bibliography

- [1] K. S. Novoselov, A. K. Geim, S. V. Morozov, D. Jiang, M. I. Katsnelson, I. V. Grigorieva, S. V. Dubonos, and A. A. Firsov, *Nature* **438**, 197 (2005).
- [2] A. H. Castro Neto, F. Guinea, N. M. R. Peres, K. S. Novoselov, and A. K. Geim, *Rev. Mod. Phys.* **81**, 109 (2009).
- [3] J. Cai, P. Ruffieux, R. Jaafar, M. Bieri, T. Braun, S. Blankenburg, M. Muoth, A. Seitsonen, M. Saleh, X. Feng, K. Moller, and R. Fasel, *Nature* **466**, 470 (2010).
- [4] X. Wang, Y. Ouyang, L. Jiao, H. Wang, L. Xie, J. Wu, J. Guo and H. Dai, *Nature Nanotechnology*, **6**, 563 (2011).
- [5] D. Marchenko, A. Varykhalov, M. R. Scholz, G. Bihlmayer, E. I. Rashba, A. Rybkin, A. M. Shikin, and O. Rader, arXiv:1208.4265.
- [6] P. Streda and P. Seba, *Phys. Rev. Lett.* **90**, 256601 (2003).
- [7] J. Klinovaja, M. J. Schmidt, B. Braunecker, and D. Loss, *Phys. Rev. Lett.* **106**, 156809 (2011).
- [8] J. Klinovaja, S. Gangadharaiah, and D. Loss, *Phys. Rev. Lett.* **108**, 196804 (2012).
- [9] J. Klinovaja, G. J. Ferreira, and D. Loss, *Phys. Rev. B* **86**, 235416 (2012). .
- [10] C. H. L. Quay, T. L. Hughes, J. A. Sulpizio, L. N. Pfeiffer, K. W. Baldwin, K. W. West, D. Goldhaber-Gordon, and R. de Picciotto, *Nat. Phys.* **6**, 336 (2010).
- [11] K. Sato, D. Loss, and Y. Tserkovnyak, *Phys. Rev. B* **85**, 235433 (2012).
- [12] J. Alicea, *Rep. Prog. Phys.* **75**, 076501 (2012).
- [13] B. Karmakar, D. Venturelli, L. Chirolli, F. Taddei, V. Giovannetti, R. Fazio, S. Roddaro, G. Biasiol, L. Sorba, V. Pellegrini, and F. Beltram, *Phys. Rev. Lett.* **107**, 236804 (2011).
- [14] C. L. Kane and E. J. Mele, *Phys. Rev. Lett.* **95**, 226801 (2005).
- [15] L. Brey and H. Fertig, *Phys. Rev. B* **73**, 235411 (2006).
- [16] E. McCann and V. I. Falko, *Journal of Physics: Condensed Matter* **16**, 2371 (2004).
- [17] A. Akhmerov and C. Beenakker, *Phys. Rev. B* **77**, 085423 (2008).
- [18] D. Huertas-Hernando, F. Guinea, and A. Brataas, *Phys. Rev. B* **74**, 155426 (2006).

- [19] J. Klinovaja, M. J. Schmidt, B. Braunecker, and D. Loss, Phys. Rev. B **84**, 085452 (2011).
- [20] B. Braunecker, G. I. Japaridze, J. Klinovaja, and D. Loss, Phys. Rev. B **82**, 045127 (2010).
- [21] M. Kjaergaard, K. Wolms, and K. Flensberg, Phys. Rev. B **85**, 020503 (2012).
- [22] J. Klinovaja, P. Stano, and D. Loss, Phys. Rev. Lett. **109**, 236801 (2012).
- [23] J. Klinovaja and D. Loss, Phys. Rev. B **86**, 085408 (2012).
- [24] L. S. Levitov and E. I. Rashba, Phys. Rev. B **67**, 115324 (2003).

Chapter 8

Chapter 9

Exchange-based CNOT gates for ST-qubits with spin orbit interaction

We propose a scheme for implementing the CNOT gate over qubits encoded in a pair of electron spins in a double quantum dot. The scheme is based on exchange and spin orbit interactions and on local gradients in Zeeman fields. We find that the optimal device geometry for this implementation involves effective magnetic fields that are parallel to the symmetry axis of the spin orbit interaction. We show that the switching times for the CNOT gate can be as fast as a few nanoseconds for realistic parameter values in GaAs semiconductors. Guided by recent advances in surface codes, we also consider the perpendicular geometry. In this case, leakage errors due to spin orbit interaction occur but can be suppressed in strong magnetic fields.

This chapter has been published in Physical Review B 86, 085423 (2012).

9.1 Introduction

Standard quantum computing [1] is based on encoding, manipulating, and measuring quantum information encoded in the state of a collection of quantum two-level systems - qubits. Spin-1/2 is an ideal implementation of a qubit, since it is a natural two-level system, and every pure state of a spin-1/2 corresponds to a state of a qubit. For this reason, spins have been considered as carriers of quantum information in a variety of proposals [2]. The initial proposal [3] called for spins in single-electron quantum dots electrically manipulated by the exchange interaction and local time-dependent Zeeman fields. A variety of other encoding schemes and manipulation techniques [4, 5, 6, 7, 8, 9, 10, 11] rely upon encoded qubits. In these schemes, the simplicity of qubit states and minimal number of physical carriers of quantum information are traded for less stringent requirements for experimental implementations. On one hand, the alternative setups protect from the most common types of errors by decoupling the computational degrees of freedom from the most common sources of noise, and therefore allow for longer gating times. On the other hand, in some alternative setups the manipulation without fast switching of the local magnetic fields becomes possible.

The optimization in the encoding and manipulation protocols is always guided by the state of the art in the experiments. Recent results suggest that spin qubits can reside in a variety of material hosts with novel properties. Quantum dots in graphene [12] and carbon nanotubes [13] are less susceptible to the decoherence due to nuclei and spin-orbit interaction. Spins in nanowires show very strong confinement in two spatial directions, and the gating is comparably simple [8, 9]. In hole systems, the carriers have distinct symmetry properties, and show coupling to the nuclear spins of a novel kind [14]. Recently, the experiments in silicon [15] have demonstrated coherent manipulation of spins similar to the one achieved in the GaAs-based nanostructures. Within these hosts, the manipulation techniques that use exchange interaction, spatially inhomogeneous time independent Zeeman splitting, and nuclear hyperfine interactions are within reach. Despite these developments, GaAS remains a promising route to spin qubits due to the highly advanced experimental techniques developed for this material.

Here, we study the implementation of the quantum gates on the encoded two-spin singlet-triplet (ST) qubits [5, 4, 7, 16, 17, 10] using resources that closely resemble the ones available in the current experimental setups. There, the application of the time-dependent electric fields through the gates fabricated into a structure [11] are preferred to time-dependent local magnetic fields. In addition, the nuclear spins [7, 16, 18, 19, 17] and inhomogeneous magnetic fields [20, 21] are possible resources for spin control. In the setups based on semiconductors, the electrons or holes in the quantum dots are influenced by the spin orbit interaction (SOI), which can contribute to the control [22].

In this work we present a scheme for control of ST-qubits which uses switching of the exchange interaction as a primary resource. We consider the scheme that is optimized for the application of quantum gates in the network of quantum dots. The construction of the CNOT gate uses pulses of the exchange interaction as the only parameter that is time

dependent. The exchange interaction itself is not sufficient for the universal quantum computation over the ST-qubits due to its high symmetry. The additional symmetry breaking is provided by nonuniform, but static magnetic fields. These fields describe the influence both of magnetic fields, provided by the nearby magnets, and of the coupling to the nuclear spins in the host material via hyperfine interaction. Depending on the scheme used for the application of the quantum gates, the optimal geometry is either the one in which the magnetic fields point parallel to the axis of symmetry of the SOI or perpendicular to it.

One major problem in the realization of two-qubit quantum gates (in particular, we consider here the CNOT gate based on conditional phase gates), is the possibility of leakage errors where the spin states defining the logical qubit leave the computational space. These errors move the state of four spins from the 4-dimensional computational space of two qubits into some other portion of the 16-dimensional Hilbert space of four spin-1/2 particles. We consider two ways of addressing this problem. One scheme possesses the axial symmetry due to the fact that the SOI vector and magnetic fields are parallel. For this ‘parallel scheme’ we are able to construct a perfect CNOT gate, if we are able to control all the available parameters. Having in mind 2D architectures, we also consider the CNOT gate between two qubits in the case when the SOI vector and magnetic fields are perpendicular to each other. Here we cannot prevent the leakage out of the computational space, however, we show that it is suppressed by a ratio between the SOI and Zeeman energy coming from a strong external magnetic field.

All our constructions assume that the controlled interactions are switched in time by rectangular pulses. Any deviations from this form of time dependence lead to additional corrections and affect the fidelity of the gate.

The paper is organized as follows. In Sec. 9.2, we introduce the model for the double dots and effective Hamiltonians for field gradients and exchange and spin orbit interactions. In Sec. 9.3, we consider the parallel geometry and derive the CNOT gate via the conditional phase gates and swap gates, all based on exchange. There we also give estimates for the switching times. The scheme for the perpendicular geometry is then addressed in Sec. 9.4, and we conclude in Sec. 9.5.

9.2 Model

We consider in the following singlet-triplet (ST) qubits that are implemented by two electrons confined to a double quantum dot system [5, 4], see Figs. 9.1 and 9.2. Such ST-qubits have been realized successfully in several labs [23], and single and two-qubit operations have also been demonstrated recently [7, 24, 17, 10]. There are several schemes for the fundamental CNOT gate, which can be divided into two classes, schemes which make use of exchange interaction and schemes which do not, but instead rely on coupling of dipole moments [10]. The latter schemes has the disadvantage to be rather slow and also to be affected by charge noise rather strongly. Here, we focus on exchange-based schemes specifically adapted to quantum dots in III-V semiconducting materials, that

have the SOI, such as in GaAs or InAs quantum dots. Although the SOI is typically small compared to the level spacing of the dots, it needs to be taken into account in order to achieve high fidelities in gate operations.

We focus now on two such ST-qubits and assume them to be encoded in four quantum dots that are arranged in a row, see Figs. 9.1 and 9.2. The external magnetic field \mathbf{B} is assumed to give the largest energy scale and determines the spin quantization axis z . The Hilbert space of four spins-1/2 is spanned by $2^4 = 16$ basis states. The total spin of the system is given by $\hat{\mathbf{S}} = \sum_{i=1}^4 \hat{\mathbf{S}}_i$, where $\hat{\mathbf{S}}_i$ is a spin-1/2 operator acting on the spin in a dot $i = 1, 2, 3, 4$. Due to axial symmetry, the z -component, \hat{S}^z , becomes a good quantum number, and the eigenstates corresponding to $S^z = 0$ span a six-dimensional subspace. The singlet state of a qubit is defined as $|S\rangle = (|\downarrow\uparrow\rangle - |\uparrow\downarrow\rangle)/\sqrt{2}$ and the triplet state as $|T\rangle = (|\downarrow\uparrow\rangle + |\uparrow\downarrow\rangle)/\sqrt{2}$. We define the computational basis of the two ST-qubits in this subspace as

$$\begin{aligned} |00\rangle &= |\downarrow\uparrow\downarrow\uparrow\rangle, & |11\rangle &= |\uparrow\downarrow\uparrow\downarrow\rangle, \\ |01\rangle &= |\downarrow\uparrow\uparrow\downarrow\rangle, & |10\rangle &= |\uparrow\downarrow\downarrow\uparrow\rangle, \end{aligned} \quad (9.1)$$

where $\{0, 1\}^{\otimes 2}$ denotes the ST-qubit space, ‘ \uparrow ’ and ‘ \downarrow ’ denote states of the quantum dot spins corresponding to the projection $S_i^z = \pm 1/2$ on the z axis. The remaining two states,

$$|l_1\rangle = |\uparrow\uparrow\downarrow\downarrow\rangle, \quad |l_2\rangle = |\downarrow\downarrow\uparrow\uparrow\rangle, \quad (9.2)$$

belong to the non-computational leakage space. We note that the basis given in Eq. (9.1) is simply related to the common ST-basis [5, 4] via rotations on the Bloch sphere (corresponding to a unitary basis transformation).



Figure 9.1: Parallel geometry: four quantum dots (yellow discs) aligned along the x -axis in the presence of an external magnetic field \mathbf{B} that is applied parallel to the SOI vector β (red arrow), which must be perpendicular to the line of the dots and which we take to be the z -direction. At each dot, there is a local magnetic field \mathbf{B}_i (blue arrows), also assumed to be parallel to \mathbf{B} , but with alternating orientations as indicated. The direction of \mathbf{B} defines the spin quantization axis. The dots are defined electrostatically by metallic gates (light green structures). Each dot contains a spin-1/2, and the exchange (J_{ij}) and the SOI-induced (β_{ij}) interactions between the spins can be controlled by changing the electrostatic potential between the dots. The dots 1 and 2 (from left to right) define the first ST-qubit, and the dots 3 and 4 the second ST-qubit.

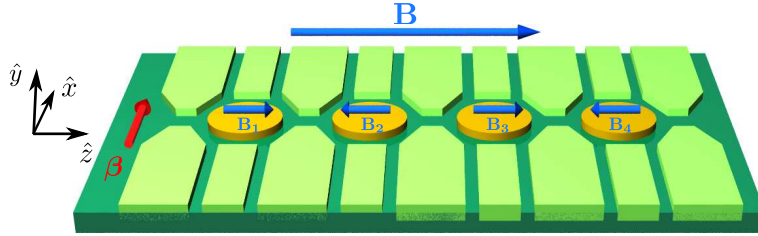


Figure 9.2: Perpendicular geometry: similar to the setup shown in Fig. 9.1 but with the difference that here the SOI vector β (red arrow) is *perpendicular* to the magnetic fields \mathbf{B} and \mathbf{B}_i , which define the spin quantization axis z .

Besides the externally applied magnetic field \mathbf{B} , we allow also for local magnetic fields \mathbf{B}_i that are constant in time (at least over the switching time of the gate). Such local fields can be generated e.g. by nearby micromagnets [21] or by the hyperfine field [25, 26, 27, 28, 29, 30] produced by the nuclear spins of the host material. In the latter case, in order to reach a high fidelity, it is important to perform a nuclear state narrowing [25], *i.e.* to suppress the natural variance $\delta B_i \sim A/\sqrt{N} \sim 10\text{mT}$ to a smaller value, where N is the number of nuclear spins in the quantum dot, and A is the strength of the hyperfine coupling. In the ideal case, one should try to reach a limit where $|\mathbf{B}_i| \sim 50\text{mT} \ll |\mathbf{B}|$ and the fluctuations in \mathbf{B}_i are much smaller than $|\mathbf{B}_i|$.

The magnetic fields \mathbf{B}_i are assumed to point along the external field \mathbf{B} , so that they preserve the axial symmetry of the problem. However, the \mathbf{B}_i 's should have different values (to create field gradients between the dots), a simple scenario being local fields of opposite directions on neighboring dots, see Figs. 9.1 and 9.2. The corresponding Zeeman Hamiltonian is given by

$$H^B = \sum_{i=1}^4 (b + b_i) \hat{S}_i^z, \quad (9.3)$$

where the effective magnetic fields are defined in terms of energy as $b = g\mu_B B$ and $b_i = g\mu_B B_i$, respectively, with g being the electron g-factor and μ_B the Bohr magneton.

The exchange interaction $J_{ij}(t)$ couples the electron spins of nearest neighbor dots i and j and can be controlled electrostatically [23, 7, 21]. If the tunnel barrier between the dots is high we can treat them as independent. If the tunnel barrier is lowered and/or a detuning between the dots is applied, the two spins interact with each other, leading to an effective description in terms of an Heisenberg Hamiltonian [3, 31, 22],

$$H^{ex} = J_{12}(t) \hat{\mathbf{S}}_1 \cdot \hat{\mathbf{S}}_2 + J_{23}(t) \hat{\mathbf{S}}_2 \cdot \hat{\mathbf{S}}_3 + J_{34}(t) \hat{\mathbf{S}}_3 \cdot \hat{\mathbf{S}}_4. \quad (9.4)$$

We assume that the magnetic field is sufficiently large compared to exchange energies, *i.e.* $J_{ij} \ll B$, to avoid admixture of triplets via the SOI (see the discussion of perpendicular geometry below).

We note that ideally it is best to switch the exchange J_{ij} by changing the corresponding inter-dot barrier-height or distance, instead of detuning the double dot by a bias ϵ . Detuning is harmful for two reasons. First, detuning can admix other unwanted states (for example, (0,2)S, see Fig. 2 in [22]). To analyze the errors coming from detuning, one needs to go beyond the effective spin Hamiltonian and consider the microscopic model for the double dots which includes Rashba and Dresselhaus SOI and inhomogeneous fields, see Ref. [22]. Second, the control of J_{ij} via the tunnel barrier preserves the symmetry of the charge distribution in the double dot and thus, in particular, avoids the creation of dipole moments. In contrast, such dipole moments are unavoidable for detuning, and in the regime with $dJ_{ij}/d\epsilon \neq 0$ charge noise can enter most efficiently the qubit space, causing gate errors and decoherence of the ST-qubits [25]. Thus, symmetric exchange switching is expected to be more favourable for achieving high gate fidelities.

Next, we account for the effects of spin orbit interaction. Following Refs. [32, 33, 34] we model the SOI by a Dzyaloshinskii-Moriya (DM) term for two neighboring quantum dots (see e.g. Eq. (1) in [33]),

$$H_{ij}^{SOI} = \boldsymbol{\beta}_{ij}(t) \cdot (\hat{\mathbf{S}}_i \times \hat{\mathbf{S}}_j), \quad (9.5)$$

where the SOI vector $\boldsymbol{\beta}_{ij}(t)$ is perpendicular to the line connecting the dots. First we consider a ‘parallel geometry’ (see Fig. 9.1) where the SOI vectors $\boldsymbol{\beta}_{ij}$ are all parallel to each other and the magnetic fields \mathbf{B} and \mathbf{B}_j are assumed to be parallel to the SOI vectors. This preserves the axial symmetry of the spin system, and by definition, we choose the direction of \mathbf{B} to be the z -axis. This leads to

$$H_{\parallel}^{SOI} = \sum_{i,j} \beta_{ij}(t) (\hat{S}_i^x \hat{S}_j^y - \hat{S}_i^y \hat{S}_j^x), \quad (9.6)$$

where the summation runs over neighboring dots i and j . The strength of the SOI, β_{ij} , depends on the distance between the dots as well as on the tunnel coupling between them. This allows us to assume that both $J_{ij}(t)$ and $\beta_{ij}(t)$ are switched on and off simultaneously [35, 36, 37].

We note here that both H^{ex} and H_{\parallel}^{SOI} , being axially symmetric interactions, preserve the z -component of the total spin S^z . This means that our set-up is protected from leakage to the subspace with $S^z \neq 0$. However, it is not protected from the leakage to the non-computational space given by Eq. (9.2). By a proper design of gates this leakage can be minimized.

Alternatively, in a ‘perpendicular geometry’ (see Fig. 9.2) the axis of the quantum dots is aligned parallel to the applied magnetic field, in the z -direction. The SOI vector $\boldsymbol{\beta}_{ij}$ is perpendicular to this, and we take it to be in x-direction. The corresponding Hamiltonian becomes

$$H_{\perp}^{SOI} = \sum_{i,j} \beta_{ij}(t) (\hat{S}_i^y \hat{S}_j^z - \hat{S}_i^z \hat{S}_j^y). \quad (9.7)$$

Here, the SOI vector $\boldsymbol{\beta}_{ij}$ breaks the axial symmetry of the system, and the total spin S^z is no longer a good quantum number. As a consequence, leakage into the non-computational

space $S^z \neq 0$ is possible, in principle. However, this coupling involves higher-energy states and can thus be suppressed by choosing a sufficiently large magnetic field such that $\beta/B \ll 1$. In contrast, the SOI does not couple states within the computational space, since the matrix elements of H_{\perp}^{SOI} between the states $|\downarrow\uparrow\rangle$ and $|\uparrow\downarrow\rangle$ vanish. We finally note that, similarly, a finite angle between the fields \mathbf{B} and \mathbf{B}_j leads to a leakage error of order $(\mathbf{B}_j)_{x,y}/B \ll 1$.

9.3 Parallel geometry

In this section we concentrate on the parallel geometry, see Fig. 9.1. Using the axial symmetry of the problem we are able to construct a sequence of gate operations that implements the CNOT gate [1], defined on the logical ST-qubits given in Eq. (9.1) by $U_{CNOT}|a, b\rangle = |a, a \oplus b\rangle$, where $a, b = 0, 1$.

One important step in this construction is the implementation of the $\pi/4$ -gate $U_{\pi/4}$ (see discussion below and [1]). For this gate we propose the following scheme consisting of four steps,

$$C_{23} \rightarrow (\pi_{12}, \pi_{34}) \rightarrow C_{23} \rightarrow (\pi_{12}, \pi_{34}), \quad (9.8)$$

where the conditional phase gate C_{23} exchange-couples the dots 2 and 3 and adds a phase factor to the two ST-qubits (see below). The swap gates π_{12} and π_{34} exchange spin states on the dots 1 and 2 and the dots 3 and 4, and can be performed in parallel.

A major issue in the implementation of $U_{\pi/4}$ is the avoidance of leakage errors during the coupling of qubits. To keep qubits in the computational space, operations on spins 2 and 3 must be constructed in such a way that the resulting gate is diagonal in the basis given by Eq. (9.1). This can be achieved in two ways. The first approach is to use strong pulses that lead to fast rotations around the Bloch sphere. The second approach is to use adiabatic pulses that are protected from the leakage to states with different energies [38]. However, the adiabaticity requires a longer pulse time. In the present work we focus on the first approach.

9.3.1 Conditional phase gate C_{23}

In this subsection we describe the phase gate, C_{23} , involving the exchange and SOI interactions only between dot 2 and 3, while dots 1 and 4 are decoupled from dots 2 and 3, *i.e.*, $J_{12} = J_{34} = 0$ and $\beta_{12} = \beta_{34} = 0$. In this case, the effective Hamiltonian is given by

$$H^C = H^B + H^{ex} + H_{\parallel}^{SOI} = H_1^C + H_{23}^C + H_4^C, \quad (9.9)$$

where we present it in block-diagonal form. The part of the Hamiltonian $H_i^C = (b + b_i)\hat{S}_i^z$ acts only on spins located at the dot $i = 1, 4$. The other part of the Hamiltonian, H_{23}^C , acts on spins located at the dots 2 and 3,

$$\begin{aligned} H_{23}^C = & (b + b_2)\hat{S}_2^z + (b + b_3)\hat{S}_3^z + J_{23}\hat{\mathbf{S}}_2 \cdot \hat{\mathbf{S}}_3 \\ & + \beta_{23}(\hat{S}_2^x\hat{S}_3^y - \hat{S}_2^y\hat{S}_3^x). \end{aligned} \quad (9.10)$$

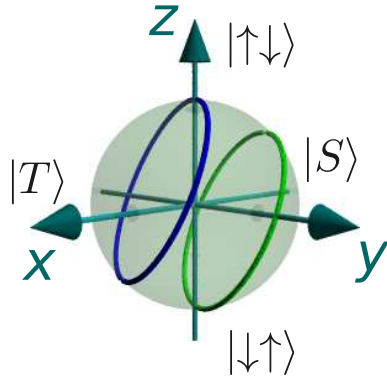


Figure 9.3: The Bloch sphere is defined with the north pole corresponding to $|\uparrow\downarrow\rangle$ and the south pole corresponding to $|\downarrow\uparrow\rangle$. The effect of the unitary evolution operator U_0^C [see Eq. (9.17)] on a state in the space $\{|\uparrow\downarrow\rangle, |\downarrow\uparrow\rangle\}$ is equivalent to the rotation on the Bloch sphere around the vector $J_{23}\mathbf{e}_x - \beta_{23}\mathbf{e}_y + \Delta b_{23}\mathbf{e}_z$. The conditional phase gate C_{23} corresponds to the full rotation on the Bloch sphere (shown by blue and green circles).

Here, we assume a rectangular pulse shape for the exchange and spin orbit interactions, and from now on we treat J_{23} and β_{23} as time-independent parameters. In this case, the unitary gate U^C is a simple exponential of the Hamiltonian,

$$U^C = e^{-iH^CT_C} = e^{-iH_1^CT_C}e^{-iH_{23}^CT_C}e^{-iH_4^CT_C}. \quad (9.11)$$

The spins of dot 1 and 4 do not change in time apart from a phase factor coming from the corresponding magnetic field. In contrast, the spins of dot 2 and 3 change in time and acquire phases, as we describe next. For this we express H_{23}^C as matrix in the basis $\{|\uparrow\uparrow\rangle, |\uparrow\downarrow\rangle, |\downarrow\uparrow\rangle, |\downarrow\downarrow\rangle\}$,

$$\begin{pmatrix} H_+^C & 0 & 0 \\ 0 & H_0^C & 0 \\ 0 & 0 & H_-^C \end{pmatrix}, \quad (9.12)$$

where the block-diagonal form reflects the conservation of S^z . In the case of two parallel spins, the corresponding Hamiltonian is given by $H_\pm^C = J_{23}/4 \pm (b_2 + b_3)/2$, which just assigns a phase to the spins. In the case of antiparallel spins, the Hamiltonian H_0^C is given by

$$H_0^C = \frac{1}{2} \begin{pmatrix} -J_{23}/2 + \Delta b_{23} & J_{23} + i\beta_{23} \\ J_{23} - i\beta_{23} & -J_{23}/2 - \Delta b_{23} \end{pmatrix}, \quad (9.13)$$

where $\Delta b_{23} = b_2 - b_3$. Here, H_0^C describes the coupling between the states $|\uparrow\downarrow\rangle$ and $|\downarrow\uparrow\rangle$, which, in general, leads to leakage errors. This leakage can be prevented by choosing the pulse duration, T_C , in such a way that the corresponding unitary operator $U_0^C = \exp[-iH_0^CT_C]$ is diagonal in the basis $\{|\uparrow\downarrow\rangle, |\downarrow\uparrow\rangle\}$. It is more convenient to consider the evolution given by H_0^C on the Bloch sphere. For that we rewrite H_0^C in terms of

pseudospins,

$$H_0^C = -J_{23}/4 + (\tilde{J}_{23}/2) \mathbf{n}_{23} \cdot \boldsymbol{\tau}, \quad (9.14)$$

$$\tilde{J}_{23} = \sqrt{J_{23}^2 + \beta_{23}^2 + (\Delta b_{23})^2}, \quad (9.15)$$

$$\mathbf{n}_{23} = (J_{23}, -\beta_{23}, \Delta b_{23})/\tilde{J}_{23}, \quad (9.16)$$

where the unit vector \mathbf{n}_{23} defines the rotation axis on the Bloch sphere, see Fig. 9.3, and the pseudospin, acting on the states $\{| \uparrow \downarrow \rangle, | \downarrow \uparrow \rangle\}$, is described by the Pauli matrices $\boldsymbol{\tau}$. The north pole corresponds to $| \uparrow \downarrow \rangle$ and the south pole to $| \downarrow \uparrow \rangle$. The exchange interaction, J_{23} , being the largest scale in H_0^C , forces \mathbf{n}_{23} to be aligned mostly along the x -axis. If we neglect the SOI and any field gradients, the rotation on the Bloch sphere takes place in the yz -plane. In the presence of SOI and field gradients the rotation axis \mathbf{n}_{23} deviates from the x -axis.

The unitary time evolution operator U_0^C corresponding to H_0^C takes the form

$$U_0^C = \exp(-iJ_{23}T_C/4)(\cos \alpha_C + i \mathbf{n}_{23} \cdot \boldsymbol{\tau} \sin \alpha_C), \quad (9.17)$$

where $\alpha_C = \tilde{J}_{23}T_C/2$. The duration of a pulse is determined by the condition that we obtain full rotations on the Bloch sphere (see Fig. 9.3),

$$T_C = \frac{2\pi N_C}{\tilde{J}_{23}}, \quad (9.18)$$

where N_C is a positive integer. Note that deviations from Eq. (9.18) lead, again, to leakage errors.

As a result, the qubit states with parallel spins on dot 2 and 3, acquire the phases

$$\begin{aligned} \phi_{01} &= \frac{1}{2}(J_{23}/2 - b_1 + b_2 + b_3 - b_4)T_C, \\ \phi_{10} &= \frac{1}{2}(J_{23}/2 + b_1 - b_2 - b_3 + b_4)T_C, \end{aligned} \quad (9.19)$$

while the qubit states with antiparallel spins on dot 2 and 3 acquire the phases

$$\begin{aligned} \phi_{11} &= \frac{1}{2}(b_1 - b_4 - J_{23}/2)T_C + \pi N_C, \\ \phi_{00} &= \frac{1}{2}(-b_1 + b_4 - J_{23}/2)T_C + \pi N_C. \end{aligned} \quad (9.20)$$

Here, ϕ_{ab} corresponds to a phase acquired by a two-qubit state $|ab\rangle$. We note that phases produced by the magnetic fields terms will be canceled during the second C_{23} pulse after the π -pulses have been applied to the qubits.

9.3.2 Swap gates π_{12} and π_{34}

In this subsection we discuss the swap gates π_{12} and π_{34} that exchange spin states between dot 1 and 2, and dot 3 and 4, respectively. The swap operation is a one-qubit-operation, so dots 2 and 3 should be decoupled during the swap pulse, *i.e.*, $J_{23} = 0$ and $\beta_{23} = 0$. The swap gate $\pi = (\pi_{12}, \pi_{34})$ is implemented, again, by a rectangular pulse and all parameters are assumed to stay constant during the switching process. This simplifies the unitary evolution operator,

$$U^\pi = U_{12}^\pi U_{34}^\pi = e^{-iH_{12}^\pi T_\pi} e^{-iH_{34}^\pi T_\pi}. \quad (9.21)$$

Further, we focus on the first ST-qubit (dots 1 and 2) and consider only π_{12} (π_{34} can be obtained analogously). We also note that since S^z is conserved separately for each qubit, the final state is always given by a linear combination of the states $|\downarrow\uparrow\rangle$ and $|\uparrow\downarrow\rangle$ on dot 1 and 2. Within this subspace the effective Hamiltonian is given by

$$H_{12}^\pi = \frac{1}{2} \begin{pmatrix} -J_{12}/2 + \Delta b_{12} & J_{12} + i\beta_{12} \\ J_{12} - i\beta_{12} & -J_{12}/2 - \Delta b_{12} \end{pmatrix}, \quad (9.22)$$

or in pseudospin representation [see Eq. (9.14)],

$$H_{12}^\pi = -J_{12}/4 + (\tilde{J}_{12}/2) \mathbf{n}_{12} \cdot \boldsymbol{\tau}, \quad (9.23)$$

$$\tilde{J}_{12} = \sqrt{J_{12}^2 + \beta_{12}^2 + (\Delta b_{12})^2}, \quad (9.24)$$

$$\mathbf{n}_{12} = (J_{12}, -\beta_{12}, \Delta b_{12})/\tilde{J}_{12}, \quad (9.25)$$

where $\Delta b_{12} = b_1 - b_2$ and the Pauli matrix τ_i acts in the pseudospin space spanned by $|\uparrow\downarrow\rangle$ and $|\downarrow\uparrow\rangle$. Again, the unit vector \mathbf{n}_{12} defines the rotation axis. The corresponding unitary evolution operator reduces to the form

$$U_{12}^\pi = \exp(iJ_{12}T_\pi/4)(\cos \alpha_\pi + i\mathbf{n}_{12} \cdot \boldsymbol{\tau} \sin \alpha_\pi), \quad (9.26)$$

where $\alpha_\pi = \tilde{J}_{12}T_\pi/2$.

The swap operation should exchange the states $|\uparrow\downarrow\rangle$ and $|\downarrow\uparrow\rangle$. In the absence of SOI and field gradients, the unitary evolution operator U_{12}^π corresponds to a rotation around the x -axis ($\mathbf{n}_{12} = \mathbf{e}_x$) in the yz -plane. At half the period, $T_\pi^0 = \pi/2\tilde{J}_{12}$, a state evolves from the north to the south pole and vice versa, *i.e.*, $U_{12}^\pi|_{T_\pi^0} \propto \tau_x$.

However, in the presence of SOI and/or field gradients, the rotation axis \mathbf{n}_{12} is not aligned with \mathbf{e}_x (compare with Fig. 9.3), so the trajectory starting at the north (south) pole would never go exactly through the south (north) pole. The corresponding deviations lead to errors in the π_{12} gate on the order of $\sqrt{\Delta b_{12}^2 + \beta_{12}^2}/J_{12}$. This means that it is impossible to produce a perfect swap operation with only one single rectangular pulse. However, by applying a sequence of several rectangular pulses, it is still possible to produce a perfect π_{12} gate, as we demonstrate next.

Indeed, this goal can be achieved by the following three steps (see also Fig. 9.4). First, we switch on the exchange interaction J_{12} between the dots 1 and 2 (this also

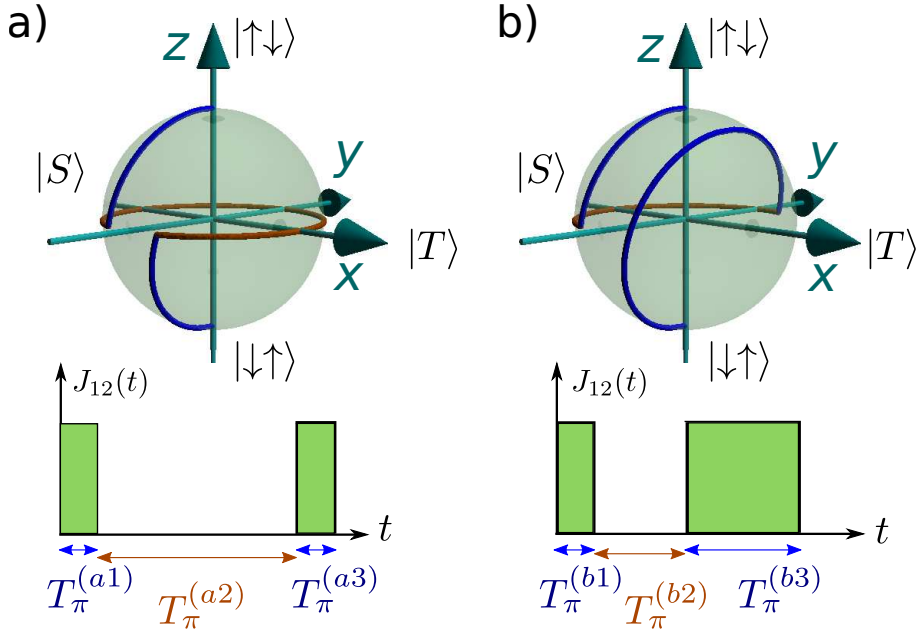


Figure 9.4: Two schemes for the swap gate, π_{12} : $|\uparrow\downarrow\rangle \rightarrow |\downarrow\uparrow\rangle$, composed of three consecutive rotations on the Bloch sphere where the offset induced by Δb_{12} and β_{12} is fully compensated. a) First, starting from the north pole, we turn on J_{12} and β_{12} to induce rotation around $J_{12}\mathbf{e}_x - \beta_{12}\mathbf{e}_y + \Delta b_{12}\mathbf{e}_z$ (upper blue arc) until we reach the equator where we turn off J_{12} and β_{12} . Second, we let the state precess around the z -axis in the equatorial plane until the mirror point of the starting point on the equator is reached (brown arc). Third, we induce once more rotation around $J_{12}\mathbf{e}_x - \beta_{12}\mathbf{e}_y + \Delta b_{12}\mathbf{e}_z$ (lower blue arc) until we reach the south pole. Lower panel: associated rectangular gate pulses and switching times $T_\pi^{(a1,a2,a3)}$ for the three steps. b) Alternative scheme where during the second step the state precesses along the equator until it reaches the point diametrically opposite to its starting point (brown arc).

automatically switches on the SOI β_{12}). We assume J_{12} to be larger than Δb_{12} and/or β_{12} . The rotation axis \mathbf{n}_{12} in polar coordinates is given by

$$\mathbf{n}_{12} = (\sin \vartheta \cos \varphi, \sin \vartheta \sin \varphi, \cos \vartheta). \quad (9.27)$$

From now on we work in the coordinate system in which the x -axis points along $J_{12}\mathbf{e}_x - \beta_{12}\mathbf{e}_y$, so $\varphi = 0$ and $0 \leq \cos \vartheta = \Delta b_{12}/J_{12} \leq 1/\sqrt{2}$. The strength and the duration of the rectangular pulse is chosen in such a way that the rotation reaches the equator of the Bloch sphere. The initial and final vectors on the Bloch sphere are given by

$$\chi_i = (0, 0, 1), \quad (9.28)$$

$$\chi_f = (\cot \vartheta, \sqrt{\sin(2\vartheta - \pi/2)}/\sin \vartheta, 0), \quad (9.29)$$

allowing us to find the rotation angle $\alpha_\pi^{(a1)} = \pi/2 + \arcsin(\cot^2 \vartheta)$, and the corresponding pulse duration

$$T_\pi^{(a1)} = [\pi + 2 \arcsin(\cot^2 \vartheta)]/2\tilde{J}_{12}. \quad (9.30)$$

Second, after switching off exchange and spin orbit interactions, $J_{12} = 0$ and $\beta_{12} = 0$, the rotation takes place around the z -axis in the equatorial plane, at a precession frequency determined by the field gradient Δb_{12} . The rotation angle becomes $\alpha_\pi^{(a2)} = 2[\pi - \arccos(\cot \vartheta)]$, and the pulse duration is given by

$$T_\pi^{(a2)} = \alpha_\pi^{(a2)}/\Delta b_{12}. \quad (9.31)$$

Finally, we repeat the first step by applying a pulse of the same strength J_{12} (β_{12}) and during the same time, $T_\pi^{(a3)} = T_\pi^{(a1)}$.

An alternative scheme (b) is presented in Fig. 9.4b. During the second step the state evolves on the Bloch sphere only over half of the equator, $\alpha_\pi^{(b2)} = \pi$, with the corresponding pulse duration $T_\pi^{(b2)} = \alpha_\pi^{(b2)}/\Delta b_{12}$. The duration of the third pulse is given by

$$T_\pi^{(b3)} = [3\pi - 2 \arcsin(\cot^2 \vartheta)]/2\tilde{J}_{12}. \quad (9.32)$$

The second step is the slowest one in these schemes, so the scheme (b) has an advantage over the scheme (a) by being faster as it requires less rotation on the equator. However, scheme (b) requires better control of parameters, since $T_\pi^{(b1)} \neq T_\pi^{(b3)}$.

Here we note that it is also possible to switch off the exchange coupling J_{12} not only on the equator but also at any other point on the Bloch sphere. Moving away from the equator speeds up the gate performance, but demands greater precision in the tuning, since the rotation proceeds along a smaller arc and in shorter time.

The scheme presented above confirms that it is possible to construct a perfect π swap gate even in the presence of z -component of the SOI vector, β_{12} , or local field gradients, Δb_{12} , by adjusting the pulse durations. The other two components of the SOI vector couple states of different total spin S^z , and thus cause leakage errors. Therefore, it is optimal to orient the magnetic fields (defining the spin quantization axis z) along the SOI vector, β_{12} .

9.3.3 CNOT gate

After the execution of the four-step sequence given by Eq. (9.8) an initial qubit state is restored but with a phase factor [see Eqs. (9.19) and (9.20)]:

$$\begin{aligned} [00] &\xrightarrow{C_{23}} e^{i\phi_{00}}[00] \xrightarrow{(\pi_{12}, \pi_{34})} e^{i\phi_{00}}[11] \xrightarrow{C_{23}} e^{i(\phi_{11}+\phi_{00})}[11] \xrightarrow{(\pi_{12}, \pi_{34})} [00]e^{i(\phi_{11}+\phi_{00})}, \\ [11] &\xrightarrow{C_{23}} e^{i\phi_{11}}[11] \xrightarrow{(\pi_{12}, \pi_{34})} e^{i\phi_{11}}[00] \xrightarrow{C_{23}} e^{i(\phi_{11}+\phi_{00})}[00] \xrightarrow{(\pi_{12}, \pi_{34})} [11]e^{i(\phi_{11}+\phi_{00})}, \\ [01] &\xrightarrow{C_{23}} e^{i\phi_{01}}[01] \xrightarrow{(\pi_{12}, \pi_{34})} e^{i\phi_{01}}[10] \xrightarrow{C_{23}} e^{i(\phi_{01}+\phi_{10})}[10] \xrightarrow{(\pi_{12}, \pi_{34})} [01]e^{i(\phi_{01}+\phi_{10})}, \\ [10] &\xrightarrow{C_{23}} e^{i\phi_{10}}[10] \xrightarrow{(\pi_{12}, \pi_{34})} e^{i\phi_{10}}[01] \xrightarrow{C_{23}} e^{i(\phi_{01}+\phi_{10})}[01] \xrightarrow{(\pi_{12}, \pi_{34})} [10]e^{i(\phi_{01}+\phi_{10})}, \end{aligned} \quad (9.33)$$

with $\phi_{01} + \phi_{10} = -(\phi_{11} + \phi_{00}) = J_{23}T_C/2$, where we omit a trivial phase $2\pi N_C$. The total gate acting on the qubits as defined by Eq. (9.33) can be written in the compact form

$$e^{-i(J_{23}T_C/2)\sigma_1^z\sigma_2^z}, \quad (9.34)$$

where the Pauli matrix σ_1^j acts on the first ST-qubit (formed by dot 1 and 2) and σ_2^j on the second one (formed by dot 3 and 4) with $j = x, y, z$. Choosing

$$T_C = \left(4\pi m - \frac{\pi}{2}\right) / J_{23}, \quad (9.35)$$

where m is a positive integer, we obtain the $\pi/4$ -gate,

$$U_{\pi/4} = e^{i\frac{\pi}{4}\sigma_1^z\sigma_2^z}. \quad (9.36)$$

Both Eqs. (9.18) and (9.35) should be satisfied simultaneously. For example, if $m = 1$ and $N_C = 2$, we get

$$T_C = \frac{\pi}{2} \sqrt{\frac{15}{\Delta b_{23}^2 + \beta_{23}^2}}, \quad (9.37)$$

$$J_{23} = \frac{7}{\sqrt{15}} \sqrt{\Delta b_{23}^2 + \beta_{23}^2}. \quad (9.38)$$

From this we can estimate the total switching time to perform the $\pi/4$ -gate that is a sum of the switching times at each step [see Eq. (9.8)]. For the scheme discussed in Subsecs. 9.3.1 and 9.3.2 the slowest part is given by the swap gates π_{12} and π_{34} , whose switching time is limited by field gradients (due to nuclear spins [7, 16, 18, 19, 17] and/or micromagnets [20, 21]), $|\Delta b_{12}| = |\Delta b_{34}| \approx 10$ mT, which corresponds to $T_\pi^{(b2)} \approx 10$ ns. The gate can be faster if the rotations around the z -axis are performed not on the equator but more closely to the poles. This allows us to decrease the switching time of the swap gate to 2 ns; however, this would require a more precise control over the pulses. The same trick can be used to decrease the switching time of the conditional phase gate C_{23} (compare Figs. 9.3 and 9.5). If field gradients larger than 10 mT are used, the switching rates will be proportionately larger.

Using the $\pi/4$ -gate, we construct the controlled phase flip (CPF) gate $U_{CPF} = \text{diag}(1, 1, 1, -1)$ (see footnote [13] in [3]) as

$$U_{CPF} = U_{\pi/4} e^{-i\frac{\pi}{4}(\sigma_1^z + \sigma_2^z - 1)}. \quad (9.39)$$

Finally, we obtain the CNOT gate,

$$U_{CNOT} = \begin{pmatrix} \mathbb{I} & 0 \\ 0 & \sigma_2^x \end{pmatrix}, \quad (9.40)$$

by using the CPF gate and performing a basis rotation on qubit 2 (a single-qubit rotation by $\pi/2$ about the y -axis),

$$U_{CNOT} = e^{i\frac{\pi}{4}\sigma_2^y} U_{CPF} e^{-i\frac{\pi}{4}\sigma_2^y}. \quad (9.41)$$

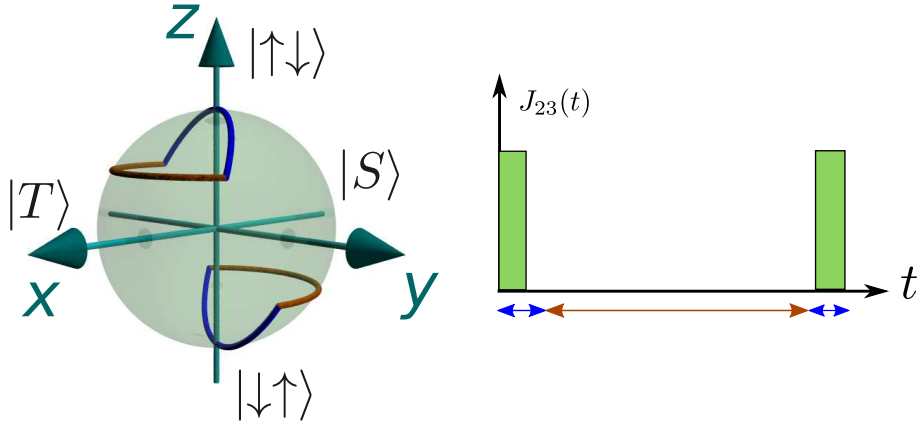


Figure 9.5: An alternative scheme for the conditional phase gate C_{23} (see also Fig. 9.3). Instead of the rotation with the pulse defined by Eqs. (9.18) and (9.35) we consider a sequence of three pulses. During the first and the third pulses (blue arcs) the state precesses quickly acquiring the $\pi/4$ -phase, see Eq. (9.35). During the second pulse, $J_{23} = 0$, the state precesses around the z -axis over a shorter path than the one in Fig. 9.3. As a result, the switching is faster.

In summary, the full sequence of operations for the CNOT gate, U_{CNOT} , is given by

$$e^{i\frac{\pi}{4}\sigma_2^y}[(\pi_{12}\pi_{34})C_{23}(\pi_{12}\pi_{34})C_{23}]e^{-i\frac{\pi}{4}(\sigma_1^z+\sigma_2^z)}e^{-i\frac{\pi}{4}\sigma_2^y}. \quad (9.42)$$

We note again that this result has been derived under the assumption of rectangular pulse shapes. This is certainly an idealization, and in practice we expect deviations from this shape to cause errors for the gates and to affect the gate fidelity. The study of this issue, being very important for practical purposes, requires a separate investigation and is beyond the scope of this work.

9.4 Perpendicular geometry

In the previous section we have discussed the parallel geometry for which we were able to construct a perfect CNOT gate under the assumption that we have a complete control over the parameters. The CNOT gate, together with single-qubit gates, allows us to simulate any other quantum gate and its implementation is a crucial step toward the realization of a quantum computer [1]. In a next step, many such elementary gates need to be connected into a large network. In recent years, the surface code [39] has emerged as one of the most promising platforms for this goal due to its large threshold of about 1% for fault tolerant error correction [39]. This platform requires a two-dimensional (2D) geometry and can be implemented in semiconductors of the type considered here. [11].

The basic 2D scheme is illustrated in Fig. 9.6. There, we show an array of quantum dots where two neighboring dots in a given row represent one ST-qubit. These quantum

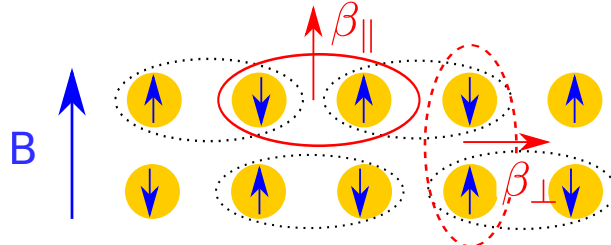


Figure 9.6: Schematic setup for 2D architecture. Two dots define an ST-qubit (black dotted ellipses). An external magnetic field \mathbf{B} and local magnetic fields (blue arrows) are parallel. In the case of the coupling between two qubits from the same row (red solid ellipse) the SOI vector β_{\parallel} is parallel to the magnetic field \mathbf{B} , corresponding to the parallel geometry (see Fig. 9.1). In the case of coupling between two qubits from two neighboring rows (red dashed ellipse) the SOI vector β_{\perp} is perpendicular to the magnetic field \mathbf{B} , corresponding to the perpendicular geometry (see Fig. 9.2).

dots are embedded in a semiconductor where the SOI is of the same type in the entire structure. As a typical example we mention Rashba and/or Dresselhaus SOI that both depend on the momentum of the electron. As a result, the direction of the SOI vector β is always perpendicular to the line along which two quantum dots are coupled by exchange interaction [22]. Thus, for the coupling of two such qubits in the *same* row, the SOI vector β is parallel to the external magnetic field \mathbf{B} , so we can use the scheme designed for the parallel geometry in the previous section. In contrast, if we want to couple two qubits from *neighboring* rows, we should also consider a ‘perpendicular geometry’ (see Figs. 9.1 and 9.6) in which the SOI vector β is perpendicular to the magnetic field \mathbf{B} .

This perpendicular geometry is characterized by several features. As was mentioned before, the axial symmetry in this case is broken by the SOI, leading to the coupling between computational ($S_z = 0$) and non-computational ($S_z \neq 0$) space. If the magnetic field B is sufficiently large to split the triplet levels T_{\pm} far away from the computational space ($g\mu_B B \gg \beta$), we can neglect this leakage. We estimate for GaAs $B = 5\text{T} \approx 100\mu\text{eV}/g\mu_B$. At the same time, the SOI does not couple states within the computational space, so for the realization of the phase gate C_{23} and the swaps gates π_{12} and π_{34} we can use the same scheme as in Sec. 9.3 only with $\beta = 0$.

9.5 Conclusions

We have studied the implementation of the CNOT gate for ST-qubits in a model that is appropriate for current experiments [7, 24, 17]. The setup consists of an array of quantum dots with controlled growth direction and the relative orientation of the dots. Pairs of neighboring dots build the ST-qubits, where the quantization axis is determined by an externally applied magnetic field \mathbf{B} . Moreover, we introduce an inhomogeneity in

magnetic fields, \mathbf{B}_i , by local micromagnets or by the hyperfine field. The resources used for time-dependent control are the exchange interaction $J_{ij}(t)$ and the SOI vector $\beta_{ij}(t)$.

If the SOI vector β is parallel to the external (\mathbf{B}) and local magnetic fields (\mathbf{B}_i), we are able to construct a perfect scheme for the CNOT gate based on the $\pi/4$ -phase gate, $U_{\pi/4}$, consisting of four basic steps. Two of the steps involve interaction of spins that belong to different qubits, and open the possibility of leakage errors. Under condition of total control over system parameters, we show that the leakage can be eliminated. In the other two steps, the tuning of exchange interaction enables perfect swap gates even in the presence of field gradients and SOI.

Motivated by recent results on the surface code, we shortly comment also on the 2D architecture. Here we encounter a situation in which the SOI vector β and the magnetic fields, \mathbf{B} and \mathbf{B}_i , are perpendicular. In this case, the leakage to the non-computational space with $S_z \neq 0$ is inevitable. However, it can be made very small as long as $\beta/g\mu_B B \ll 1$.

Depending on the pulsing scheme, the switching times for the conditional phase gate are shown to lie in the range 1-100 ns for typical GaAs parameters. Compared to the experimentally established decoherence times of about 250 μ s [17], this switching is sufficiently fast and shows that a CNOT gate based on exchange is a promising candidate for experimental realizations.

Acknowledgements. We acknowledge discussions with Andrew Doherty, Charles Marcus, Izhar Neder, and Mark Rudner. This work is supported by IARPA/MQCO program, DARPA/QUEST program, the Swiss NSF, NCCR Nanoscience, and NCCR QSIT.

Bibliography

- [1] A. Nielsen, Michael and I. L. Chuang, *Quantum Computation and Quantum Information*, (Cambridge University Press, Cambridge2000).
- [2] C. Kloeffel and D. Loss, arXiv:1204:5917 (2012).
- [3] D. Loss and D. P. DiVincenzo, Phys. Rev. A **57**, 120 (1998).
- [4] J. Levy, Phys. Rev. Lett. **89**, 147902 (2002).
- [5] S. C. Benjamin, Phys. Rev. A **64**, 054303 (2001).
- [6] D. P. DiVincenzo, D. Bacon, J. Kempe, G. Burkard, and K. B. Whaley, Nature **408**, 339 (2000).
- [7] J. R. Petta, A. C. Johnson, J. M. Taylor, E. A. Laird, A. Yacoby, M. D. Lukin, C. M. Marcus, M. P. Hanson, and A. C. Gossard, Science **309**, 2180 (2005).
- [8] M. Trif, V. N. Golovach, and D. Loss, Phys. Rev. B **75**, 085307 (2007).
- [9] M. Trif, V. N. Golovach, and D. Loss, Phys. Rev. B **77**, 045434 (2008).
- [10] M. D. Shulman, O. E. Dial, S. P. Harvey, H. Bluhm, V. Umansky, and A. Yacoby, Science **336**, 202 (2012).
- [11] L. Trifunovic, O. Dial, M. Trif, J. R. Wootton, R. Abebe, A. Yacoby, and D. Loss, Phys. Rev. X **2**, 011006 (2012).
- [12] B. Trauzettel, D. V. Bulaev, D. Loss, and G. Burkard, Nat. Phys. **3**, 192 (2007).
- [13] D. V. Bulaev, B. Trauzettel, and D. Loss, Phys. Rev. B **77**, 235301 (2008).
- [14] J. Fischer, W. A. Coish, D. V. Bulaev, and D. Loss, Phys. Rev. B **78**, 155329 (2008).
- [15] B. M. Maune, M. G. Borselli, B. Huang, T. D. Ladd, P. W. Deelman, K. S. Holabird, A. A. Kiselev, I. Alvarado-Rodriguez, R. S. Ross, A. E. Schmitz, M. Sokolich, C. A. Watson, M. F. Gyure, and A. T. Hunter, Nature **481**, 344 (2012).
- [16] A. C. Johnson, J. R. Petta, C. M. Marcus, M. P. Hanson, and A. C. Gossard, Phys. Rev. B **72**, 165308 (2005).
- [17] H. Bluhm, S. Foletti, I. Neder, M. Rudner, D. Mahalu, V. Umansky, and A. Yacoby, Nat. Phys. **7**, 109 (2011).
- [18] S. Tarucha, Y. Kitamura, T. Kodera, and K. Ono, physica status solidi (b) **243**, 3673 (2006).

- [19] H. Ribeiro, J. R. Petta, and G. Burkard, Phys. Rev. B **82**, 115445 (2010).
- [20] J. Baugh, Y. Kitamura, K. Ono, and S. Tarucha, Phys. Rev. Lett. **99**, 096804 (2007).
- [21] R. Brunner, Y.-S. Shin, T. Obata, M. Pioro-Ladrière, T. Kubo, K. Yoshida, T. Taniyama, Y. Tokura, and S. Tarucha, Phys. Rev. Lett. **107**, 146801 (2011).
- [22] D. Stepanenko, M. Rudner, B. I. Halperin, and D. Loss, Phys. Rev. B **85**, 075416 (2012).
- [23] R. Hanson, L. P. Kouwenhoven, J. R. Petta, S. Tarucha, and L. M. K. Vandersypen, Rev. Mod. Phys. **79**, 1217 (2007).
- [24] C. Barthel, J. Medford, C. M. Marcus, M. P. Hanson, and A. C. Gossard, Phys. Rev. Lett. **105**, 266808 (2010).
- [25] W. A. Coish and D. Loss, Phys. Rev. B **70**, 195340 (2004).
- [26] A. Khaetskii, D. Loss, and L. Glazman, Phys. Rev. B **67**, 195329 (2003).
- [27] I. A. Merkulov, A. L. Efros, and M. Rosen, Phys. Rev. B **65**, 205309 (2002).
- [28] L. Cywiński, W. M. Witzel, and S. Das Sarma, Phys. Rev. B **79**, 245314 (2009).
- [29] R.-B. Liu, W. Yao, and L. Sham, Advances in Physics **59**, 703 (2010).
- [30] S. Foletti, H. Bluhm, D. Mahalu, V. Umansky, and A. Yacoby, Nat. Phys. **5**, 903 (2009).
- [31] G. Burkard, D. Loss, and D. P. DiVincenzo, Phys. Rev. B **59**, 2070 (1999).
- [32] N. E. Bonesteel, D. Stepanenko, and D. P. DiVincenzo, Phys. Rev. Lett. **87**, 207901 (2001).
- [33] G. Burkard and D. Loss, Phys. Rev. Lett. **88**, 047903 (2002).
- [34] D. Stepanenko, N. E. Bonesteel, D. P. DiVincenzo, G. Burkard, and D. Loss, Phys. Rev. B **68**, 115306 (2003).
- [35] L. Shekhtman, O. Entin-Wohlman, and A. Aharony, Phys. Rev. Lett. **69**, 836 (1992).
- [36] T. Yildirim, A. B. Harris, O. Entin-Wohlman, and A. Aharony, Phys. Rev. Lett. **73**, 2919 (1994).
- [37] F. Baruffa, P. Stano, and J. Fabian, Phys. Rev. B **82**, 045311 (2010).
- [38] A. Doherty *et al.*, To be published.
- [39] D. S. Wang, A. G. Fowler, and L. C. L. Hollenberg, Phys. Rev. A **83**, 020302(R) (2011).

Chapter 10

RKKY interaction in carbon nanotubes and graphene nanoribbons

We study Rudermann-Kittel-Kasuya-Yosida (RKKY) interaction in carbon nanotubes (CNTs) and graphene nanoribbons in the presence of spin orbit interactions and magnetic fields. For this we evaluate the static spin susceptibility tensor in real space in various regimes at zero temperature. In metallic CNTs the RKKY interaction depends strongly on the sublattice and, at the Dirac point, is purely ferromagnetic (antiferromagnetic) for the localized spins on the same (different) sublattice, whereas in semiconducting CNTs the spin susceptibility depends only weakly on the sublattice and is dominantly ferromagnetic. The spin orbit interactions break the SU(2) spin symmetry of the system, leading to an anisotropic RKKY interaction of Ising and Moryia-Dzyaloshinsky form, besides the usual isotropic Heisenberg interaction. All these RKKY terms can be made of comparable magnitude by tuning the Fermi level close to the gap induced by the spin orbit interaction. We further calculate the spin susceptibility also at finite frequencies and thereby obtain the spin noise in real space via the fluctuation-dissipation theorem.

This chapter has been published as Physical Review B **87**, 045422 (2013).

10.1 Introduction

The Rudermann-Kittel-Kasuya-Yosida (RKKY) interaction is an indirect exchange interaction between two localized spins induced by itinerant electrons in a host material.[1, 2, 3] This effective spin interaction, being determined by the static spin susceptibility, is not only a fundamental characteristics of the host system but also finds interesting and useful applications. One of them is the long-range coupling of spins between distant quantum dots, [4, 5] which is needed in scalable quantum computing architectures such as the surface code [6] built from spin qubits. [7] In addition, the RKKY interaction, enhanced by electron-electron interactions, can initiate a nuclear spin ordering that leads to striking effects such as helical nuclear magnetism at low temperatures. [8, 9] Such a rotating magnetic field, equivalent to the presence of a uniform magnetic field and Rashba spin orbit interaction (SOI) in one-dimensional systems,[10] is interesting for Majorana fermion physics in its own right. [10, 11, 12, 13] The RKKY interaction, proposed long ago for normal metals of Fermi liquid type,[1, 2, 3, 14] was later extended in various ways, in particular to low-dimensional systems with Rashba SOI in the clean [15] and the disordered [16] limit, and to systems with electron-electron interactions in one [17, 8, 9] and two dimensions with [18] and without [19, 20] Rashba SOI. Also, a general theorem of Mermin-Wagner type was recently proven for isotropic RKKY systems that excludes magnetic ordering in one and two dimensions at any finite temperature but allows it in the presence of SOI. [21, 22]

Moreover, due to recent progress in magnetic nanoscale imaging,[23] one can expect that the direct measurement of the static spin susceptibility has become within experimental reach.[24] For this latter purpose, graphene offers the unique advantage over other materials such as GaAs heterostructures in that its surface can be accessed directly on a atomistic scale by the sensing device. All this makes the spin susceptibility and the RKKY interaction important quantities to study.

Recently, the RKKY interaction in graphene has attracted considerable attention.[25, 26, 27, 28, 30, 29] Graphene is known for its Dirac-like spectrum with a linear dispersion at low energies. This linearity, however, can give rise to divergences in the expression for the spin susceptibility in momentum space [27] and complicates the analysis compared to systems with quadratic dispersion. However, Kogan recently showed that these divergences can be avoided by working in the Matsubara formalism. [30]

In the present work we consider the close relatives of graphene,[31] namely carbon nanotubes (CNTs) and graphene nanoribbons (GNRs), with a focus on spin orbit interaction and non-uniform magnetic fields. Metallic CNTs also have a linear spectrum, so for them the imaginary time approach developed in Ref. [30] is also most convenient and will be used here. Analogously to graphene, we find that the static spin susceptibility changes sign, depending on whether the localized spins belong to the same sublattice or to different sublattices. [32] No such dependence occurs for CNTs in the semiconducting regime, characterized by a gap and parabolic spectrum at low fillings.

The spin orbit interaction in CNTs is strongly enhanced by curvature effects in compar-

ison to flat graphene, [33, 34, 35] while in GNRs strong SOI-like effects can be generated by magnetic fields that oscillate or rotate in real space. [12, 13] Such non-uniform fields can be produced for instance by periodically arranged nanomagnets. [36] Spin orbit effects break the SU(2) spin-symmetry of the itinerant carriers and thus lead, besides the effective Heisenberg interaction, to anisotropic RKKY terms of Moryia-Dzyaloshinsky and of Ising form. Quite remarkably, when the Fermi level is tuned close to the gap opened by the SOI, we find that the isotropic and anisotropic terms become of comparable size. This has far reaching consequences for ordering in Kondo lattices with RKKY interaction, since this opens up the possibility to have magnetic phase transitions in low-dimensional systems at finite temperature that are tunable by electric gates.

We mention that similar anisotropies have been found before for semiconductors with parabolic spectrum and with Rashba SOI in the clean [15] and in the disordered [16] limit. However, the spin orbit interactions in CNTs and in GNRs are of different symmetry and thus both of these problems require a separate study, apart from the fact that the spectrum is linear.

For all itinerant regimes we consider, the RKKY interaction is found to decay as $1/R$, where R is the distance between the localized spins, thus following the standard behavior for RKKY interaction in non-interacting one-dimensional systems. [14] [In interacting systems, described by Luttinger liquids, the decay becomes slower. [17, 9, 37]] In contrast, the overall sign as well as the spatial oscillation periods of the RKKY interaction are non-generic and depend strongly on the system and the regimes considered.

Finally, we will also consider the dynamical spin susceptibility at finite frequency. Via the fluctuation-dissipation theorem we obtain from this the spin-dependent dynamical structure factor in position space, which describes the equilibrium correlations of two localized spins separated by a distance R .

The paper is organized as follows. Sec. 10.2 contains different approaches to the RKKY interaction including imaginary time formalism for metallic CNTs with a linear spectrum and the retarded Green functions in the real space formalism for semiconducting CNTs. In Sec. 10.3 the low energy spectrum of CNTs is shortly discussed. Afterwards the spin susceptibility is calculated both in the absence of the SOI (Sec. 10.4) and in the presence of the SOI (Sec. 10.5). In addition, in Sec. 10.6 we present results for the case of a magnetic field along the nanotube axis. Such a field breaks both orbital and spin degeneracy, leading to non-trivial dependence of the spin susceptibility on the chemical potential. The fluctuation-dissipation theorem connects the spin susceptibility and the spin fluctuations, allowing us to explore the frequency dependence of the spin noise at zero temperature in Sec. 10.7. The RKKY interaction in armchair graphene nanoribbons is briefly considered in Sec. 10.8. Finally, we conclude with Sec. 10.9 in which we shortly summarize our main results.

10.2 Formalism for RKKY

The RKKY interaction[1, 2, 3] was studied for a long time and several approaches were developed. In this section we briefly review those used in this work.

The RKKY interaction is an effective exchange interaction between two magnetic spins, \mathbf{I}_i and \mathbf{I}_j , localized at lattice sites \mathbf{R}_i and \mathbf{R}_j , respectively, that are embedded in a system of itinerant electrons with spin-1/2. These electrons have a local spin-interaction with the localized spins, described by the Hamiltonian

$$H_{int} = J \sum_{l=i,j} \mathbf{s}_l \cdot \mathbf{I}_l, \quad (10.1)$$

where $\hbar\mathbf{s}_l/2$ is the electron spin operator at site \mathbf{R}_l , and J is the coupling strength. Using second order perturbation expansion in J , [14, 15, 9, 30] the RKKY Hamiltonian [1, 2, 3] becomes

$$H_{RKKY} = J^2 \chi_{\alpha\beta}^{ij} I_i^\alpha I_j^\beta, \quad (10.2)$$

where $\chi_{\alpha\beta}^{ij} = \chi_{\alpha\beta}(\mathbf{R}_{ij}, \omega = 0)$ is the static (zero-frequency) spin susceptibility tensor, and where summation is implied over repeated spin indices $\alpha, \beta = x, y, z$ (but not over i, j). Here, we assumed that the system is translationally invariant so that the susceptibility depends only on the relative distance $\mathbf{R}_{ij} \equiv \mathbf{R}_i - \mathbf{R}_j$. The RKKY interaction can be expressed in several equivalent ways. For example, in terms of the retarded Green function $G(\mathbf{R}_{ij}; \epsilon + i0^+)$ the RKKY Hamiltonian is given by

$$\begin{aligned} H_{RKKY} = & -\frac{J^2}{\pi} \text{Im} \int_{-\infty}^{\epsilon_F} d\epsilon \text{Tr} [(\mathbf{I}_i \cdot \mathbf{s})(\mathbf{I}_j \cdot \mathbf{s}) \\ & \times G(\mathbf{R}_{ij}; \epsilon + i0^+) G(-\mathbf{R}_{ij}; \epsilon + i0^+)], \end{aligned} \quad (10.3)$$

where the integration over energy ϵ is limited by the Fermi energy ϵ_F (see Ref. [15]). Here \mathbf{s} is a vector of the Pauli matrices acting on the spin of the itinerant electrons, and the trace Tr runs over the electron spin. The retarded Green function $G(\mathbf{R}_{ij}; \epsilon + i0^+)$, which are spin-dependent here and represented as 2×2 -matrices in spin space, are taken in real (\mathbf{R}_{ij}) and energy space (ϵ). In the presence of spin orbit interaction, we will use Eq. (10.3) as a starting point.

In the absence of spin orbit interaction, the spin is a good quantum number, so the effective Hamiltonian H_{RKKY} can be significantly simplified, $\chi_{\alpha\beta}^{ij} = \delta_{\alpha\beta}\chi_0^{ij}$, and the RKKY interaction is of Heisenberg type (isotropic in spin space). Expressing the Green functions in terms of the eigenfunctions $\psi_n(\mathbf{R}_i)$ of the electron Hamiltonian, we obtain

$$\begin{aligned} \chi_0^{ij} = & 2 \sum_{n,m} \psi_n^*(\mathbf{R}_i) \psi_m(\mathbf{R}_i) \psi_n(\mathbf{R}_j) \psi_m^*(\mathbf{R}_j) \\ & \times \frac{n_F(\xi_n) - n_F(\xi_m)}{\xi_n - \xi_m}, \end{aligned} \quad (10.4)$$

where the sum runs over all eigenstates of the spinless system, and the factor 2 accounts for the spin degeneracy. The energy is calculated from the Fermi level, $\xi_n = \epsilon_n - \epsilon_F$, and the Fermi distribution function at $T = 0$ is given by $n_F(\xi) = \theta(-\xi)$.

The sum in Eq. (10.4) is divergent in case of a linear spectrum. [38, 30] To avoid these divergences we follow Ref. [30] and work in the imaginary time formalism, again neglecting the spin structure of the Green functions. The static real space spin susceptibility at zero temperature is given by

$$\chi_0^{ij} = \frac{2}{\hbar} \int_0^\infty d\tau G_0(\mathbf{R}_{ij}, \tau) G_0(-\mathbf{R}_{ij}, -\tau), \quad (10.5)$$

where the factor 2 again accounts for the spin degeneracy. The Matsubara Green functions for $\tau \geq 0$ are found as

$$G_0(\mathbf{R}_{ij}, \pm\tau) = \mp \sum_n \psi_n^*(\mathbf{R}_i) \psi_n(\mathbf{R}_j) e^{\mp \xi_n \tau / \hbar} \theta(\pm \xi_n). \quad (10.6)$$

All three approaches to the RKKY interaction described above [see Eqs. (10.3), (10.4), and (10.5)] are equivalent to each other. Which one is used for a particular case depends on calculational convenience.

10.3 Carbon nanotubes

In this section, we discuss the effective Hamiltonian for a carbon nanotube. A carbon nanotube is a rolled-up sheet of graphene, a honeycomb lattice composed of two types of non-equivalent atoms A and B . The (N_1, N_2) -CNTs can be alternatively characterized by the chiral angle θ and the diameter d .[31] The low-energy physics takes place in two valleys \mathbf{K} and \mathbf{K}' . These two Dirac points are determined by $\mathbf{K} = -\mathbf{K}' = 4\pi(\hat{\mathbf{t}} \cos \theta + \hat{\mathbf{z}} \sin \theta)/3a$, where a is the lattice constant. The unit vector $\hat{\mathbf{z}}$ points along the CNT axis, and $\hat{\mathbf{t}}$ is the unit vector in the transverse direction.

10.3.1 Effective Hamiltonian

In the absence of spin orbit interaction CNTs are described by the effective Hamiltonian H_0 ,

$$H_0 = \hbar v_F (k_G \sigma_1 + k \gamma \sigma_2). \quad (10.7)$$

The Pauli matrices σ_i act in the space defined by the sublattices A and B . The Fermi velocity in graphene v_F is equal to 10^6 m/s. Here, $\gamma = 1$ ($\gamma = -1$) labels the \mathbf{K} (\mathbf{K}') Dirac points, and k is the momentum along the z -axis calculated from the corresponding Dirac point. The momentum in the circumferential direction k_G is quantized, $k_G = 2(m - \gamma \delta/3)/d$, with d the CNT diameter, leading to two kinds of nanotubes: metallic and semiconducting. Here, $m \in \mathbb{Z}$ is the subband index and $\delta = (N_1 - N_2) \bmod 3$ for a (N_1, N_2) -CNT (see Ref. [31]). The spectrum of metallic CNTs (with $k_G = 0$) is a Dirac

cone, *i.e.* linear and gapless. In contrast to that, the spectrum of semiconducting CNTs (with $k_G \neq 0$) has a gap given by $2\hbar v_F |k_G|$. In the following we consider only the lowest subband with energies

$$\epsilon_n = \nu \hbar v_F \sqrt{k^2 + k_G^2}, \quad (10.8)$$

where $\nu = 1$ ($\nu = -1$) corresponds to electrons (holes), and $n = (k, \gamma, \nu)$ labels the eigenstates. The corresponding wavefunctions with sublattice spinor are given by

$$\psi_n(\mathbf{R}_i) = e^{i(\gamma\mathbf{K}+\mathbf{k}) \cdot \mathbf{R}_i} \frac{1}{\sqrt{2}} \begin{pmatrix} 1 \\ \nu \gamma e^{i\phi_k} \end{pmatrix}, \quad (10.9)$$

$$e^{i\phi_k} = \frac{k_G + ik}{\sqrt{k_G^2 + k^2}}, \quad (10.10)$$

where $\mathbf{k} = (k_G, k)$. From now on we redefine Dirac points by shifting the circumferential value of \mathbf{K} (\mathbf{K}') by k_G , so that $\mathbf{K} = -\mathbf{K}' = 4\pi(\hat{\mathbf{t}} \cos \theta + \hat{\mathbf{z}} \sin \theta)/3a + \hat{\mathbf{t}} k_G$ and $\mathbf{k} = (0, k)$.

10.3.2 Spin orbit interaction

Spin orbit interaction in nanotubes arises mostly from curvature effects, which substantially increase its value in comparison with flat graphene. [33, 34, 35, 39, 40, 41] The effective Hamiltonian, which includes the spin orbit interaction terms, is given by

$$H_{so} = H_0 + \alpha \sigma_1 s_z + \gamma \beta s_z, \quad (10.11)$$

where s_i are the Pauli matrices acting on the spin. The SOI is described by two parameters, α and β , which depend on the diameter d . The values of these parameters can be found in the framework of the tight-binding model, $\alpha = -0.16 \text{ meV}/d$ [nm] and $\beta = -0.62 \text{ meV} \cos(3\theta)/d$ [nm] (see Refs. [34, 35]). The valley index γ and the spin projection on the nanotube axis s are good quantum numbers due to the rotation invariance of the CNT. The conduction band spectrum ($\nu = 1$) is given by

$$\epsilon_n = \pm \gamma \beta s + \sqrt{(\hbar v_F k)^2 + (\gamma \hbar v_F k_G + \alpha s)^2}, \quad (10.12)$$

and the corresponding wavefunctions are given by

$$\psi_n(\mathbf{R}_i) = e^{i(\gamma\mathbf{K}+\mathbf{k}) \cdot \mathbf{R}_i} \frac{1}{\sqrt{2}} \begin{pmatrix} 1 \\ e^{i\phi_{s,\gamma}} \end{pmatrix} |s\rangle, \quad (10.13)$$

$$e^{i\phi_{s,\gamma}} = \frac{\gamma k_G + s\alpha + i\gamma k}{\sqrt{k^2 + (\gamma k_G + s\alpha)^2}}, \quad (10.14)$$

where the index $n = (k, \gamma, s)$ labels the eigenstates. Here $|s\rangle$, the eigenstate of the Pauli matrix s_z , corresponds to the spin state with spin up ($s = 1$) or down ($s = -1$). We note that the SOI lifts the spin degeneracy and opens gaps at zero momentum, $k = 0$. In

case of semiconducting nanotubes ($k_G \gg k$), we use the parabolic approximation of the spectrum,

$$\epsilon_n = \hbar v_F k_G + \gamma s(\beta + \alpha) + \hbar v_F k^2 / 2k_G. \quad (10.15)$$

Further we denote the sum of the SOI parameters α and β as $\beta_+ \equiv \beta + \alpha$. Such kind of a spectrum is similar to the spectrum of a CNT in the presence of a pseudo-magnetic field that has opposite signs at opposite valleys. We note that there is a principal difference between a semiconducting CNT and a semiconducting nanowire with Rashba SOI. In the latter, the Rashba SOI can be gauged away by a spin-dependent unitary transformation.[15, 10] In contrast, the spectrum of CNTs consists of parabolas shifted along the energy axis and not along the momentum axis as in the case of semiconducting nanowires, so the SOI cannot be gauged away. As shown below, this leads to a less transparent dependence of the spin susceptibility on the SOI compared to nanowires. [15]

10.4 RKKY in the absence of SOI

In this section we calculate the spin susceptibility neglecting spin orbit interaction, so all states are two-fold degenerate in spin. We can thus consider a spinless system and account for the spin degeneracy just by introducing a factor of 2 in the expressions for the spin susceptibility, see Eqs. (10.4) and (10.5).

10.4.1 Metallic nanotubes

The spectrum of a metallic nanotube is linear, see Eq. (10.8), with the momentum in the circumferential direction k_G equal to zero, $k_G = 0$. As was mentioned above, in this case the integrals over the momentum in Eq. (10.4) are divergent, [30] so it is more convenient to work in the imaginary time formalism [see Eq. (10.5)], where all integrals remain well-behaved. To simplify notations, we denote the distance between the localized spins as $\mathbf{R} \equiv \mathbf{R}_i - \mathbf{R}_j$ and its projection on the CNT axis as z . Using the wavefunctions given by Eq. (10.9), we find the Green functions from Eq. (10.6), where we replaced sums by integrals, $\sum_k \rightarrow (a/2\pi) \int dk$. The Green functions on the same sublattices are given by

$$G_0^{AA}(\mathbf{R}, \tau) = G_0^{BB}(\mathbf{R}, \tau) = -\frac{a}{\pi} \cos(\mathbf{K} \cdot \mathbf{R}) \times \frac{v_F \tau \cos(k_F z) - z \sin(k_F z)}{(v_F \tau)^2 + z^2}. \quad (10.16)$$

The Green function on different sublattices is given by

$$G_0^{AB}(\mathbf{R}, \tau) = i \frac{a}{\pi} \sin(\mathbf{K} \cdot \mathbf{R}) \times \frac{v_F \tau \sin(k_F z) + z \cos(k_F z)}{(v_F \tau)^2 + z^2}. \quad (10.17)$$

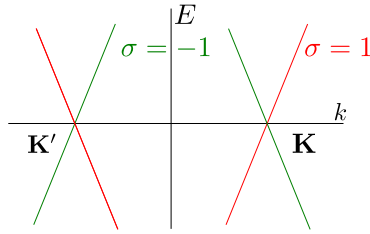


Figure 10.1: The Dirac spectrum of a metallic nanotube. Each branch is characterized by the isospin value σ , which is an eigenvalue of the Pauli matrix σ_2 . We note that the Kramers partners at K and K' , respectively, are characterized by the same value of the isospin, and two partner states at the same cone are characterized by opposite isospins.

Here, the Fermi wavevector k_F is determined by the Fermi energy ϵ_F as $k_F = \epsilon_F / \hbar v_F$. For the corresponding spin susceptibilities [see Eq. (10.5)] we then obtain after straightforward integration

$$\chi_0^{AA}(\mathbf{R}) = \frac{-a^2}{4\pi\hbar v_F |z|} [1 + \cos(2\mathbf{K} \cdot \mathbf{R})] \cos(2k_F z), \quad (10.18)$$

$$\chi_0^{AB}(\mathbf{R}) = \frac{a^2}{4\pi\hbar v_F |z|} [1 - \cos(2\mathbf{K} \cdot \mathbf{R})] \cos(2k_F z). \quad (10.19)$$

If the chemical potential is tuned strictly to the Dirac point, $k_F = 0$, the spin susceptibility is purely ferromagnetic for the atoms belonging to the same sublattices, $\chi_0^{AA}, \chi_0^{BB} \leq 0$, whereas it is purely antiferromagnetic for the atoms belonging to different sublattices, $\chi_0^{AB} \geq 0$. [32] For the chemical potential tuned away from the Dirac point we observe in addition to the sign difference oscillations of the spin susceptibility in real space with period of half the Fermi wavelength π/k_F . This oscillation, together with the $1/z$ decay, is typical for RKKY interaction in one-dimensional systems.[14]

An immediate consequence of the opposite signs of the susceptibilities in Eqs. (10.19) is that any ordering of spins localized at the honeycomb lattice sites will be antiferromagnetic. Such order produces a staggered magnetic field that can act back on the electron system and give rise to scattering of electrons between branches of opposite isospin σ at the same Dirac cone (see Fig. 10.1). It has been shown elsewhere that such backaction effects can lead to a spin-dependent Peierls gap in the electron system. [8, 9, 10]

10.4.2 Semiconducting nanotubes

Zero chemical potential

Now we consider semiconducting CNTs that are characterized by a non-zero circumferential wavevector k_G and a corresponding gap in the spectrum. We begin with the case of the Fermi level ϵ_F lying in the middle of the gap, $\epsilon_F = 0$. As a result, there are no states at the Fermi level. This leads to a strong suppression of the RKKY interaction. For

example, the Green function on the same sublattice, found from Eqs. (10.6) and (10.9), is given by

$$G^{AA}(\mathbf{R}, \tau) \approx -\frac{a}{2\pi} \cos(\mathbf{K} \cdot \mathbf{R}) e^{ik_G z - v_F |\tau| k_G} \times \sqrt{\frac{2\pi k_G}{v_F |\tau|}} e^{-z^2 k_G / 2v_F |\tau|}, \quad (10.20)$$

where we used the simplified parabolic spectrum, see Eq. (10.15). The spin susceptibility is then obtained from Eq. (10.5),

$$\chi^{AA}(\mathbf{R}) = -\frac{2a^2 k_G}{\pi \hbar v_F} \cos^2(\mathbf{K} \cdot \mathbf{R}) K_0(2\sqrt{2}k_G |z|), \quad (10.21)$$

where $K_0(x)$ is the modified Bessel function of second kind, which decays exponentially at large distances, $K_0(x) \approx e^{-x} \sqrt{\pi/2x}$ for $x \gg 1$. This exponential decay (on the scale of the CNT diameter d) of the spin susceptibility in the case when the Fermi level lies in the gap is not surprising. There are just no delocalized electron states that can assist the effective coupling between two separated localized spins. From now on we neglect any contributions coming from higher or lower bands.

Non-zero chemical potential

In this subsection we assume that the Fermi level is tuned in such a way that it crosses, for example, the conduction band. Thus, the itinerant states assist the RKKY interaction between localized spins. The spectrum of a semiconducting CNT is parabolic [see Eq. (10.15)], so it is more convenient to work with the spin susceptibility given by Eq. (10.4). In momentum space the spin susceptibility on the same sublattice is given by $\chi^{AA}(q) = \sum_{\gamma, \gamma'} \chi^{AA}(\gamma, \gamma'; q)$ with

$$\chi^{AA}(\gamma, \gamma'; q) = \frac{1}{2} \sum_k \frac{\theta[\xi_{\gamma'}(k+q)] - \theta[\xi_{\gamma}(k)]}{\xi_{\gamma'}(k+q) - \xi_{\gamma}(k)}. \quad (10.22)$$

Performing integration over momentum k , we arrive at an expression similar to the Lindhard function,

$$\chi^{AA}(\gamma, \gamma'; q) = -\frac{ak_G}{2\pi \hbar v_F q} \ln \left| \frac{q + 2k_F}{q - 2k_F} \right|, \quad (10.23)$$

where the Fermi momentum k_F is defined as $k_F = \sqrt{2k_G(\epsilon_F - \hbar v_F k_G)/\hbar v_F}$. Next we go to real space by taking the Fourier transform of $\chi^{AA}(\gamma, \gamma'; q)$. This can be readily done by closing the integration contour in the upper (lower) complex plane for $z > 0$ ($z < 0$) and deforming it around the two branch cuts of the logarithm in Eq. (10.23) that run from $\pm 2k_F$ to $\pm \infty$. This yields,

$$\chi^{AA}(\mathbf{R}) = \frac{a^2 k_G}{\pi \hbar v_F} \text{si}(2k_F |z|) [1 + \cos(2\mathbf{K} \cdot \mathbf{R})]. \quad (10.24)$$

Here, the sine integral is defined as

$$\text{si}(x) = \int_0^x dt \frac{\sin t}{t} - \frac{\pi}{2}, \quad (10.25)$$

and at large distances, $x \gg 1$, its asymptotics is given by $\text{si}(x) \approx -\cos(x)/x$.

The evaluation of the spin susceptibility for different sublattices is more involved,

$$\chi^{AB}(\gamma, \gamma'; q) = \frac{\gamma\gamma'}{2} \sum_k e^{-i\Delta\phi_{k,q}} \frac{\theta[\xi_{\gamma'}(k+q)] - \theta[\xi_\gamma(k)]}{\xi_\gamma(k) - \xi_{\gamma'}(k+q)}, \quad (10.26)$$

where the phase difference given by $\Delta\phi_{k,q} = \phi_k - \phi_{k+q}$ depends on the momenta k and q , see Eq. (10.10). Taking into account that k_G is the largest momentum characterizing the system, we expand the phase factor as $e^{i(\phi_k - \phi_{k+q})} \approx 1 - iq/k_G$. The main contribution to the spin susceptibility comes from the momentum-independent part and is given by

$$\chi^{AB}(\mathbf{R}) = \frac{a^2 k_G}{\pi \hbar v_F} \text{si}(2k_F|z|) [1 - \cos(2\mathbf{K} \cdot \mathbf{R})]. \quad (10.27)$$

In the next step we evaluate the correction $\Delta\chi^{AB}(\mathbf{R})$ to the spin susceptibility $\chi^{AB}(\mathbf{R})$ arising from the momentum-dependent part in the phase factor $e^{i\Delta\phi_{k,q}}$. In momentum space it is given by

$$\Delta\chi^{AB}(\gamma, \gamma'; q) = \frac{ia\gamma\gamma'}{2\pi\hbar v_F} \ln \left| \frac{q + 2k_F}{q - 2k_F} \right|. \quad (10.28)$$

By taking the Fourier transform of Eq. (10.28), we arrive at the following expression,

$$\begin{aligned} \Delta\chi^{AB}(\mathbf{R}) &= \sum_{\gamma, \gamma'} e^{i(\gamma-\gamma')\mathbf{K} \cdot \mathbf{R}} \frac{ia^2 \gamma\gamma'}{2\pi\hbar v_F} \\ &\times \int_{-\infty}^{\infty} dq e^{iqz} \ln \left| \frac{q + 2k_F}{q - 2k_F} \right|. \end{aligned} \quad (10.29)$$

The integral in Eq. (10.29) can be evaluated easily by recognizing it as the derivative of $\text{si}(x)$ [see Eq. (10.23)],

$$I = \int_{-\infty}^{\infty} dx e^{i\alpha x} \ln \left| \frac{x+1}{x-1} \right| = -i \frac{\sin \alpha}{|\alpha|}, \quad (10.30)$$

where α is real. As a result, the correction to the spin susceptibility on different sublattices $\chi^{AB}(\mathbf{R})$ is given by

$$\Delta\chi^{AB}(\mathbf{R}) = \frac{a^2 \sin(2k_F z)}{\pi \hbar v_F |z|} [1 - \cos(2\mathbf{K} \cdot \mathbf{R})]. \quad (10.31)$$

We note that $\Delta\chi^{AB}(\mathbf{R})$ is small in comparison with $\chi^{AB}(\mathbf{R})$ by a factor $k_F/k_G \ll 1$, and, thus, this correction plays a role only around the points where the oscillating function $\chi^{AB}(\mathbf{R})$ vanishes. We emphasize that the spin susceptibility for semiconducting CNTs does not possess any significant dependence on the sublattices in contrast to metallic CNTs.

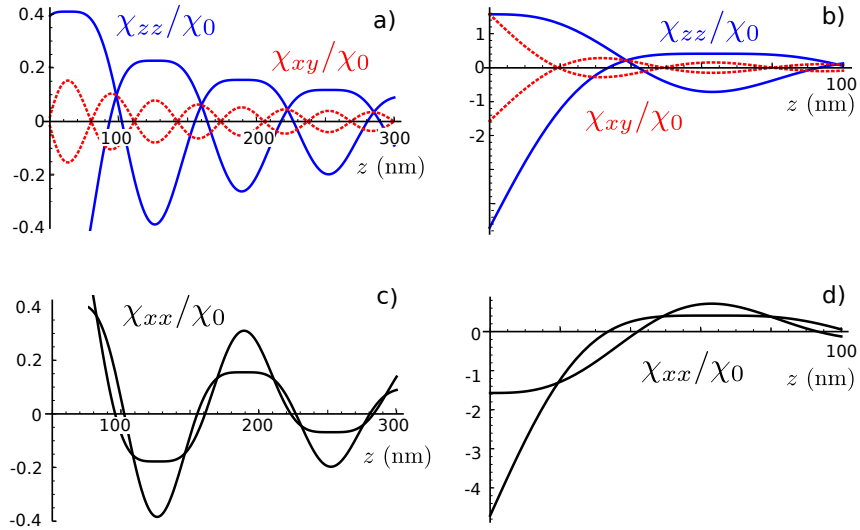


Figure 10.2: The spin susceptibility $\chi_{\alpha\beta}$, given in Eqs. (10.44)-(10.46), plotted as a function of distance between localized spins z , for a semiconducting (11,1)-CNT in the presence of spin orbit interaction and at zero B-field. Here, $\chi_0 = a^2 k_G / 2\pi \hbar v_F$. For clarity we suppress the fast oscillating factors and plot only the slowly varying envelopes at small (a,c) and large scales (b,d). The chemical potential $\mu = 472$ meV ($\delta\mu \equiv \mu - \hbar v_F k_G + \beta_+ = 1$ meV) is tuned inside the gap opened by SOI with corresponding value $2\beta_+ = 1.7$ meV for a (11,1)-CNT. [34] The diagonal components χ_{zz} [(a,b) blue full curve] and χ_{xx} (c,d) oscillate with period $2\pi/k_{+,-} \approx 2\pi/k_F$. In contrast to that, the off-diagonal component χ_{xy} [(a,b) red dashed curve], oscillates with period $2\pi/k_{+,+} \approx \pi/k_F$. All components decay as $1/z$. Note that the diagonal and off-diagonal components are of comparable size.

10.5 RKKY in the presence of SOI

In the presence of spin orbit interaction, the spin space is no longer invariant under rotations, and as a consequence the spin susceptibility is described by the tensor $\chi_{\alpha\beta}^{ij}$ [see Eq. (10.2)] with non-vanishing off-diagonal components. In this case it is more convenient to work in the framework of retarded Green functions[15] in which the RKKY Hamiltonian H_{RKKY} is given by Eq. (10.3). Below we neglect the weak dependence of the susceptibility on the sublattice discussed above and focus on the SOI effects. The Green functions in the energy-momentum space can be expressed as

$$G(k, \epsilon + i0^+) = \sum_{\gamma} [G_0(\gamma, k, \epsilon) + G_1(\gamma, k, \epsilon)s_z], \quad (10.32)$$

where the diagonal and off-diagonal (in spin space) Green functions are given by

$$G_0(\gamma, k, \epsilon) = \frac{k_G}{\hbar v_F} \sum_{\eta=\pm 1} \frac{1}{k_{\gamma\eta}^2 - k^2 + i0^+}, \quad (10.33)$$

$$G_1(\gamma, k, \epsilon) = -\frac{k_G}{\hbar v_F} \sum_{\eta=\pm 1} \frac{\eta}{k_{\gamma\eta}^2 - k^2 + i0^+}. \quad (10.34)$$

Here, to simplify notations, we introduced the wavevector $k_{\eta'}$, defined as (with $\eta' = \gamma\eta$)

$$k_{\eta'} = \sqrt{2k_G(\epsilon - \hbar v_F k_G - \eta' \beta_+)/\hbar v_F}, \quad (10.35)$$

which can take both real and imaginary values. In a next step we transform the Green functions from momentum to real space,

$$G_{0,1}(\mathbf{R}, \epsilon + i0^+) = \frac{a}{2} \sum_{\gamma} \int \frac{dk}{2\pi} G_{0,1}(\gamma, k, \epsilon) e^{i(\gamma \mathbf{K} + \mathbf{k}) \cdot \mathbf{R}}, \quad (10.36)$$

leading to

$$G_0(\mathbf{R}, \epsilon) = -i \frac{ak_G}{2\hbar v_F} \cos(\mathbf{K} \cdot \mathbf{R}) \sum_{\eta=\pm 1} \frac{e^{ik_{\eta}|z|}}{k_{\eta} + i0^+}, \quad (10.37)$$

$$G_1(\mathbf{R}, \epsilon) = \frac{ak_G}{2\hbar v_F} \sin(\mathbf{K} \cdot \mathbf{R}) \sum_{\eta=\pm 1} \frac{\eta e^{ik_{\eta}|z|}}{k_{\eta} + i0^+}. \quad (10.38)$$

Substituting $G(\mathbf{R}, \epsilon) = G_0(\mathbf{R}, \epsilon) + G_1(\mathbf{R}, \epsilon)s_z$ into Eq. (10.3), we find for the RKKY Hamiltonian,

$$\begin{aligned} H_{RKKY} = & -\frac{J^2}{\pi} \text{Im} \left[-4I_i^z I_j^z \int_{-\infty}^{\epsilon_F} d\epsilon G_1^2(\mathbf{R}, \epsilon) \right. \\ & -4i(\mathbf{I}_i \times \mathbf{I}_j)_z \int_{-\infty}^{\epsilon_F} d\epsilon G_1(\mathbf{R}, \epsilon) G_0(\mathbf{R}, \epsilon) \\ & \left. + 2\mathbf{I}_i \cdot \mathbf{I}_j \int_{-\infty}^{\epsilon_F} d\epsilon [G_0^2(\mathbf{R}, \epsilon) + G_1^2(\mathbf{R}, \epsilon)] \right]. \end{aligned} \quad (10.39)$$

Here, the trace over spin degrees of freedom were calculated by using the following identities

$$\text{Tr}\{(\mathbf{I}_i \cdot \mathbf{s})(\mathbf{I}_j \cdot \mathbf{s})\} = 2\mathbf{I}_i \cdot \mathbf{I}_j, \quad (10.40)$$

$$\text{Tr}\{(\mathbf{I}_i \cdot \mathbf{s})s_z(\mathbf{I}_j \cdot \mathbf{s})\} = -2i(\mathbf{I}_i \times \mathbf{I}_j)_z, \quad (10.41)$$

$$\text{Tr}\{(\mathbf{I}_i \cdot \mathbf{s})s_z(\mathbf{I}_j \cdot \mathbf{s})s_z\} = 2(2I_i^z I_j^z - \mathbf{I}_i \cdot \mathbf{I}_j). \quad (10.42)$$

All integrals in Eq. (10.39) are of the same type,

$$\text{Im} \int_{-\infty}^{\epsilon_F} d\epsilon \frac{e^{ik_{\eta}|z|}}{k_{\eta} + i0^+} \frac{e^{ik_{\eta'}|z|}}{k_{\eta'} + i0^+} = \frac{\hbar v_F}{k_G} \text{si}(k_{\eta\eta'}|z|), \quad (10.43)$$

and can be easily evaluated by changing variables from the original ϵ to $k_\eta + k_{\eta'}$. We denote the real part of the sum of two Fermi wavevectors as $k_{\eta,\eta'} = \text{Re}[k_\eta(\epsilon_F) + k_{\eta'}(\epsilon_F)]$ with the indices $\eta, \eta' = \pm 1$. As a result, we arrive at the RKKY Hamiltonian in the form of Eq. (10.2), where the components of the spin susceptibility tensor $\chi_{\alpha\beta}^{ij} \equiv \chi_{\alpha\beta}(\mathbf{R})$ are explicitly given by

$$\begin{aligned}\chi_{zz} &= \frac{a^2 k_G}{2\pi\hbar v_F} \left[\text{si}(k_{+,+}|z|) + \text{si}(k_{-,-}|z|) \right. \\ &\quad \left. + 2 \cos(2\mathbf{K} \cdot \mathbf{R}) \text{si}(k_{-,+}|z|) \right],\end{aligned}\quad (10.44)$$

$$\begin{aligned}\chi_{xx} &= \frac{a^2 k_G}{2\pi\hbar v_F} \left(2\text{si}(k_{-,+}|z|) + \cos(2\mathbf{K} \cdot \mathbf{R}) \right. \\ &\quad \left. \times [\text{si}(k_{+,+}|z|) + \text{si}(k_{-,-}|z|)] \right),\end{aligned}\quad (10.45)$$

$$\begin{aligned}\chi_{xy} &= \frac{a^2 k_G}{2\pi\hbar v_F} \sin(2\mathbf{K} \cdot \mathbf{R}) \\ &\quad \times \left[\text{si}(k_{+,+}|z|) - \text{si}(k_{-,-}|z|) \right],\end{aligned}\quad (10.46)$$

with $\chi_{xx} = \chi_{yy}$, $\chi_{xy} = -\chi_{yx}$, and all other components being zero. First, we note that the off-diagonal components χ_{xy}, χ_{yx} are non-zero. They describe the response to a perturbation applied perpendicular to the nanotube axis. This opens up the possibility to test the presence of SOI in the system by measuring off-diagonal components of the spin susceptibility tensor $\chi_{\alpha\beta}$. Second, the spin response in a direction perpendicular to the z -axis cannot be caused by a perturbation along the z -axis, thus $\chi_{yz} = \chi_{xz} = 0$. This simply reflects the rotation-invariance of CNTs around their axes. The difference between the diagonal elements of the spin susceptibility tensor, $\chi_{xx} = \chi_{yy}$ and χ_{zz} , again arises from the SOI and is another manifestation of the broken rotation invariance of spin space. In total this means that the RKKY interaction given in Eq. (10.39) is anisotropic in the presence of SOI, giving rise to an Ising term $\propto I_i^z I_j^z$ and a Moryia-Dzyaloshinsky term $\propto (\mathbf{I}_i \times \mathbf{I}_j)_z$, in addition to the isotropic Heisenberg term $\propto \mathbf{I}_i \cdot \mathbf{I}_j$.

Quite remarkably, when the Fermi level is tuned close to the gap opened by the SOI, then the off-diagonal and diagonal components of the susceptibility tensor become of comparable magnitude, see Figs. 10.2 and 10.3. This has important consequences for a Kondo lattice system, where a highly anisotropic RKKY interaction will give rise to an ordered magnetic phase even at finite temperatures.[21] As a potential candidate for such a Kondo lattice [9] we might mention a CNT made out of the ^{13}C -isotope, [42] where each site of the graphene lattice contains a nuclear spin-1/2 to which the itinerant electrons couple via hyperfine interaction. [43]

We note that the susceptibility depends on two Fermi wavevectors via $k_{m'}$ in a rather complicated way (see Figs. 10.2 and 10.3). In the absence of SOI, we recover the result for the spin susceptibility on the same sublattice, $\chi^{AA}(\mathbf{R})$ [see Eq. (10.24)]. The leading term in the spin susceptibility for different sublattices, $\chi^{AB}(\mathbf{R})$, can be obtained from Eqs. (10.44) - (10.46) by putting a minus sign in front of $\cos(2\mathbf{K} \cdot \mathbf{R})$. In addition, as shown in

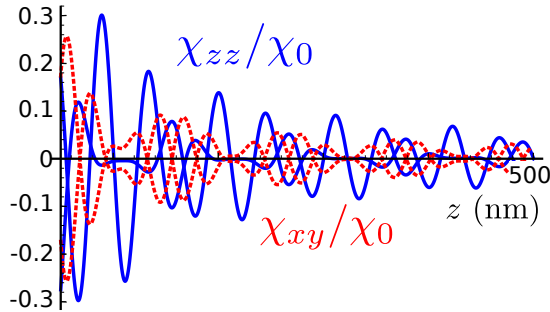


Figure 10.3: The same as Fig. 10.2 (a,b) but with the chemical potential $\mu = 474$ meV being tuned above the gap opened by SOI. The spin susceptibility decays as $1/z$ and exhibits beatings, with period determined by the SOI parameters.

Sec. 10.4.2, the spin susceptibility vanishes if the Fermi level is tuned inside the gap in semiconducting CNTs, so that both $k_{\pm}(\epsilon_F)$ are purely imaginary. If the chemical potential is inside the gap opened by the SOI, the Fermi wavevector $k_-(\epsilon_F)$ is still imaginary, at the same time $k_+(\epsilon_F)$ is real, giving $k_{+,+} = 2k_+(\epsilon_F)$, $k_{-,-} = 0$, and $k_{+,-} = k_+(\epsilon_F)$. This results in the behavior of the spin susceptibility shown in Fig. 10.2. The strength of the RKKY interaction decays oscillating as $1/R$. The oscillation period is determined by $k_{+,+}$ for χ_{xy} and by $k_{+,-}$ for χ_{xx} and χ_{zz} , see Fig. 10.2. If the chemical potential is above the SOI gap, then both wavevectors $k_{\pm}(\epsilon_F)$ are real, giving rise to oscillations with two different frequencies that result in beating patterns for the spin susceptibility, see Fig. 10.3.

10.6 RKKY with magnetic field

In Sec. 10.5 we demonstrated that the presence of SOI, which breaks rotation invariance in spin space, leads to an anisotropic spin susceptibility. Another way to break this rotation invariance is to apply a magnetic field, which also breaks time-reversal invariance. In this section we again neglect sublattice asymmetries discussed above and focus on the effects of a magnetic field \mathbf{B} applied along the nanotube axis z for a semiconducting nanotube. The Zeeman term $H_Z = \Delta_Z s_z = \mu_B B s_z$ lifts the spin degeneracy. Here, μ_B is the Bohr magneton. The orbital term $H_{orb} = \gamma \hbar v_F k_{mag}$ leads to a shift of the transverse wavevector k_G by k_{mag} , which finds its origin in the Aharonov-Bohm effect and is given by $k_{mag} = \pi B d |e| / 2h$ for a nanotube of diameter d . Thus, the valley degeneracy of the levels is also lifted. The spectrum of the effective Hamiltonian $H_0 + H_Z + H_{orb}$ in the case of a semiconducting nanotube is given by

$$\epsilon_{\gamma,s} = \hbar v_F k_{G,\gamma} + s(\gamma \beta_+ + \Delta_z) + \hbar v_F k^2 / 2k_{G,\gamma}, \quad (10.47)$$

where $k_{G,\gamma} = k_G + \gamma k_{mag}$. The Green functions in momentum space can be found similar to Eq. (10.32). As a result, we arrive at the following expression for the Green functions,

$$G(k, \epsilon + i0^+) = \sum_{\gamma} [G_0(\gamma, k, \epsilon) + G_1(\gamma, k, \epsilon)s_z], \quad (10.48)$$

where

$$G_0(\gamma, k, \epsilon) = \frac{k_{G,\gamma}}{\hbar v_F} \sum_s \frac{1}{\kappa_{\gamma,s}^2 - k^2 + i0^+}, \quad (10.49)$$

$$G_1(\gamma, k, \epsilon) = -\frac{k_{G,\gamma}}{\hbar v_F} \sum_s \frac{s}{\kappa_{\gamma,s}^2 - k^2 + i0^+}. \quad (10.50)$$

Here, we define wavevectors $\kappa_{\gamma,s}$ as a function of the energy ϵ from Eq. (10.47) as

$$\kappa_{\gamma,s} = \sqrt{\frac{2k_{G,\gamma}[\epsilon - \hbar v_F k_{G,\gamma} - s(\gamma\beta_+ + \Delta_z)]}{\hbar v_F}}, \quad (10.51)$$

which can take both non-negative real and imaginary values. The Green functions in real space are found by Fourier transformation,

$$G_0(\mathbf{R}, \epsilon) = -i \sum_{\gamma,s} \frac{ak_{G,\gamma}}{2\hbar v_F} e^{i\gamma\mathbf{K}\cdot\mathbf{R}} \frac{e^{i\kappa_{\gamma,s}|z|}}{\kappa_{\gamma,s} + i0^+}, \quad (10.52)$$

$$G_1(\mathbf{R}, \epsilon) = -i \sum_{\gamma,s} \frac{ak_{G,\gamma}}{2\hbar v_F} e^{i\gamma\mathbf{K}\cdot\mathbf{R}} \frac{se^{i\kappa_{\gamma,s}|z|}}{\kappa_{\gamma,s} + i0^+}. \quad (10.53)$$

By substituting Eqs. (10.52) and (10.53) into Eq. (10.39), we arrive at the effective RKKY Hamiltonian. Since $k_{mag}/k_G \ll 1$, we can neglect the dependence of the spectrum slope on the magnetic field, which simplifies the calculations considerably.

At the end we arrive at the following expressions for the spin susceptibility tensor components

$$\begin{aligned} \chi_{xx} &= \frac{a^2 k_G}{4\pi \hbar v_F} \\ &\times \sum_{\gamma,s} \left[\text{si}(k_{\gamma,s;\gamma,\bar{s}}|z|) + \cos(2\mathbf{K} \cdot \mathbf{R}) \text{si}(k_{\gamma,s;\bar{\gamma},\bar{s}}|z|) \right], \end{aligned} \quad (10.54)$$

$$\begin{aligned} \chi_{zz} &= \frac{a^2 k_G}{4\pi \hbar v_F} \\ &\times \sum_{\gamma,s} \left[\text{si}(k_{\gamma,s;\gamma,s}|z|) + \cos[2\mathbf{K} \cdot \mathbf{R}] \text{si}(k_{\gamma,s;\bar{\gamma},s}|z|) \right], \end{aligned} \quad (10.55)$$

$$\chi_{xy} = \frac{a^2 k_G}{4\pi \hbar v_F} \sum_{\gamma,s} \gamma s \sin[2\mathbf{K} \cdot \mathbf{R}] \text{si}(k_{\gamma,s;\bar{\gamma},\bar{s}}|z|), \quad (10.56)$$

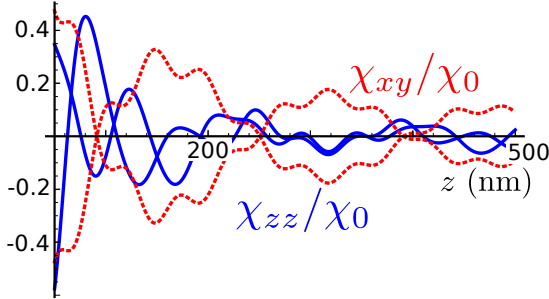


Figure 10.4: The same as Fig. 10.2 (a,b) but with the chemical potential $\mu = 472.7$ meV being tuned in such a way that there are three pairs of states at the Fermi level and with a magnetic field $B = 1$ T. The spin susceptibility decays as $1/z$ and exhibits beatings, with period determined by the SOI parameters and the magnetic field.

with $\chi_{xx} = \chi_{yy}$, $\chi_{xy} = -\chi_{yx}$, and the rest being zero. Here, we use the notation $k_{\gamma,s;\gamma',s'} = \text{Re}[\kappa_{\gamma,s}(\epsilon_F) + \kappa_{\gamma',s'}(\epsilon_F)]$. Again, the RKKY interaction decays at large distances as $1/R$. The spin susceptibility also exhibits oscillations and beating patterns (similar to ones shown in Fig. 10.3) determined by four different Fermi wavevectors $k_{\gamma s}(\epsilon_F)$, see Fig. 10.4. Finally, we note that the same beating patterns arises also for nanowires with parabolic spectrum in the presence of a magnetic field giving rise to a Zeeman splitting.

10.7 Spin Fluctuations

The spin susceptibility is a fundamental characteristics of the system. At zero frequency it describes the RKKY interaction between localized spins. At finite frequencies ω the spin susceptibility gives access to the equilibrium spin noise in the system. For a general observable, s_α , the fluctuation-dissipation theorem[14] connects the dynamical structure factor $S_{\alpha\alpha}(\mathbf{q}, \omega) = (1/2\pi) \int dt \langle s_\alpha(\mathbf{q}, t) s_\alpha(-\mathbf{q}, 0) \rangle e^{i\omega t}$, describing equilibrium fluctuations, with the linear response susceptibility, $\chi_{\alpha\alpha}(\mathbf{q}, \omega) = (-i/\hbar) \int dt \Theta(t) \langle [s_\alpha(\mathbf{q}, t), s_\alpha(-\mathbf{q}, 0)] \rangle e^{i\omega t}$,

$$\text{Im}\chi_{\alpha\alpha}(\mathbf{q}, \omega) = \frac{\pi}{\hbar} (e^{-\frac{\hbar\omega}{k_B T}} - 1) S_{\alpha\alpha}(\mathbf{q}, \omega), \quad (10.57)$$

for $\omega > 0$. Below we calculate the spin susceptibility for both metallic and semiconducting nanotubes at finite frequencies, and obtain via Eq. (10.57) the spin correlation function (spin noise) $S_{\alpha\alpha}(\mathbf{R}, \omega)$ in real space at zero temperature,

$$S_{\alpha\alpha}(\mathbf{R}, \omega) = -\frac{\hbar}{\pi} \text{Im}\chi_{\alpha\alpha}(\mathbf{R}, \omega), \quad (10.58)$$

Here, we assumed that the system is invariant under parity transformation so that $\chi(\mathbf{q}, \omega)$ becomes an even function of \mathbf{q} . For simplicity, we consider only the case without SOI.

10.7.1 Metallic nanotubes

The spin susceptibility at finite Matsubara frequencies ω_n is given by

$$\chi_0(\mathbf{R}, i\omega_n) = \frac{2}{\hbar} \int_0^\infty d\tau G_0(\mathbf{R}, \tau) G_0(-\mathbf{R}, -\tau) e^{i\omega_n \tau}, \quad (10.59)$$

where we modified Eq. (10.5) accordingly, and the Green function $G_0(\mathbf{R}, \tau)$ was found before [see Eqs. (10.16) and (10.17)]. For the spin susceptibility on the same sublattice we get

$$\begin{aligned} \chi_0^{AA}(\mathbf{R}, i\omega_n) &= \frac{2a^2}{\pi^2 \hbar} \cos^2(\mathbf{K} \cdot \mathbf{R}) \\ &\times \int_0^\infty d\tau e^{i\omega_n \tau} \frac{[z \sin(k_F z)]^2 - [v_F \tau \cos(k_F z)]^2}{[(v_F \tau)^2 + z^2]^2}. \end{aligned} \quad (10.60)$$

Introducing the notation

$$I_n(x) = \int_0^\infty d\tau \frac{\tau^n e^{i\tau x}}{(1 + \tau^2)^2}, \quad (10.61)$$

where $n = 0, 2$, the susceptibility can be rewritten as

$$\begin{aligned} \chi_0^{AA}(\mathbf{R}, i\omega_n) &= \frac{2a^2}{\pi^2 \hbar v_F |z|} \cos^2(\mathbf{K} \cdot \mathbf{R}) \\ &\times \left[\sin^2(k_F z) I_0 \left(\frac{\omega_n |z|}{v_F} \right) - \cos^2(k_F z) I_2 \left(\frac{\omega_n |z|}{v_F} \right) \right]. \end{aligned} \quad (10.62)$$

The asymptotics of $I_n(x)$ for small x is given by $I_0(x) \approx \pi/4 + ix/2$ and $I_2(x) \approx \pi(1 - 2x)/4 - ix(\ln x + \gamma_e - 1/2)$, where γ_e is the Euler constant. Performing the standard analytic continuation from Matsubara to real frequencies, [14] we obtain the spin susceptibility $\chi_0^{AA}(\omega)$, and from its imaginary part the spin noise, see Eq. (10.58). Explicitly, the dynamical structure factor at zero temperature and for $v_F \gg \omega |z| \geq 0$ is given by

$$S^{AA}(\mathbf{R}, \omega) = -\frac{2a^2 \omega}{\pi^2 v_F^2} \cos^2(\mathbf{K} \cdot \mathbf{R}) \cos^2(k_F z). \quad (10.63)$$

For the susceptibility on different sublattices we find

$$\begin{aligned} \chi_0^{AB}(\mathbf{R}, i\omega_n) &= -\frac{2a^2}{\pi^2 \hbar v_F |z|} \sin^2(\mathbf{K} \cdot \mathbf{R}) \\ &\times \left[\sin^2(k_F z) I_2 \left(\frac{\omega_n |z|}{v_F} \right) - \cos^2(k_F z) I_0 \left(\frac{\omega_n |z|}{v_F} \right) \right], \end{aligned} \quad (10.64)$$

with the corresponding dynamical structure factor being given by

$$S^{AB}(\mathbf{R}, \omega) = -\frac{2a^2 \omega}{\pi^2 v_F^2} \sin^2(\mathbf{K} \cdot \mathbf{R}) \sin^2(k_F z). \quad (10.65)$$

The dynamical structure factors $S^{AA}(\mathbf{R}, \omega)$ and $S^{AB}(\mathbf{R}, \omega)$ are linear in ω , and, as expected, vanish at zero frequency (we recall that we work at zero temperature). Moreover, the noise is strongly suppressed at some special points R_z in space that satisfy the condition $k_F z = n\pi/2$, where n is an integer.

In the opposite limit $\omega|z| \gg v_F$ we use the following asymptotics, $I_0(x) \approx i/x + \pi x e^{-x}/2$ and $I_2(x) \approx -2i/x^3 - \pi x e^{-x}/2$ for $x \gg 1$. After analytic continuation, the dynamical structure factor is then given by

$$S^{AA}(\mathbf{R}, \omega) = \frac{a^2 \omega}{\pi^2 v_F^2} \cos^2(\mathbf{K} \cdot \mathbf{R}) \cos\left(\frac{\omega|z|}{v_F}\right), \quad (10.66)$$

$$S^{AB}(\mathbf{R}, \omega) = \frac{a^2 \omega}{\pi^2 v_F^2} \sin^2(\mathbf{K} \cdot \mathbf{R}) \cos\left(\frac{\omega|z|}{v_F}\right). \quad (10.67)$$

In this regime, $S^{AA}(\mathbf{R}, \omega)$ and $S^{AB}(\mathbf{R}, \omega)$ are not only linearly proportional to the frequency but also oscillate rapidly as a function of frequency. This implies that in real time the spin noise is only non-zero for times t and distances z satisfying $|z| = v_F t$.

10.7.2 Semiconducting nanotubes

For semiconducting CNTs all calculations for the frequency dependent susceptibility are similar to the ones for one-dimensional systems with parabolic spectrum, being available in the literature. [14] At zero temperature $\text{Im}\chi_{\alpha\alpha}(q, \omega)$ is given by

$$\begin{aligned} \text{Im}\chi_{\alpha\alpha}(q, \gamma, \gamma', \omega) &= -\frac{\pi}{2} \sum_k [\theta(\xi_{k,\gamma}) - \theta(\xi_{k+q,s,\gamma'})] \\ &\times \delta(\hbar\omega + \xi_{k,s,\gamma} - \xi_{k+q,s,\gamma'}). \end{aligned} \quad (10.68)$$

The upper and lower frequencies ω_{\pm} are defined as

$$\omega_{\pm}(q) = \left| \frac{v_F q^2}{2k_G} \pm \frac{v_F k_F}{k_G} |q| \right|. \quad (10.69)$$

The imaginary part of the spin susceptibility is non-zero only for frequencies

$$\omega_-(q) \leq |\omega| \leq \omega_+(q) \quad (10.70)$$

and is given by

$$\text{Im}\chi_{\alpha\alpha}(q, \gamma, \gamma', \omega) = -\frac{ak_G}{4\hbar v_F |q|} \text{sgn}(\omega). \quad (10.71)$$

To arrive at the expression in real space we perform the Fourier transformation,

$$\begin{aligned} \text{Im}\chi_{\alpha\alpha}(\mathbf{R}, \omega) &= (1 \pm \cos(2\mathbf{K} \cdot \mathbf{R})) \\ &\times \frac{a^2 k_G}{4\pi\hbar v_F} \text{Im} \int dq \frac{e^{iqz}}{|q|} \text{sgn}(\omega), \end{aligned} \quad (10.72)$$

where the range of the q -integration is determined from Eq. (10.70), and the positive (negative) sign corresponds to $\chi_{\alpha\alpha}^{AA}$ ($\chi_{\alpha\alpha}^{AB}$). For high frequencies, $\omega > v_F k_F^2 / 2k_G$, the dynamical structure factor is given by

$$S(\mathbf{R}, \omega) = (1 \pm \cos(2\mathbf{K} \cdot \mathbf{R})) \frac{a^2 k_G}{2\pi^2 v_F} \times [\text{si}(q_+(\omega)|z|) - \text{si}(q_-(\omega)|z|)] \text{sgn}(\omega), \quad (10.73)$$

where wavevectors $q_{\pm}(\omega)$ are positive solutions of the equations $|\omega| = |\omega_{\pm}(q_{\pm})|$. For low frequencies, $0 < \omega \leq v_F k_F^2 / 2k_G$, the same equation $|\omega| = |\omega_{-}(q_{-,i})|$ has three non-negative solutions, [14] $q_{-,1} \leq q_{-,2} \leq q_{-,3}$. In this case $S(\mathbf{R}, \omega)$ is given by

$$S(\mathbf{R}, \omega) = (1 \pm \cos(2\mathbf{K} \cdot \mathbf{R})) \frac{a^2 k_G}{2\pi^2 v_F} \text{sgn}(\omega) \times [\text{si}(q_+(\omega)|z|) - \text{si}(q_{-,1}(\omega)|z|) + \text{si}(q_{-,2}(\omega)|z|) - \text{si}(q_{-,3}(\omega)|z|)]. \quad (10.74)$$

We note that the expression is composed of several contributions and thus leads to beating patterns of the spin noise, similar to the one before for the spin susceptibility.

10.8 Graphene nanoribbons

10.8.1 The effective Hamiltonian

In the last part of this work, we turn to graphene nanoribbons, which are finite-size sheets of graphene.[44] The nanoribbon is assumed to be aligned along the z -direction and to have a finite width $W = Na$ in x -direction, with N being the number of unit cells in this transverse direction. Here, we focus on armchair nanoribbons, characterized by the fact that the x -axis points along one of the translation vectors of the graphene lattice. The effective Hamiltonian is given by

$$H_0 = \hbar v_F (\gamma k_x \sigma_1 + k_z \sigma_2), \quad (10.75)$$

which determines the low-energy spectrum around the two Dirac points $\mathbf{K} = -\mathbf{K}' = (4\pi/3a, 0)$. Here, k_z is the momentum in z -direction. The momentum k_x in x -direction is quantized due to the vanishing boundary conditions imposed on the extended nanoribbon.[44] If the width of the GNR is such that $N = 3M + 1$, where M is a positive integer, the GNR is metallic with $k_x = 0$. Otherwise, the nanoribbon is semiconducting.

The eigenstates are written as $\psi = \sum_{\sigma\gamma} \phi_{\sigma\gamma} e^{i\gamma K_x x}$, $\Phi = (\phi_{AK}, \phi_{BK}, \phi_{AK'}, \phi_{BK'})$, where $\sigma = A, B$. The corresponding spectrum and wavefunctions that satisfy the vanishing boundary conditions (for ψ) are given by

$$\Phi_{\zeta}^{\epsilon, k_z} = e^{ik_z z} (-i\zeta, 1, i\zeta, -1), \quad (10.76)$$

$$\epsilon_{\zeta} = \zeta \hbar v_F k_z \quad (10.77)$$

for a metallic GNR, and

$$\Phi_{\pm}^{\epsilon, k_z} = e^{ik_z z} (\pm e^{i\varphi_s + ixk_x^{min}}, e^{ixk_x^{min}}, \mp e^{i\varphi_s - ixk_x^{min}}, -e^{-ixk_x^{min}}), \quad (10.78)$$

$$\epsilon_{\pm} = \pm \hbar v_F \sqrt{(k_x^{min})^2 + k_z^2} \quad (10.79)$$

for a semiconducting GNR. Here, $\zeta = \pm 1$ is the eigenvalue of the Pauli matrix σ_2 , and we use the notation $e^{i\varphi_s} = [k_x^{min} - ik_z]/\sqrt{(k_x^{min})^2 + k_z^2}$, with $|k_x^{min}| = \pi/3(N+2)a$.

10.8.2 Spin susceptibility

Without SOI

To calculate the spin susceptibility for a metallic nanoribbon that has a linear spectrum given by Eq. (10.77), we again work in the imaginary time formalism, see Eq. (10.5). The calculations are quite similar to the ones presented before in Sec. 10.4.1. The only change in the expressions for the spin susceptibility in comparison with a metallic nanotube [see Eqs. (10.18) and (10.19)] is in the fast oscillating prefactor,

$$\chi_0^{AA}(\mathbf{R}_i, \mathbf{R}_j) = -\chi_0^{AB}(\mathbf{R}_i, \mathbf{R}_j) = -\frac{a^2}{2\pi\hbar v_F |z|} \times \sin^2(\mathbf{K} \cdot \mathbf{R}_i) \sin^2(\mathbf{K} \cdot \mathbf{R}_j) \cos(2k_F z). \quad (10.80)$$

Similarly, for semiconducting nanoribbons the spin susceptibility is given by Eqs. (10.24) and (10.27), where the fast oscillating prefactors $1 \pm \cos(2\mathbf{K} \cdot \mathbf{R})$ are replaced by $\sin^2(\mathbf{K} \cdot \mathbf{R}_i) \sin^2(\mathbf{K} \cdot \mathbf{R}_j)$.

With SOI

The intrinsic SOI in graphene is only several μeV , so it is rather weak. Moreover, the Rashba SOI generated by an externally applied electric field E is in the range of tenths of μeV for $E = 1 \text{ V/nm}$. [34, 45] Such small SOI values might be hard to observe. However, the Rashba SOI generated by a spatially varying magnetic field opens new perspectives for spintronics in graphene. [13] In this case, the SOI strength can be exceptionally large, reaching hundreds of meV. A nanoribbon in the presence of a rotating magnetic field with period $2\pi/k_n$, described by the Zeeman Hamiltonian

$$H_n^\perp = \Delta_Z [s_y \cos(k_n z) + s_z \sin(k_n z)], \quad (10.81)$$

is equivalent to a nanoribbon with Rashba SOI in the presence of a uniform magnetic field,

$$H^\perp = U_n^\dagger (H_0 + H_n^\perp) U_n = H_0 + \Delta_Z s_y + \Delta_{so}^n s_x \sigma_2, \quad (10.82)$$

where the unitary gauge transformation is given by $U_n = \exp(ik_n z s_x / 2)$. The period of the magnetic field determines the strength of the Rashba SOI $\Delta_{so}^n = \hbar v_F k_n / 2$, while the amplitudes of the uniform and the rotating fields are the same and given by Δ_Z .[10, 13] The spectrum of a metallic (semiconducting) GNR in the presence of such SOI consists of two cones (parabolas) shifted along the momentum axis against each other by $k_n / 2$. Every branch of the spectrum possesses a well-defined spin polarization perpendicular to the z -axis that is along the nanoribbon. A uniform magnetic field only slightly modifies the spectrum by opening a gap at zero momentum. In the following discussion we neglect the uniform magnetic field working in the regime where the induced Rashba SOI is stronger than the Zeeman energy $2\Delta_Z$.

As a result, similar to the semiconducting nanowire, one can gauge away the momentum shifts by rotating the spin coordinate system as follows,

$$I_x(\mathbf{R}) = I_x \cos(k_n z) + I_y \sin(k_n z), \quad (10.83)$$

$$I_y(\mathbf{R}) = I_y \cos(k_n z) - I_x \sin(k_n z), \quad (10.84)$$

$$I_z(\mathbf{R}) = I_z. \quad (10.85)$$

The same transformation should be applied to the electron spin operators $\hbar \mathbf{s}/2$. The effective RKKY Hamiltonian in this rotated coordinate system is the same as in the system without SOI and is given by Eq. (10.80). To return to the laboratory frame, we perform the following change

$$\begin{aligned} \mathbf{I}_i \cdot \mathbf{I}_j \rightarrow \mathbf{I}_i(\mathbf{R}_i) \cdot \mathbf{I}_j(\mathbf{R}_j) &= \cos(k_n z) \mathbf{I}_i \cdot \mathbf{I}_j \\ &+ [1 - \cos(k_n z)] I_i^z I_j^z - \sin(k_n z) (\mathbf{I}_i \times \mathbf{I}_j)_z. \end{aligned} \quad (10.86)$$

The spin susceptibility tensor has non-vanishing off-diagonal components, which, again, indicate a broken invariance of spin space induced by the magnetic field or the Rashba SOI. As before, this gives rise to anisotropic RKKY interactions of Ising and Moryia-Dzyaloshinski form.

10.9 Conclusions

In the present work we studied the Rudermann-Kittel-Kasuya-Yosida (RKKY) interaction in carbon nanotubes and graphene nanoribbons at zero temperature in the presence of spin orbit interaction. Our main results are summarized in the following.

The spin susceptibility in metallic CNTs, characterized by a Dirac spectrum (gapless and linear), crucially depends on whether the localized spins that interact with each other are from the same or from different sublattices. In particular, if the Fermi level is tuned exactly to the Dirac point where the chemical potential is zero the interaction is of ferromagnetic type for spins on A - A or B - B lattice sites, whereas it is of antiferromagnetic type for spins on A - B lattice sites. In semiconducting CNTs, with a sizable bandgap, the spin susceptibility depends only slightly on the sublattices. In all cases, the spin

susceptibility is an oscillating function that decays as $1/R$, where R is the distance between the localized spins.

The spin orbit interaction breaks the spin degeneracy of the spectrum and the direction invariance of the spin space. As a result, the spin susceptibility is described by the tensor $\chi_{\alpha\beta}$ that has two non-zero off-diagonal components $\chi_{xy} = -\chi_{yx}$, the finite values of which signal the presence of SOI in the system. Moreover, the RKKY interaction is also anisotropic in the diagonal terms, $\chi_{zz} \neq \chi_{xx} = \chi_{yy}$. Quite surprisingly, we find that all non-zero components, diagonal and off-diagonal, can be tuned to be of equal strength by adjusting the Fermi level. These anisotropies, giving rise to Ising and Moriya-Dzyaloshinski RKKY interactions, thus open the possibility to have magnetic order in low-dimensional systems at finite temperature. [21]

We note that, in contrast to semiconducting nanowires, the SOI cannot be gauged away by a unitary transformation in CNTs, giving rise to a more complicated dependence of $\chi_{\alpha\beta}$ on the SOI parameters. In the same way, a magnetic field along the CNT axis breaks both the spin and the valley degeneracy, leading to a dependence of the spin susceptibility on four different Fermi wavevectors.

The spin susceptibility at finite frequencies also allows us to analyze the spin noise in the system via the fluctuation-dissipation theorem. We find that the dynamical structure factor $S_{\alpha\alpha}(\mathbf{R}, \omega)$ is linear in frequency and oscillates in real space.

Metallic armchair GNRs behave similarly to metallic CNTs. Indeed, in both cases the spin susceptibility shows a strong dependence on the sublattices, with, however, different fast oscillating prefactors. A Rashba-like SOI interaction can be generated in armchair GNR by periodic magnetic fields. In contrast to CNTs with intrinsic SOI, this field-generated SOI can be gauged away giving rise to a simple structure of the spin susceptibility tensor.[46]

In this work we have ignored interaction effects. However, it is well-known that in one- and two-dimensional systems electron-electron interactions can lead to interesting modifications of the spin susceptibility, for instance with a slower power law decay such as $1/R^g$, with $0 < g \leq 1$ in a Luttinger liquid approach to interacting one-dimensional wires. [17, 8] It would be interesting to extend the present analysis and to allow for interaction effects[37] in the spin susceptibility for carbon based materials in the presence of spin orbit interaction, in particular for metallic CNTs and GNRs at the Dirac point.

Acknowledgements This work is supported by the Swiss NSF, NCCR Nanoscience, and NCCR QSIT.

Bibliography

- [1] M. A. Ruderman and C. Kittel, Phys. Rev. B **96**, 99 (1954).
- [2] T. Kasuya, Prog. Theor. Phys. **16**, 45 (1956).
- [3] K. Yosida, Phys. Rev. **106**, 893 (1957).

- [4] N. J. Craig, J. M. Taylor, E. A. Lester, C. M. Marcus, M. P. Hanson, and A. C. Gossard, *Science* **304**, 565 (2004).
- [5] Y. Rikitake and H. Imamura, *Phys. Rev. B* **72**, 033308 (2005).
- [6] D. S. Wang, A. G. Fowler, and L. C. L. Hollenberg, *Phys. Rev. A* **83**, 020302 (2011).
- [7] L. Trifunovic, O. Dial, M. Trif, J. R. Wootton, R. Abebe, A. Yacoby, and D. Loss, *Phys. Rev. X* **2**, 011006 (2012).
- [8] B. Braunecker, P. Simon, and D. Loss, *Phys. Rev. Lett.* **102**, 116403 (2009).
- [9] B. Braunecker, P. Simon, and D. Loss, *Phys. Rev. B* **80**, 165119 (2009).
- [10] B. Braunecker, G. I. Japaridze, J. Klinovaja, and D. Loss, *Phys. Rev. B* **82**, 045127 (2010).
- [11] M. Kjaergaard, K. Wolms, and K. Flensberg, *Phys. Rev. B* **85**, 020503 (2012).
- [12] J. Klinovaja, P. Stano, and D. Loss, *Phys. Rev. Lett.* **109**, 236801 (2012).
- [13] J. Klinovaja and D. Loss, *Phys. Rev. X* **3**, 011008 (2013).
- [14] G. Giuliani and G. Vignale, *Quantum Theory of the Electron Liquid*, (Cambridge University Press, Cambridge, 2005).
- [15] H. Imamura, P. Bruno, and Y. Utsumi, *Phys. Rev. B* **69**, 121303 (2004).
- [16] S. Chesi and D. Loss, *Phys. Rev. B* **82**, 165303 (2010).
- [17] R. Egger and H. Schoeller, *Phys. Rev. B* **54**, 16337 (1996).
- [18] R. A. Zak, D. L. Maslov, and D. Loss, *Phys. Rev. B* **85**, 115424 (2012).
- [19] P. Simon, B. Braunecker, and D. Loss, *Phys. Rev. B* **77**, 045108 (2008).
- [20] S. Chesi, R. A. Zak, P. Simon, and D. Loss, *Phys. Rev. B* **79**, 115445 (2009).
- [21] D. Loss, F. L. Pedrocchi, and A. J. Leggett, *Phys. Rev. Lett.* **107**, 107201 (2011).
- [22] M. Governale and U. Zülicke, *Physics* **5**, 34 (2012).
- [23] M. S. Grinolds, S. Hong, P. Maletinsky, L. Luan, M. D. Lukin, R. L. Walsworth, and A. Yacoby, arXiv:1209.0203.
- [24] L. Zhou, J. Wiebe, S. Lounis, E. Vedmedenko, F. Meier, S. Blugel, P. H. Dederichs, and R. Wiesendanger, *Nature Phys.* **6**, 187 (2010).
- [25] M. A. H. Vozmediano, M. P. Lopez-Sancho, T. Stauber, and F. Guinea, *Phys. Rev. B* **72**, 155121 (2005).

- [26] V. K. Dugaev, V. I. Litvinov, and J. Barnas, Phys. Rev. B **74**, 224438 (2006).
- [27] S. Saremi, Phys. Rev. B **76**, 184430 (2007).
- [28] A. M. Black-Schaffer, Phys. Rev. B **81**, 205416 (2010).
- [29] M. Sherafati and S. Satpathy, Phys. Rev. B **83**, 165425 (2011).
- [30] E. Kogan, Phys. Rev. B **84**, 115119 (2011).
- [31] R. Saito, G. Dresselhaus, and M. S. Dresselhaus, *Physical Properties of Carbon Nanotubes*, (Imperial College Press, London, 1998).
- [32] We note that this sublattice dependence was missed in previous work. [9] However, the results of that work remain valid except that the short-distance ordering changes from ferro- to antiferromagnetic.
- [33] W. Izumida, K. Sato, and R. Saito, J. Phys. Soc. Jpn. **78**, 074707 (2009).
- [34] J. Klinovaja, M. J. Schmidt, B. Braunecker, and D. Loss, Phys. Rev. Lett. **106**, 156809 (2011).
- [35] J. Klinovaja, M. J. Schmidt, B. Braunecker, and D. Loss, Phys. Rev. B **84**, 085452 (2011).
- [36] B. Karmakar, D. Venturelli, L. Chirolli, F. Taddei, V. Giovannetti, R. Fazio, S. Roddaro, G. Biasiol, L. Sorba, V. Pellegrini, and F. Beltram, Phys. Rev. Lett. **107**, 236804 (2011).
- [37] A. Imambekov, T. L. Schmidt, and L. I. Glazman, Rev. Mod. Phys. **84**, 1253 (2012).
- [38] Y. Yafet, Phys. Rev. B **36**, 3948 (1987).
- [39] F. Kuemmeth, S. Ilani, D. C. Ralph, and P. L. McEuen, Nature **452**, 448 (2008).
- [40] T. S. Jespersen, K. Grove-Rasmussen, J. Paaske, K. Muraki, T. Fujisawa, J. Nygard, and K. Flensberg, Nat. Phys. **7**, 348 (2011).
- [41] F. Pei, Edward A. Laird, G. A. Steele, and L. P. Kouwenhoven, arXiv:1210.2622.
- [42] H. O. H. Churchill, A. J. Bestwick, J. W. Harlow, F. Kuemmeth, D. Marcos, C. H. Stwertka, S. K. Watson, and C. M. Marcus, Nat. Phys. **5**, 321 (2009).
- [43] J. Fischer, B. Trauzettel, and D. Loss, Phys. Rev. B **80**, 155401 (2009).
- [44] L. Brey and H. A. Fertig, Phys. Rev. B **73**, 235411 (2006).
- [45] J. Klinovaja, S. Gangadharaiah, and D. Loss, Phys. Rev. Lett. **108**, 196804 (2012).

- [46] We note that one-dimensional quantum wires can also be formed in gated bilayer graphene.[47] In this system, an effective SOI can be created by a fold (curvature) or by rotating magnetic fields.[48] The RKKY interaction in such quantum wires has a form similar to the one considered in Sec. 10.8.
- [47] I. Martin, Y. M. Blanter, and A. F. Morpurgo, Phys. Rev. Lett. **100**, 036804 (2008).
- [48] J. Klinovaja, G. J. Ferreira, and D. Loss, Phys. Rev. B **86**, 235416 (2012).

Chapter 10

Acknowledgements

First and foremost, I thank my supervisor Prof. Daniel Loss who accepted me as a PhD student three years ago and who guided me through all ups and downs of modern competitive research. I thank him for his knowledge and expertise, which he shared with me so generously, for all his patience, and for his sense of humour. His fascination about physics in general and about every problem in particular impresses me deeply. I am grateful to Prof. Daniel Loss for all discussions we had even if they were sometimes heated.

I would like to thank all my close collaborators. I am grateful to Dr. Denis Bulaev who introduced me to the field of carbon-based materials. I have benefited enormously from discussions with Dr. Manuel Schmidt with whom I spent a lot of time not only talking about physics but also searching for mistakes in Mathematica. I also would like to thank Dr. Suhas Gangadharaiah for all our conversations: no matter if they were about physics or about matters of life. I am also grateful to Dr. Peter Stano for the fruitful collaboration with a lot of intense discussions until the moment when even the smallest detail is completely clear. I thank Dr. Bernd Braunecker for sharing with me his profound knowledge of interacting systems.

I have enjoyed all these years in Basel. I would like to thank all members of the condensed matter theory group. In particular, I would like to acknowledge Prof. Dr. Christoph Bruder, Franziska Meier, Dr. Peter Stano, Fabio Pedrocchi, Dr. Diego Rainis, Luka Trifunovic, Dr. Dimitrije Stepanenko, Dr. Daniel Becker, Dr. Alexander Zyuzin, Christoph Kloeffel, Robert Zielke, Dr. Beat Roethlisberger, Dr. Vladimir Stojanovic, Dr. Kevin van Hoogdalem, Dr. Oleg Chalaev, Dr. Stefano Chesi, Dr. Mathias Duckheim, Dr. Jan Fisher, and Dr. Mircea Trif for all fruitful discussions we had, both scientific and otherwise.

I would like to thank my first teachers of physics and mathematics, Boris Timofeevich Yakovlev and Liliya Adamovna Pomaskina from the Pskov Technical Lyceum and Sergey Segreevich Vlasenko from the Academic Gymnasium of the St. Petersburg State University. These three persons awoke my interest to physics at the early stage. Especially, I am grateful to Prof. Dr. Nikolay Aleksandrovich Kirichenko. I still remember all late hours we spend trying to penetrate into the mysteries of physics (and also to get our marks). He was always strict but fair and his passion about physics was contagious. His style of work and his requirements to the understanding of the physical phenomena left an imprint on

me.

Last, but not least I would like to thank Prof. Pascal Simon for refereeing this thesis and Prof. Richard Warburton for chairing the defence exam.

Curriculum Vitae

Jelena Klinovaja

- Since September 2013 **Prize Postdoctoral Fellowship in Physics at Harvard University.**
- Since December 2012 **Postdoctoral associate in the Condensed Matter Theory group at the University of Basel.**
- 2009 - 2012 **PhD Student in the Condensed Matter Theory group at the University of Basel**, under the supervision of Prof. Dr. Daniel Loss. PhD degree with summa cum laude.
- 2007 - 2009 **Master studies at the Moscow Institute of Physics and Technology**, Department of General and Applied Physics. Thesis at the Institute of Solid State Physics of the Russian Academy of Science. Degree with summa cum laude.
Supervisor: Prof. V. Shikin. Master thesis: Reconstruction and instability of the charged surface of liquid helium.
- 2003 - 2007 **Bachelor studies at the Moscow Institute of Physics and Technology**, Department of General and Applied Physics. Thesis at the Institute of Solid State Physics of the Russian Academy of Science. Degree with summa cum laude.
Supervisor: Prof. V. Shikin. Bachelor thesis: Binodal-spinodal instabilities of the charged surface of liquid helium.
- 2003 **Graduated from the Academic Gymnasium of the St. Petersburg State University**, majoring in physics and mathematics.

List of Publications

1. **Topological Edge States and Fractional Quantum Hall Effect from Umklapp Scattering.**
Jelena Klinovaja and Daniel Loss,
arXiv:1302.6132.
2. **Fractional Fermions with Non-Abelian Statistics.**
Jelena Klinovaja and Daniel Loss,
Phys. Rev. Lett. **110**, 126402 (2013).
3. **Local Spin Susceptibilities of Low-Dimensional Electron Systems.**
Peter Stano, Jelena Klinovaja, Amir Yacoby, and Daniel Loss,
arXiv:1303.1151.
4. **RKKY interaction in carbon nanotubes and graphene nanoribbons.**
Jelena Klinovaja and Daniel Loss,
Phys. Rev. B **87**, 045422 (2013).
5. **Giant spin orbit interaction due to rotating magnetic fields in graphene nanoribbons.**
Jelena Klinovaja and Daniel Loss,
Phys. Rev. X **3**, 011008 (2013).
6. **Helical States in Curved Bilayer Graphene.**
Jelena Klinovaja, Gerson J. Ferreira, and Daniel Loss,
Phys. Rev. B **86**, 235416 (2012) (2012).
7. **Transition from fractional to Majorana fermions in Rashba nanowires.**
Jelena Klinovaja, Peter Stano, and Daniel Loss,
Phys. Rev. Lett. **109**, 236801 (2012).
8. **Realistic transport modeling for a superconducting nanowire with Majorana fermions.**
Diego Rainis, Luka Trifunovic, Jelena Klinovaja, and Daniel Loss,
Phys. Rev. B **87**, 024515 (2013).

-
9. **Exchange-based CNOT gates for singlet-triplet qubits with spin orbit interaction.**
Jelena Klinovaja, Dimitrije Stepanenko, Bertrand I. Halperin, and Daniel Loss,
Phys. Rev. B 86, 085423 (2012).
 10. **Composite Majorana Fermion Wavefunctions in Nanowires.**
Jelena Klinovaja and Daniel Loss,
Phys. Rev. B 86, 085408 (2012).
 11. **Electric-Field Induced Majorana Fermions in Armchair Carbon Nano-tubes.**
Jelena Klinovaja, Suhas Gangadharaiah, and Daniel Loss,
Phys. Rev. Lett. 108, 196804 (2012).
 12. **Carbon nanotubes in electric and magnetic fields.**
Jelena Klinovaja, Manuel J. Schmidt, Bernd Braunecker, and Daniel Loss,
Phys. Rev. B 84, 085452 (2011).
 13. **Helical modes in carbon nanotubes generated by strong electric fields.**
Jelena Klinovaja, Manuel J. Schmidt, Bernd Braunecker, and Daniel Loss,
Phys. Rev. Lett. 106, 156809 (2011).
 14. **Spin-selective Peierls transition in interacting one-dimensional conductors with spin-orbit interaction.**
Bernd Braunecker, George I. Japaridze, Jelena Klinovaja, and Daniel Loss,
Phys. Rev. B 82, 045127 (2010).
 15. **Mixed scenario of the charged helium surface reconstruction.**
Valerii Shikin and Elena Klinovaya,
Low Temp. Phys. 36, 142 (2010).